University of Bath

University of Bath

PHD

Erosive wear failure of spool valves

Pomeroy, Paul E.

Award date:
1995

Awarding institution:
University of Bath

Link to publication

Erosive Wear Failure of
Spool valves

Submitted by Paul E Pomeroy

for the degree of PhD

of the University of Bath

1995

Copyright

P.E. Pomeroy

UMI Number: U071057

UMI

Dissertation Publishing

ProQuest®

Synopsis

This thesis describes an investigation into the erosive wear of hydraulic spool valves. From this, two techniques have been identified to analyse both field and test specimens. Firstly, scanning electron micrographs to give pictorial information which allows visual comparisons to be made between components, and secondly, a new method has been developed using a Form Talysurf instrument to record component geometry in either a two or three dimensional format.

To complement the field results, controlled erosion tests have been performed on a purpose built test rig which produces accelerated particle erosion results at a known test condition with either Air Cleaner Fine Test Dust or a classified quartz dust. Using this facility it has been shown that:

- The erosion rate is independent of the spool opening, providing the spool opening is greater than the maximum particle size.

- The erosion rate is dependent upon the gravimetric concentration and the particle size distribution. This result confirms that component life can be extended with fine fluid filtration.

- The amount of material removed has been found to be approximately proportional to the differential pressure across the spool orifice. This supports the established view that the erosion rate is proportional to the kinetic energy of the impacting particles.

- Oil viscosity is the most important oil property in the prevention of erosion. The results indicate that the wear rate increases with a corresponding increase in viscosity.

- For the different oil formulations examined, the results show that the sulphur/phosphorous (S/P) based anti-wear additives give an improvement in the wear resistance when compared with base oil.

- From the different surface engineering techniques tested, the results confirm that the erosive wear resistance increases with material hardness. Significant improvements can be made when the hardness of the target surface is greater than the impinging particles.

- Comparing the spool results with the established particle erosion models has shown that the spool valve wear is significantly lower than that predicted by theory. Using computation fluid dynamics, this discrepancy has been found to be associated with a low particle collision efficiency, i.e. the majority of particles are carried in the oil streamlines through the metering orifice, and at shallow particle impact angles.

Acknowledgements

I would like to thank friends and colleagues from the University of Bath who have provided help and advice during my time at the University. A special mention should go to my academic supervisors Dr Nick Vaughan and Dr Derek Tilley for their support and guidance throughout the project.

Thanks goes to Gerry Jayne and Ron Barton of BP Lubricants Ltd, Sunbury, David Lakin of Ultra Hydraulics Ltd, Cheltenham, and the Science and Engineering Research Council (SERC) Grant No. GR/S 63206, for their technical and financial support.

Finally, a special thank you to my wife, Jayne, who has provided continuous encouragement and support throughout.

Contents

List of Figures

List of Tables

Nomenclature & Abbreviations

Nomenclature

d	Spool diameter	m
k	Erosion constant	
m_p	Mass of erosive particles	kg
m_s	Mass of target surface removed	kg
t	Time	s
x	Spool opening	m
A_o	Orifice flow area	m^2
A_p	Particle surface area	m^2
C_q	Orifice flow coefficient	
D_a	Sieve diameter of an irregular particle	m
D_L	Maximum cord length of an irregular particle	m
D_p	Equivalent spherical diameter of an irregular particle	m
D_s	Spherical particle diameter	m
D_w	Maximum cord width of an irregular particle	m
E	Erosion (m_s / m_p)	
H_p	Particle hardness	$N\,m^{-2}$
H_v	Vickers hardness number	$kgf\,mm^{-2}$
H_s	Target surface hardness	$N\,m^{-2}$
P	Pressure (1 bar = 10^5 N m^{-2})	$N\,m^{-2}$
Q	Flow rate (1 L min^{-1} = 6×10^{-4} m^3 s^{-1})	$m^3\,s^{-1}$
R_e	Reynolds number	
S_e	Elongation shape factor (D_L / D_w)	
U	Velocity	$m\,s^{-1}$
V_p	Particle volume	m^3
α_a	Surface area shape factor	
α_v	Volume shape factor	
μ	Dynamic viscosity (1 cP = 0.1 Ns m^{-2})	$Ns\,m^{-2}$
ν	Kinematic viscosity (1 cSt = 1×10^{-6} m^2 s^{-1})	$m^2\,s^{-1}$

ρ Density   . . . . kg m^{-3}

Abbreviations

ACCTD	Air Cleaner Coarse Test Dust
ACFTD	Air Cleaner Fine Test Dust
ADC	Analogue to Digital Converter
AISI	American Iron and Steel Institute
APC	Automatic Particle Counter
ASCII	American Standard Code for Information Interchange
ASTM	American Society for Testing Materials
BSi	British Standards Institution
CETOP	Comité Européen des Transmissions Oléohydrauliques et Pneumatiques
CFD	Computational Fluid Dynamics
CLSM	Confocal Laser Scanning Microscope
CVD	Chemical Vapour Deposition
DAC	Digital to Analogue Converter
DIN	Deutsches Institut für Normung
EDM	Electro Discharge Machining
EDX	Energy Dispersive Analysis (X-ray spectrometer)
EEC	European Economic Community
EP	Extreme Pressure additive
I/O	Digital Input/Output
IP	Institute of Petroleum
ISO	International Organisation for Standardisation
NAS	National Aerospace Standard
O/D	Outside diameter
PQ	Particle Quantifier
PVD	Physical Vapour Deposition
RPD	Rotary Particle Depositor
SAE	Society of Automotive Engineers
SEM	Scanning Electron Microscope
S/P	Sulphur / Phosphorus
VI	Viscosity Index
XRF	X-Ray Fluorescence (smear analysis)
ZDDP	Zinc Dialkyl Dithiophosphate

1

Introduction

1.1. Preface

Hydraulic systems are used extensively throughout the world to transmit power between two or more points. To fulfil this function, they contain four key elements: a method of converting mechanical to hydraulic power (pumps), a fluid capable of transferring the hydraulic power, a method of converting the hydraulic power back into either linear or rotary motion (actuators and motors), and finally a control device which limits the flow (speed) and/or the pressure (force) within the system (spool or poppet valves).

In the majority of applications, the working fluid is based upon a mineral oil formulation. This has the advantage of providing good lubrication/load carrying properties over a wide range of operating temperatures. To ensure and maintain a satisfactory system performance, it is important that the oil properties do not degrade and the levels of solid particles carried by the oil are controlled. Unfortunately, it is common for these two simple requirements to be neglected and therefore the sensitive components within the system become unreliable or fail completely.

A primary candidate for this role is an electro-hydraulic servo valve. Generally, these are recognised as being contaminant sensitive due to the manufacturing precision required to produce the necessary valve characteristics, i.e. fast response, good linearity, low hysteresis, small leakage flows, etc. Many of these features are dependent upon the condition of the spool metering orifices within the valve.

This demonstrates that there is an industrial and an academic requirement to obtain an understanding into the wear processes occurring within spool valves. To address this requirement, the project reported within this thesis has been undertaken at the University of Bath, with support from the Science and Engineering Research Council (SERC) and two industrial partners: BP Lubricants Ltd and Ultra Hydraulics Ltd, to examine the effects of solid particles and the mineral oil formulation on the erosive wear mechanism occurring within servo valves.

1.2. Hydraulic System Contaminants

Contamination has been defined as *Any substrate or material which interferes with the ability of the hydraulic fluid to transmit power and lubricate the moving parts of components* [1]. The source of the contaminant may be attributed to three distinct areas: built-in, internally generated, or introduced either unintentionally by the operator or by the environmental operating conditions. Across these areas, the contamination may take the form of air, chemical or solid particles.

Air contamination may be in the form of free or dissolved air. If free air exists within the oil, the system performance is usually affected by the reduction in the bulk modulus [2]. It will also accelerate the degradation of the mineral oil by increasing the oxidation rate. By good system design it is possible to minimise the problems associated with air. For example, air can be released in a correctly designed reservoir which allows the return oil flow to recirculate around the tank, encouraging air release from the free surface. A common source for air entrainment is in pump suction lines, where often the pressure falls below atmospheric pressure.

Chemical contamination is usually associated with an increase in the acidity level of the oil. However, there are other associated conditions. For example, free water in a mineral oil system can cause surface corrosion, promote fluid oxidation and acid formation which irreversibly degrades the fluid and decreases its lubricity. Often if solvents are used in the manufacturing process and are not completely removed, they can have an adverse effect. It has been shown that even dissolved levels of halogenated solvents (1.1.1 Trichloroethane, etc) can cause severe corrosion and erosion of component surfaces [1].

The type and quantity of solid particles, as with the other two categories, is very system dependent. The majority of the problems associated with solid particles are concerned with erosion and abrasive wear within the clearances of moving components, an area which has previously attracted some research work. The solid particle types present in the system are usually similar to the materials used in the manufacture of the individual components and to the external working environment.

In many systems, significant contaminant ingression occurs during the manufacture and assembly of the components. Once the contaminant is included in the system, it will play a significant role in the generation of the internal debris. Typical manufacturing contaminants include: machining burrs and swarf, casting sand, scale, rust, paint, weld splatter, grinding debris, workshop dust, water, etc. Similarly on assembly, more contamination is added, which may be any of the items

mentioned previously or newly generated debris. For example, tests have shown that screwing a 1 inch male fitting into an aluminium boss can introduce up to 60,000 particles larger than 5 μm into a system [1]. Often pipework is cleaned using an air line or workshop wiper, but again experience has shown that although cutting swarf and scale may be removed, the operator is replacing it with a different form of contaminant. This may be water from the air line or large quantities of fibres from the wiper which can cause as many problems as the initial debris in the pipework.

Internally generated particles are produced whenever two or more surfaces move relative to one another or from the release of built-in contaminants. Particles may also be generated from cavitation erosion. The quantity of debris is usually high in the initial stages of operation due to the running-in process. If this level is not reduced and controlled, the debris will promote further generation of wear particles. Once particles enter the internal clearances of components, they can cause additional wear damage to the surfaces, usually through abrasive wear. The presence of debris also causes particle erosion to occur in areas of high fluid velocities. These wear processes are often known as the *chain reaction of wear.*

Finally, contamination may be introduced into the system either unintentionally by the operator or by the environmental operating conditions. It is often said that if a hydraulic system is operating correctly, then it should be left alone. The logic behind this statement is based on problems associated with the introduction of new contaminant from replacement parts and the environment on re-assembly.

Environmental debris is being continuously introduced into the system as it operates, typically through rotating shaft or actuator rod seals and reservoir breathers. An area often overlooked is the introduction of new oil into a system. Although oil is refined and blended under relatively clean conditions, it is usually stored in steel drums or in bulk tanks at the customer site. At this point the oil is no longer clean because the filling lines will contribute metal and rubber particles, and the drums will always introduce flakes of metal and scale. Test have shown that with oil from reputable suppliers, the oil samples have an average of 300 to 500 particles greater than 5 μm per mL [3].

1.3. Servo Valve Systems

The author is not aware of any literature concentrating on contamination levels for servo valve systems, but there are two comprehensive documents [4 & 5] relating to the contaminant types

and distributions for various hydraulic applications. From the applications listed in the documents, it can be considered that the size, shape, type and distribution of solid particles found in servo valve systems will depend upon the working duty cycle, the system maintenance and the environmental operating conditions.
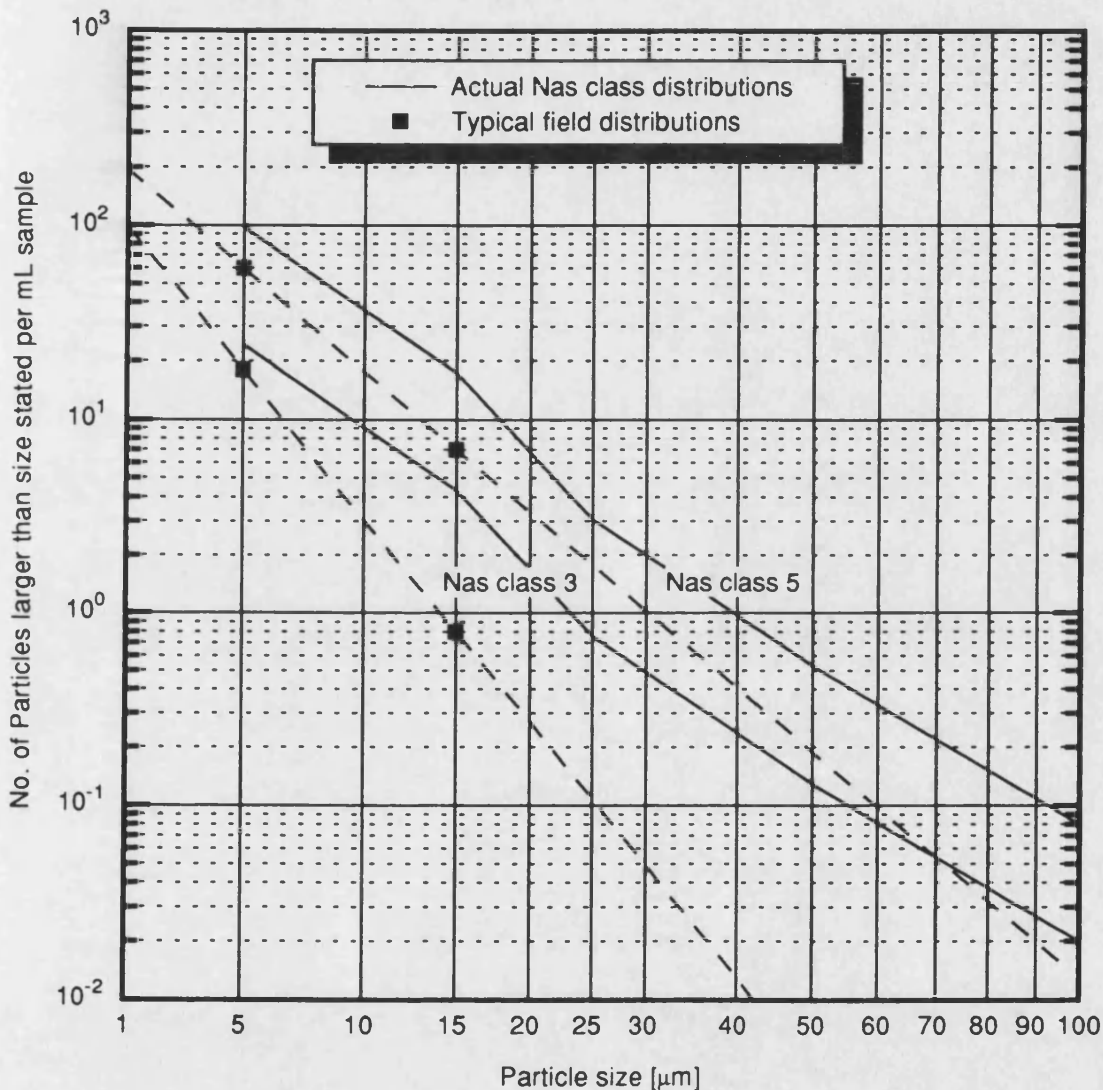
Figure 1.1 - Typical servo valve contamination levels.

From experience gained at Ultra Hydraulics Ltd with servo valves, it has been found that low contamination levels are essential for reliable valve performance and they have recommended that the circuit contamination levels fall between NAS 1638 class 3 and class 5 [6] (ISO 4406 class 12/9 and 14/11 [7]). If the valve performance is classed as critical, then class 3 or better is the target value, but for many less critical applications, class 5 or 6 may be acceptable. To

obtain the required contamination levels, good quality system filtration is required with elements having typically a 3 µm absolute rating, although in some applications 6 or even 12 µm elements are used. The major advantage of using a 3 µm element is that the overall circuit clean-up time will be reduced to a minimum. This gives better protection to the servo valve if the circuit has a fast contaminant generation rate (from internal wear, environmental ingression, etc). However, if the circuit has a low contaminant ingression rate, a larger rated filter element will maintain the required contamination level once the circuit has been brought under control.

Figure 1.1 shows graphically the NAS class 3 and 5 standards combined with actual measured circuit contamination levels (obtained from University of Bath records) which were required to achieve these classes. The figure indicates that the field distributions have a steeper gradient than the standards. The reduction in the large particle sizes is typical of most hydraulic systems fitted with fine filtration. It is generally considered that the distribution of commonly used contamination classes is no longer appropriate for modern filtration systems, and a number of researchers have called for the development of a new classification method.

1.4. Effects and Control of Solid Particles

Research [4] has indicated that in the majority of hydraulic systems, it is the presence of solid particles that are the main cause of failure. The reliability of the system is often dictated by the contaminant sensitivity of a single component. This is usually the component with small metering orifices or working clearances. Traditionally, servo valves have had a bad reputation for contaminant sensitivity. But recently, the new generation of hydraulic pumps and proportional valves often require the same degree of cleanliness as the old servo systems to obtain a reliable working product. This has arisen because the market now requires components with greater volumetric efficiencies, higher operating speeds, working pressures and flow rates.

Failures arising from contamination fall into three main categories; sudden or catastrophic failure, intermittent failure or degradation failure. Catastrophic failures occur when a few large particles or a very large number of small particles enter a component and cause seizure of the pumping elements or jamming of spool valves. Often the chip shearing capability of the component dictates whether seizure is likely to occur.

Intermittent failures are the most difficult problems to overcome in system diagnostics, since they only occur occasionally and usually have different symptoms. They are usually caused by particles momentarily interfering with the function of components. For example, a poppet valve

may not fully close because a hard particle has been trapped under the poppet seat, then when the valve opens again, the particle is washed away allowing the valve to operate normally.

Degradation failures are characterised by a gradual loss of performance and are usually associated with wear. Often they are not noticed until the performance tests are conducted on the equipment. The loss of performance is usually seen by the increased leakage flow within the system and failure is judged when the equipment cannot meet the required duty. Often if degradation failure is allowed to continue it may eventually lead to catastrophic failure.

Effective contamination control starts with the manufacture and assembly of the system, and continues through its working life. As stated in Section 1.1, the majority of the system contamination is in-built and needs to be brought under control quickly and efficiently. After this initial period, the system must then continue to operate at this level by the positioning and selection of the correct filtration.

Good working practice requires that before commissioning, the system is fitted with the less dirt sensitive or essential components and then cleaned up to the required cleanliness level before the sensitive components are fitted. Some systems use the circuit filters for this purpose and others an external flushing unit. For the flushing process to be effective, it is important that flows in excess of the normal operating conditions at low operating pressures are used. It has been observed that wear will increase rapidly if high pressures and contaminant levels occur together, due to the increased forces and the reduced working clearances within the components.

There are two schools of thought on the acceptable levels of contamination within a system. The first requires the system to contain filter elements sufficient to maintain the system at a general level and then use fine filters fitted at dirt sensitive components. The second, requires the complete system to be maintained at the level required for the most dirt sensitive component with coarser last chance filters fitted before the sensitive components. In practice both methods are employed throughout the fluid power industry, and often the final decision depends upon the system design and restraints imposed on the designer. Usually the first approach is adopted on financial grounds and is considered to be a more practical solution. Its opponents however, argue that the increased life and reliability obtained by the lower particle levels in the second approach more than offsets the extra capital costs for the finer filtration over the life of the plant. In addition, the finer filters block more quickly as they will remove the contaminant which passes through the main system filters.

Once the cleanliness of a hydraulic system is brought under control, it is important that a regular particle monitoring programme is enforced. The important aspect of these tests is not to determine isolated particle levels but to obtain trends. If the trend is increasing, this gives an indication that the filtration is no longer effective, or that a component is degrading and is on the way to a possible catastrophic failure.

Since the introduction of ferrography in the early seventies, various research establishments have been investigating the properties of the wear debris found within fluid systems. Ferrography [8] is a technique developed to separate wear debris from the lubricant and arrange it according to size on a transparent substrate for examination in an optical or scanning electron microscope (SEM). By comparing the debris with published data [5, 9 & 10] it is possible to determine the wear mechanisms occurring within the equipment. This technique has been applied to predictive maintenance [11 & 12]. However, the majority of the work has been directly aimed at transmission and engine systems where the particle levels are more heavily concentrated than that found in most fluid power systems. The Department of Trade and Industry (DTI) research study [5] proposed that the results from ferrography and automatic particle counters should be used together to give reliable information on the type, quantity and morphology of contaminant particles in fluid power systems. Ferrography is now used infrequently within the industry because of the relatively high expertise required to analyse the debris correctly. Alternative techniques including particle image detection systems are currently being developed specifically for wear analysis [13 & 14].

1.5. Wear Mechanisms

The term wear is difficult to define, but a committee of Mechanical Engineers decided on the following definition *The progressive loss of substrate from the surface of a body brought about by mechanical action* [15]. Wear usually occurs as a natural consequence when two surfaces with a relative motion interact with each other. Although there is an understanding of the basic wear mechanisms individually, the interaction between them is very difficult to quantify. Often, the wear process will start with one mechanism being dominant, but as time progresses, this mechanism reduces and a different wear process takes over.

To recognise the various wear mechanisms within a fluid power system it is important to have some appreciation of the possible mechanisms. A paper by Burwell [16], groups the general engineering wear mechanisms into major and minor categories. The major groups are adhesive wear, abrasive wear, corrosive wear, surface fatigue and the minor types include erosion and cavitation.

Adhesive Wear - Whenever two surfaces are brought together, contact is usually made with relatively few isolated asperities. As a normal load is applied, the local pressure at the asperities becomes extremely high and they deform plastically until the contact area has increased sufficiently to support the load. In the absence of any surface films, the two surfaces would adhere together to form a cold weld joint. This junction work hardens the metal around it, which becomes stronger than the parent metal, i.e. the adhesion of the junction is stronger than the base metal. Upon relative motion between the two surfaces, the weaker parent metal surrounding the cold joint is pulled from either one or both surfaces. If material becomes un-attached, it will contribute to the wear particles present within the system, usually playing a roll in another wear mechanism. It is for this reason that two dissimilar materials are often chosen to run together as they do not easily weld together. Alternatively, if similar materials are used, they may undergo a manufacturing process to make the surfaces very hard, hence preventing any further work hardening.

There are two classes of adhesive wear; mild wear and severe wear. The mild wear particles are small and usually appear as a metal oxide, since it is the oxide film that is being torn away from the parent material. As the load increases, the mild wear changes suddenly to severe wear. Now the particles become metal flakes and the wear rate may have increased several hundred fold. In this case, the load has so distorted the surface that the oxide film cracks off, exposing two fresh metal surfaces which easily adheres together.

Abrasive Wear - The term abrasive wear covers two different situations, but in both cases wear is attributed to the ploughing of the softer material by a harder surface. The first case is when a harder rough surface slides against a softer one and the second is the action of hard particles being forced across the surface of a softer material. Often the wear from hard particles is described as *two-body* or *three-body abrasion*, the latter being dominant in fluid power systems. Two-body abrasion is caused when particles are embed into a surface to form hard protuberances, while in three-body abrasion, the particles are free to roll and/or slide between two surfaces. Generally, the wear rates due to three-body abrasion are lower than the two-body case [17]. The difference between the two mechanisms is shown diagrammatically in Figure 1.2.

The problems of a hard rough surface can be controlled or eliminated with the correct manufacturing processes, but the action of the hard particles is more difficult to control. The hard particles may be formed under the action of adhesive wear or introduced from an external source. Often, as discussed in Section 1.1, airborne dust and grit may prove to be a considerable problem and should be minimised by using good sealing and filtration. Due to the environmental

aspects of abrasive wear, it is often extremely difficult for a manufacturer to assess the working life of a component or system.

Two-body abrasion   Three-body abrasion
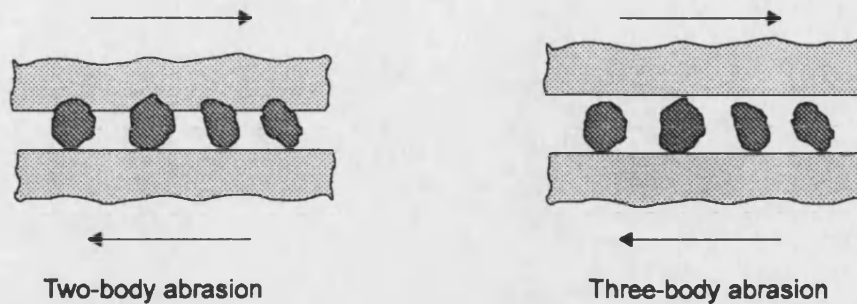
Figure 1.2 - Variation between abrasive wear modes.

Corrosive Wear - When rubbing occurs in a corrosive environment, a surface reaction takes place with the reaction products being deposited on both surfaces. Usually, these products are poorly bonded to the surfaces and may be subsequently removed by further rubbing. Hence, corrosive wear requires corrosion and rubbing. For example, the rate of growth of an oxide layer on steel will decrease exponentially with time and therefore, unless the oxide film is removed, the metal to oxide reaction will become negligible. Corrosion may also occur by the relative electrical potential between two dissimilar materials.

The presence of a lubricant usually protects the surfaces from a corrosive environment. However, it is not unusual for the corrosive element to become dissolved within the lubricant, for example water in oil. Often hydraulic systems working at high temperatures are prone to corrosion problems, where during shutdowns, the system cools and condensation or water ingression can occur. Then at start up, but before the water can be entirely driven off, the combination of water and high temperature creates conditions for rapid corrosion reaction rates.

Other fluid constituents known to be associated with reactions of component materials include, oxygen, organic and inorganic acids, water, chlorinated hydrocarbon solvents and some extreme pressure (EP) additives.

Fatigue wear - Fatigue wear may be sub-divided into two categories; rolling and sliding contact. Adhesive and abrasive wear mechanisms depend upon direct contact between two surfaces and usually progresses from rubbing wear. However, if the surfaces are separated by a lubricating film, these wear mechanisms cannot occur. This situation arises in rolling element bearings, where failure occurs due to a mechanism known as fatigue. In this case the opposing surfaces

experience large stresses transmitted through the lubricant during the rolling motion. The magnitude and sign of the shear stresses will obviously change as the rolling elements rotate, if these are above the endurance limit of the material, then failure will occur. Rolling contact fatigue wear is initially characterised by the formation of flat platelets with a major dimension to thickness ratio of 10:1. They have a smooth surface and a random irregular shaped circumference. Once fatigue cracks have formed, the platelets become spherical particles and are usually about 1 to 5 μm in diameter [5, 9 & 10].

Sliding contact fatigue occurs when the asperities of two surfaces make contact without adhering to each other. In this case the asperities can be plastically deformed and after a critical number of cycles become detached and results in wear particles. Gears are a good example where the surface is subjected to a combination of rolling and sliding fatigue wear.
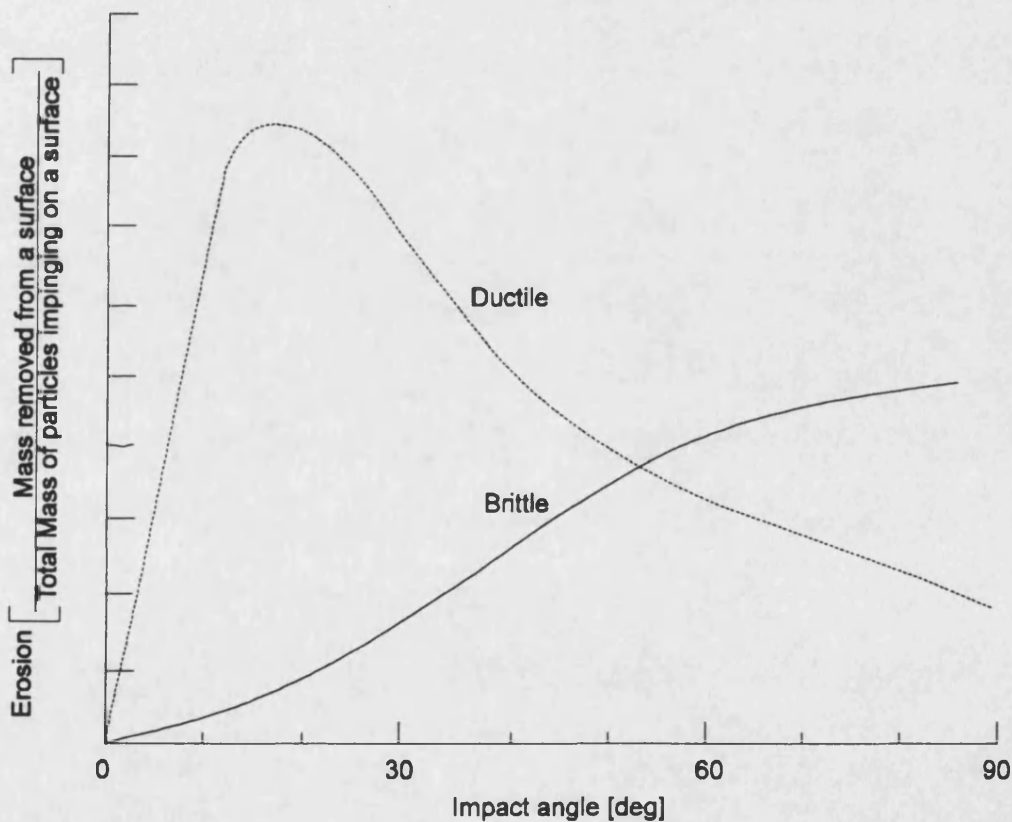
Figure 1.3 - Dependence rate of erosion on angle of attack of impinging particles (from [18]).

Erosion - The term erosion usually applies to a situation where fluid containing solid particles impinges onto or around the surface of a body. When a stream of solid particles is directed at a surface, it is found that the wear rate is dependent upon many variables. Two key parameters

are the angle of incidence and particle velocity at impact. It has been shown that the wear rate for ductile and brittle materials follow different curves [18], typically as shown in Figure 1.3.

In the case of ductile materials, it is thought that the mechanism near to the wear peak is similar to that of abrasion. At angles close to 90° for the ductile material, a fatigue mechanism is probably dominant. For brittle materials, surface cracks are formed and propagate allowing pieces of material to be removed which form further wear debris. For both material types, the wear rate is proportional to the kinetic energy of the impinging particles.

However, the implication of these and other factors to the spool valve erosion project requires a greater understanding of the erosive wear mechanism. This is discussed in detail with the spool valve wear modelling contained in Chapter 8.

Cavitation erosion - Cavitation erosion occurs when the pressure in the fluid falls below the vapour pressure. At this condition the fluid becomes vaporised and cavitation bubbles can form, damage then occurs when they become unstable and implode against the surface of the material. The stability of the bubble is dependent upon the differential pressure between the inside and the outside of the bubble, and the surface energy of the bubble. The amount of surface energy released by the collapsing bubble dictates the potential damage at the collapse. Hence a reduction in surface tension of the liquid reduces the damage, as does an increase in the fluid vapour pressure.

1.6. Scope of Thesis

From the previous Sections, it is evident that knowledge exists to limit and control the effects of contamination within fluid power systems. However, today more than half the system failures can be attributed to the problems associated with contamination or the condition of the hydraulic fluid [19]. To combat this problem, two possibilities exist: firstly system designers and operators can be educated into the ways of reducing and controlling contamination levels, and secondly, manufacturers can produce components which are less contaminant sensitive. Unfortunately, the first of these options has been unsuccessful for many years and therefore the responsibility has fallen to the component designers resulting in the development of new components such as proportional valves.

To aid successful component design a need exists for more quantitative information regarding the performance of components in the presence of various types and levels of solid

contaminants. To date, the research and design emphasis has concentrated on hydraulic pumps and motors and little attention has been made to control valves. To address this, the work described within this thesis examines the performance deterioration of servo valve spools from the action of particle erosion.

Chapter 2 introduces the advantages and disadvantages of accelerated wear testing, and describes the established work in the area of pumps, motors and control valves. Various wear measurement techniques are discussed which have been used or developed by the author to evaluate the component wear geometries.

Properties of the test contaminants are considered in Chapter 3. Test procedures and results are presented for the classification of the Air Cleaner Fine Test Dust (ACFTD) and quartz test dusts. Also, where appropriate the properties which effect the erosion rates are discussed.

Chapter 4 considers the design and operation of servo valves to determine the specification and design strategy for an accelerated wear test rig. The salient points of the rig design are discussed and a section on the rig validation is included. This important aspect highlights the success of contaminant stability and repeatability of the test equipment developed.

The test results are divided into three chapters: in-service and experimental results, oil properties and spool materials. The in-service and experimental results, Chapter 5, contains examples of new and in-service components and quantifies the conditions where the wear levels have become unacceptable. These are compared with results from the test rig to determine the important factors affecting the erosion rates. Chapter 6 considers the influence of the hydraulic oil on the erosion rates and includes results to indicate the importance of viscosity and the performance of various anti-wear formulations. Lastly, Chapter 7 discusses the surface engineering techniques used to modify the spool wear resistance. Results are included to illustrate the problems associated with surface coatings and the advantages that hard coatings can provide.

Finally, Chapter 8 compares the results from the test programme with the established erosive wear theory and provides an insight into the difficulties of applying this to the spool valve problem.

2

Contaminant Sensitivity Testing

2.1.   Introduction

Information on wear sensitivity of hydraulic components is normally obtained by undertaking accelerated testing under controlled conditions in order to obtain results in an acceptable time period. This requires the components to be subjected to test conditions which produce repeatable and realistic results which can be directly related to field life. Since particle abrasion and erosion are the dominant wear mechanisms in fluid power systems, excess contaminants are often introduced to increase the wear rates. Alternatively, parameters such as operating speeds, pressures, flows, etc can be increased to produce a more severe loading cycle, although care must be taken to ensure that different failure modes are not obtained. In some instances small bench tests can be carried out to determine the properties of an individual item. For example, sliding wear performance of new surface treatments or materials can be found using pin-on-disc testing machines.

The following sections review contaminant sensitivity testing in pumps, motors and control valves and highlights the literature associated with erosive wear testing of spool valves. In addition to the established methods used to assess wear, new methods are introduced to specifically measure the geometric changes occurring with the spools and bushings.

2.2.   Pumps and Motors

Pumps and motors were the first hydraulic components to be subjected to contaminant sensitivity testing. The original work in this area was conducted by Oklahoma State University in the early 1970s and was presented in a draft standard in 1972 [20]. From this, a draft BSi standard was produced in July 1980 [21]. Some of the information contained in this draft was based upon information obtained from the University of Aston [22] and the British Hydromechanics Research Association (BHRA) [23] as part of a Department of Trade and Industry (DTI) research programme on *Contamination Control in Fluid Power Systems*. An ISO draft ISO/TC131/SC6/N174 [24] was introduced in the early 1980s, which combined various aspects from the Oklahoma proposal and the BSi document. Since its introduction, work has continued by the Institut fur Hydraulic and Pneumatik (IHP), Aachen [25], and at the China University of Mining & Technology, Beijing [26 - 29]. Both of these institutions criticised various aspects of the

test procedure and suggested various alternatives which they consider produce a more realistic accelerated test procedure to produce a result similar to that found in the field. Finally, nearly twenty years from the initial proposal, a formal ISO standard has been agreed by all parties and was released in the early part of 1992. The new standard is ISO 9632 and is titled *Hydraulic fluid power - Fixed displacement pumps - Flow degradation due to classified A.C. fine test dust contaminant - Test method.*

The ISO pump sensitivity uses volumetric efficiency ($Q_{final} / Q_{initial}$) as the wear indicator. The test consists of an initial running-in and clean-up period to establish $Q_{initial}$. The circuit is then injected with various distributions of the test contaminant at a concentration of 30 mg L^{-1} at 30 minute intervals and the flow rate recorded. Assuming the test has not been terminated prematurely due to pump failure, Q_{final} is then determined at the end of the 6 hour test.

Since the introduction of this standard, IHP (Aachen) have been using the test procedure on variable displacement pumps [30]. Again, volumetric efficiency is used as the wear indicator, but in this case, the contribution to the flow loss from the displacement unit, the swash actuator and the control valve is found. The results from these studies have indicated that the increased leakage is primarily caused by the displacement unit and the control valve. In addition, the control valve wear has been found to be responsible for all the cases where the tests have been terminated due to pump instability. Finally, it appears that this work indicates the future direction of the pump sensitivity testing and has highlighted that little information is known about valve sensitivity testing.

2.3. Control Valves

As in pump contamination work, Oklahoma State University again contributed to the published material regarding valve wear and component sensitivity, the first of which appeared in 1965 [31]. Later in 1976, a descriptive paper titled *The Problem of Valve Contaminant Sensitivity Testing - A New and Positive Direction* [32], highlighted the key areas of the problems associated with valves. The following points were identified :

- Unlike pumps, spool valves are manufactured in numerous designs, and all have their own individual functions and applications. Therefore, any test procedure produced may require different sub-procedures to match the duty of the component.

- At present, the contaminant performance of pumps is assessed using volumetric efficiency. Since torque and flow are the available performance parameters, flow appears

to be the obvious choice for ease of measurement. However, in the case of valves, finding a discriminating performance factor which can be used as a measure of contaminant wear is not easy, since their performance degradation is very difficult to evaluate.

● A practical accelerated test must consider the effects of the static and dynamic performance of the valve and may require various contaminant distributions to establish different failure parameters. The effect of contamination on spool valves can be divided into two categories, either contaminant interference or contaminant wear.

In association with the above paper, Oklahoma State University released a series of five papers looking at the various aspects of hydraulic lock in spool valves [33 - 37]. These examine the influence of different contaminant distributions on spool locking, silting, break-out and actuating forces. Reference is also made about the lack of quantitative field data regarding contaminant wear within spool valves which could be used in conjunction with this data to produce a realistic test procedure.

A paper by Black [38] considers the contaminant sensitivity testing of servo valves and proposes two test conditions to show the detrimental effects of contaminant on different aspects of the valve performance. Firstly, a test using small hard particles (1 to 5 μm) to examine the abrasive/silting effects and secondly, a test using a particle distribution with larger particles present for the erosion effects. Results from Black's studies indicate that the valve performance deteriorates faster due to abrasion than erosion.

As an alternative to spool valves, Graham & Ball [39] looked at the influence of particle erosion on a hydraulic unloading valve whilst working in a water based system. Their work concentrated on the performance of the valve spool manufactured from various materials, including different ceramic coatings. The specimens were subjected to small concentration (100 ppm by weight) of fine (sub 38 μm) quartz particles moving at velocities of about 250 m s^{-1}. The results show that the above test conditions rapidly erodes valve materials with Vickers hardness values below a 1000 (9.8 GPa). The wear performance of each material was found by the volume loss and was calculated from a measured weight loss at fixed time intervals. A typical time period for the softer materials is one hour and for the harder coated materials, ten hours.

An area that has received some attention is servo valves using water based fluids. From discussions between the author and Moog Controls Ltd, Moog disclosed information regarding studies to investigate the performance of servo valves when working with high water based fluids. The work concentrated on the wear of spool and bushing metering lands and it was found that

cavitation was the dominant factor compared with particle abrasion and erosion. Cavitation or lack of film lubrication is usually found to be the limiting criteria for most hydraulic components. This is due to water having poor lubrication properties and having a higher vapour pressure compared with mineral oils.

Similarly, a paper presented by Kelly [40] examined the affects of high water based fluids on hydraulic valves. The test specimens consisted of a mixture of field and laboratory components. The results show that components manufactured in a through heat treated steel last appreciably longer than case hardened material when subjected to identical test conditions. Although the results quote the various test parameters and give details of the worn specimens, there appears to be no mention of the contamination levels for any of the tests. Since no values are given, one must assume that they considered it not important, or have failed to mention it. Hopefully the second case was true, since different contamination levels will produce varying results, although Kelly may have found that particle erosion was insignificant compared to the cavitation wear occurring.

2.4. Wear Measurement Techniques

From initial project investigations, the work identified two different requirements for wear measurement. The first was an on-line method to determine the wear rates within the test rig and secondly, a method to compare the test and field components. This section describes the various methods used to fulfil these requirements.

2.4.1. Gravimetric Analysis

A classic method used in many wear related projects is gravimetric analysis. The method simply relies on an accurate balance to measure the component mass at the start and end of the test. Although this method has the advantage of being non-destructive, it was not selected for the following reasons:

- For use as an on-line method it would be necessary to remove the components periodically during testing. This is not desirable since the probability of continuing a test after re-assembly without changing the contaminant distribution within the oil is very slim.
- The spool and bushing (spool sleeve) have an original mass of 15 and 55 g respectively. It has been estimated that the maximum wear change per metering land will alter the

mass by about 10 mg, therefore putting the changes beyond the resolution of most analytical balances.

• Field samples could not be assessed in this way since the original mass is unknown.

2.4.2. Microscopy

There are several microscope based techniques that can be used to examine worn components. All of these are not suitable for on-line measurements but can be used to analyse field and test specimens on completion of a test. Any assessment of the internal metering edges within the bushing cannot be conducted without first sectioning it.

The basic form of microscopy is the bench microscope. This uses transmitted or reflected light to illuminate the specimen at various magnifications. Unfortunately, as the magnification increases, the depth of field reduces and therefore limits this technique to flat specimens. For example, this technique is well suited to polished, resin mounted metrology specimens without any component form.

The next level of sophistication is the scanning electron microscope (SEM). The SEM is a well established instrument which can provide good micrographic images at very high magnifications with a good depth of field. In an attempt to generate 3-D images, the SEM was used in conjunction with a powerful image analyser. Unfortunately, the perspective was insufficient to allow the wear damage to be quantified. The micrographs in Chapters 5, 6 & 7 indicate that the SEM does produce excellent photographic results which may be used for visual comparison between the various wear specimens.

As an alternative to the SEM, a confocal laser scanning microscope (CLSM) has been used in an attempt to produce quantitative 3-D image of the components. The principle of the CLSM is that the final image is produced by a multiple number of individually scanned layers. The number of layers used is dictated by the total depth of view required and the resolution required, although these may be restricted by the memory capabilities of the instrument.

For the worn spools and bushings examined, the final 2-D images produced by the CLSM resembles very closely that from the SEM. In addition, the scanned layers can be superimposed to produce either a contour or 3-D profile map of the surface. Since the wear profiles are very small and are superimposed on to a corner of a round component, the contour and 3-D profile maps became dominated by the component geometry and the wear changes were not clearly

visible. Although the CLSM worked very well with wear scars on a flat surface, the results obtained for the worn spools and bushings were disappointing and therefore the CLSM technique has not been used.

2.4.3. Stylus Profilometers

Traditionally, surface roughness or texture measurements have been conducted by dragging a mechanical contact stylus across a surface. The vertical displacement of the stylus is then measured, often by employing inductive coils around the stylus arm. These instruments have good resolution (typically 1 µm) but unfortunately have a small maximum working range (typically 60 µm). This obviously limits the measurements to flat surfaces without any form.

However, the latest instruments available have extended capability. The Form Talysurf (manufactured by Rank Taylor Hobson Ltd) has increased the range to the order of mm's with a potential resolution of 10 nm. By using this new instrument a technique has been developed to record the profile of the metering corners.

The following Form Talysurf equipment was used:

- 50 mm (inductive) traverse unit Horizontal data resolution: 0.25 µm

                  Vertical range/resolution: 1.180 mm @ 36 nm

                                                   0.240 mm @ 8.0 nm

                                                   0.118 mm @ 3.6 nm

                                                   0.024 mm @ 0.8 nm

- Modified 2 µm conisphere diamond stylus with a 60° included angle
- Hewlett Packard 386 Vectra PC operating with the Form Talysurf version 4.0 software.

To permit the profiles of the metering edges to be measured on the spool and within the bore of the bushing, the components must be first sectioned in a similar manner to that required for the SEM. Unfortunately, this restricts the inspection process to test components that have completed a wear test programme.

To record the profile of the metering corners, the spool and bushing must be inclined at an angle of 45°, as shown in Figure 2.1, to permit the stylus to track over both faces of the component. To avoid stylus flanking (using the side apposed to the tip of the stylus) as the stylus tracks over

the corner, a special stylus has been produced which has an included tip angle of 60° as apposed to the standard 90°.
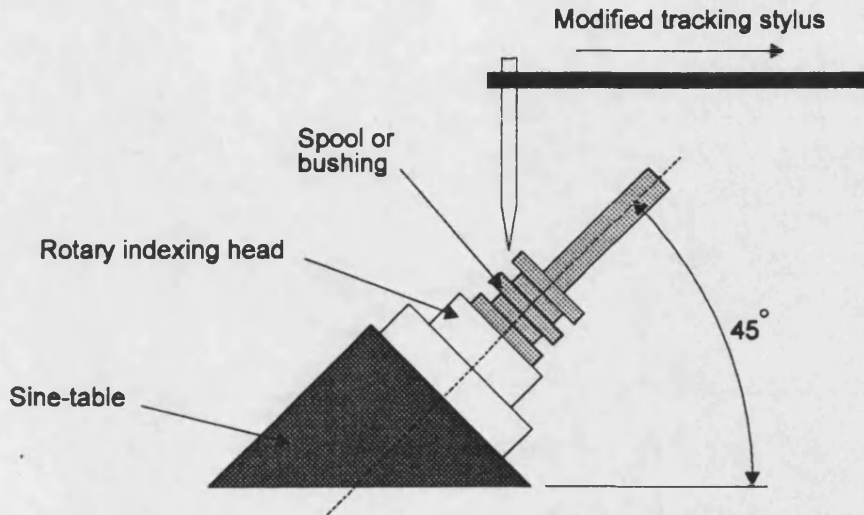
Figure 2.1 - Schematic layout of profile measuring system.

To mount the components in the required orientation for the stylus, different methods have been developed for the 2-D and 3-D contour maps. Firstly, for the 3-D work where the components need to be rotated at a known angle, a rotary indexing head mounted on a Sine-table has been used to provide angular increments of 0.05°. This value corresponds to a circumferential step size of 3.5 μm on the spool diameter and bushing bore. For the 2-D work, a simple fixture produced from a modified V-block with the V at an included angle of 45° to the base has been used in preference to the indexing head.

Once the components are mounted correctly, the methods for recording and analysing the 2-D and 3-D profiles are similar. The procedure used may be summarised as:

i.   Using the Form Talysurf software, record the component profile. Without using any roughness or waviness filters, produce an ASCII data file containing the profile co-ordinates. (Note - the standard Form Talysurf file requires modification from a binary to an ASCII format).

ii.   Using Microsoft Excel (or similar package) normalise and reduce the data files into a suitable format so that they can be compared with other traces or plotted using a suitable graphics package. For the 3-D work, this stage must also include the addition of the circumferential step data.

2.5.   Conclusions

This chapter has highlighted the important aspects of contaminant sensitivity testing of hydraulic components and has identified a shortage of quantitative information associated with control valves. From the work associated with the pumps and motors, volumetric efficiency has been shown to be the obvious wear indicator. Unfortunately, due to the diversity of valve design, this cannot be used in all instances and therefore different wear indicators must be developed for various valve functions.

The wear measurement investigations have identified two useful methods to provide analysis of both field and test specimens. Firstly, the SEM micrographs give excellent pictorial results which can be used to make visual comparisons between components and secondly, a method has been developed using the Form Talysurf instrument to record the component geometry.

3

Test Contaminants

3.1. Introduction

From Chapter 1 it is evident that specifying and obtaining a general field test contaminant is not feasible for the majority of applications. In order to establish a particular field contaminant, an extensive research programme will need to be undertaken to identify the key features and properties of the contaminant. This leads to the difficult task of combining the various elements in the correct form to provide the overall contaminant properties. An alternative approach used extensively throughout the fluid power industry and by research institutions, is to accept that an universal field contaminant is not a available and to use a standard product with known properties.

3.2. Test Contaminants

From the test contaminants available, Air Cleaner Fine Test Dust (ACFTD) has emerged to become a fluid power industry standard for both filter performance and component wear sensitivity testing. ACFTD was initially introduced by General Motors as a test contaminant for vehicle air conditioning filters and is sourced from a natural dust found in the Arizona desert. However, during July 1992 it was announced that the production of ACFTD and ACCTD (Air Cleaner Coarse Test Dust) would cease, and therefore a suitable replacement must be sourced. Since this announcement, it now appears that the likely replacement for ACFTD will be a standard dust produced by PTI (Powder Technologies Inc, Minnesota, USA).

The introduction of ACFTD into the fluid power industry is generally attributed to Fitch who documented its properties [41]. In addition to ACFTD, ACCTD is available but this is not generally used since its particle distribution has too many large particles (>100 µm) which is not considered representative of many contaminant distributions found in fluid power systems.

An alternative to ACFTD is a quartz test dust as described in ISO 5011 [42] for air cleaners. From the available literature [41 & 42], ACFTD and quartz should have similar composition and particle distributions and, therefore, either could be used. To investigate the effects of particle size on the erosion mechanism in spool valves it was important that different particle distributions (cuts) were available. After inquiries into the availability of different distributions, it became

evident that various cuts could be obtained in quartz dust and therefore quartz became the working test dust for the project. The following cuts of quartz were obtained: uncut (nominally 0-80 μm), 0-60, 0-40, 0-20 and 0-10 μm. It should be noted that some tests have been performed with ACFTD for comparison purposes.

As discussed above, Fitch documented many of the properties of ACFTD, although the particle size data has been often questioned by many research establishments, it is still widely used as a reference. Therefore, to compare the properties of the ACFTD batch at Bath with the Fitch data and to determine the quartz dust properties, various forms of analysis have been undertaken. The results and methods used to determine the properties are discussed in the following sections.

3.2.1. Chemical Composition

		Established ACFTD	Bath ACFTD result		Bath quartz result	
Element	Oxide	% Oxide	% Element	% Oxide	% Element	% Oxide
Si	Si O_2	69.2	35.0	69.6	48.0	95.8
Al	$Al_2 O_3$	13.6	7.4	13.0	0.6	1.1
K	$K_2 O$		4.4	5.0	0.4	0.4
Fe	$Fe_2 O_3$	4.35	2.9	3.8	0.4	0.5
Na	$Na_2 O$		2.9	3.7	0.8	0.9
Ca	Ca O	0.05	2.0	2.6	0.3	0.5
Mg	Mg O	1.64	1.0	1.6		
Ti	Ti O_2		0.4	0.7	0.1	0.2
Ba	Ba O				0.6	0.6

Table 3.1 - Composition analysis of ACFTD and quartz test dust.

Table 3.1 shows a comparison between the established ACFTD chemical composition data [41] and the Bath data for ACFTD and quartz. The Bath results were obtained using XRF (X-Ray Fluorescence) smear analysis. It should be noted that some traces of additional elements may be present below the detection limits set on the equipment. Since the ACFTD results are in good agreement, it is reasonable to assume the results obtained for the quartz dust are equally accurate.

Comparing the results for quartz and ACFTD, it can been seen that although they both contain similar elements, their percentage composition is quite different. For example, quartz contains

95.8% silicon oxide (Si O_2) and only small amounts of the remaining elements, compared with ACFTD which has 69.6%.

3.2.2. Density

From Section 1.4, it is evident that the mass of the impinging particle is an important parameter for the erosive wear analysis. The density of ACFTD is not reported in the established literature [41], although quartz and silicon are listed with a relative density of 2.65. In the field of powder technology, several definitions for density terms exist. The term *true density* is defined in BS 2955 [43] as *The mass of a particle divided by the volume of the particle excluding open and closed pores.*

The true density was found using a Rees-Hugil powder density flask and Xylene as described in BS 1902 [44]. The standard uses the *Archimedes* principle of fluid displacement by a known mass of powder. The true density of ACFTD and quartz was found to be 2.55 and 2.79 respectively. It should be noted that the powder densities were obtained from samples that were previously stored in a heated cabinet to remove any moisture content.

3.2.3. Hardness

A standard hardness test consists of loading a pointed diamond or a hardened steel ball into the surface of the material being examined. The further into the material the indentor sinks, the softer is the material and lower is its yield strength. A common hardness method is the Vickers hardness test (H_v) which refers to the applied load divided by the total surface area of the indent (H_v = kgf mm^{-2}).

Unfortunately, due to their size and hard brittle properties, the application of this method to the quartz and ACFTD test dusts is not possible. However, from standard tables [45] the hardness of quartz is thought to be approximately 8 GPa.

Since no documentary evidence to the hardness of ACFTD has been found, it was thought that its composition may give an indication to the likely hardness. From Table 3.1, it can be seen that unlike the quartz with 95.8% Si O_2 (silicon oxide), the ACFTD contains about 30% of other oxides. Approximately half of this is attributed to $Al_2 O_3$ (aluminium oxide) which has an estimated hardness twice that of quartz. However, the other elements known as network modifiers, are likely to reduce the overall hardness [45]. Therefore, it is considered that the

ACFTD is softer than the quartz, although this difference is not thought to be significant when compared to the softer valve material which was measured as H_v = 650 (6.4 GPa).

3.2.4. Particle Sizing and Shape Factors

When particles are regular in shape, e.g. spherical, the particle geometric properties can be easily found. However, most natural contaminants are irregular in size and the particle sizing result will depend upon the type of measuring equipment used. Also, for a natural contaminant, the chosen method is said to be true on a statistical basis for a large number of particles in a random orientation. Therefore, all particle sizes for natural contaminant should really be termed *statistical diameters*.
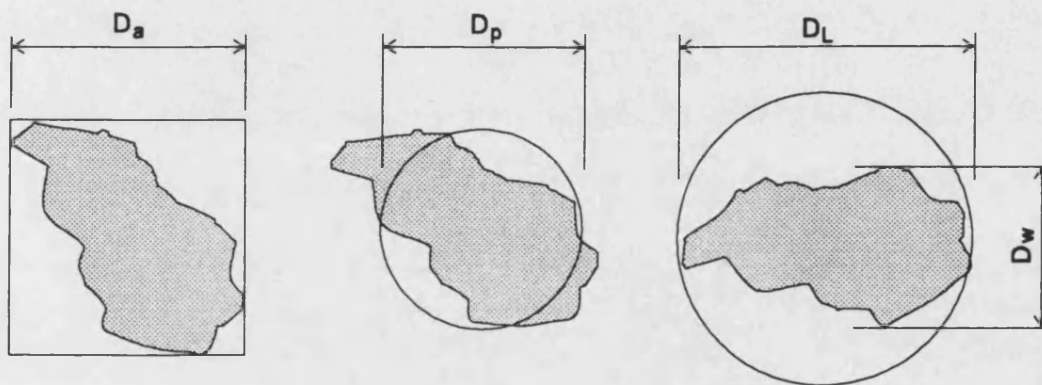
Figure 3.1 - Different types of geometric diameters.

An example of the relevant particle sizing diameters are shown in Figure 3.1. The longest diameter (D_L) is normally associated with microscope inspection and is used in the reference data. The sieve diameter (D_a) is the width of the minimum square aperture through which the particle will pass. This method is usually used in the production of cut dusts, i.e. a 0-10 μm cut would be passed through a sieve with a 10 μm square mesh. The projected area (D_P) is applicable where automatic particle counters are used (Hiac etc) which rely on the light blockage principle as the particle detection method.

Winter & Hutchings [46] and Bahadur & Badruddin [47] have suggested that the particle shape is a critical factor in the erosion rates. For example, an impinging particle can be considered similar to a lathe cutting tool where a change in tool rake angle will affect the efficiency of the cutting process. To enable some critical assessment of the particle shapes to be obtained, a concept called a shape factor is used. As with the definition for particle size, there are also

various definitions for shape factors. The three commonly used shape factors are: volume (α_v), surface area (α_a) and elongation (S_e). The volume and surface area shape factors allow a correlation to be obtained between the volume (V_p) and the area (A_p) of irregular particles and an equivalent spherical particle as shown in Equations 3.1 and 3.2.

$$V_p = \alpha_v \frac{\pi}{6} D_s^3 \qquad \ldots\ldots 3.1$$

$$A_p = \alpha_a \pi D_s^2 \qquad \ldots\ldots 3.2$$

Measuring these shape factors for natural contaminants is very time consuming and requires a sufficiently large statistically correct sample to be examined. However, the elongation ratio (S_e) can be found easily by measuring the longest diameter (D_L) and the maximum cord width (D_w) of the particle. The ratio is then found from D_L/D_w. For example, S_e in the case of a sphere equals unity. In some applications a reciprocal of the elongation is used, this is known as the *aspect ratio*.

The elongation ratio was obtained using a SEM fitted with an image analyser. This was undertaken at BP Sunbury who had successfully applied this technique to polymer fillers and catalysts, but had not used it with natural contaminants such as ACFTD and quartz dust. The following method was used:

i)   A microscope sample of each dust was prepared by mixing the dust into an epoxy resin to form a paste and then left to harden in a pressure vessel.

ii)   After curing, the specimens were polished down to a 1 µm grit size.

iii) The test specimens were then gold sputter coated for use in the SEM.

iv)   Using the SEM, a suitable magnification was selected such that the image analyser had sufficient range to count over the required particle sizes. In this case, the selected particle range was 1 to 150 µm which gave a convenient magnification of x100.

v)   The SEM and image analyser was then driven by a software macro to take 100 different images over the surface of the specimen to produce the results file. Typically, 20,000 to 30,000 particles were sampled on each test specimen to produce a statistical average.

Figure 3.2 shows graphically the elongation shape factor (S_e) for the different test dust distributions and Figures 3.3 to 3.4 contain typical SEM micrographs of the uncut and 0-10 µm quartz test dust. Comparing the micrographs, it is evident that both test materials are very similar in appearance. In each case, the particles have an irregular, sharp edge appearance which when
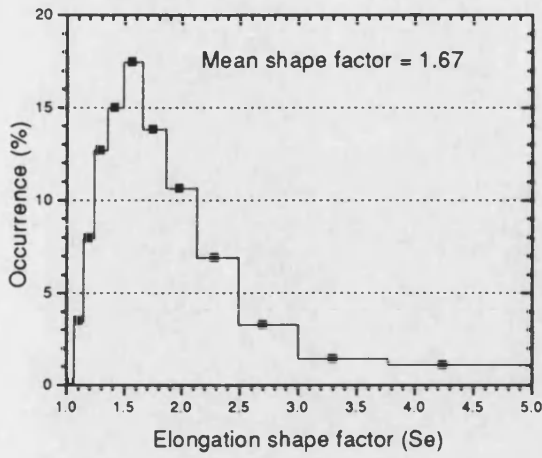
Figure 3.2a - ACFTD
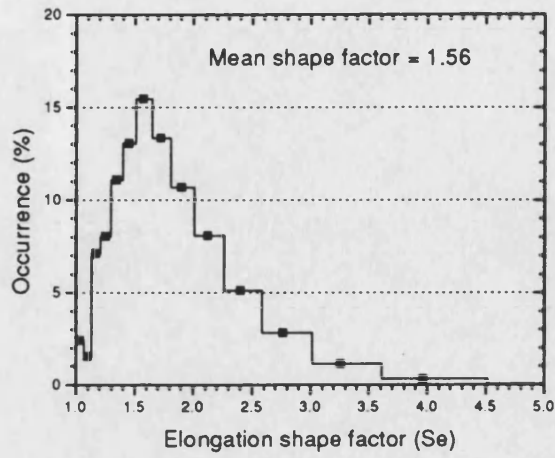
Figure 3.2b - Uncut quartz
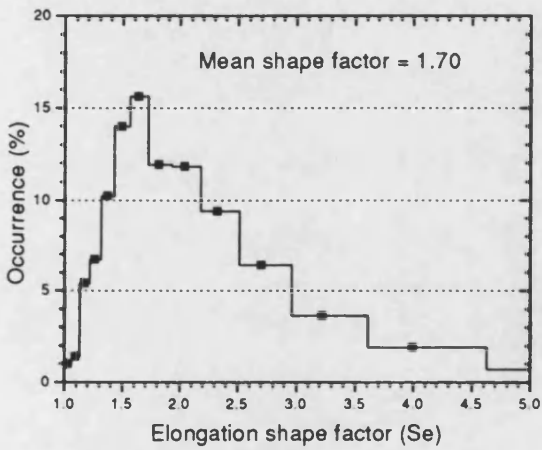
Figure 3.2c - 0-60 μm quartz
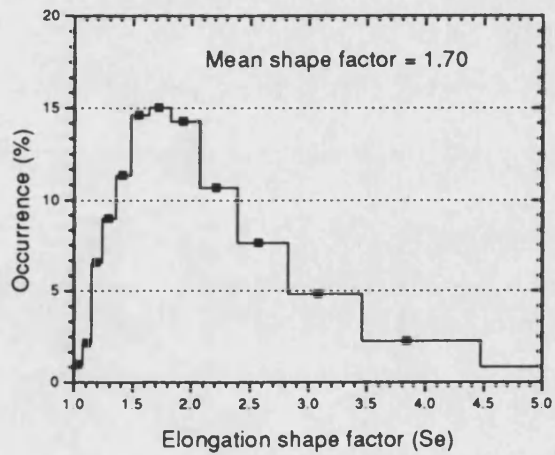
Figure 3.2d - 0-40 μm quartz
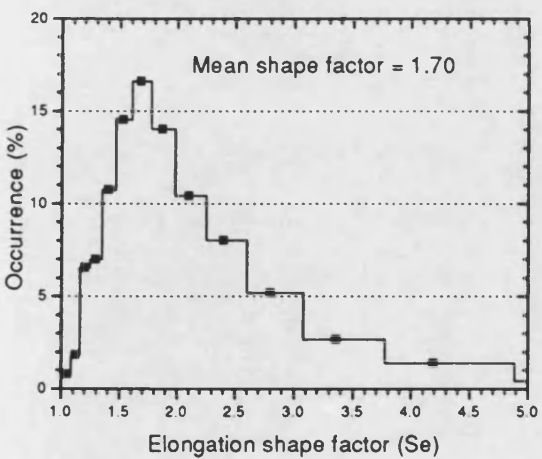
Figure 3.2e - 0-20 μm quartz
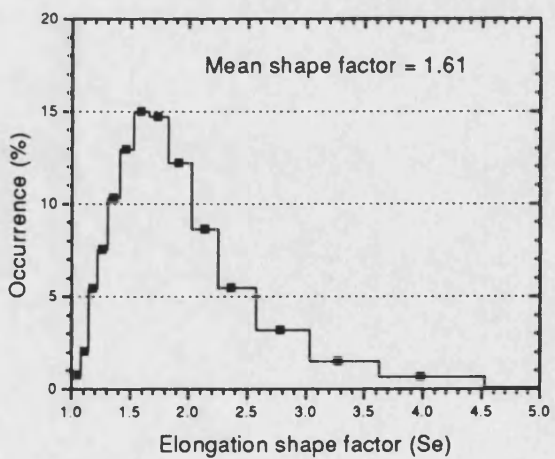
Figure 3.2f - 0-10 μm quartz

Figure 3.2 - ACFTD and quartz shape factors.
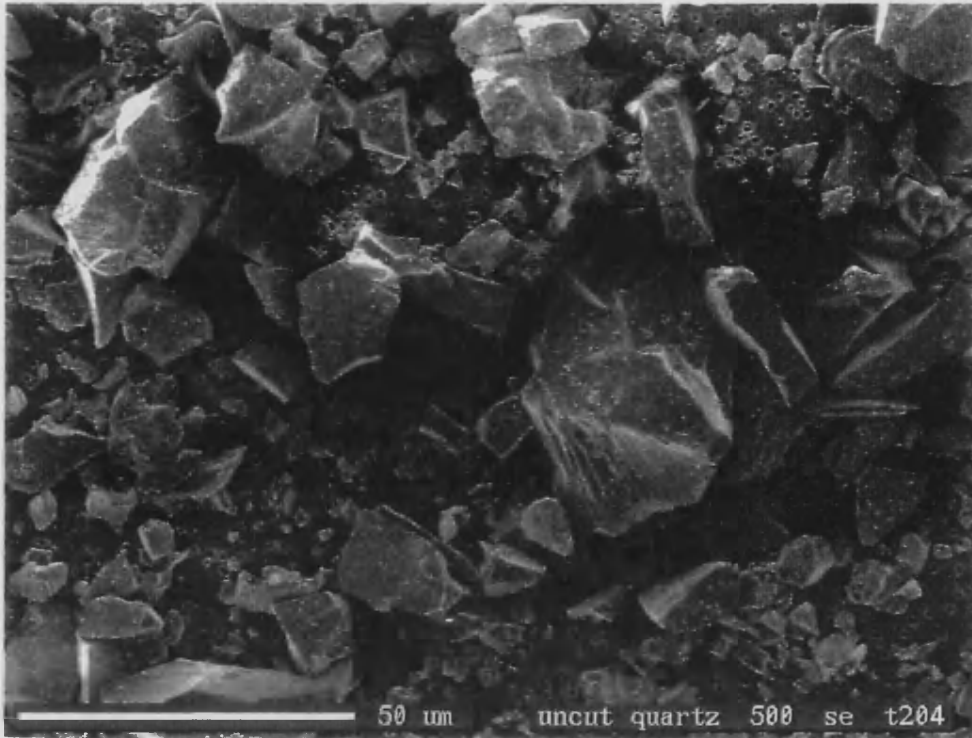
Figure 3.3 - Typical SEM micrograph of uncut quartz.
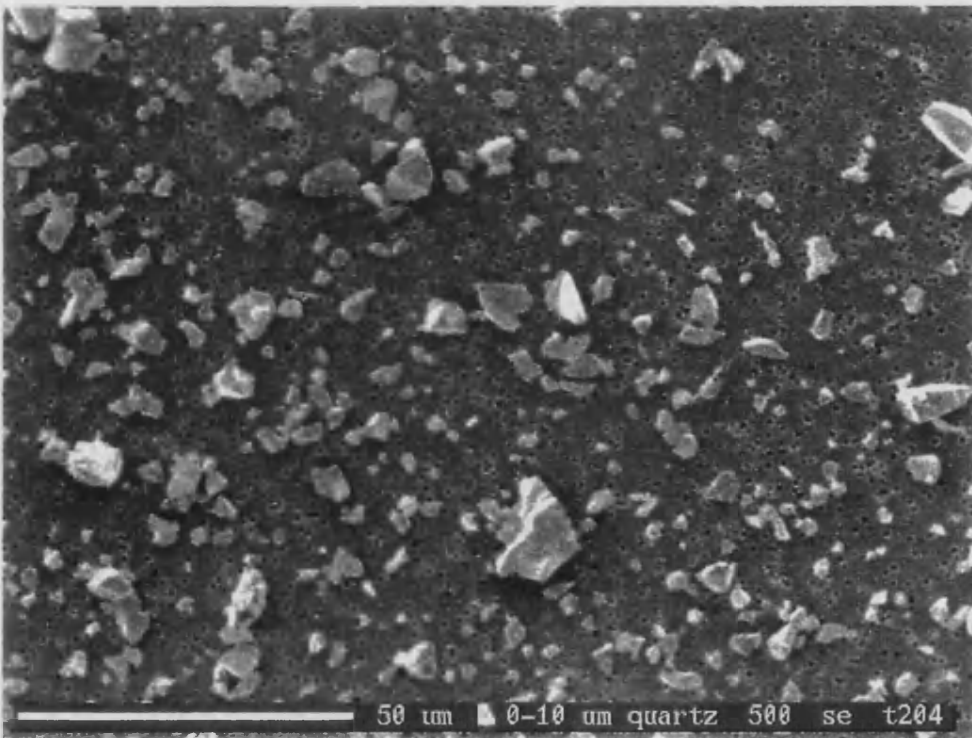
Figure 3.4 - Typical SEM micrograph of 0-10 μm quartz.

combined to their hard composition, will produce a very abrasive test material ideally suited to accelerated wear testing.

From Figure 3.2, the mean value of S_e for the ACFTD was found to be 1.67 compared with the Fitch value of 1.49. In addition to the overall mean value of 1.65 for quartz, the results also give an indication of S_e for different particle sizes that contribute towards the uncut dust. The results show that the S_e for the 0-60, 0-40 and 0-20 µm cuts have an identical value of 1.7, with the uncut and 0-10 µm quartz having values of 1.56 and 1.61 respectively. Unlike the ACFTD, the quartz result compares very well to the value of 1.65 reported by Fitch [41].

3.2.5. Particle Distributions

There are numerous methods for obtaining particle distributions. Some are conducted in the dry powder state and others with the particles dispersed within a carrier fluid. In fluid power applications, the particle distributions are obtained from particle counts for a given fluid volume, often using a Hiac automatic particle counter (the Hiac is recognised as an industry standard instrument). The Hiac uses a light extinction technique and requires the fluid sample to pass between a light source and a detector. The calibration of automatic particle counters may be conducted using ACFTD [48] or latex spheres [49]. At Bath the Hiac is calibrated using latex spheres. Therefore, when working with natural contaminants the actual particle shape, etc is unknown, but the operator has the knowledge that the particle has an equivalent projected area according to the calibration method used.

To validate the mixing and counting process it was decided to compare the measured particle distribution with the published particle data [41]. This requires conversion of the longest length particle counts to an equivalent spherical particle size. Fitch reported that this process may be conducted by multiplying the ACFTD longest length size by 0.65. These distributions are shown in a graphical form using cumulative data on a log-log^2 graph in Figure 3.5. The use of log-log^2 graphs is discussed in detail by Fitch [41], is considered to be the best method for plotting particle count data, since it gives a straight line approximation for naturally occurring contaminants such as ACFTD.

To determine the ACFTD and quartz particle distributions, the contaminants were mixed as described in Section 4.7.2 with base oil (viscosity 32 cSt @ 40 °C) at a concentration of 2 mg L^{-1}. This concentration level was selected to prevent saturation of the Hiac sensor at the 3 µm particle

size and eliminates the need to dilute the sample, thus allowing the Hiac sensor to be used on-line.

From Figure 3.5 it can be seen that a difference exists between the Hiac modified Fitch data and the Bath results. Initially, this discrepancy was attributed to the sample bottle counting method used. However, this hypothesis was discounted when similar results were obtained with the sensor fitted on-line. Therefore, it must be concluded that the latex sphere calibration undertaken at Bath produced a distribution with a steeper gradient than suggested by the modified Fitch data. These results are also presented in a tabular form in Table 3.2.

From Figure 3.5, both the ACFTD and uncut quartz result can be seen to produce a good straight line distribution when plotted on the log-log^2 graph as suggested by Fitch. It is also apparent that the quartz has a steeper gradient than the ACFTD. This result confirms that the density of the quartz is greater than the ACFTD as fewer larger particles will be necessary to produce the 2 mg L^{-1} concentration.

Figure 3.6 contains the distribution curves for the uncut and cut quartz dust (0-60, 0-40, 0-20, 0-10 μm) at a concentration of 1 mg L^{-1}. The results confirm that there is a variation between the different cuts, although the difference between the uncut, 0-60 and 0-40 μm distribution is not significant. The results from the five different distributions suggest that the uncut, 0-20 and 0-10 μm are the most suited for determining the influence of particle size in the valve erosion project since there is a clear difference between these distributions.

3.3. Conclusions

Methods have been used and developed to determine the geometric and physical properties of the quartz test dust and ACFTD. Where possible, these results have been verified using published data, especially for ACFTD where a comprehensive classification has been previously performed by Fitch [41]. The results have indicated that quartz is a suitable alternative to ACFTD.

Particle Dia [microns]	Fitch ACFTD No > size per L	Mod Fitch No > size per L	ACFTD No > size per L	Uncut quartz No > size per L	0-60 quartz No > size per L	0-40 quartz No > size per L	0-20 quartz No > size per L	0-10 quartz No > size per L
2	1396884.0	907067.5	1060511.3	1705194.9	1733719.3	1812708.0	1979717.2	3170852.2
3	991813.0	644034.4	721253.2	1091145.7	1147627.3	1142745.6	1299229.7	2388002.7
4	708078.0	459790.9	493561.4	703228.0	748703.3	728436.7	848846.8	1608936.0
5	516688.0	335511.7	346165.9	466325.2	495544.0	480180.2	565824.9	1016005.4
7	293984.0	190898.7	183481.3	223573.4	232597.1	230458.5	270182.4	371023.8
10	143913.0	93450.0	82105.1	88104.9	88695.2	92719.3	103812.6	78333.9
15	55230.0	35863.6	27935.8	25280.5	25113.8	27685.7	27431.0	6502.3
20	25483.0	16547.4	11695.2	9222.7	9406.4	10142.8	8656.3	627.6
25	13254.0	8606.5	5603.0	3933.3	4163.8	4096.8	2959.4	66.4
30	7503.0	4872.1	2953.0	1873.4	2034.9	1727.2	1040.0	7.3
35	4526.0	2939.0	1671.6	969.2	1052.0	737.4	364.5	0.8
40	2869.0	1863.0	1000.4	534.9	559.6	313.1	125.2	
45	1892.0	1228.6	626.2	310.9	300.7	130.9	41.7	
50	1290.0	837.7	406.7	188.6	161.1	53.5	13.4	
55	903.5	586.7	272.5	118.6	85.3	21.3	4.1	
60	648.1	420.8	187.5	76.9	44.4	8.2	1.2	
65	474.4	308.1	131.9	51.2	22.6	3.1		
70	353.5	229.5	94.7	34.9	11.2	1.1		
75	267.5	173.7	69.2	24.3	5.4			
80	205.3	133.3	51.4	17.2	2.5			
85	159.5	103.6	38.7	12.4	1.2			
90	125.4	81.4	29.5	9.0				
95	99.5	64.6	22.8	6.7				
100	79.8	51.8	17.7	5.0				

Table 3.2 - Particle distribution counts per litre (concentration @ 1 mg L^{-1})
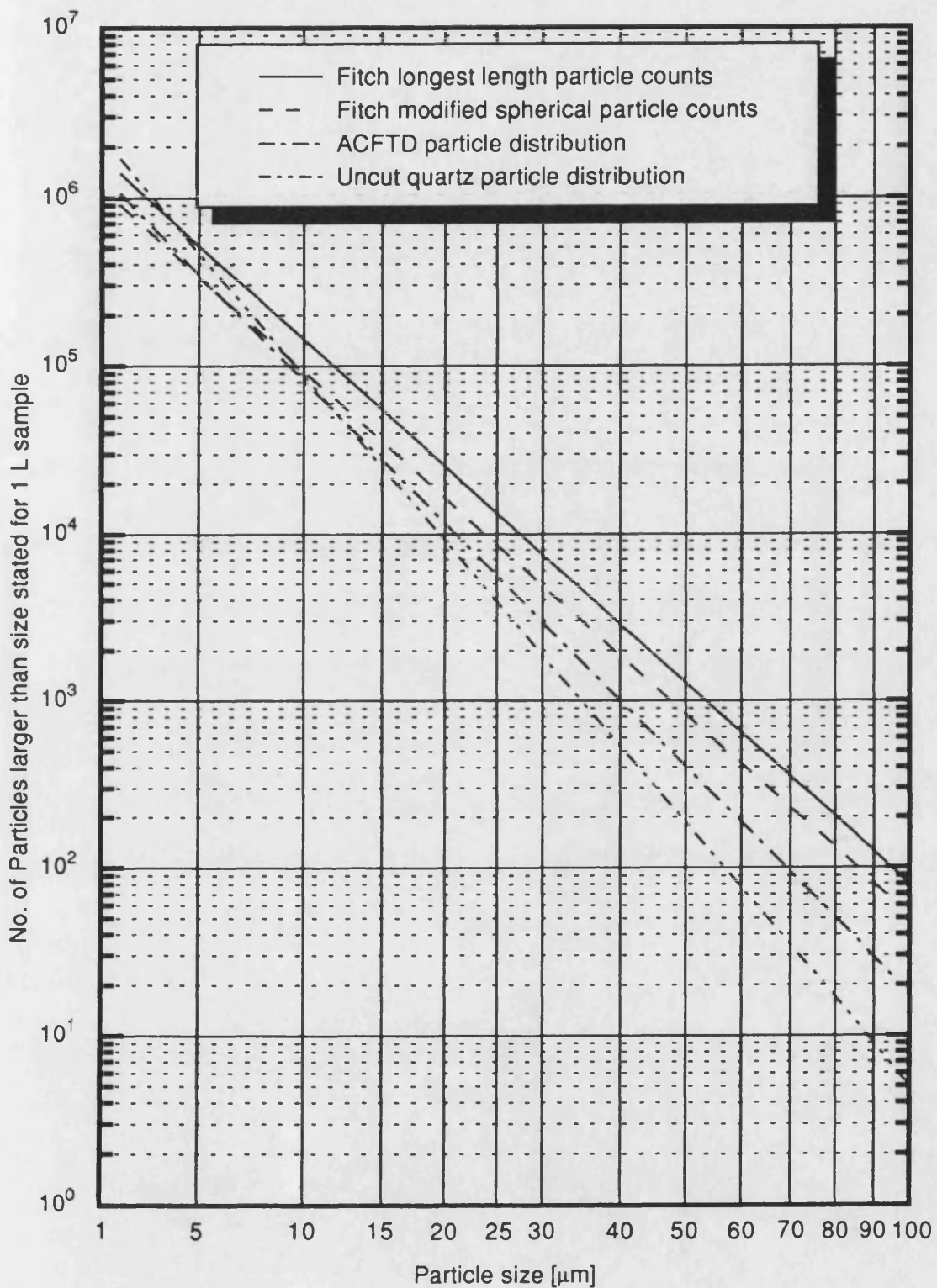
Figure 3.5 - ACFTD and uncut quartz particle distribution curves.
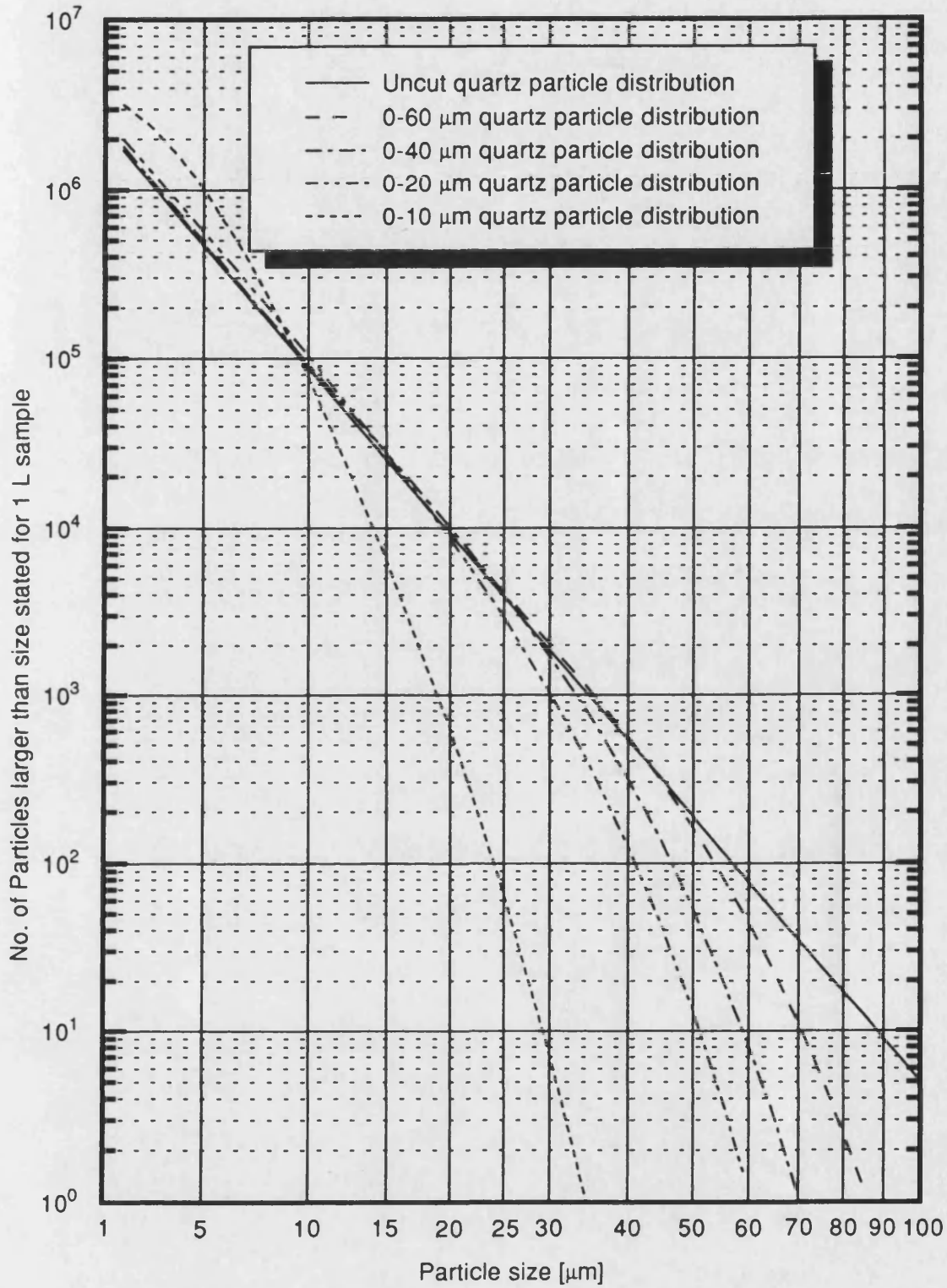
Figure 3.6 - Quartz particle distribution curves.

4

Test Rig Design and Validation

4.1. Introduction

This chapter discusses the features associated with electro-hydraulic servo valves, in particular the Ultra Hydraulics Ltd, type 4551 valve. From this, details are established to provide the specification and operational requirements of a test rig to give accelerated wear test results on a servo valve second stage spool/bushing pair.

Finally, different areas in the rig validation and test procedures are examined to indicate the success and repeatability of the test equipment.

4.2. Test Rig Design Considerations

4.2.1. Design and Operation of Servo Valves
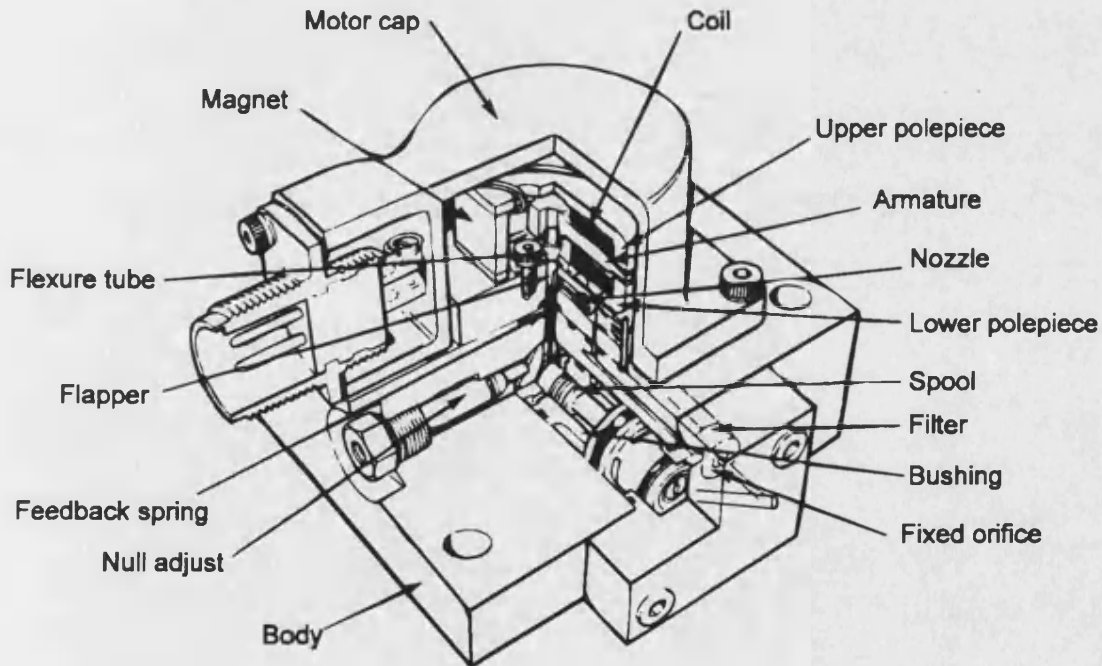
Figure 4.1 - Servo valve section.

Servo valves are electrically operated proportional, directional flow and/or pressure control valves. They are usually four port designs incorporating a four land closed centre spool sliding either in a bushing or directly in the valve body. Rectangular porting gives fluid flow proportion to spool displacement, which is linear to the applied current. Typically, the servo valve is a two stage design with a physical layout as shown in Figure 4.1.

The first or pilot stage is a symmetrical nozzle-flapper arrangement driven by a double air gap dry torque motor. The torque motor consists of coils, coil pieces, magnets and an armature. The armature is pivoted on a flexure tube which also acts as a seal between the electro-magnetic first stage and a hydro-mechanical stage. A flapper rigidly attached to the armature passes through the flexure tube and is centrally disposed between the two fixed nozzles.
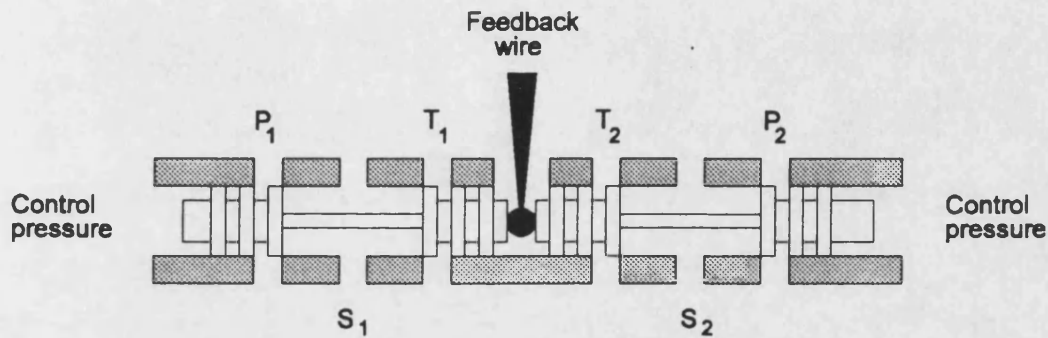
Figure 4.2 - Simplified spool/bushing layout at the null position.

The second stage consists of a spool and bushing which is accurately manufactured to produce a precision fit both radially and longitudinally between the components. A simplified layout of spool/bushing assembly is presented in Figure 4.2. During normal operation, the service ports S_1 and S_2 are connected to a linear or rotary actuator and to either a pressure or a tank port. Therefore, with this arrangement flow is both metered-in (P→S) and metered-out (S→T) through the valve.

The flow gain characteristics for the valve are dictated by the flow area across the metering orifice generated by the spool land and bushing metering slot. This area can be controlled by either changing the spool opening or the circumference of the spool. However, it is not desirable to minimise the spool travel since this removes the metering resolution and for standardisation, it is desirable to keep the spool diameter similar for each case. Therefore, the flow area is restricted by modifying the size of the flow slots within the bushing to effectively give a reduced spool circumference. Examples of this are shown in Figure 4.3.
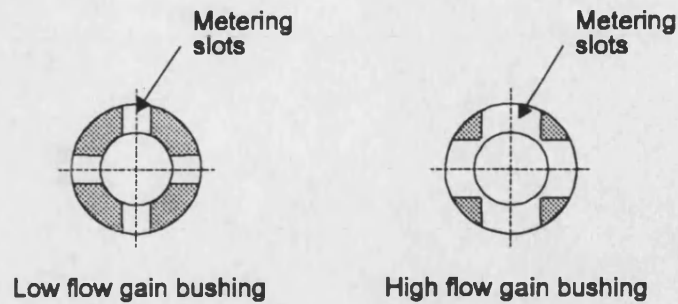
Figure 4.3 - Different types of bushing metering slots.

The results described within this thesis have been obtained using a spool/bushing pair taken from an Ultra Hydraulics Ltd, 4551 servo valve. The valve is a four port design capable of operating with flow rates up to 80 L min^{-1} and a maximum pressure of 305 bar (4500 PSI). From the different flow gains available, the maximum size unit has been selected to give a fully annular metering slot within the bushing (see high flow example in Figure 4.3). This was considered to be an important feature for the experimental programme in order to obtain even wear patterns around the circumference of the components. Using this arrangement, a typical operating characteristics for the valve would be a flow of 57 L min^{-1} at a 70 bar differential pressure drop (35 bar per metering land).

Physically the spool has a nominal diameter of 8 mm and has a maximum travel of ± 0.7 mm about the null position within the bushing. The bushing has a matched diameter bore (typical diametral clearance is 3 μm) and has four fully annular metering slots approximately 2 mm wide. This provides a condition where only one side of the slot is required for metering purposes.

4.2.2. Test Rig Design Strategy

In the section above, it was stated that the test spool/bushing has a nominal rated flow of 58 L min^{-1} at a 70 bar differential pressure drop. From the early literature surveys it became evident that the particle velocity would be dominant in any accelerated wear testing. Therefore, it was decided to provide a test facility capable of providing higher pressures at the rated valve flow rate. This lead to the selection of a 15 kW power unit capable of providing flows of 60 L min^{-1} at a maximum supply pressure of 140 bar.

An important feature of the test rig design was the provision of a continuous flow of contaminated oil across the valve without causing failure of other system components. Although contaminant

insensitive pumps are available, experience at Bath had shown them to be very costly and likely to modify the contaminant distribution by breaking down the larger particles. To eliminate this problem, a circuit was designed which uses the piston of a hydraulic accumulator as a transfer barrier between two different circuits, one clean and one contaminated. By using two such accumulators, it became possible to use a conventional hydraulic power pack and a separate erosive wear circuit, which is effectively driven by a two piston pump.

To provide a continuous flow, the two piston accumulators must operate 180° out of phase with each other. Flow from the power pack then displaces the piston in one accumulator and the erosive wear circuit retracts the second unit until full stroke is achieved. The power pack supply is then connected to the second accumulator which returns the flow of contaminated fluid around the erosive wear circuit. This approach was attractive for two reasons. Firstly, it was possible to manufacture a specialised circuit to operate with contaminated fluids which could be designed to minimise both the effects of particles settling and large particles being broken down. And secondly, it is possible to operate the erosive wear circuit with any fluid independent of the power pack.

The complete test rig assembly consists of four sub-assemblies known as: the power pack, the erosive wear test rig, the fluid conditioning rig and the instrumentation and data acquisition system. These assemblies are shown from left to right in Figure 4.4.

The power pack is a stand-alone unit and provides the power source using conventional fluid power components driven by an electric motor. The erosive wear circuit is the specialised part of the complete assembly and has required the most attention in its design and construction. The function of the wear circuit is to provide a constant source of contaminated fluid across the metering lands of a spool and bushing during the test period. The fluid conditioning rig is a multi-function unit used to clean-up both new oil and the erosive wear test circuit before the commencement of a test. It is also used in the contaminant mixing process to obtain an even particle distribution throughout the test fluid before filling the erosive wear circuit. The instrumentation and data acquisition system is used to control the test rig on a continuous 24 hour basis and has been designed with various safety features to allow for unsupervised operation. The heart of the system is PC data acquisition system running dedicated software, written in-house. It is used to monitor the status of the test rig and to maintain constant test conditions within the erosive wear circuit for the duration of a test. Various test parameters are sampled and stored during a test by the PC at specified time intervals for later analysis.
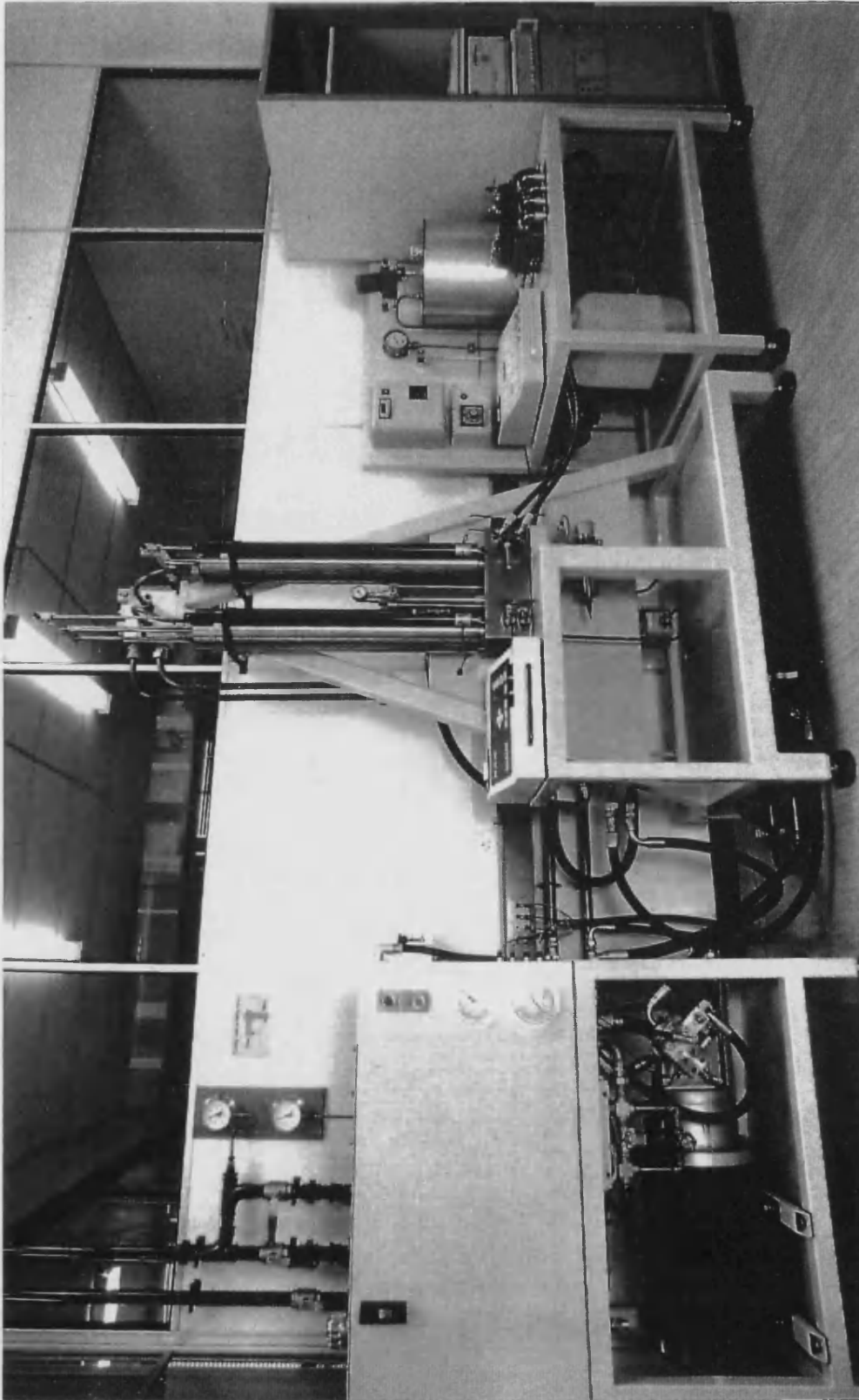
Figure 4.4 - Test rig assembly.

4.3. Power Pack

As discussed in the overall design strategy, the separation of the contaminated fluid from the power source allowed standard components to be used in the power pack. This permits the use of a stand alone unit with the component selection based upon the pressure and flow requirements to drive the two piston accumulators at the required rate. Details of the power pack are itemised as circuit reference numbers 1 to 23 in Appendix 1, Figure 4.5 shows the power pack assembly in detail.

The circuit consists of a fixed displacement gear pump driven by a 15 kW three phase electric motor. This arrangement is capable of providing flows rates of up to 60 L min^{-1} at 140 bar to the erosive wear circuit. The pump is supplied from a 150 litre reservoir and its output is pressure controlled by a proportional relief valve. Flow from the pump is supplied to the accumulator logic element manifold before entering the piston accumulator which is being driven down. The excess flow from the pump is combined with the return flow from the piston accumulator being driven up. The return line flow then passes through a 6 μm filter element, a 5 kW oil cooler and then back to the reservoir. This arrangement ensures that all the pump flow passes through the filter and cooler before returning to the reservoir. This gives an oil recirculation ratio of 2.5 which conforms to the general design practice of between 2 and 4. The circuit operates with BP Energol HLP 32 mineral oil with a viscosity of 32 cSt at 40 °C. During operation of the test rig the running temperature is normally maintained at about 55 °C, although it can be adjusted to any specific value if required.

The power pack pressure is maintained at the required value by an open or closed loop controller operating the proportional relief valve. The controller can operate in three operating modes; constant power pack pressure, constant differential pressure and constant flow across the test specimen (the selection and operation of these different modes are discussed in detail in Section 4.6.2). For safety reasons, the relief valve also contains an over pressure stage which is set at 140 bar. This is a purely mechanical device operating separately to the proportional stage as a safety over-ride.
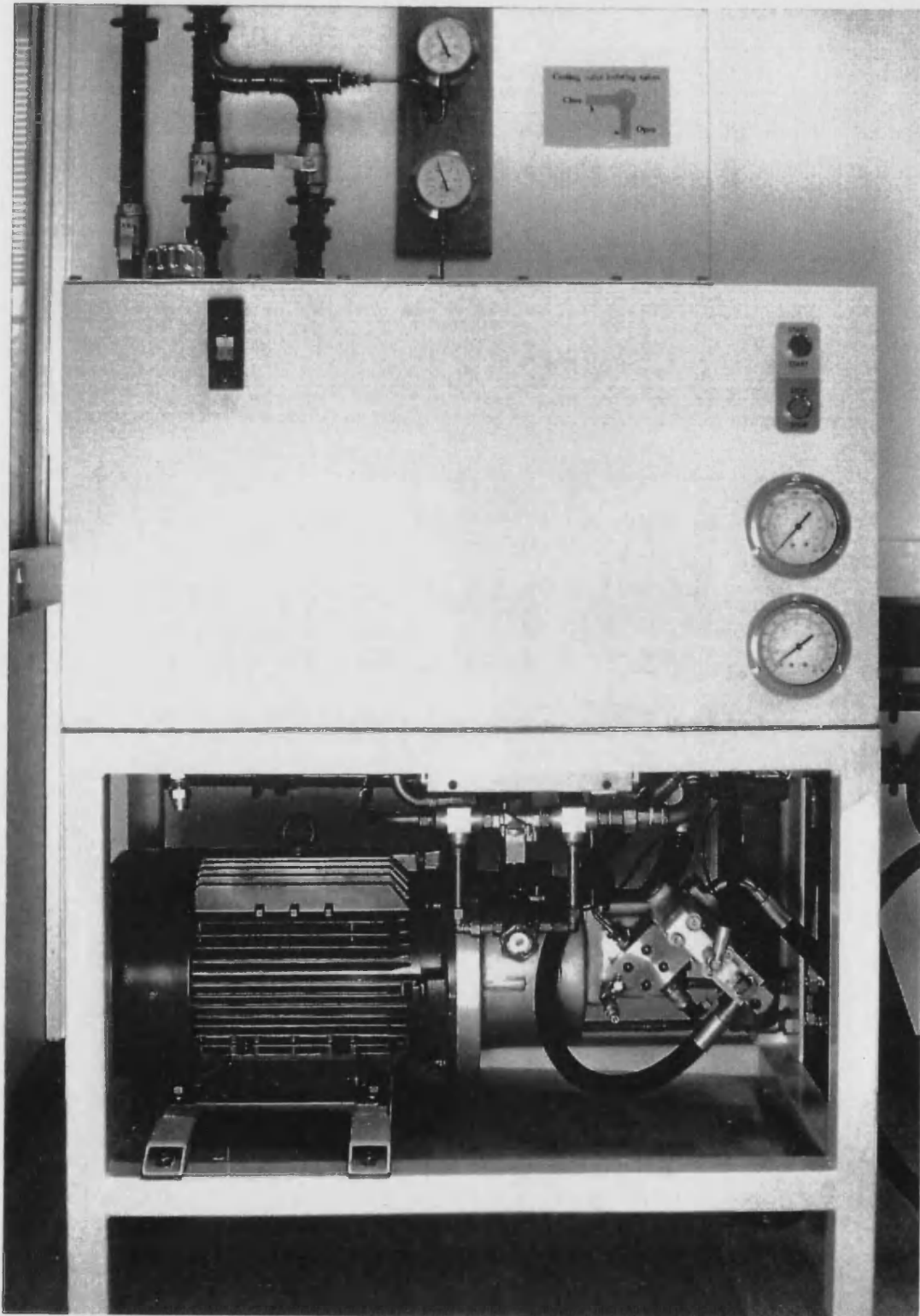
Figure 4.5 - Power pack assembly.

4.4. Erosive Wear Circuit

The essential feature of this circuit is to provide a continuous supply of contaminated fluid across the test specimen over a period of several days without any significant changes in particle distribution. Previous experience at Bath has indicated that by good circuit design, the distribution changes can be minimised by using the following basic rules:

- The fluid flow in interconnecting flow passages should be turbulent at all times, this requires that the Reynolds number should exceed 2000.

- If possible the flow area should be constant without discontinuities in order to reduce particle settling, thus maintaining an even contaminant distribution within the fluid.

- Dead or reduced flow paths should be eliminated where possible, in order to allow the circuit to be cleaned up and to reduce the possibilities of contaminant settling out.

- Components which may crush or break down the larger particles within the contaminant distributions should be eliminated

Other desirable features include selecting components which are not contaminant sensitive. This is generally achieved by using components without small metering orifices or working clearances.

The erosive wear circuit is driven from the two piston accumulators which cycle up and down acting as a two piston pump. The switching of the power pack supply between the two accumulators is controlled by logic elements switched by a potentiometer attached to each accumulator. These were used in preference to a directional control valve to improve the switching response and minimise the flow rate transient. Details of the erosive wear circuit are itemised as circuit reference numbers 30 to 64 in Appendix 1 and are shown pictorially in Figure 4.6.

To produce flow in a single direction around the erosive wear circuit, each accumulator has two check valves contained in the bottom end cap. The high pressure flow from the accumulators is then fed directly into the spool/bushing valve block. This block contains the test specimens and has various transducers to record the spool opening, the oil temperatures and pressures acting across the valve block. Between the accumulators and the valve block are two connections to the fluid conditioning rig. During accelerated wear testings the fluid conditioning rig is isolated from the wear circuit by two manifold mounted ball valves. The ball valves are mounted on the accumulator manifold block, thus eliminating the need for threaded connections and tees within the pipework.
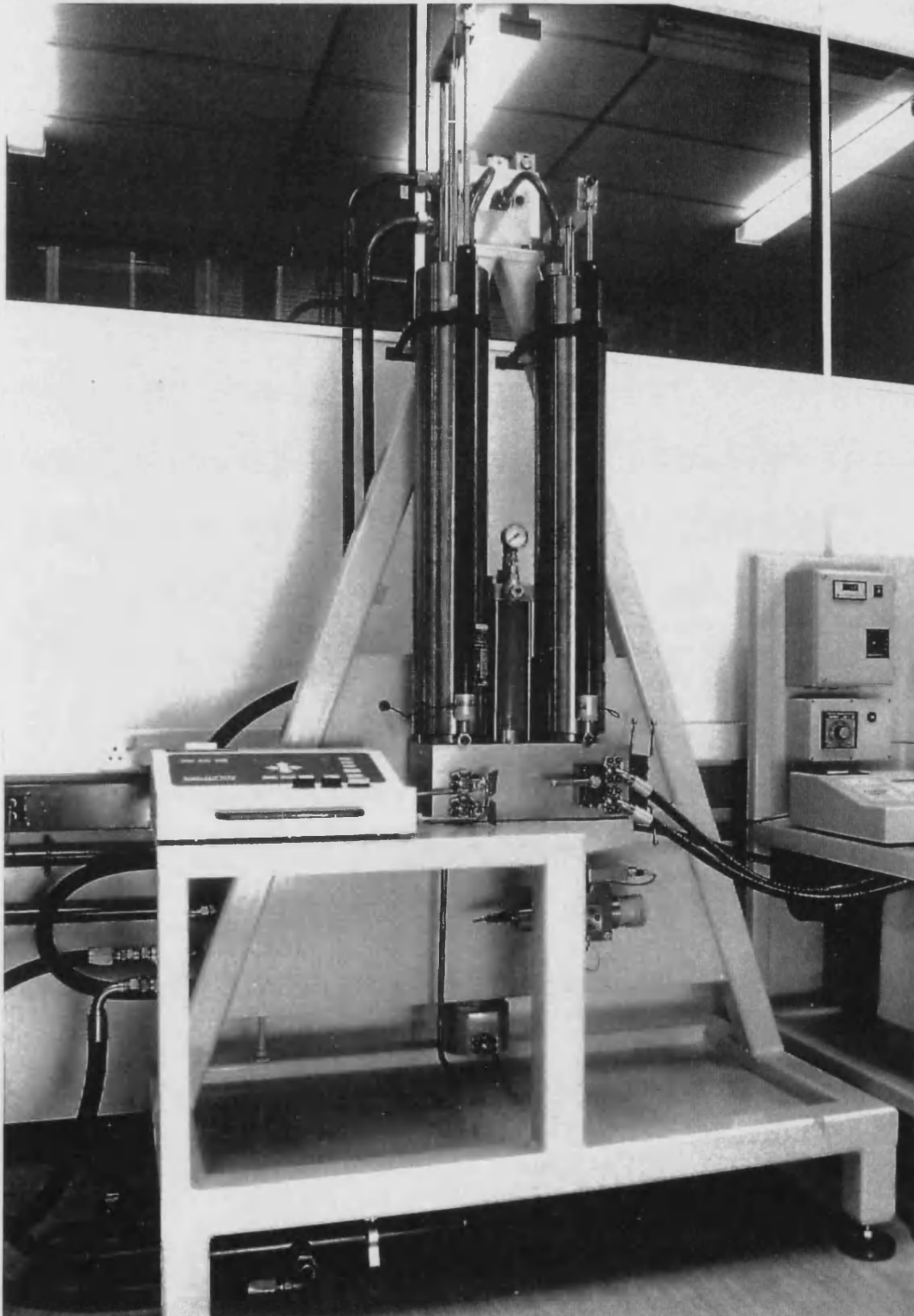
Figure 4.6 - Erosive wear test rig.

The back pressure acting on the valve block exit is established from the flow losses and the force required to retract the piston in the non-driven accumulator. Before the low pressure flow enters the accumulator it passes through a modified oil cooler to maintain the oil at the required operating temperature.

The remaining items connected to the low pressure circuit are; a safety check valve (acting as a contaminant insensitive relief valve), a ball valve to allow the circuit to be drained, a small overflow accumulator and two connections for a Coulter LCM II particle monitor. The LCM II is the limiting criterion for the oil return line pressure and temperature, and restricts the circuit to 3.5 bar (50 PSI) and 50 °C. To protect this unit, two small ball valves are fitted in the pipework which can be closed when the operating conditions are outside the LCM II limits.

It was considered that an in-line flow measurement instrument would not have sufficient life and reliability if used with the contaminated fluid. Therefore, the output from the linear potentiometers attached to each accumulator piston rod is used by the data acquisition system to calculate the flow rates within the circuit. The signals are also used to cycle the accumulators at the end of their working stroke.

4.4.1. Manifolds and Pipework

To comply with the design requirements, it was desirable that a constant fluid velocity is maintained throughout the circuit and excess cavities are eliminated which could collect contaminants. To determine the oil velocity it was thought that a target Reynolds number of 4000 should achieved to maintain a turbulent flow regime. Conventional analysis based on an oil viscosity of 32 cSt at 40 °C showed that an internal diameter of 10 mm was required at the maximum flow condition. By evaluating the tube sizes available, a ½" O/D Tungum alloy tube was selected that had a 10 mm nominal bore. To comply with the no cavity and flow discontinuity design requirement, standard fittings for connecting components and pipework would not be used. The final solution involved using a customised SAE J518c, 3000 PSI standard split flange fitting assembly, as shown in Figure 4.7.

The customised fitting uses the two split flanges and the four retaining bolts of the standard fitting, but has a different tube adaptor. The new tube adaptor was produced with an internal bore to suit the O/D of the tube, thus permitting a continuous flow diameter into the adjoining manifold. The sealing requirements are accommodated with an O-ring face seal between the adapter and the manifold. The adaptors have been attached to the Tungum tube using two different methods.

On the high pressure pipework between the accumulators and the valve block, the adaptors are silver soldered. The remaining adaptors are all bonded to the pipework using a Loctite type 638 high strength retainer.
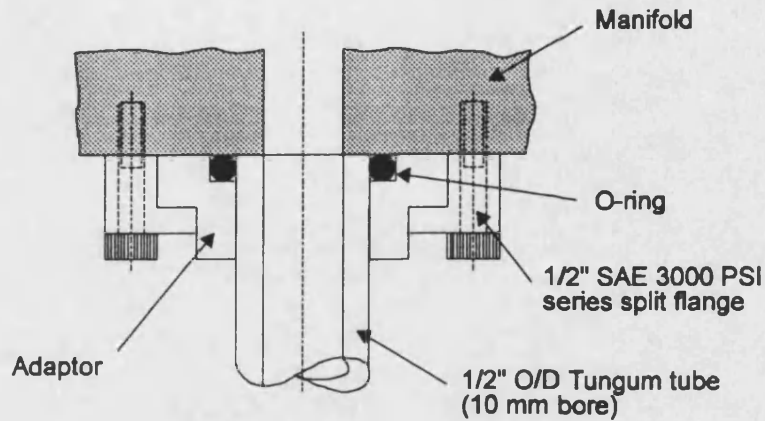
Figure 4.7 - Cross sectional view of customised SAE fitting

Where possible the pipework has been kept to a minimum by the use of manifold blocks. There are two manifolds in the wear circuit: the first is a large block which connects and surface mounts the two piston accumulators and the second contains the test spool/bushing. To maintain the design requirements, it was important that the manifolds were configured to minimise any cross drillings or cavities where low or no flows may occur. To achieve this, careful attention was made during the manufacture that intersection of cross drillings occurred without any over-drill.

4.4.2. Transfer Accumulators

To comply with the design requirements, the two piston accumulators were mounted vertically so that any contaminant settling out would fall to the bottom where it could be collected and re-mixed into the flow. Fitch [41] reported that if the included angle of a conical base was less than 90°, then particles will roll down the face and collect in the bottom. Adopting this principle, conical end caps were produced with a central port to allow the contaminated fluid to enter and leave the accumulator. A sectional view is shown in Figure 4.8.

The two piston accumulators were originally designed to operate as transfer barriers between an oil and a gas system. Consequently, the accumulators pistons were not designed for a continuous cycling duty. Therefore, new pistons were fitted with low friction PTFE seals in-place of the pair of O-ring seals fitted as standard. To eliminate the problems of air entrapment below the pistons,
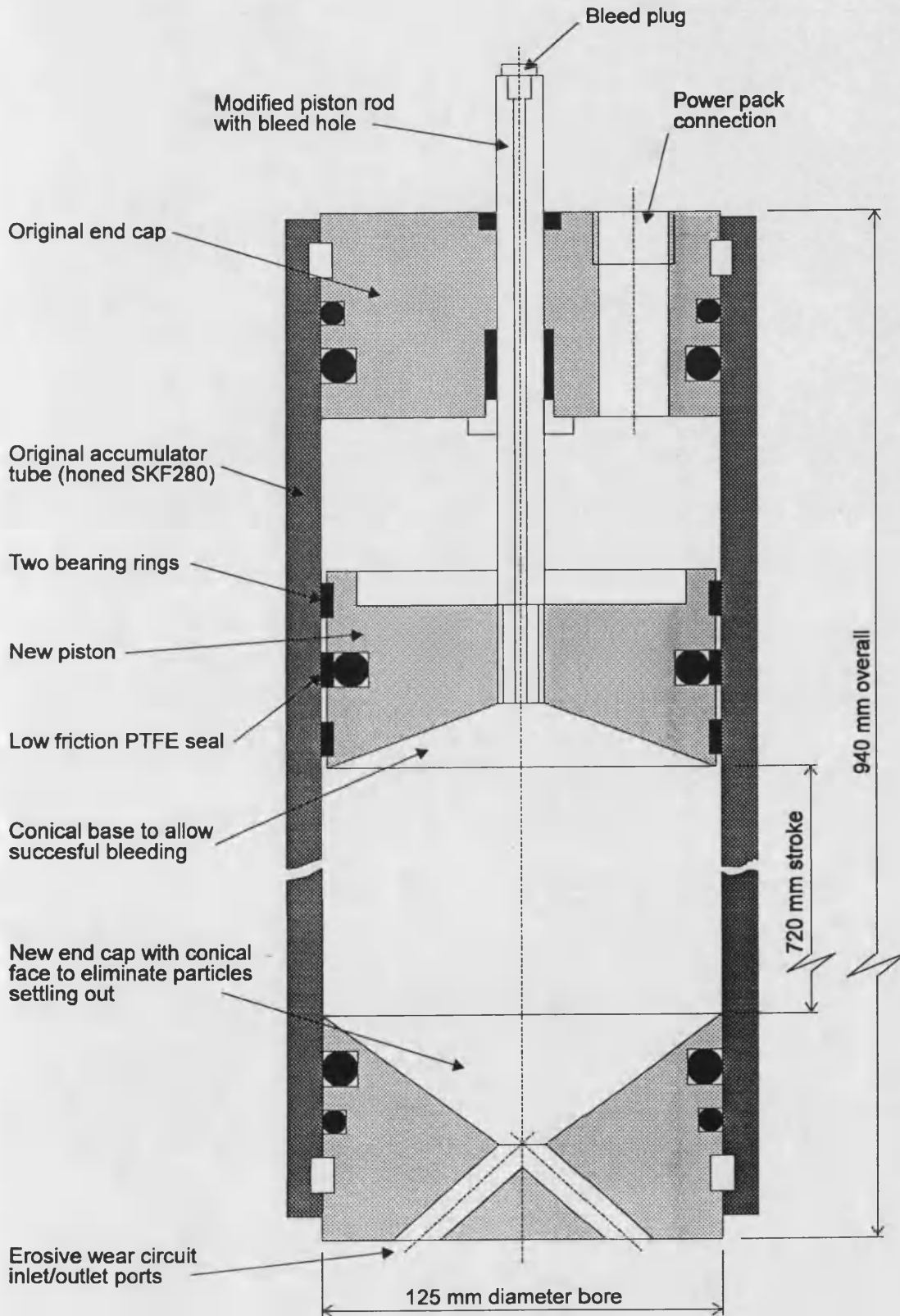
Figure 4.8 - Sectional view through piston accumulators

the underside of the pistons were made slightly conical and the piston rods were gun drilled to enable all the air to be bled from the test circuit.

4.4.3. Overflow Accumulator

Because the erosive wear circuit is a closed, self contained circuit, provision must be made for expansion and contraction of the oil volume with temperature. To fulfil this requirement, an overflow accumulator is fitted on the low pressure side of the spool/bushing orifice enabling a low pressure unit to be used. The final solution involved the incorporation of an appropriate sized pneumatic cylinder with piston seals capable of working with mineral oils at operating temperatures of up to 60 °C.

The physical location of this accumulator is shown in Figure 4.6. As with the two main accumulators, steps were taken to prevent contamination and air problems by modifying the base end cap, piston and piston rod.

The accumulator has a nominal 1 litre capacity and is precharged with compressed air to give an approximate storage oil volume of 0.5 litre when working at a return line pressure of 3.5 bar. Assuming the compression of the air is isothermal, this required the gas precharge pressure to be set at 1.75 bar to achieve the 0.5 litre storage capacity.

4.4.4. Oil Cooler

From the erosive wear circuit power requirements, it was calculated that a 12 kW oil cooler was required. Because of the availability of a cooling water supply within the contamination laboratory (typically at 3 bar and 20 °C), it appeared feasible to use some form of water jacket cooler. Initially, to maintain constant fluid velocities within the wear circuit, a single pipe heat exchanger was considered. This looked attractive when considering the contamination aspects, but was very poor on capital cost and performance compared with conventional hydraulic heat exchangers. The poor performance aspect is related to the overall length of the heat exchanger pipework which would introduce excessive pressure losses into the circuit.

The arrangement selected was based on a modified multi-pass hydraulic heat exchanger as shown in Figure 4.9. Although this compromised the requirement for turbulent oil flow, it was considered to be the best overall solution. Unlike conventional coolers, the modified cooler has hydraulic fluid passing through the inside of the cooling tubes and water around the outside. The

Bleed point

New top cap

New tube extension with
a conical inlet port

Tube extension bonded
onto original tube stack

Original cooler body
and tube stack

New end cap with
conical outlet port

Oil
inlet

Water
outlet

1050 mm overall

Water
inlet

Oil
outlet

160 mm diameter
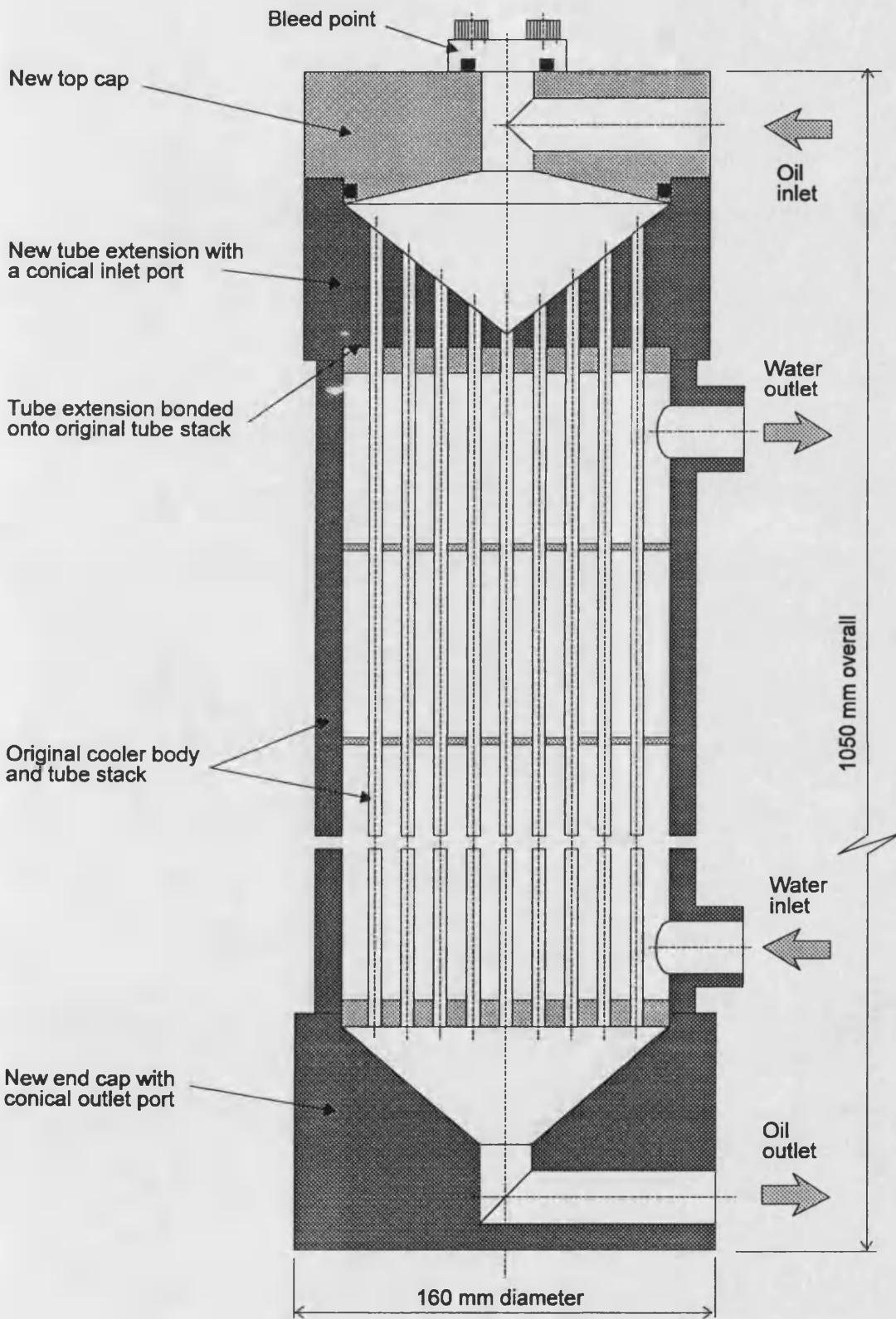
Figure 4.9 - Section view through oil cooler.

cooler is mounted vertically with the oil entering at the top and leaving from the bottom. Using this approach, particles would be prevented from settling from the oil flow by the specially shaped end caps. The bottom end cap has an 90° conical base with the outlet port at the bottom. At the top, contaminant could settle out onto the top plate surrounding the tubes. To prevent this, a conical adaptor was produced which was attached directly onto the tube stack using a suitable epoxy resin.

The cooler top cap also accommodates a fluid sampling point which can also be used as an air bleed point for the cooler. The sample point consists of a full flow ball valve and conforms to the standard design requirements for sampling points [50].

4.4.5. Spool/Bushing Valve Block

Initially it was thought that a standard servo valve body could be adapted for the erosion tests, but once the design requirements were established, it was considered that a new block should be constructed. The key design requirements for the valve block were identified as:

- To locate the spool and bushing to permit flow across one pair of metering lands.
- If possible, the valve block should accommodate the spool and bushing so that flow may cross the metering lands in either direction ($P \rightarrow T$ and $S \rightarrow T$).
- To accurately adjust the spool position to within 1 µm with good repeatability.
- To provide monitoring of the oil temperature and pressure drop across the metering lands of the spool and bushing.
- Eliminate any flow stagnation areas which may encourage particle settling.

By examining the spool and bushing manufacturing drawings it became evident that the components are symmetrical about their centre and that the pressure, service and tank ports in the bushing are based on an even pitch. Hence, it became apparent that if the spool/bushing assembly could located about the centre, two tests could be performed on each specimen simply by rotating the components. Further more, if the bushing could be positioned one port pitch within the valve body, then all four metering lands could be tested for a given specimen. In a conventional servo valve body the bushing is located using a small eccentric dowel known as a null adjustment pin which is an accurate fit into a slot in the side of the bushing. However, this approach did not appear an attractive method for two reasons; firstly the additional manufacturing

Flow in

Pressure transducers
(surface mounted diaphram type)

Test spool and bushing

LDVT

Micrometer head
(2 μm resolution)

2
0
0 5 1 48

LDVT assembly (spring loaded
against spool and bushing)

Spool/bushing manifold

Note - The bushing is located by an eccentric
pin (not shown) that allows the flow to enter
the pressure or service port of the bushing

Flow out
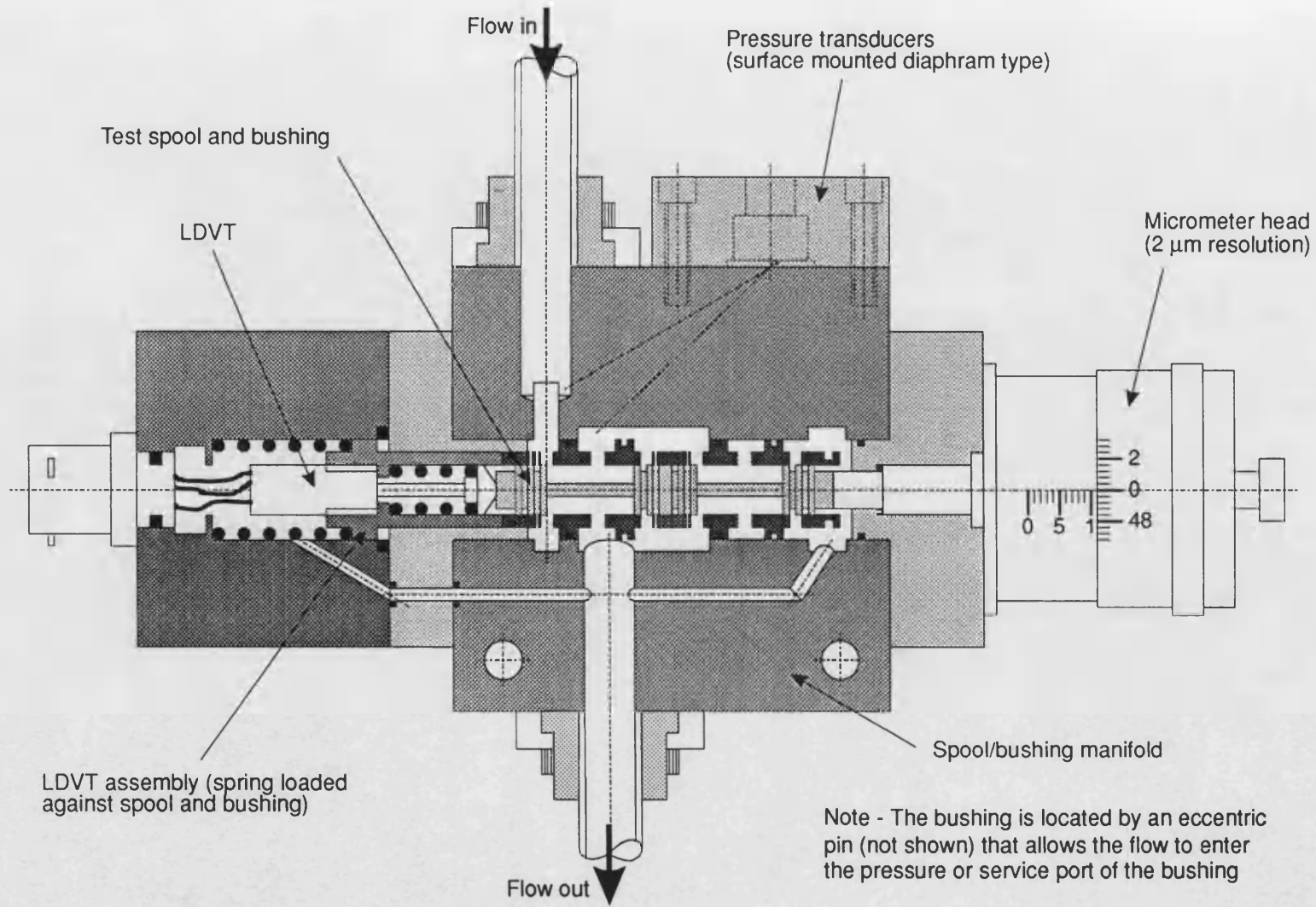
Figure 4.10 - Cross sectional view of spool/bushing valve block, flow P to S.

Flow in

Pressure transducers
(surface mounted diaphram type)

Test spool and bushing

Micrometer head
(2 μm resolution)

LDVT

2

0

0 5 48

LDVT assembly (spring loaded
against spool and bushing)

Spool/bushing manifold

Adaptor (only fitted for flow
between the service and tank port)

Note - The bushing is located by an eccentric
pin (not shown) that allows the flow to enter
the pressure or service port of the bushing

Flow out

Figure 4.11 - Cross sectional view of spool/bushing valve block, flow S to T.

cost in providing a null pin with each test specimen, and secondly, the provision of the two pin location points within the valve body could not be easily accommodated.

The solution adopted uses a single tapered pin positioned eccentrically on a single location dowel. Unlike the production valve, the null pin location slot is not used and the tapered pin locates in the un-used feedback wire hole in the bushing. Adopting this approach produces a general purpose location fixture capable of positioning the bushing in the four locations required and also eliminates the need for the null adjustment pins to be manufactured. Figures 4.10 and 4.11 show the bushing located in the two positions, and it can be seen that Figure 4.11 has an additional adaptor fitted to move the LVDT assembly by one port pitch.

The most suitable method for accurately positioning the spool was to spring load the spool against a precision micrometer head. Initially, it was intended to measure the position to within 1 μm, but this was found to be unrealistic and a micrometer head with a 2 μm resolution has been used. To verify that the spring was locating the spool against the micrometer spindle, a small precision LVDT was included in the spring assembly. Initially this was considered a simple task, but when thermal expansion between the spool/bushing and valve body was taken into account, it was found that large errors may be introduced in the LVDT reading. This was overcome by using two separate springs, one to hold the LVDT body against the end of the bushing and a second to hold the LVDT armature against the spool.

The measurement of the pressure and temperature within the valve body assembly required careful attention. The main areas of concern and the solutions adopted are summarised as follows:

- To provide the actual temperature and pressure measurements across the metering lands of the valve assembly is not feasible and therefore a comprise must be accepted by measuring the variables as the flow enters and leaves the bushing.

- Any pressure measurements should be static pressures and that the transducers should be located to ensure that no dynamic pressure effects generated by high velocity fluid jets are experienced.

- Most pressure transducers use threaded connections and often have complex oil cavities within their design. If this type of transducer was included, then flushing and cleaning out of previous contaminants would prove to be difficult. Similarly, transducer pilot drillings should be minimised for the same reasons. Therefore, the chosen solution used two pressure transducers that are manifold mounted and have a sealed diaphragm on the front face. The transducers are located on the top of the valve block and measure the

oil pressure through two vertical pilot drillings. Using this arrangement it was thought that contaminants would fall back under the action of gravity into the test fluid.

• To obtain representative oil temperatures it was important that the transducers recorded the bulk oil temperature leaving and entering the valve block. To obtain this, the tip of a thermocouple is located in the centre of both the supply and exit port of the valve block where the fluid flow should be fully mixed. Unfortunately two small threaded connection are used as gland nuts to retain the thermocouples in position. However, to minimise contaminant settling problems, the thermocouple body was made an interference fit at the oil boundary restricting any contaminant entering into the threaded portion.

4.4.6. Coulter LCM II Particle Monitor

To obtain an understanding of the erosive wear process it is important that the contamination levels are known throughout the test. From the available methods for particle counting, the Coulter LCM II appeared an acceptable solution. The LCM II is a general purpose, robust particle monitor that may be used to measure the contaminant concentration levels at three different particle sizes, >25 μm, >15 μm and >5 μm for a known sample volume. A complete description for the LCM II may be found in its operating manual [51].

As discussed in Section 4.4, the LCM II became the controlling factor for the low pressure side of the wear circuit (3.5 bar and 50 °C), although the LCM II could be isolated from the wear circuit when required. The LCM II was chosen for two main reasons. Firstly, the LCM II may be interfaced directly with a PC data acquisition system via a RS232 communication port and secondly, the unit may take oil samples directly on-line and return oil back into the wear circuit. This facility is an extremely important aspect in maintaining constant contamination levels , since no oil or contaminants are removed from the circuit.

4.5.   Fluid Conditioning Rig

The functions of the fluid conditioning rig may be divided into two categories. Firstly, as a filtration unit to clean-up new test fluid and the erosive wear circuit at the beginning of a test, and secondly, to mix and distribute evenly the test contaminants within the test fluid before transferring it into the erosive wear circuit.

Since contaminated fluid is being used in this circuit it is important that the general design rules detailed in Section 4.4 are applied to minimise particle settling and to improve the circuit clean up efficiency.

The rig is a stand-alone unit which is permanently connected to the erosive wear circuit, although it may be operated independently of the erosive wear circuit if required. The key components that contribute to the circuit are: a fixed displacement gear pump driven by a variable speed DC electric motor, a manifold block containing a number of ball valves and a 3 μm filter, a Coulter LCM II particle monitor, a specially designed mixing tank and a 25 litre waste drum. Details of the fluid conditioning rig are itemised in Appendix 1 as circuit reference numbers 70 to 86 and are shown pictorially in Figure 4.12.

The test fluid is supplied in 205 litre drums and the required amount is pumped into the mixing tank on the rig. The test oil is then circulated around the fluid conditioning rig until the required conditions are obtained before being transferred into the erosive wear circuit. The waste drum is a portable unit used to collect waste fluid from the two circuits at the end of the test before disposal.

The circuit was designed to operate with the Coulter LCM II on-line and therefore a maximum pressure of 3.5 bar was imposed on the design (see Section 4.4.6). This was not considered to be a problem since the rig has only to operate at sufficient pressure to overcome the losses within the circuit. Since a variable speed electric motor is being used, the selection of the pump displacement was not a critical factor and an intuitive selection of 30 L min^{-1} at maximum speed was chosen.

4.5.1. Pump/Motor Unit

Unlike the erosive wear circuit, a fixed displacement gear pump was included in the circuit even though contaminated oils are being used. This approach was made taking into account the small number of operating hours working with contaminated oils and that the operating pressure is low, typically 3.5 bar. At these conditions, previous experience had shown the pump life would extend beyond the duration of the project and any performance degradation would be negligible.

Figure 4.12 - Fluid conditioning rig.

4.5.2. Manifolds and Pipework

Although the maximum flow rate is only 30 L min^{-1} compared with 60 L min^{-1} in the erosive wear circuit, it was decided, where possible, to use similar sized components in both circuits. This enabled the 10 mm bore Tungum tube and ½" SAE modified adaptor (see Section 4.4.1) to be used to provide the connections between components. Unlike the erosive wear circuit, the fluid conditioning rig required flexible hoses to connect various components together. Unfortunately, it is widely known that conventional nitrile hose constructions can introduce large amounts of contaminant into a circuit and that they are inherently difficult to flush clean. A proven solution to this problem in low pressure and temperature situations is to use a plastic hose construction. After discussions with various hose suppliers, the final solution used a ½" nominal bore, PTFE lined hose with ½" SAE (3000 PSI series) end connections. Using this combination it was possible to maintain approximately the desired flow diameter (actual bore = 12 mm) and to use end fittings which did not include the use of threaded connections.

The most efficient way of providing connections for the array of ball valves, filter and ancillary equipment was to use a steel manifold block. Again the design restraints of the erosive wear circuit were imposed to minimise particle entrapment within the block. The manifold was also designed in such a way that the connecting pipework went from the manifold directly to the mating component without the introduction of tees which could cause flushing problems.

4.5.3. Reservoir

Research has shown [41] that the most suitable reservoir design for working with contaminated fluids is a cylindrical drum with a conical base, where the included angle should be less than 90°. Although, the maximum storage capacity for the reservoir is approximately 45 litres, it has been designed to operate with about 30 litres of oil. Selection of the 30 litre capacity was based on an intuitive figure of two times the designed 15 litre operating volume of the erosive wear circuit (the actual erosive wear circuit operating volume has since been found to be nominally 11 litres). The oil volume contained within the reservoir is shown in a calibrated sight glass attached to the base.

The cylindrical section of the reservoir is of a double skinned design, the inner skin having a ribbon type heater wrapped around its circumference to heat the test oil. The heater ribbon is thermostatically controlled by a thermocouple positioned within the test fluid. To improve the heater efficiency the cavity between the two layers is filled with fibre glass insulation.

To ensure that the test contaminants are evenly distributed throughout the test fluid, two agitation methods have been included into the tank assembly. Firstly, a variable speed mechanical stirrer is fitted to recirculate the fluid around the tank and secondly, the return pipe contains an in-built diffuser. The diffuser was considered useful because it attempts to distributed the single return line fluid jet into a series of small radial jets. The diffuser has been constructed simply by attaching a conical end cap to the return pipe and then drilling a series of small radial holes (2 mm diameter) in the tube for the oil flow.

4.6.   Instrumentation and Data Acquisition

Where possible, the test rig has been designed to function without operator supervision and electrically operated components have been fitted where required. Because of the un-supervised operation of the rig it was essential that all equipment should operate in a fail safe manner should problems arise. Similarly, critical safety circuits have been duplicated to reduce the risk of a possible catastrophic failure occurring.

The design requirements for the control and instrumentation circuits may be summarised as:

- To provide a flexible system capable of providing constant operating conditions throughout the duration of a test.
- To obtain and record test parameters throughout the test.
- To provide a safety shutdown system if conditions extend beyond predefined limits.

To provide a continuous control and data acquisition system for the rig, a PC fitted with a multi-function input/output (I/O) board was selected as the heart of the system. Initially it was intended that all the rig control functions would be performed by the PC, but after considering the various options it became apparent that the PC could be overloaded if this approach was adopted. The final solution was obtained by using electrical hardware to provide the control of functions where the operating conditions remained constant for the duration of the test, i.e. the power pack and erosive wear circuit oil temperature settings, the switching of the two piston accumulators at the end of a stroke, etc. This permitted the PC to concentrate on providing the pressure feedback control, recording the test operating parameters and providing a safety shutdown system when the values exceed predetermined levels.

The PC and signal conditioning equipment is contained in a standard 19" free standing instrumentation rack, as shown in Figure 4.12. Where possible, the separation of analog circuits from the power circuits have been adopted to reduce the effects of electrical noise.

4.6.1. PC and Data Acquisition System

The control system is based on a Viglen 286 PC fitted with a Data Translation DT2811 multi-function I/O card. This provides an interface between the PC and the control and instrumentation electronics. The I/O card signal lines may be divided into two categories; either analog signals operating in the range of ± 5 volts or digital signals of 0 or 5 volts (logic level 0 or 1). Since the majority of the instrumentation transducers, solenoids, etc, operate outside of the I/O card voltage and current limits, signal conditioning cards are used to perform the various interface requirements. A schematic layout of the data acquisition system is shown in Figure 4.13.

The operation of the test rig is controlled by dedicated software written using Borland Turbo C. The software screen layout has been arranged to display all the required test parameters on a single screen, as shown in Figure 4.14. The screen layout is divided into four areas; the overall test parameters, the power pack circuit, the erosive wear circuit and a pull down menu bar. By incorporating the menu bar system into the software, permits all the necessary set up menus to be displayed and accessed as required. An example of this feature is shown in Figure 4.15.

The processing time for the PC is divided between two software routines operating in the foreground and background. The essential running and safety features are contained within the background software and accessed at 1 second intervals by an interrupt routine. The remaining processor time between the interrupt calls is used to perform all the ancillary duties in the foreground. The use of regular interrupt routines is an important feature in providing failsafe software, since an interrupt has processing priority.

The functions performed in the foreground and background are illustrated in the flow diagrams in Appendix 2. During normal operation the processor runs a screen display routine showing the current status of the test rig and when requested by the interrupt, actions the interrupt routine. The processor then reads in a new set of test data and compares it with defined safety and operating restraints. If no limits are exceeded, the data is made available to the foreground software and the processor continues where it left off before the interrupt call. If a limit is exceeded, the interrupt routine actions a rig shutdown and the test is terminated.
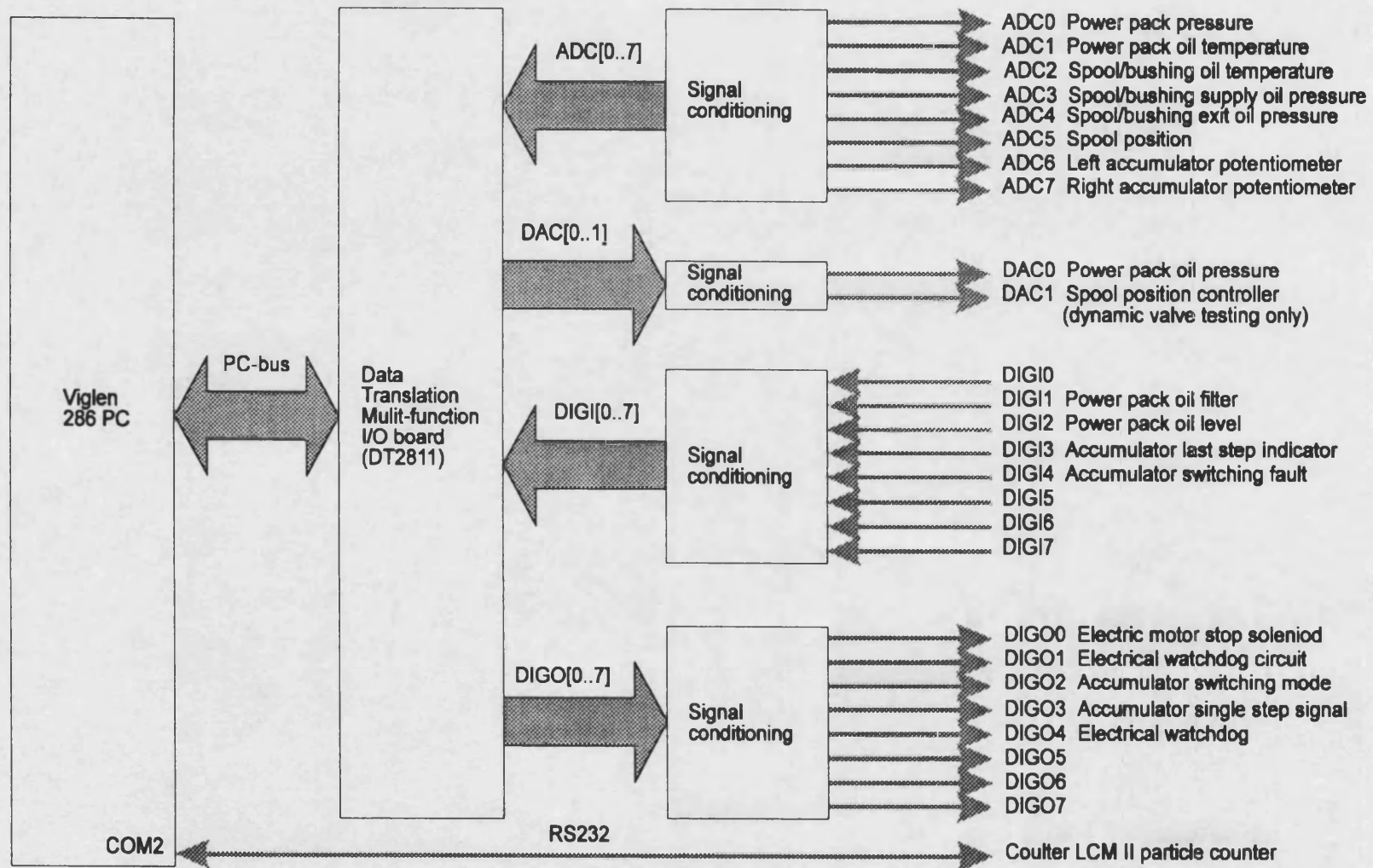
Figure 4.13 - Schematic layout of the data acquisition system.
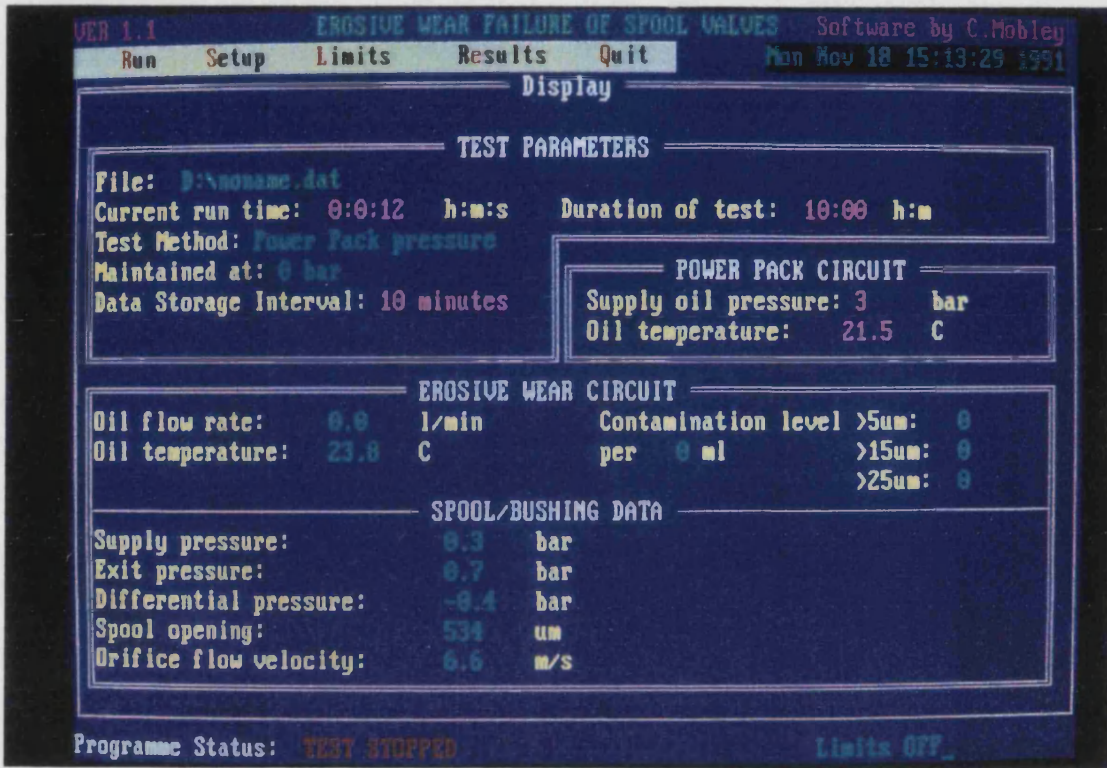
Figure 4.14 - Software screen layout.
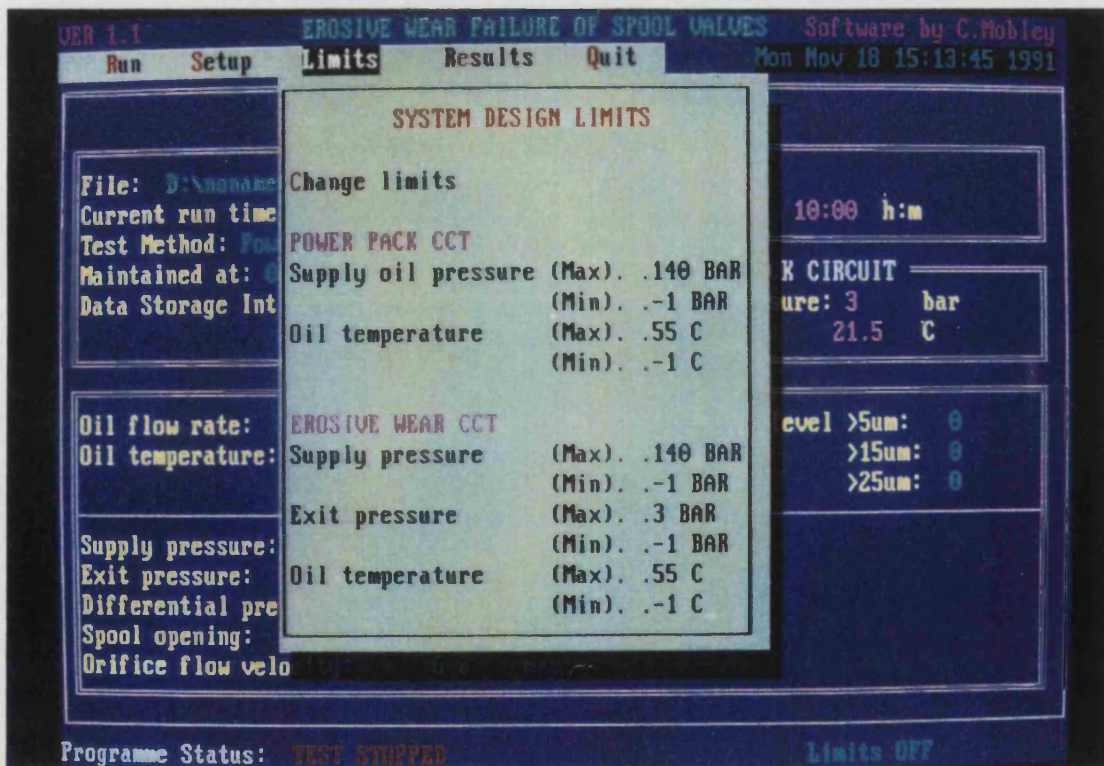
Figure 4.15 - Example of the pull down menu software.

4.6.2. Pressure Feedback Controller

The software has been written to allow the erosive wear test rig to operate in three different operating modes; constant power pack pressure, constant differential pressure and constant flow. Each mode essentially provides different ways of determining the pressure setting for the proportional relief valve fitted to the power pack.

The constant power pack pressure mode operates in open-loop control and permits any operating pressure between 0 and 140 bar to be selected. The relationship between the power pack pressure and the DAC output voltage to determined by calibration. Upon selection of a pressure, the software uses this relationship to ramp the output of the DAC to the required voltage.

The constant differential pressure and constant flow rate modes operate in a closed-loop control configuration with the purpose of maintaining constant test conditions across the test spool/bushing as the metering edges wear. On selection of either of these modes, the software ramps the DAC output voltage to an appropriate value found from calibration equations similar to that used in the constant power pack mode. Actual test values are then measured and compared with the required value. If there is an error between the two values, the DAC is incremented or decremented by a small amount as required. This process continues throughout the duration of the test with the closed loop controller effectively stepping by small increments about the required test value. Stability problems were experienced initially resulting in large pressure oscillations about the desired value. This was found to be attributed to the slow response of the test rig compared with the controller. Therefore, to reduce the magnitude of the oscillations a delay function was incorporated into the control software.

4.7.   Test Rig Validation and Operating Procedures

Successful design of a test rig is usually assessed according to the ease of obtaining and the consistency, of the test results. Unfortunately, in a research environment many of the design and operating requirements are unknown until testing has commenced. For this reason, many aspects of the test rig were based on experience and intuitive judgement. Therefore, it is important that a comprehensive validation process is undertaken allowing actual performance to be assessed. The results and procedures adopted for the erosive wear test rig are described in the following subsections.

4.7.1. Mechanical and Control Performance

No major design or operating restrictions were experienced with the test rig, although several minor adjustments were required to fine tune and optimise the performance. These are outlined below:

- To provide a fast accumulator switching response, logic elements, sequenced from one control valve were used to control the main flow. Using this arrangement, a large pressure fluctuation was created at the instance of switch over. Although this effect could be minimised by changing the logic element control orifices for any given test condition, it is not practical to make such changes for every test. An example of the spool/bushing supply and exit pressure transients when operating at 70 bar differential ($\approx$ 14 L min^{-1}) at switch over is shown in Figure 4.16.
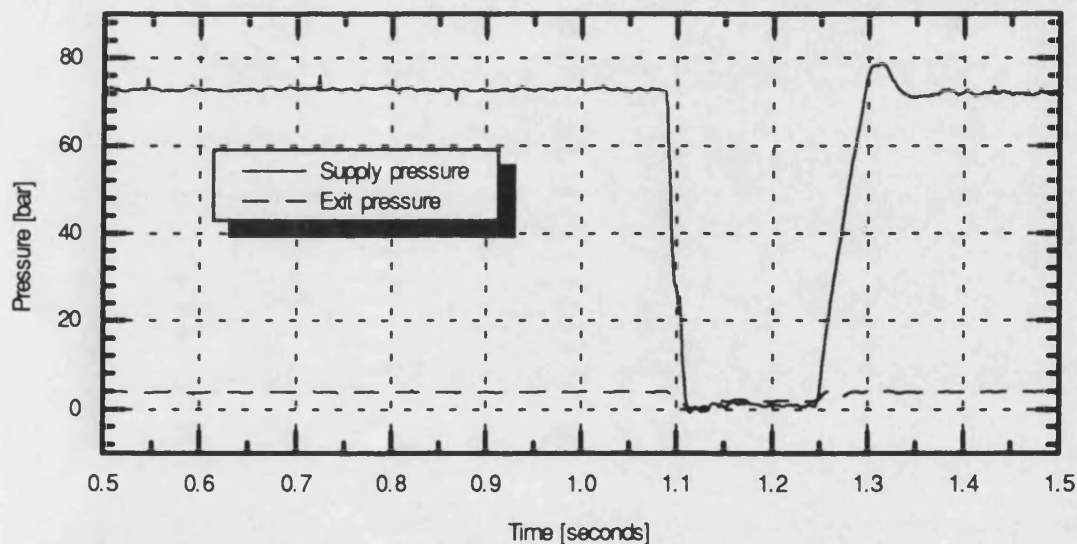
Figure 4.16 - Typical spool/bushing pressures transients at switch over.

- The erosive wear circuit was initially designed to operate at 60 L min^{-1}. This caused problems with the logic element switching and a maximum flow rate of 40 L min^{-1} been has found to adequate. To date, the reduced flow rate has not been found to be restrictive since the test work has identified that small spool openings ($\leq$300 μm) can be used which do not require the maximum flow rate.

- From the experimental work conducted, the erosive wear circuit flow rates are typically below 25 L min^{-1}. Since the cooler was sized for the theoretical maximum condition, the

temperature stability is slightly compromised at the lower flow rates. Typically, this has been found to be better than ±5 % of the selected operating temperature. Obviously, this could be reduced by fitting a smaller cooler, although this would cause problems if the full capability of the rig is utilised at a later date.

• The on-line operation of the Coulter LCM II particle monitor from the outset was a limiting operating factor, but at the time there were no other practical alternatives. On the positive side, the LCM II has been found to be reliable giving consistent results when the on-line pressures are kept below about 2 bar. If, however, the maximum operating pressure of 3.5 bar is used, operating problems were experienced. From discussions with Coulter, it appears that the LCM II was designed to operate with pressure on the inlet port without any back pressure on the outlet port. Unfortunately, this approach is not acceptable within this test rig since it is essential to return the fluid from the LCM II outlet port into the wear circuit to maintain constant contaminant stability. At present, a solution to this problem has not been found, but the LCM II has been used reliably on-line by working below this 2 bar limitation. Since the unit operates by measuring the differential pressure across a filter mesh, it is not clear why a similar static pressure on the inlet and outlet port should effect the LCM II operation.

4.7.2. Clean-up Performance

Filtering new oil and cleaning-up the erosive wear circuit is performed by the hydraulic filter attached to the fluid conditioning rig. This unit is fitted with a large flow capacity $\beta_3 \geq 200$ absolute rating glass fibre element.

Before the commencement of an erosion test, the wear circuit and the new oil is filtered to a high cleanliness level using the following technique:

i) 25 to 30 litres of new oil is filtered at a rate of 5 to 6 L min⁻¹ within the fluid conditioning rig for 12 hours at a temperature of 60 °C (usually run over night).

ii) Approximately 5 litres of clean oil is used to flush through any existing oil from the erosive wear circuit into the waste container.

iii) The erosive wear circuit is filled with clean oil and then configured with the fluid conditioning rig to permit the cyclic operation of the piston accumulators to clean-up the erosive wear circuit. This operation is completed at a large spool opening (typically 500 to 1000 µm) with a flow rate of 30 L min⁻¹ and a low operating pressure for an hour.

This ensures that any contaminant present within the circuit is flushed out without causing premature wear of the spool and bushing before a test.

iv)   Finally, the oil within the erosive wear circuit is returned to the fluid conditioning rig to be mixed with the previously cleaned oil before the commencement of the contaminant mixing process.

Using the above technique, the rig can be successfully cleaned-up to an ISO 4406, class 8/4 [7] with a typical distribution as the shown in Figure 4.17. Although the erosive wear circuit is fitted with a Coulter LCM II particle monitor, this cannot be used to record the low particle levels obtained in the clean-up process and therefore the results were obtained using a Hiac sensor temporarily fitted online with the circuit.
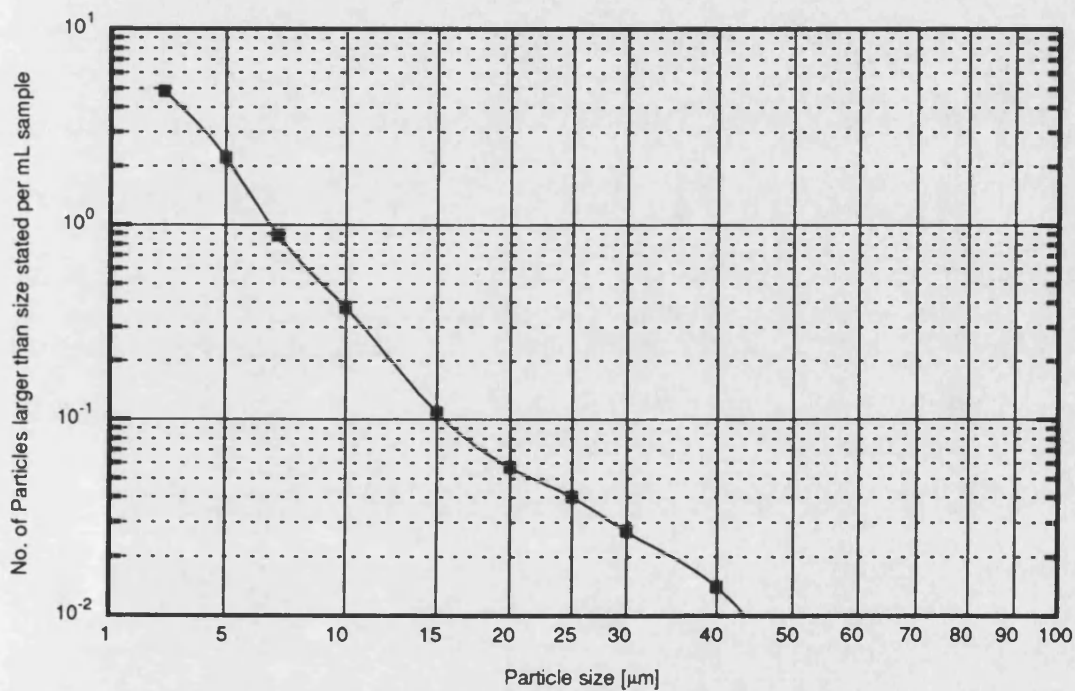
Figure 4.17 - Typical wear circuit clean-up levels.

4.7.3. Contaminant Mixing Procedure

The mixing of the test contaminants into the hydraulic oil is a very important process and must be rigorously adhered to if a consistent and repeatable particle distribution is to obtained. The method described has been adapted from past experience within the Fluid Power Centre [52].

Before the commencement of the contaminant mixing process, all the laboratory equipment used in the preparation of the test dusts and oil should be clean and contaminant free. This is achieved using similar techniques to those described in Appendix 3 for the sample bottle cleaning process.

The mixing procedure is as follows:

i) Using the clean-up procedure detailed in Section 4.7.2, filter the test oil test and the erosive wear circuit.

ii) Using a chemical balance (with a resolution better than 1 mg) and a porcelain evaporating basin, weigh out the required mass of test contaminant (previously stored in a heated cabinet to remove moisture) to provide the correct mg L^{-1} concentration.

iii) Add filtered oil to the test dust a few drops at a time and mix with a glass rod (a small stainless steel spatula may be used as an alternative) until approximately 100 mL of oil has been mixed with the dust. This suspension is then transferred to a clean 250 mL glass sample bottle. Further oil is then added to the evaporating basin and transferred to the sample bottle to ensure that little dust remains in the basin.

iv) The bottle is then capped and shaken by hand for 5 minutes before being placed in an ultrasonic bath for 5 minutes to disperse the particles in the oil and breakdown any agglomerates. The contents of the bottle are then added to a 5 litre polythene container partially filled with 3 L of clean oil taken from the fluid conditioning rig. This container is then shaken by hand for a further 5 minutes before the contents are slowly poured into the remaining volume of clean oil within the fluid conditioning reservoir.

v) The contaminated and clean oil is then thoroughly mixed together by the action of the stirrer fitted within the reservoir and recirculated around the fluid conditioning rig for 30 minutes. Using the Coulter LCM II (fitted on-line within circuit), particle counts are taken at 5 minute intervals to confirm that contaminant stability has occurred. The particle counts also confirm that a consistent mixing process has been conducted and that the correct concentration has been achieved.

vi) Using the fluid conditioning rig, recirculate the contaminated oil around the erosive wear circuit. During this process, the power pack is used to cycle the piston accumulators to improve the mixing process. This process continues until particle counts within the erosive wear circuit stabilise. The erosive wear circuit is then filled and isolated from the fluid conditioning rig before the commencement of the wear test.

4.7.4. Contaminant Stability

The contaminant stability of the rig may be considered as the difference in particle counts at the start of the test and any at instant in time, for example, the start and end of a test.
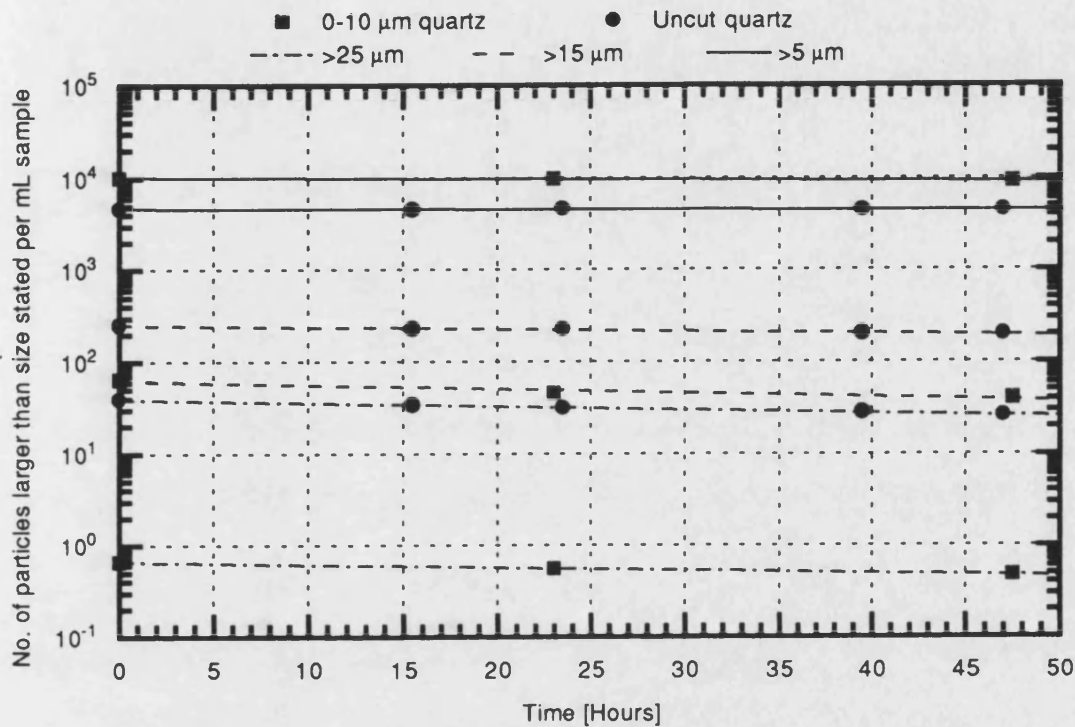
Figure 4.18 - Contaminant stability levels for uncut and 0-10 μm quartz.

Figure 4.18 shows the stability results for uncut and 0-10 μm quartz at a concentration level of 1 mg L^{-1}. The tests were conducted without any orifice restriction fitted which permitted the tests to be conducted at typical test conditions without the high operating pressure which would cause wear and hence introduce wear debris into the particle counts. It can be seen for both distributions that the particle counts fall at a linear rate during the test. Also, the settling rates increase with particle size as would be expected, although even at the >25 μm count this does not amount to a change in an ISO class [7] over the 48 hour test period.

4.7.5. Repeatability

To determine the repeatability of the test procedure and the spool/bushing wear rates, two tests were conducted with identical test conditions, the results of which are contained in Figure 4.19.

This shows the flow rate increasing through the orifice with time whilst maintaining a constant differential pressure of 70 bar.
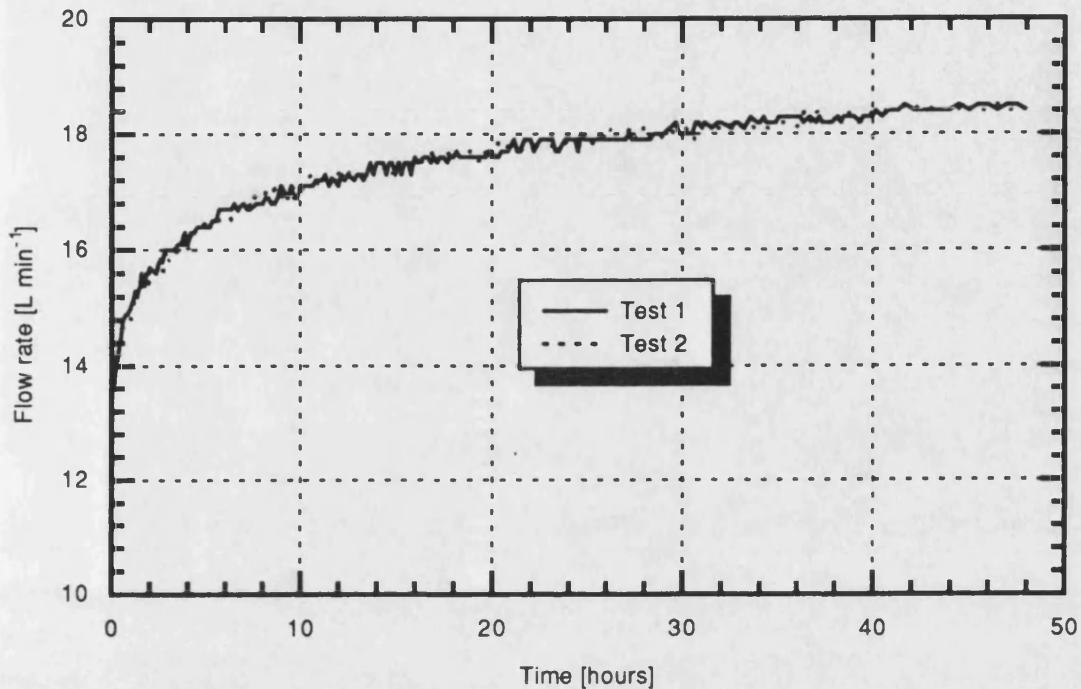
Test conditions - 70 bar differential   Contaminant concentration 10 mg L^{-1} of uncut quartz
                 Flow from P→S   Base oil grade 150N (32 cSt @ 40 °C) operating at 60 °C
                 100 µm spool opening

Figure 4.19 - Repeatability test results.

The results indicate that the starting flow rate for each test is similar. This demonstrates that it is possible to strip down and re-assemble the valve block with different components and accurately re-position the spool to obtain a repeatable pressure - flow characteristic. By repeating this process it has been found that the flow rate can be reproduced to within ± 0.1 L min^{-1}.

From Figure 4.19 it can be seen that flow rate increases in a similar manner for the two tests. This implies that the repeatability of the test method and the test rig is very good. When considering the design of the spool/bushing, it is apparent that the initial rapid flow increase can be achieved by removal of a small amount of material from the metering corner. As time progresses, if the wear rate of the material remains constant, the rate of change in flow area must decrease, this suggests that the exponential wear graph profiles are not unreasonable

4.7.6. Oil Degradation

Since the erosive wear circuit has a small working oil volume ($\approx$ 11 litres) and a maximum flow rate of 60 L min^{-1}, the oil is worked hard during a test. It is desirable that the oil properties should not change in order to permit the wear to be directly attributed to either the oil formulation, the spool/bushing material, or the type and distribution of the test contaminant.

To assess the oil stability, an oil sample was taken at the beginning and at the end of a 48 hour test and analysed at BP Sunbury. The results indicated that no physical or chemical properties had altered and therefore changes in the oil properties will not influence the erosive wear test results.

4.7.7. Contaminant Degradation

From Section 4.7.4, it is evident that a progressive reduction in the contamination level occurs during the test period, which must result in a corresponding reduction in the wear rate. In addition to these changes, any variation in the contaminant properties can also contribute to changes in the wear rates. In particular, it has been reported that the abrasive properties of test contaminants reduce if they are re-used. To demonstrate this, Sparks et al. [53] have investigated the influence of recycled glass spheres and irregular shaped quartz particles on erosion rates. Their work has suggested that a particle fracture threshold occurs between 44 and 95 m s^{-1}, beyond which the particles fragment. This progressive fragmentation leads to a reduction in the measured erosion rates as the particles are recycled. This has been attributed to the intrinsic size effect, the aerodynamic effects within the test rig, and the changes in the particle angularity due to fracture.

Due to the design and operation of the valve erosion test rig, the test contaminants will recirculate many times during the 48 hour test period with a similar impact velocity to the Sparks et al. experiments [53]. Therefore, to examine the abrasive degradation within the test rig, it was decided to perform a restart with new contaminant midway through the test period.

From Figure 4.20. it can be seen that the restart test produces an increased flow rate when compared with the standard 48 hour test. The results indicate that this increase has two salient features: firstly, a period of rapid change occurs after the introduction of the new contaminant and secondly, the wear rate then continues at a nominal 0.5 L min^{-1} offset from the standard results.
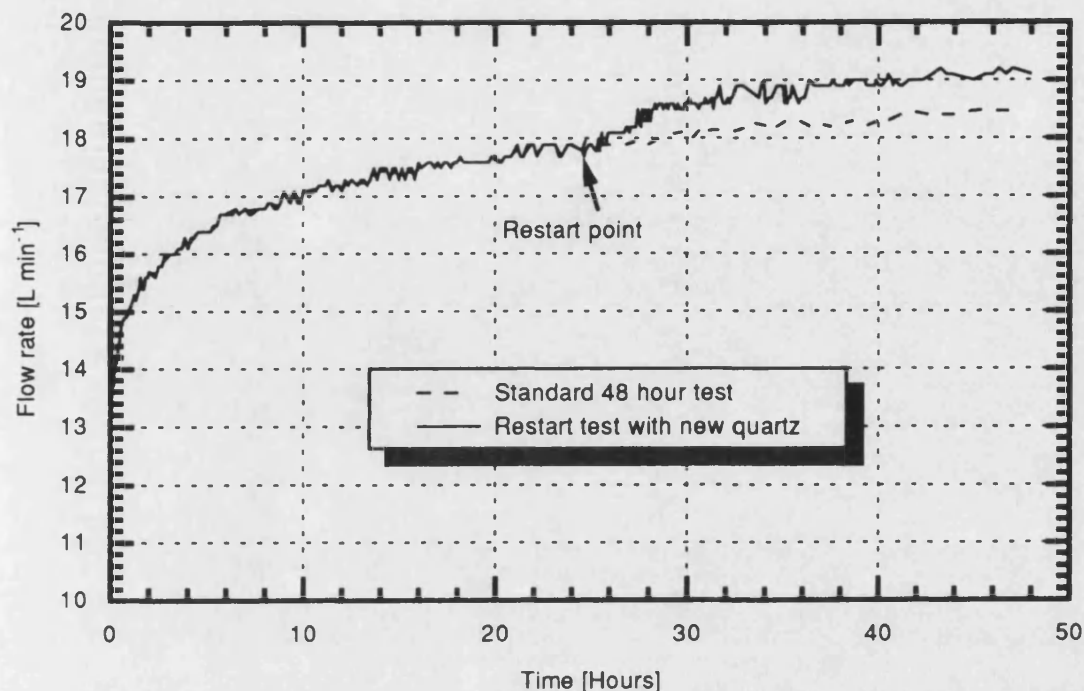
Test conditions - 70 bar differential   Contaminant concentration 10 mg L^{-1} of uncut quartz
                    Flow from P→S   Base oil grade 150N (32 cSt @ 40 °C) operating at 60 °C
                    100 μm spool opening

Figure 4.20 - Contaminant degradation results.

From this study, it is evident that the wear rate can be influenced by introducing new contaminants into a test. However, it not clear on the contribution made to this from the larger particles breaking down (see also Section 5.8) or from the changes in test dust abrasive properties. In addition, there is also the possibility of additional experimental errors being introduced during each oil/contaminant mixing process. Although small changes in the contaminant properties are unavoidable during the 48 hour test period, since many of the test results are used for comparative purposes then these effects are not considered to be significant.

4.8.   Conclusions

The test equipment discussed within the chapter has operated successfully for 5500 hours. During this period, a few minor and unfortunately one major failure has occurred. The major incident arose from an undetected software error in the safety shutdown circuit and resulted in the rig overheating. This fault should never have occurred and a parallel hardware shutdown

system has now been installed. This incidence brought home the limitations of a total commitment to software based control systems.

Although several minor concerns have been highlighted, when viewed against the very positive aspects of the test rig design in the areas of reliability, contaminant stability and repeatability, the overall test rig design and performance for a relatively unknown area of research is considered to be excellent.

5

In-Service and Experimental
Erosive Wear Results

5.1. Introduction

This chapter examines and compares the condition of in-service spools/bushings with new and worn components to establish the typical wear modes and the null leakage degradation. In addition, the hardness properties and the steady state pressure-flow characteristics have be found for the test components to provide information on the wear rates.

5.2. New Spools and Bushings

Before the in-service and the erosive wear test rig components can be compared or evaluated, it is important to establish the physical and geometric properties of the *as new* components.

The spool and bushing are both manufactured in an AISI 440C stainless steel. It is a hardenable chromium steel which can be heat treated to obtain a high degree of through hardness and has good corrosion and heat resisting properties. This grade has reasonable machining properties, although Ultra Hydraulics have experienced difficulties in obtaining a very sharp edge when in the heat treated state.

The manufacturing process for the spool and bushing can be summarised as follows:

Spool - i) Billets are sawn to length from stock material.
     ii) Billets are machined to length and the centres are added in a lathe.
     iii) Through hardened and tempered to give a minimum hardness of 650 Vickers.
     iv) The billet centres are ground true
     v)   The billet is centreless ground to produce the required profile.
     vi) The spool O/D is matched ground between centres to suit bushing bore.
     vii) The spool metering lands are matched ground between centres to produce the required lapped condition with the bushing.
     viii) The metering edges are lightly deburred to remove the sharp corner.

Bushing - i) Billets are sawn to length from stock material.

ii)   Billets are gunned drilled and the O/D profiles are machined on a centre lathe.

iii)   Through hardened and tempered to give a minimum of 650 Vickers.

iv)   The O/D and O-ring grooves are centreless ground.

v)   The metering slots and internal metering annuli are electro discharge machined (EDM).

vi)   A general cleaning process to remove any swarf and EDM products.

vii)   The bore is honed and solid lapped.

5.2.1. Component Hardness

From Section 5.2, it can be seen that the spool and bushing are heat treated during the manufacturing processes. Therefore, any subsequent machining operations after the heat treatment could potentially have a tempering effect, although Ultra Hydraulics consider this to be insignificant.
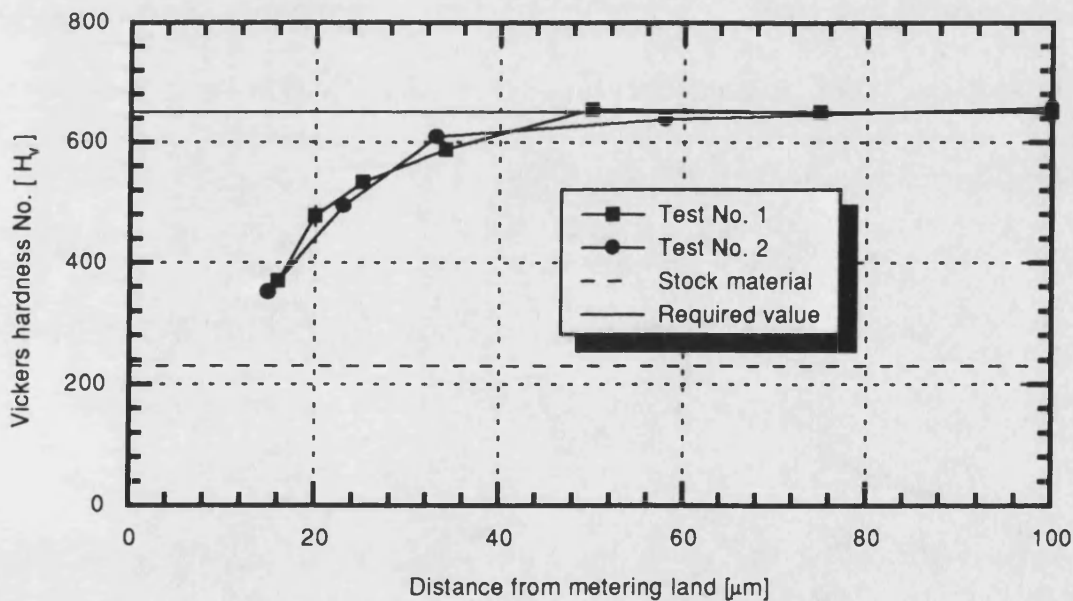
Figure 5.1 - New bushing hardness profile.

However, when considering the EDM of the metering slots within the bushing, the author considered that local tempering effects may occur, reducing the hardness of the metering corner. To verify this, a new spool and bushing was sectioned longitudinally, resin mounted and highly polished to produce a scratch free surface. Testing the specimens in a micro hardness testing machine with a Vickers pyramid diamond, it was found that both components had a bulk

hardness of $H_v \approx 650$ (6.4 GPa) as specified on the manufacturing drawings. However, when the material adjacent to the bushing metering edge was tested, there appeared to be a marked reduction in hardness in the 10 to 40 µm band from the edge, as shown in Figure 5.1. To ensure that this reduction was not just an edge effect phenomenon, other hardness tests were carried out on a different ground edge of the component. Although the results indicated a reduction in the hardness at the edge, this was not as marked as obtained at the EDM edge.
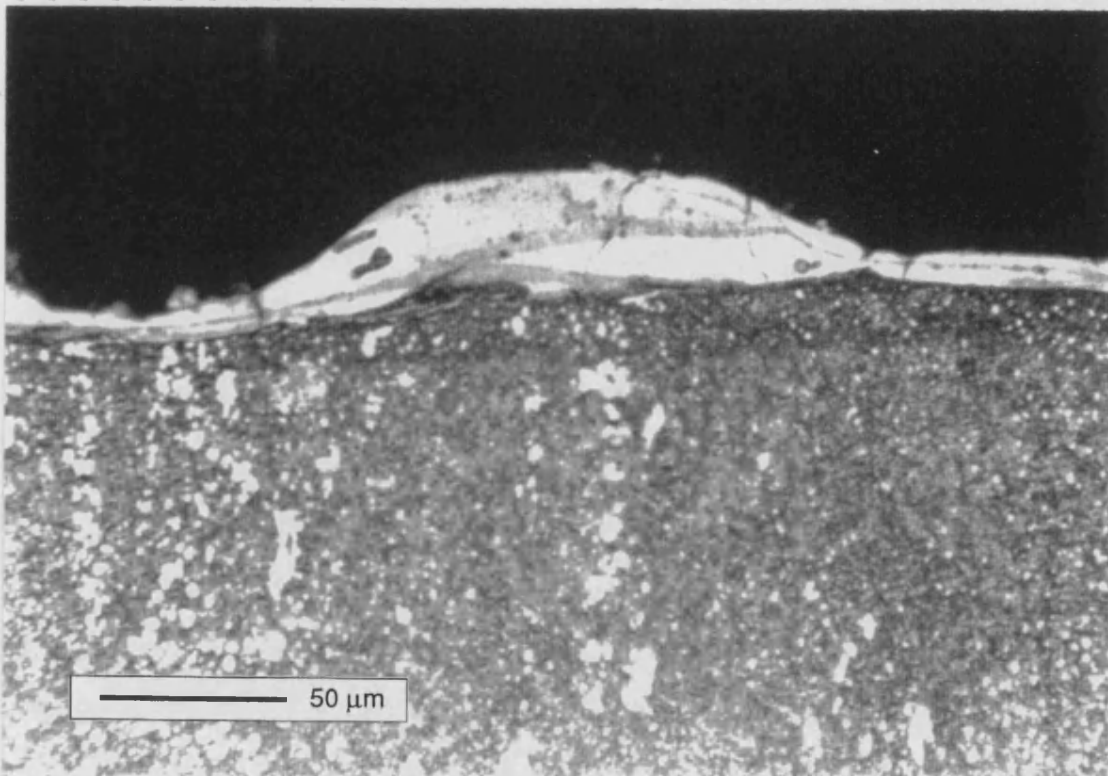
Figure 5.2 - Metallurgical structure of a new bushing.

To verify the micro-hardness results, a second bushing specimen was mounted and etched as a normal section for metallurgical examination. By using an optical microscope it was then possible to examine the material grain structure around the EDM face. It can be seen in Figure 5.2 that a boundary layer exists of about 10 to 20 µm which appears to contain no carbides as evident in the bulk material structure. To verify this finding, the specimen was subjected to an element intensity trace across the bulk of the specimen to the metering edge, Figure 5.3 shows how the composition of carbon and chromium varies with position. It can be seen that for about 20 µm from the EDM face the structure has an increase in carbon and a constant chromium content, this suggest that the bulk material matrix is tempered by the EDM process to reduce the chromium carbides and hence reduce the material hardness.
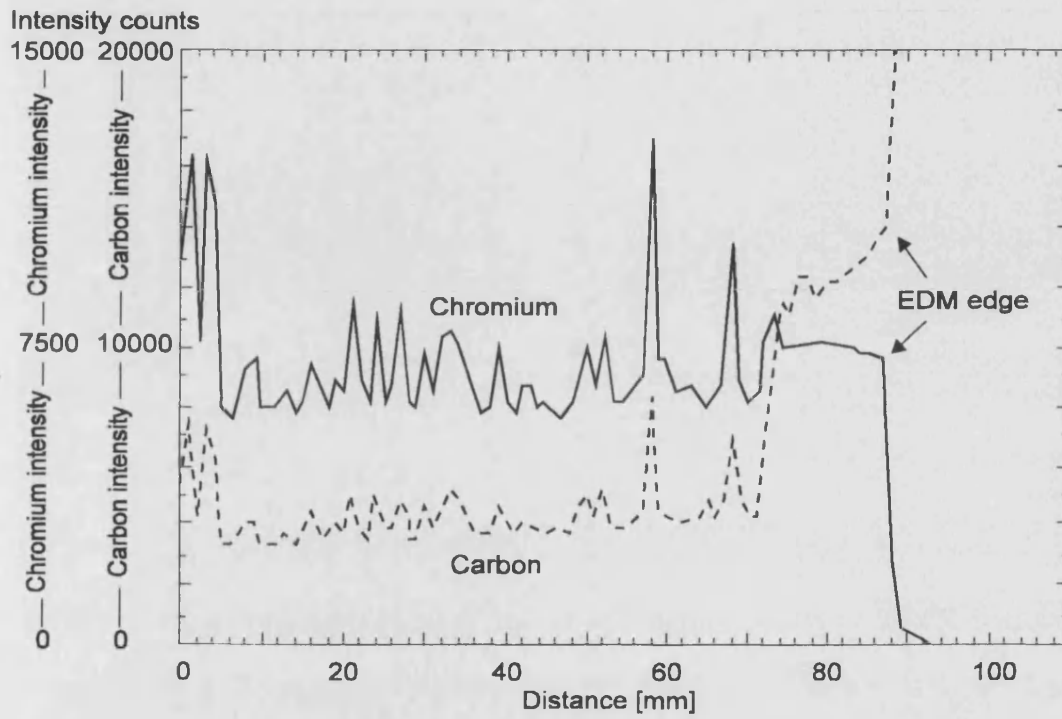
Figure 5.3 - New bushing element intensity trace.
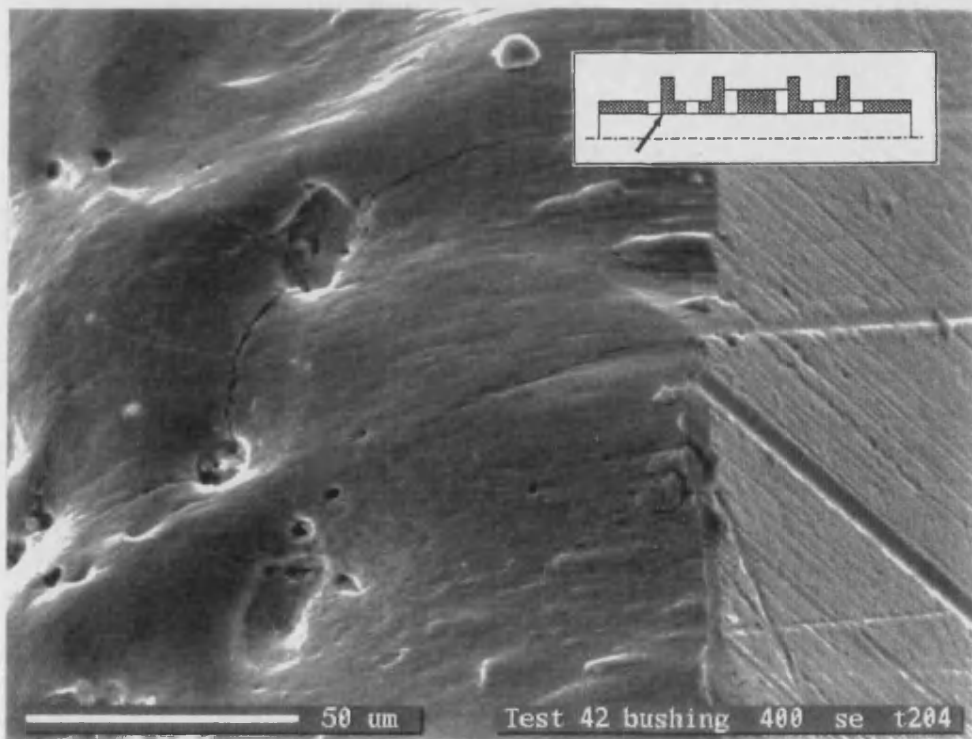
Figure 5.4 - SEM micrograph showing surface cracks in the bushing EDM face.

In addition to the change in structure of the boundary layer, Figures 5.2 and 5.4 show that this layer contains surface cracks. It has been observed in one new specimen that this boundary layer has been chipped out from the surface, although to date there is no evidence to suggest that the surface cracks propagate or allow the material to be removed in service.

5.2.2. Surface Topography

Figures 5.5 and 5.6 contain typical SEM micrographs of a new spool and bushing. For the spool, grinding marks can be clearly seen on the outside diameter and the side face of the metering corner. In theory, the intersection of these two faces should produce a perfect square corner. In practice it is very difficult to obtain this and a small machining burr is likely to be obtained. Although this feature can be seen in Figure 5.5, it is clearly very difficult to assess the actual squareness without undertaking actual profile measurement.

However, for the bushing Figure 5.6, the precise intersection of the bore and the metering slot is not so clearly defined as for the spool. In this case, the EDM of the flow slots produces an irregular edge which is more difficult to define, since it is not apparent where the axial zero datum line should be taken in the profile measurement data normalisation process. It was found that a satisfactory solution may be obtained by taking a numerical average of the radial axis co-ordinates at a predetermined distance from the corner where it is considered that no, or very little wear is likely to occur.

From the profile measurements taken on new spools and bushings, the results indicate that a consistent profile exists around the circumference. Hence, this result permits the use of a single 2-D trace to be used for comparison purposes with worn in-service and erosion test specimens. From Figure 5.7, it may be seen that the spool metering corner is produced from two very good square faces with typically a 10 μm radius at the intersection. From the bushing profile result, the irregular EDM face can be clearly seen in the radial direction. Unfortunately, this produces different metering corner radii at each circumferential location. Therefore, the result shown in Figure 5.7 must not be taken as the absolute reference but should be considered as a typical result for comparison purposes.
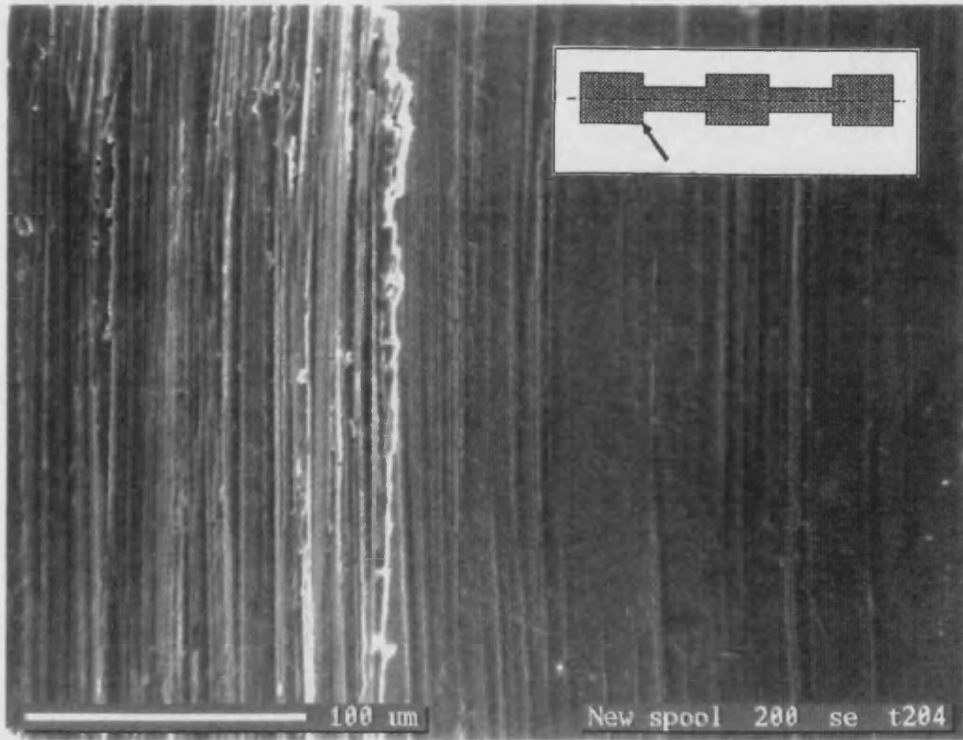
Figure 5.5 - Typical SEM micrograph of a new spool metering edge.
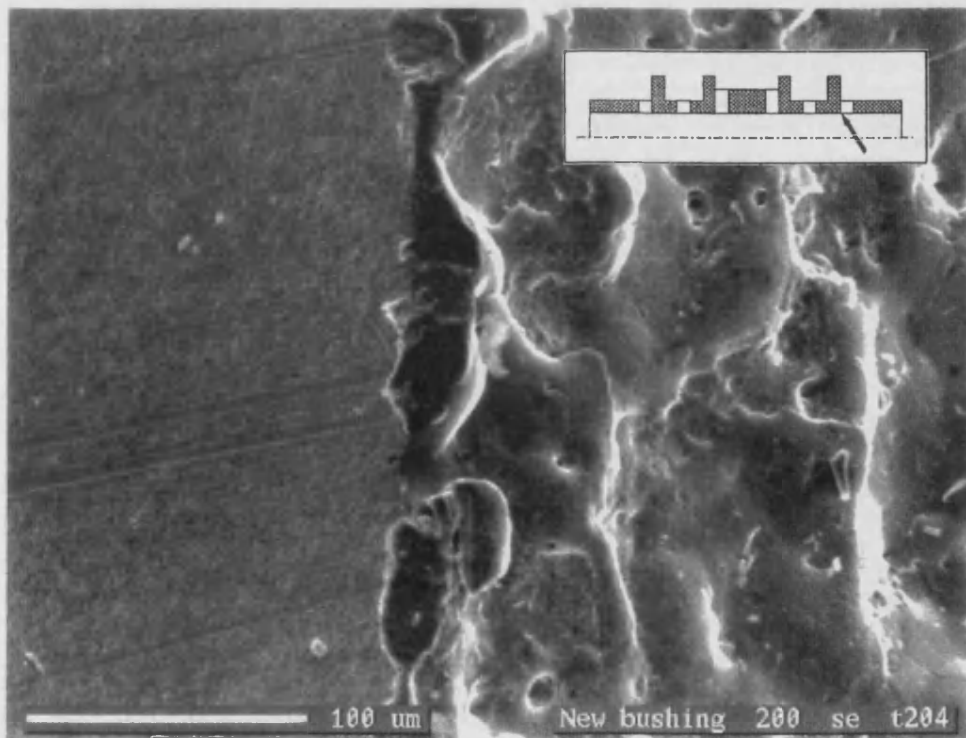
Figure 5.6 - Typical SEM micrograph of a new bushing metering edge.
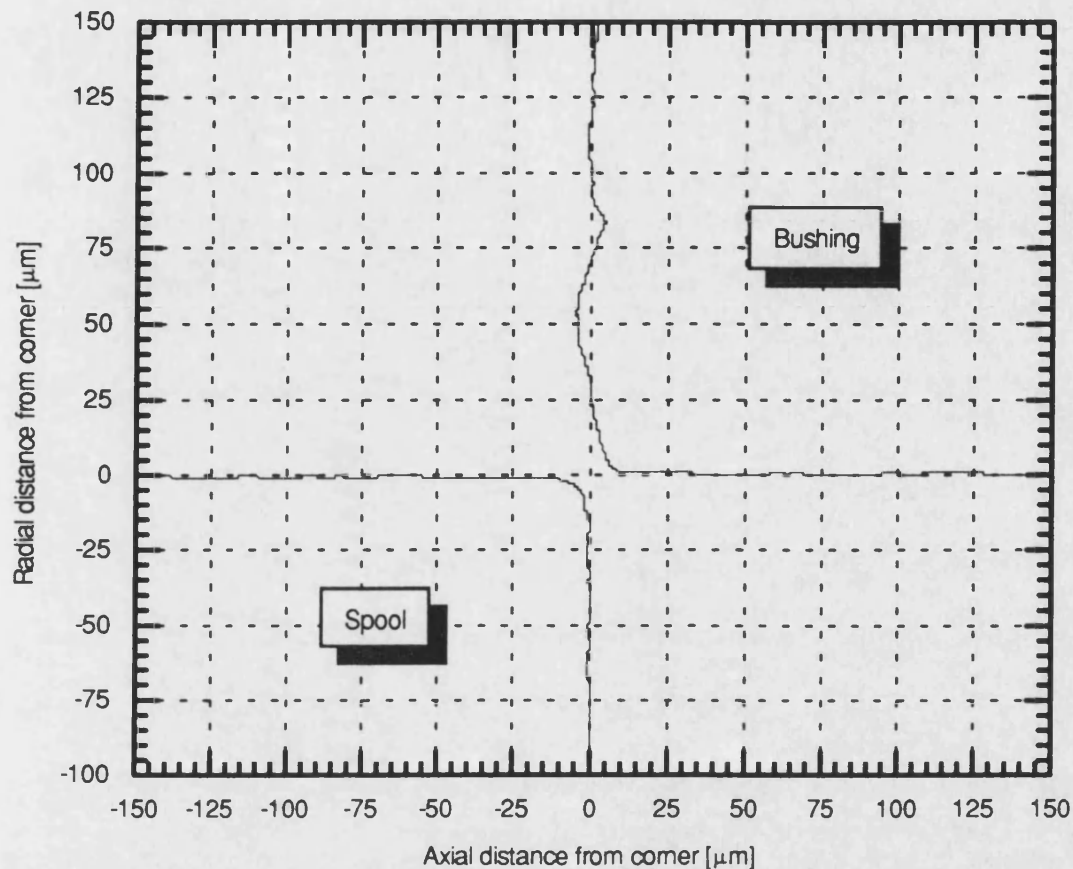
Figure 5.7 - Typical metering edge profiles of a new spool and bushing.

5.2.3. Pressure - Flow Characteristics

To permit comparison between new and worn test components, it is important to establish the pressure-flow characteristics for the single metering orifice over the test range of spool openings. These are shown in Figure 5.8 for differential pressures of 35 and 70 bar. The selection of 35 bar was derived from the quoted valve operating conditions of 70 bar pressure drop (across two lands). Similarly, the 70 bar condition enabled the results to be compared with the manufacturer's standard null leakage test which is conducted at 140 bar.

From Figure 5.8 it can be seen that there is good agreement between the pressure to service (P→S) and service to tank (S→T) results for two randomly selected spool/bushing pairs at both pressures. In each case, for spool openings above 30 μm, the flow rate increases linearly with valve opening. Substituting these points into the orifice equation, Equation 5.1, it has been found that an average flow coefficient value of 0.7 is obtained for each test condition. This result

confirmed the classic Von Mises theory [54] for turbulent flow though a sharp edge orifice and proved useful in determining the accuracy and repeatability of the spool positioning system. Tests have also indicated that this value remains constant (within rig detection limits) with changes in oil viscosity, although small changes must occur since the oil density will also change very slightly with temperature [55].

$$Q = C_q A_o \sqrt{\frac{2 \Delta P}{\rho}} = C_q (\pi d x) \sqrt{\frac{2 \Delta P}{\rho}} \qquad \dots (5.1)$$

To prevent the metering orifice from blocking with contaminant, tests indicated that the smallest spool opening must be greater than the largest particle size contained in the test dusts. Therefore, the smallest test opening for the spool was taken to be 100 μm which enabled the tests to be undertaken within the linear flow region.
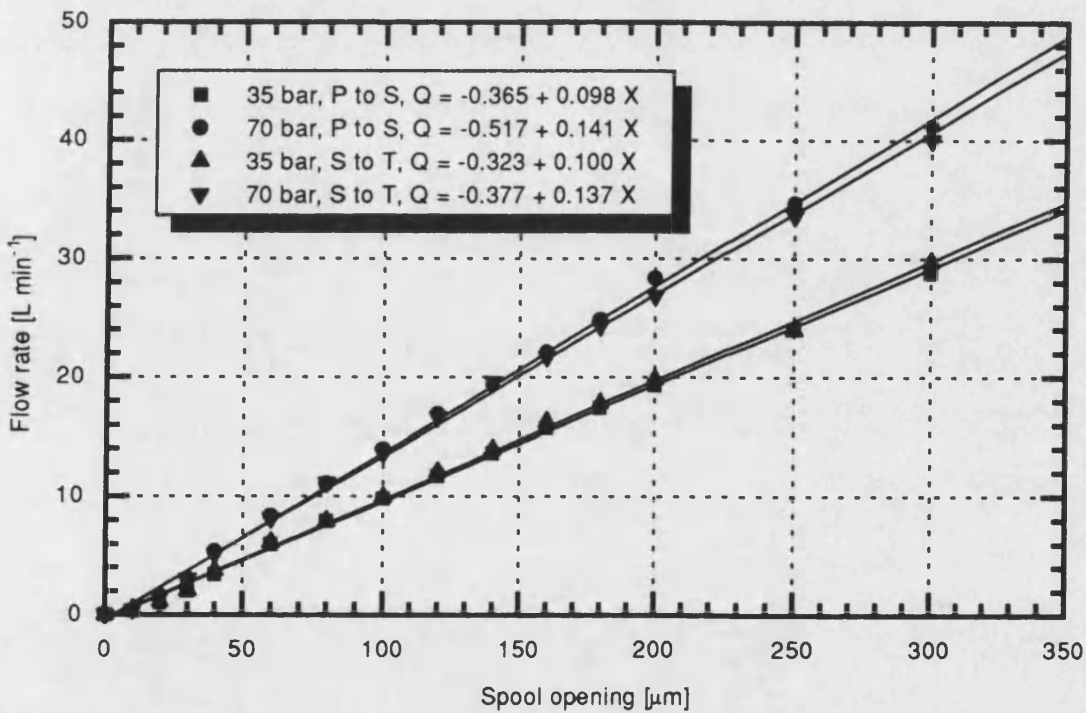
Figure 5.8 - New spool/bushing metering orifice pressure-flow characteristics.

5.3.   In-service Spools and Bushing

It was intended to establish links with several industrial users to obtain actual servo valve field results with a known operational history. Unfortunately, these arrangements could not be made and therefore the results presented are based on valves returned to Ultra Hydraulics Ltd for

repair. Although the results give a good indication to the condition of in-service spools and bushings, the operating duty/environment to achieve this degradation it not known.

5.3.1. Null Leakage Performance

The null leakage test is the established method used by the servo valve manufactures to assess wear. The test consists of measuring the leakage flow through the valve with a 140 bar differential pressure between the pressure and tank port with the valve de-energised and the two service ports blanked off. Unfortunately, this result gives the combined 1st and 2nd stage leakage and further analysis is required to find the individual values. This can be achieved by repeating the above test procedure, but in this case, the spool is driven hard over to give maximum spool travel. At this condition, the spool/bushing lands become over-lapped and therefore any leakage flow can be directly attributed to the 1st stage. This value is a good estimate to the actual value providing the radial clearance between the spool and bushing has not increased significantly due to in-service wear.

From the manufacturing conformity tests performed at Ultra Hydraulics Ltd, it has been established that a typical new valve will have a total null leakage of 1.3 to 1.7 L min^{-1}, of which 0.6 to 0.8 L min^{-1} can be attributed to the first stage. Also, it has been found by experience from the repair/service department, that the valve response and linearity performance characteristics are significantly degraded when the total leakage value is above 3.5 to 4.0 L min^{-1}. At this condition, the 2nd stage leakage is typically >3.0 L min^{-1}. However, from the in-service components examined for this thesis, it has been found that values as high as 4.0 to 6.0 L min^{-1} are not uncommon for the 2nd stage leakage.

5.3.2. Surface Topography

As discussed in Chapter 1, it is very difficult to define the operating and duty cycle conditions for a typical servo valve. However, from SEM inspection of various in-service components it has been concluded that the following three different wear failure processes occur and contribute to the degraded performance:

i)   Particle abrasion between the spool and bushing (3 body abrasion) as the spool moves. This process results in axial scratches on the outside diameter of the spool and within the bore of the bushing, thus increasing the radial clearance between the two components.

ii)   Particle chip shearing (a severe form of abrasion) causing large defects to the metering
       corner of the spool and bushing. This mechanism occurs when a particle is trapped in
       the spool opening as the spool returns or travels through the null position.

iii)   Particle erosion causing the transformation of the square metering corner of the spool
       and bushing to a curved/rounded profile.

Figures 5.9 to 5.12 contain SEM micrographs of the pressure port (P→S) and the tank port (S→T)
metering lands from a typical in-service specimen. From the two spool micrographs it can be
seen that the outside diameter has been damaged but the side face appears to unaffected. This
result is surprising for the tank port (S→T) because the fluid flow will tend to impinge onto the side
face causing erosion damage. Since this result is common with all the field samples examined
to date, it may be concluded that if particle erosion occurs on this face, it must be concentrated
at the metering corner. Also, since both spool metering lands are subjected to an identical duty
cycle (amplitude and frequency) during the valve operation, it may be expected that similar
amounts of abrasion damage would be seen at both locations. However, this result is not the
case and the spool has more damage on the pressure port than the tank port. This difference is
possibly due to the combined action of particle erosion and abrasion as the fluid enters the valve.

The evidence obtained from the bushing micrographs suggests that the areas of greatest damage
do not correspond to the same locations observed on the spool. For example, at the pressure
port, the spool appears to have more damage than the bushing. The reverse occurs for the tank
port which suggests that the fluid flow patterns and particle impact angles are critical to the high
wear locations. Unfortunately, on the test rig erosion specimens (see examples in Section 5.7)
the damage caused by particle erosion does not conform to this hypothesis.

From Figures 5.9 to 5.12 it is evident that the wear patterns are irregular and that the reliability
of a single trace being representative of the complete circumference is poor. Therefore, to
eliminate this error and to provide an additional insight into the field components, four 3-D contour
maps have been included. Figures 5.13 to 5.16 have been constructed over a 3° arc using a
circumferential step size of 3.5 μm.

Comparing the two spool corner profiles Figure 5.13 & 5.15, it can be seen that the pressure port
has greater damage as suggested by the SEM micrographs. Figure 5.13 indicates that a definite
step change (approximately 7 μm) in the outside diameter of the spool occurs before a general
rounding of the metering corner. In addition to material removal, it is also evident that the material
has been deformed in the direction of the fluid flow to produce a 2 to 3 μm overhang on the side
face. In comparison, the tank land has material removed from the side face due to particle
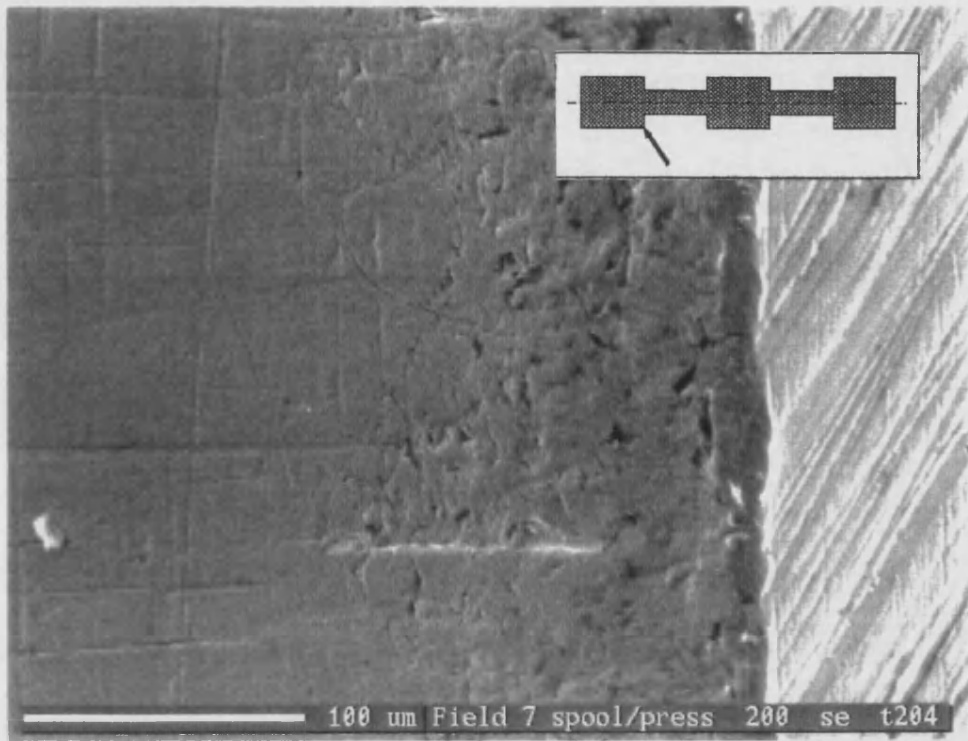
Figure 5.9 - Typical SEM micrograph of an in-service spool metering edge (pressure land).
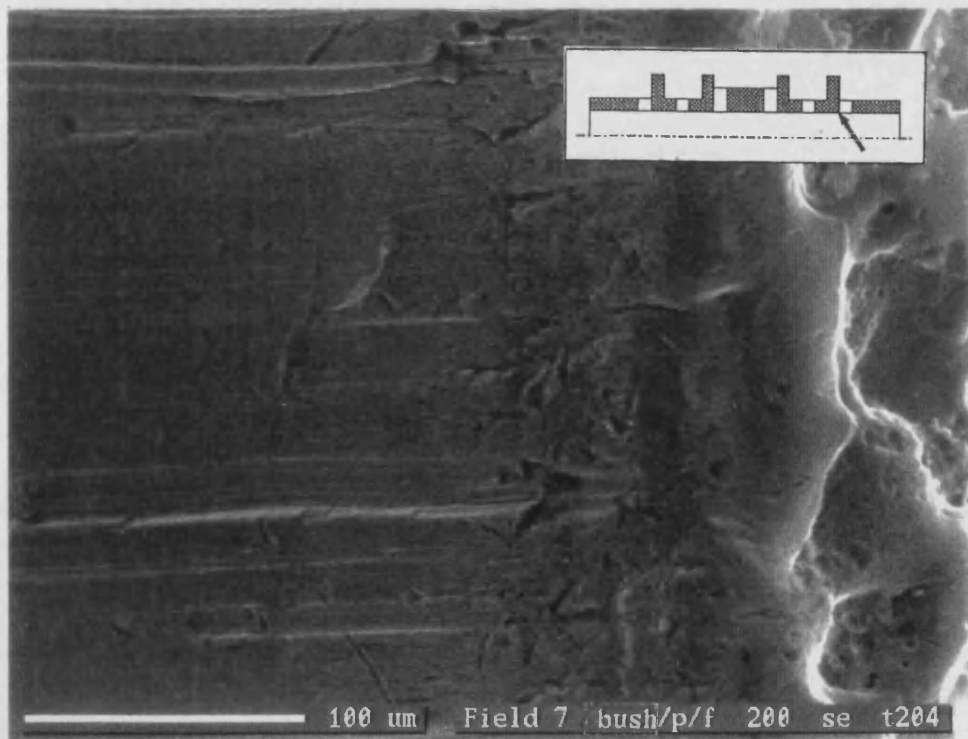
Figure 5.10 - Typical SEM micrograph of an in-service bushing metering edge (pressure land).
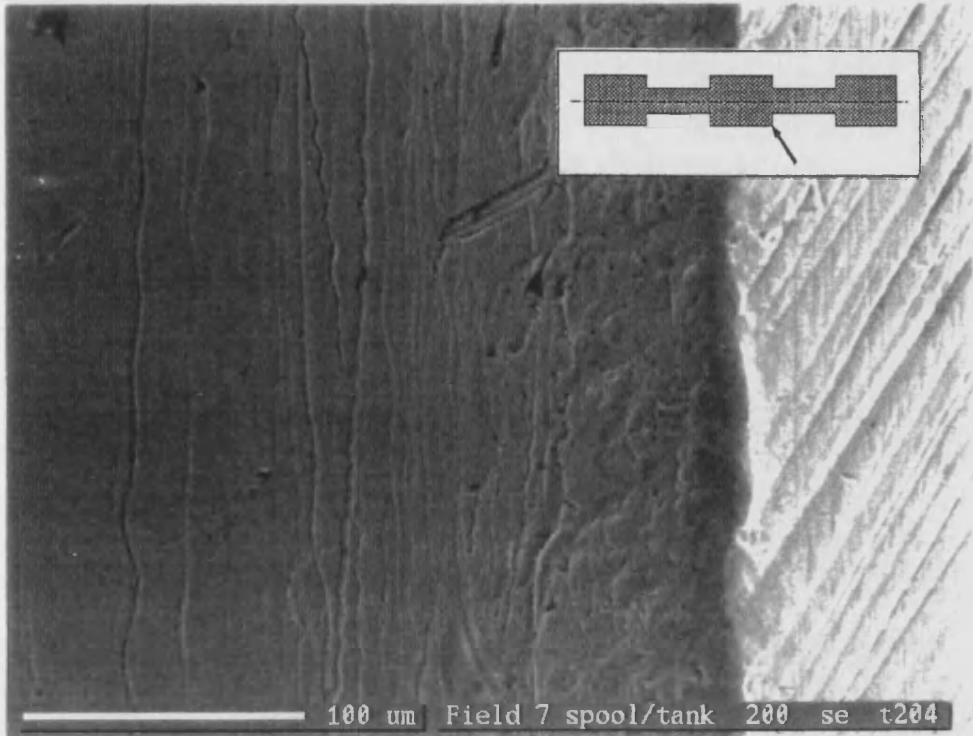
Figure 5.11 - Typical SEM micrograph of an in-service spool metering edge (tank land).
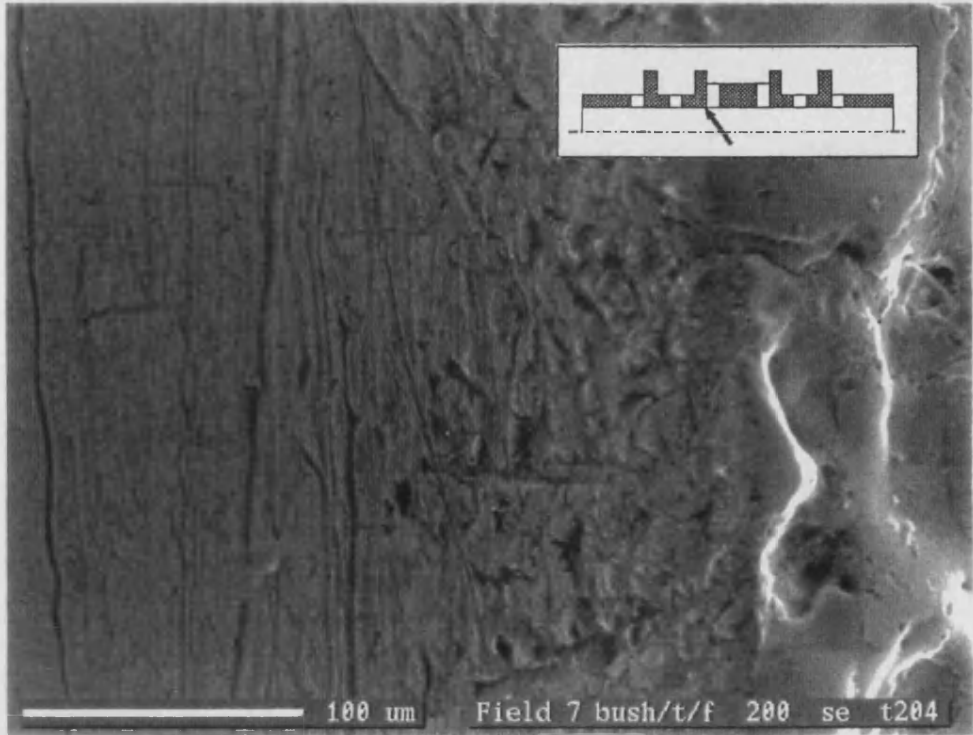
Figure 5.12 - Typical SEM micrograph of an in-service bushing metering edge (tank land).
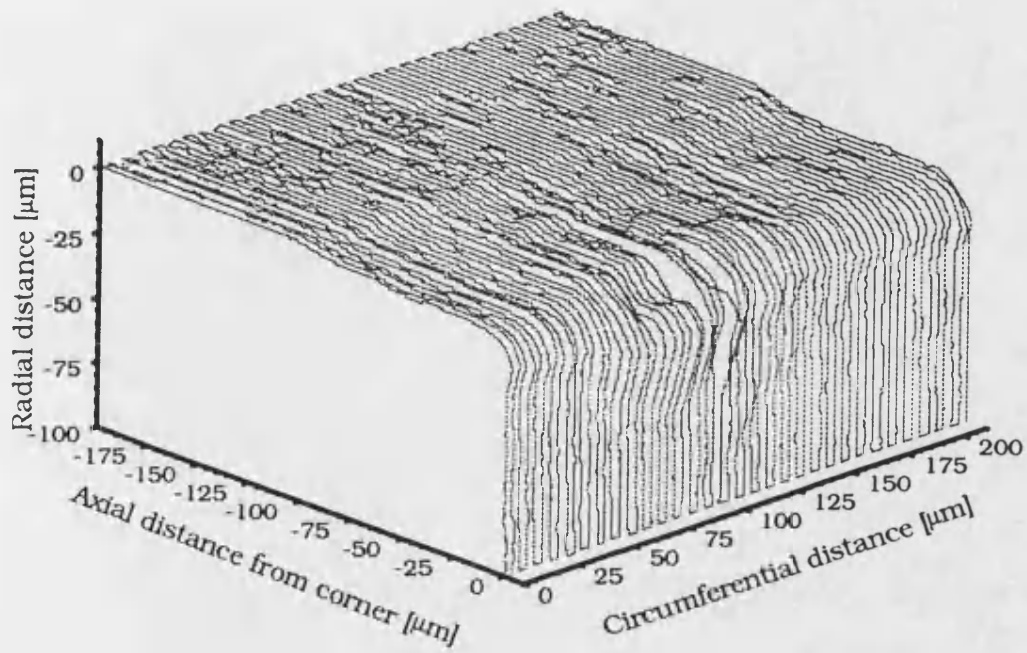
Figure 5.13 - Typical 3-D profile map from a worn spool pressure port metering land.
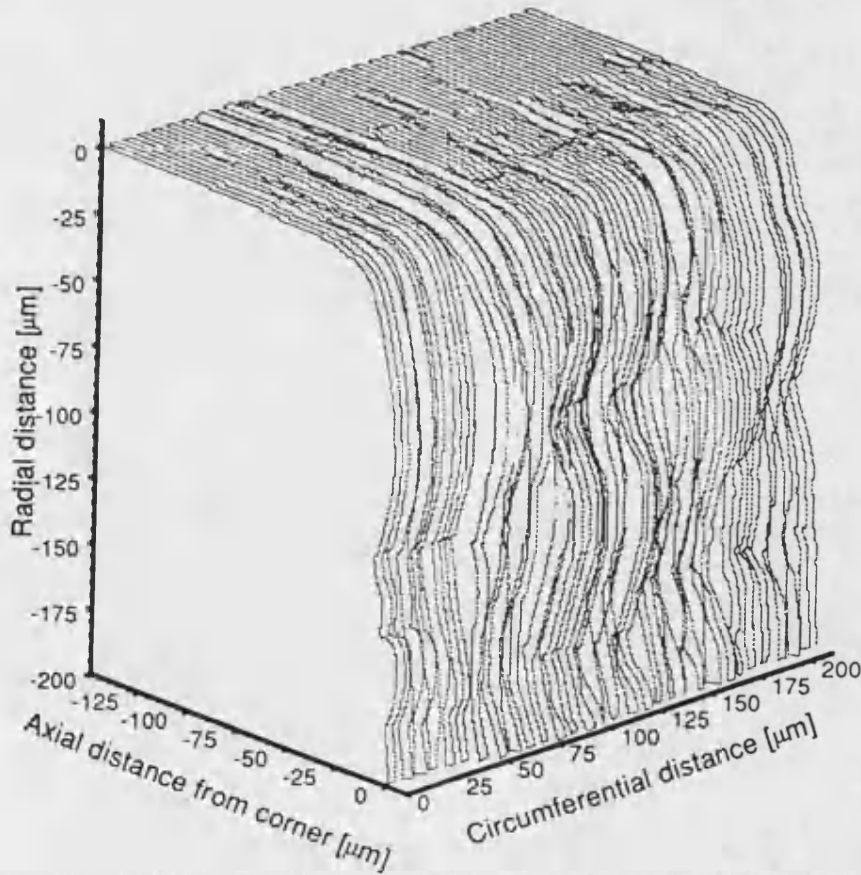
Figure 5.14 - Typical 3-D profile map from a worn bushing pressure port metering land.
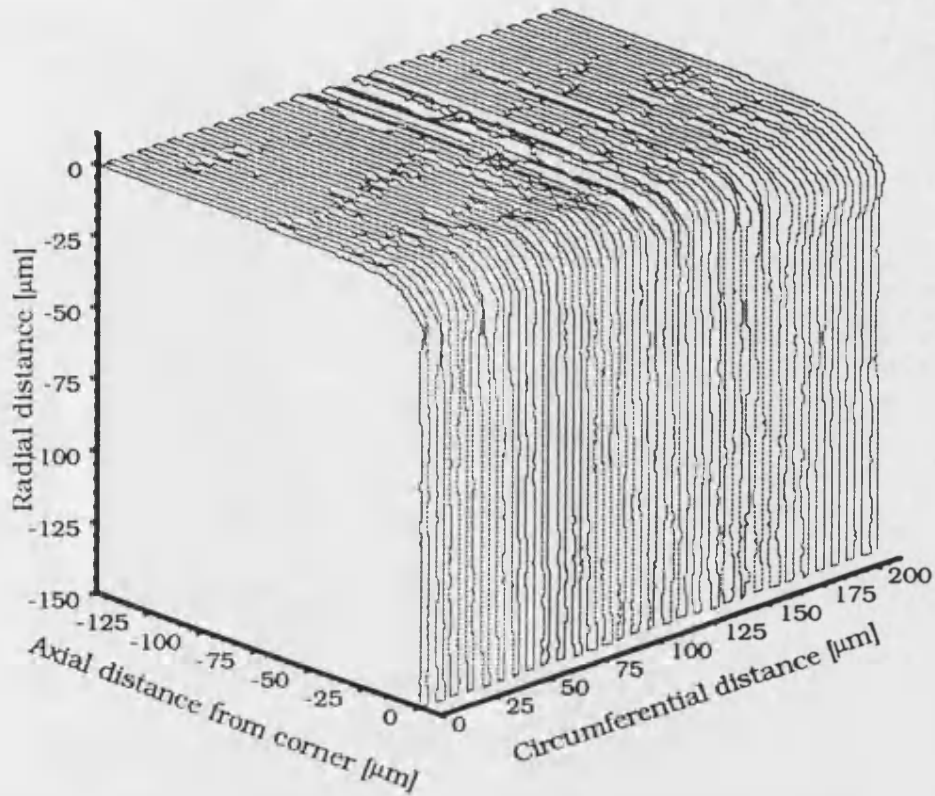
Figure 5.15 - Typical 3-D profile map from a worn spool tank port metering land.
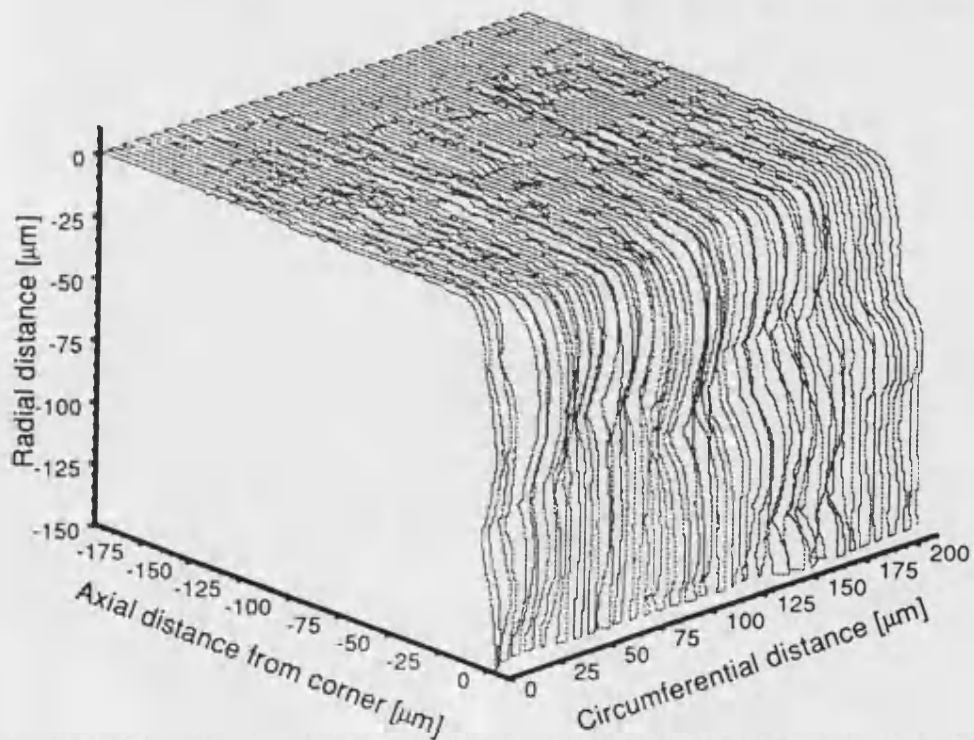
Figure 5.16 - Typical 3-D profile map from a worn bushing tank port metering land.

erosion and a general rounding of the corner with slight damage on the outer diameter from erosion and abrasion.

In comparison to the spools, the bushing wear profiles are more difficult to define due to their irregular EDM side face. However, from Figure 5.14 & 5.16 it can be seen that the tank port bore has more damage within the bore, as indicted by the SEM micrographs. It can also be seen that the pressure port metering edge has material removed from the side face, supporting the theory that particle erosion occurs on the high pressure side of the orifice.

From the in-service components examined, it may be concluded from the SEM micrographs and the component profiles that the wear damage is limited to within 100 µm from the metering corner in either, or both, the axial and radial direction. Also, when the magnitude of the damage is compared with the size of the actual valve components, it is surprising that the small changes in component geometry has such a significant effect on the valve performance.

5.4. Errors and Repeatability
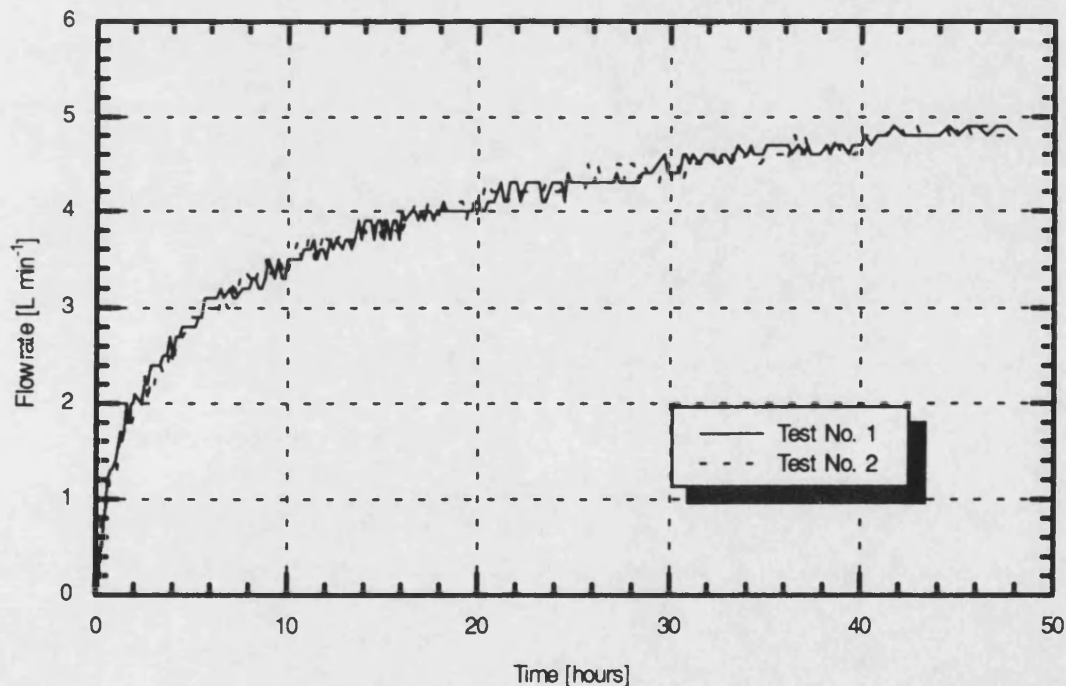
Test conditions - 70 bar differential   Contaminant concentration 10 mg L^{-1} of uncut quartz
             Flow P→S   Base oil grade 150N (32 cSt @ 40 °C) operating at 60 °C
             100 µm spool opening

Figure 5.17 - Repeatability test results.

The repeatability of the experimental test procedure used to determine the spool/bushing wear rates has been demonstrated in Section 4.7.6 by visually overlaying the results of two tests performed at identical test conditions. These results are repeated in Figure 5.17, but in this case the initial flow rate has been subtracted to give the flow increase against time.
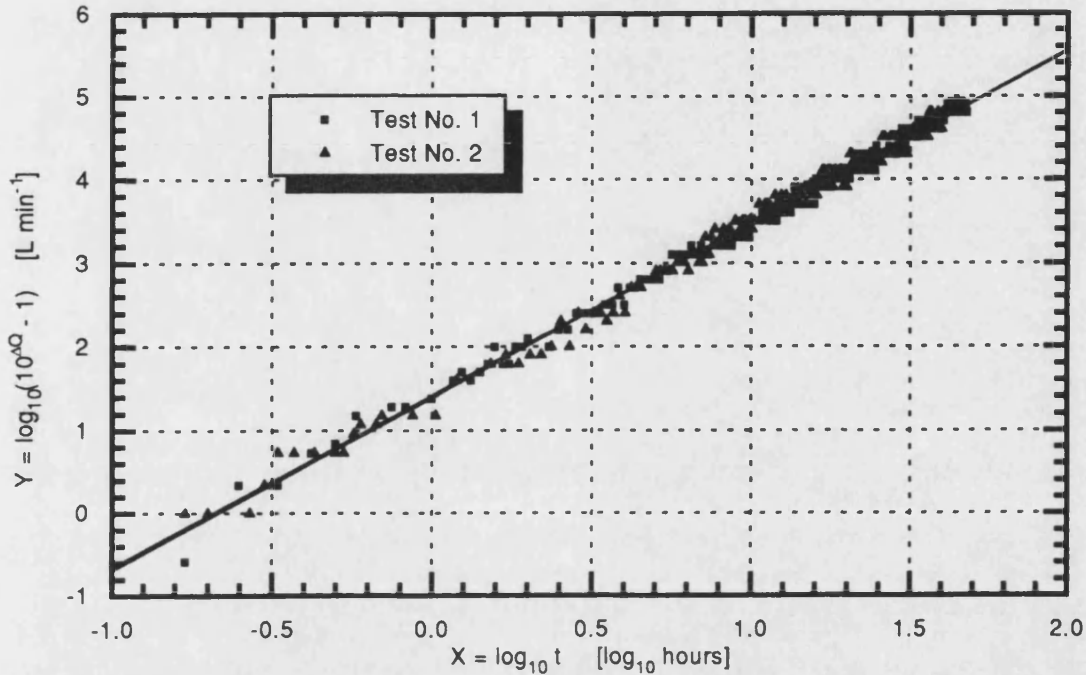
Test conditions - 70 bar differential Contaminant concentration 10 mg L^{-1} of uncut quartz
Flow P→S Base oil grade 150N (32 cSt @ 40 °C) operating at 60 °C
100 μm spool opening

Linearised fit data	Test No.1	Test No.2
A	1.409 ± 0.014	1.389 ± 0.015
B	2.066 ± 0.011	2.080 ± 0.012
R	0.997	0.996
SD	0.087	0.096
N	218	250

Figure 5.18 - Linearised test results.

From Figure 5.17 it can be seen that the two results appear to be very similar. This can be easily verified by making a visual judgement on the similarity, or alternatively a statistical approach may be used. Before any statistical analysis can be performed, it is required that a smooth curve (non-linear) or preferably a straight line (linear) is fitted to the data in the form of a regression line. It has been found that the erosive wear test results can be linearised by plotting the flow increase (ΔQ) against $\log_{10}$(time). Therefore the model equation becomes:

$$\Delta Q = A + B \log_{10} t \qquad \qquad \dots (5.2)$$

Considering the boundary conditions for the data sets: when $t = 0$ $\Delta Q = 0$

when $t \Rightarrow \infty$ $\Delta Q \Rightarrow \infty$

By substituting the first boundary condition into Equation 5.2 it can be seen that this equation is not correct since $\log_{10}(0) = -\infty$, although the equation does satisfy the second boundary condition, since no limit in the flow rate increase has been found. Therefore, to satisfy the $t = 0$ condition, Equation 5.2 may be modified to include a time shift function, as Equation 5.3:

$$\log_{10}(10^{\Delta Q} - 1) = A + B \log_{10} t \qquad \qquad \dots (5.3)$$

$$\therefore \quad \Delta Q = \log_{10}(10^A t^B + 1) \qquad \qquad \dots (5.4)$$

Therefore, from Equation 5.3 the data may be linearised by plotting the function $\log_{10}(10^{\Delta Q} - 1)$ against $\log_{10} t$ as shown in Figure 5.18.

From Figure 5.18 it can be seen that a good fit is obtained, this is confirmed by the value of the correlation coefficient (R) which equals 99.6 and 99.7%. The two straight lines obtained require some form of statistical test to confirm their similarity. However, to perform a test on two lines is not easy and therefore a comparison of a single point on the line is recommended [56]. For any regression line, a point of maximum confidence (minimum variance) occurs at the mean (or centre of gravity) of the data points. Because all the erosion tests were conducted over a similar time period (48 hours) with a similar data storage interval (10 minutes), it reasonable to assume that a mean value ($\bar{X}$) can be selected for all cases from Equation 5.5.

$$\bar{X} = \sum_{i=1}^{n} \frac{X_i}{n} = \frac{\log_{10} t_1 + \log_{10} t_2 + \dots + \log_{10} t_n}{n} \qquad \qquad \dots (5.5)$$

Hence for the erosion tests: $\bar{X} = 1.253$ $\Rightarrow \bar{t} = 17.9$ hours

From this, it is possible to calculate the spread of the observations about this mean to determine the interval in which future values of Y will probably lie. This interval is often called a *predictor interval* and can been found from the general form Equation 5.6.

$$Y = A + B X_0 \pm t_{0.5\alpha, n-2} \; S_{Y|x} \sqrt{1 + \frac{1}{n} + \frac{(X_0 - \overline{X})^2}{\sum\limits_{i=1}^{n}(X_i - \overline{X})^2}} \qquad \dots (5.6)$$

Where $S_{Y|x}$ is the standard deviation for the line, and n is the number of observations in the data set. The value of $t_{0.5\alpha, n}$ refers to the value of t used in the *t-test* significance test which will be used later to determine if a variation between the results exists. This value is obtained from standard tables [56] for a given confidence level (α). Now, since the selected comparison point occurs at the point of minimum variance, $X_0 \approx \overline{X}$, therefore Equation 5.6 may be simplified to give:

$$Y = A + B\overline{X} \pm t_{0.5\alpha, n-2} \; S_{Y|x} \sqrt{1 + \frac{1}{n}} \qquad \dots (5.7)$$

Substituting the regression results from Figure 5.18 into Equation 5.7 and determining $t_{0.5\alpha, n}$ for a 95% confidence level gives:

$$Y_1 = 3.997 \pm 0.167 \qquad Y_2 = 3.995 \pm 0.189$$

It is now possible to compare the two sample points and determine if a significant difference occurs using a *t-test*. In this case, the test hypothesis H_0 assumes that the two results are the same until the *t-test* proves otherwise. This can be found using Equation 5.8 & 5.9, where S is the combined variance of the two data sets and t_0 is the *t-test* statistic.

Now if H_0 is true, the sampling distribution of t for a 95% confidence can be found from standard t-distribution tables [56] to be $t = 1.96$. Therefore, since $t > t_0$ at the 5% level, there is a strong evidence that H_0 is true and two results are the same.

$$S = \sqrt{\frac{(n_1 - 1)\, S_1^2 + (n_2 - 1)\, S_2^2}{n_1 + n_2 - 2}} \qquad \dots (5.8)$$

$$t_0 = \frac{Y_1 - Y_2}{S \sqrt{1/n_1 + 1/n_2}} = 0.126 \qquad \dots (5.9)$$

Since the results have been obtained in a similar manner, it is reasonable to assume that each test is subjected to the same systematic errors and therefore these may be neglected. However,

in an extreme case the two values could be subjected to an opposite systematic error. From Section 4.7.6, it has been estimated that the absolute value of flow rate at t = 0 has an error of $\pm$ 0.1 L min^{-1}. This error, however, affects the offset of the line and not the gradient or the standard deviation of the data around it. Including the offset into the previously calculated values of Y_1 and Y_2 gives:

$$Y_1 = 3.997 + 0.1 = 4.097 \pm 0.167 \qquad Y_2 = 3.995 - 0.1 = 3.895 \pm 0.189$$

By comparing Y_1 and Y_2 it is clear that the values are not the same for this extreme condition and therefore it can be assumed that this is not a fair statistical test. However, this approach can be applied where a variation has been found between two data sets and an extreme test is required to ensure that the results are not the same under any circumstances.

From the above analysis it has been shown that the test results can be linearised using a simple logarithmic relationship and a point of maximum confidence has been established at 17.9 hours for a standard 48 hour test. At this point, a method has been described to assess if the two data sets are the same, or alternatively, is there a significant difference between the results obtained at different test conditions. The maximum confidence point can also be used to calculate a reference flow rate ($\Delta \dot{Q}$) using Equation 5.4, which may be used as a performance indicator between different oils, spool materials, etc.

5.5.   Spool Openings

Because of the diverse applications of servo valves it is impossible to specify a typical spool opening. For example, in a position control system the spool will initially be fully open and then progressively reduce to the null. Alternatively, for a speed control circuit, the valve will operate around some nominal opening point. Based on subjective judgement it is considered that in many valve applications a mean spool opening will be in the order of several hundreds of μm. From the rig commissioning programme it was found that repeatability and contaminant stability levels were affected with spool openings below 100 μm due to the metering orifice being blocked by the test contaminant. Therefore, the selected spool opening for the test programme became 100 μm. Results are also presented below at 200 and 300 μm to compare the influence of spool openings on the particle erosion rates.
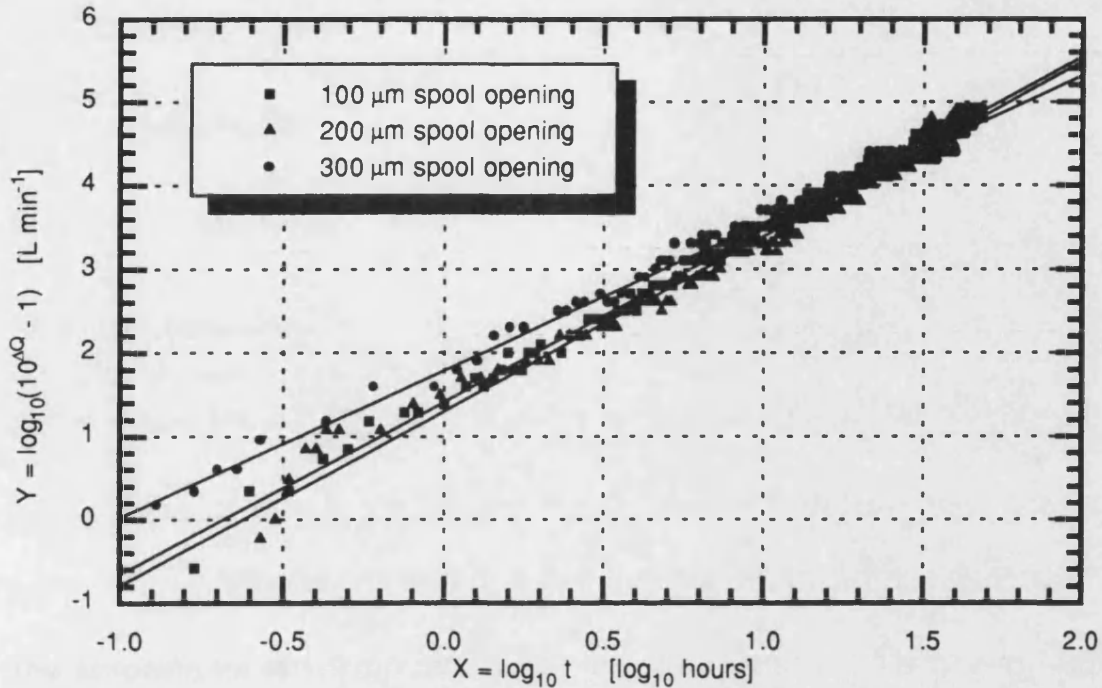
Figure 5.19 - Effects of different spool openings.

Test conditions - 70 bar differential Contaminant concentration 10 mg L^{-1} of uncut quartz
                   Flow P→S   Base oil grade 150N (32 cSt @ 40 °C) operating at 60 °C

Linearised fit data	100 μm test	200 μm test	300 μm test
A	1.409 ± 0.014	1.300 ± 0.023	1.789 ± 0.018
B	2.066 ± 0.012	2.093 ± 0.018	1.763 ± 0.014
R	0.997	0.991	0.993
SD	0.087	0.135	0.106
N	218	259	229

From Figure 5.19 it can be seen that the three test results produce a similar characteristic, although the figure suggests that the 300 μm may be different. Using the $\bar{t}$ = 17.9 hours and Equation 5.4, enabled the flow rates at the comparison point to be calculated as:

$$\Delta\bar{Q}_{100\ \mu m} = 4.00 \pm 0.17\ L\ min^{-1}\quad \Delta\bar{Q}_{200\ \mu m} = 3.92 \pm 0.26\ L\ min^{-1}\quad \Delta\bar{Q}_{300\ \mu m} = 4.00 \pm 0.21\ L\ min^{-1}$$

From the comparison point data, a variation obtained at the 200 μm opening. This result is also confirmed when the *t-test* is applied to the data, although the difference is within the ±0.1 L min^{-1} systematic error. Therefore, it is not unreasonable to consider that the erosion rate is not dependent upon spool opening over the range of 100 to 300 μm. This result has practical

implications for the test programme, since it implies that the spool opening and hence the flow rate does not have to precisely the same at the start of each test.

5.6.   Contamination Aspects

5.6.1. Clean Oil

Before the commencement of a test programme to examine the effects of concentration, distribution and type of contaminant on the erosion rates, results were determined from a *clean oil* test. To perform this, a 48 hour test was conducted with the following conditions:

Test conditions - 70 bar differential Cleanliness level ISO 4406, class 8/4 [8]
             Flow from P→S   Base oil grade 150N (32 cSt @ 40 °C) operating at 60 °C
             100 μm spool opening

After completing the 48 hour test, no increase in the flow rate (t = 48 hours, $\Delta Q = 0$ L min^{-1}) could be detected. However, from the SEM micrographs of the spool and bushing metering edge, Figures 5.20 & 5.21, it can be seen that very slight damage has occurred on the corner. Therefore, this result implies that liquid impact or cavitation erosion [57] has no influence on the test results and any changes if flow rate must be attributed to the solid particles. This result also supports the general opinion that wear in servo valves is not a problem for systems with low contamination levels.
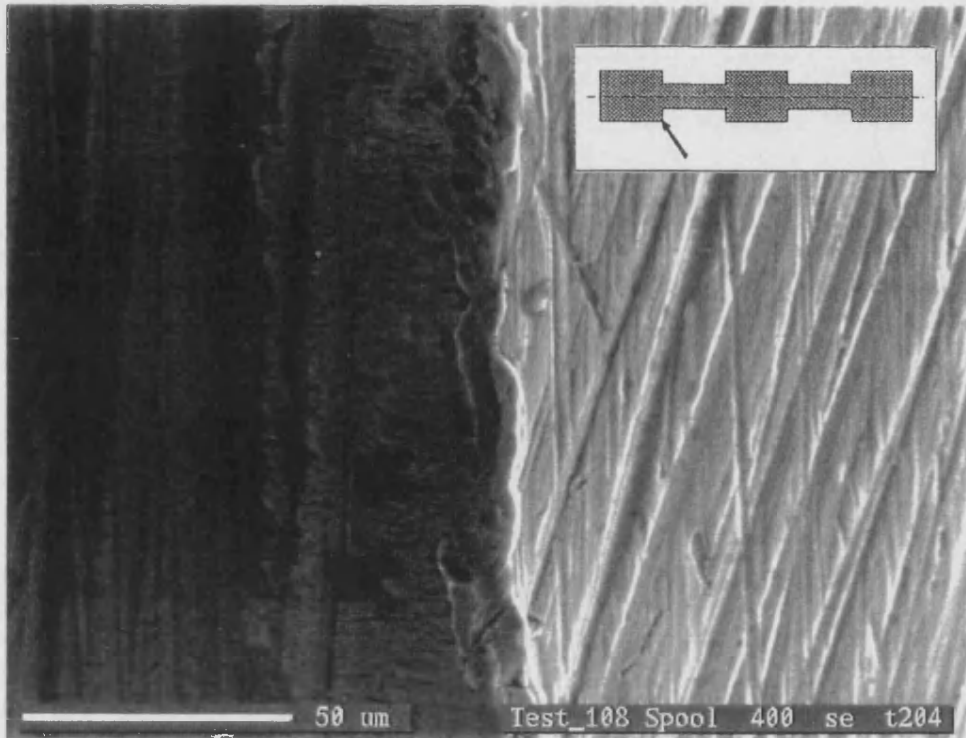
Figure 5.20 - SEM micrograph of the spool metering edge following a *clean oil* test.
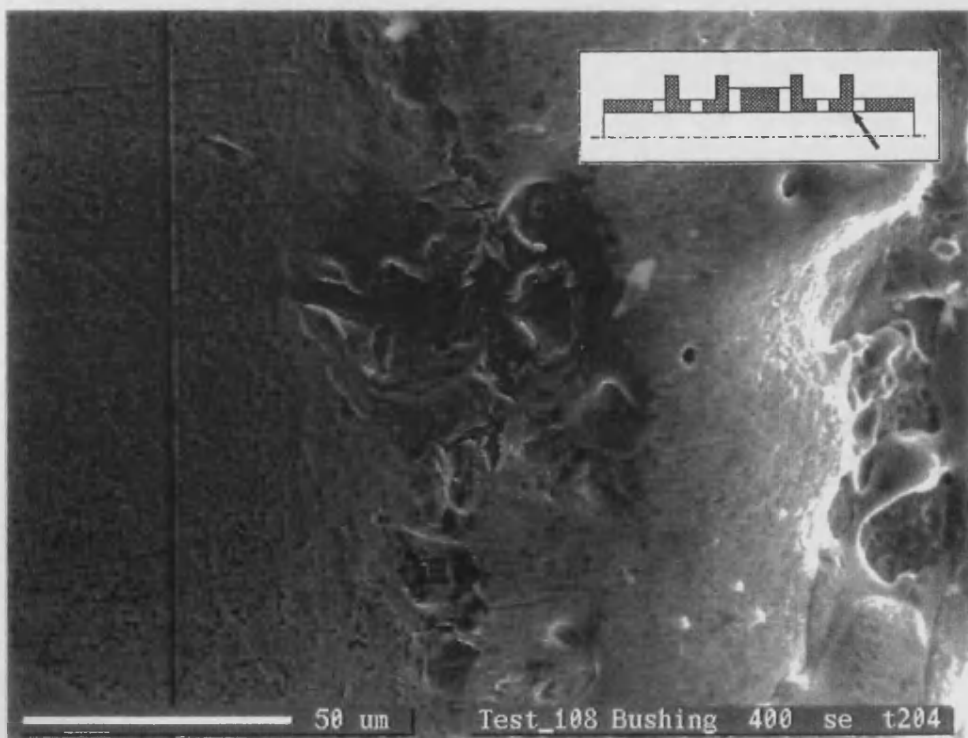
Figure 5.21 - SEM micrographs of the bushing metering edge following a *clean oil* test.

5.6.2. Air Cleaner Fine Test Dust (ACFTD)

As discussed in Section 3.2, ACFTD has become a fluid power industry standard product for filter and component sensitivity testing. However, due to the difficulty in obtaining different cuts (distributions), a quartz dust has been used as an alternative. Therefore, to compare the erosive wear properties of the ACFTD (0-80 μm) and uncut quartz (0-70 μm), two tests were conducted at the conditions detailed in Figure 5.22.
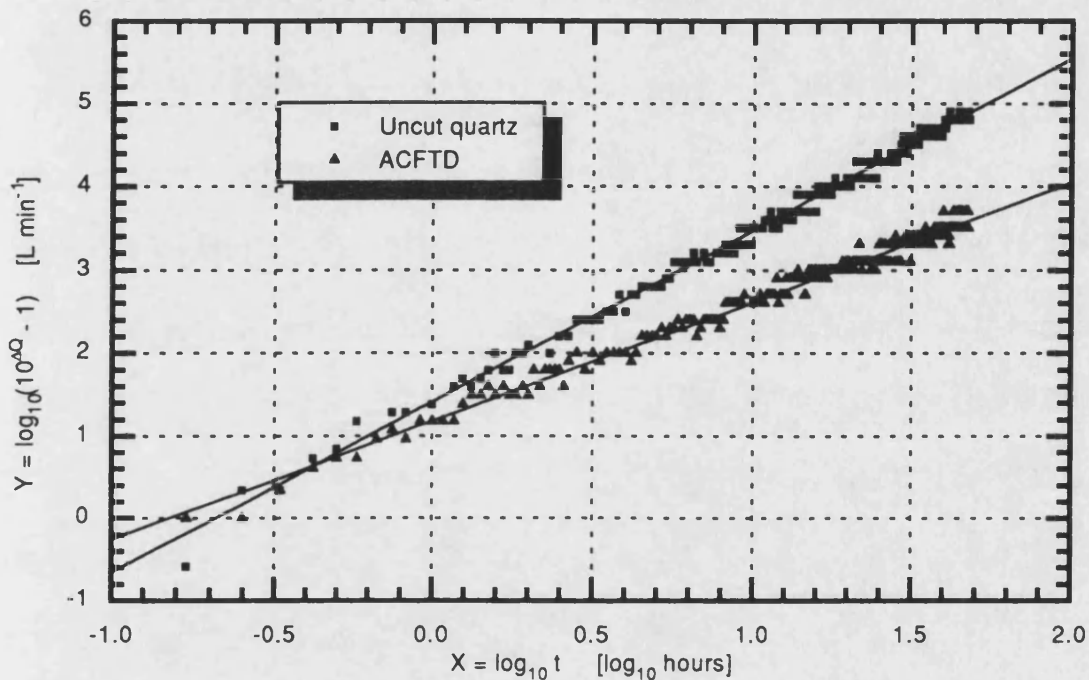
Test conditions - 70 bar differential Contaminant concentration 10 mg L^{-1}
Flow P→S Base oil grade 150N (32 cSt @ 40 °C) operating at 60 °C
100 μm spool opening

Linearised fit data	Uncut quartz	ACFTD test
A	1.409 ± 0.014	1.178 ± 0.013
B	2.066 ± 0.012	1.434 ± 0.011
R	0.997	0.992
SD	0.087	0.088
N	218	296

Figure 5.22 - Comparison between ACFTD and uncut quartz.

From Figure 5.22 it can be clearly seen that the uncut quartz is more severe than the ACFTD. Using the $\bar{t}$ comparison criterion gives $\Delta\bar{Q}_{quartz}$ = 4.00 L min^{-1} and $\Delta\bar{Q}_{ACFTD}$ = 2.97 L min^{-1} indicating a difference of 25% in the wear rate. From the component SEM micrographs contained
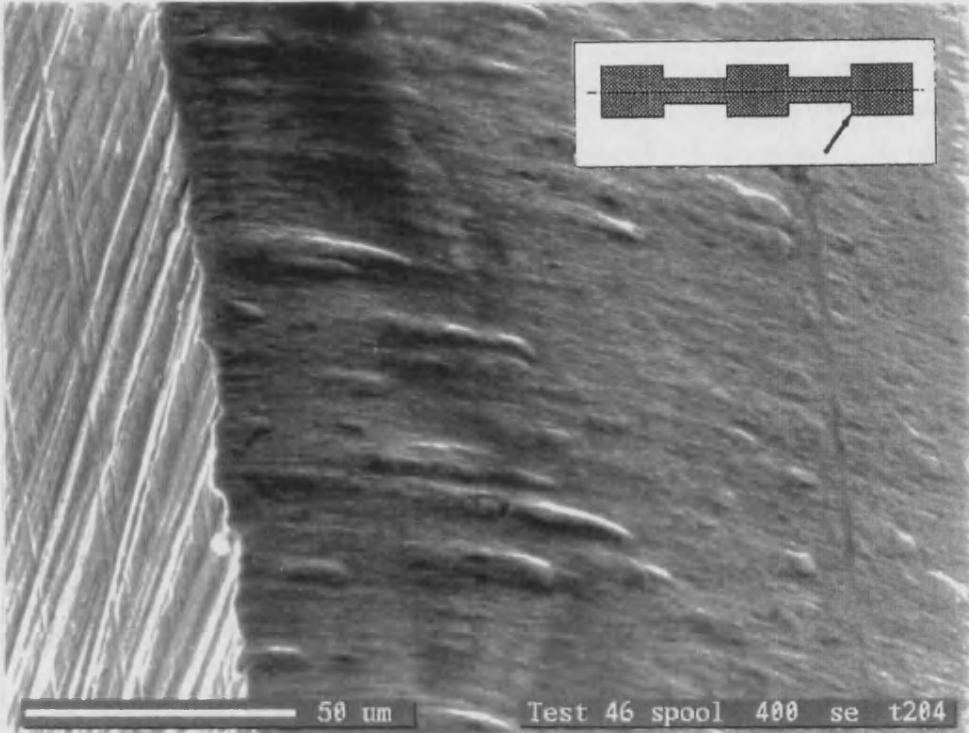
Figure 5.23 - SEM micrograph of the spool metering edge for a 70 bar uncut quartz test (P→S).
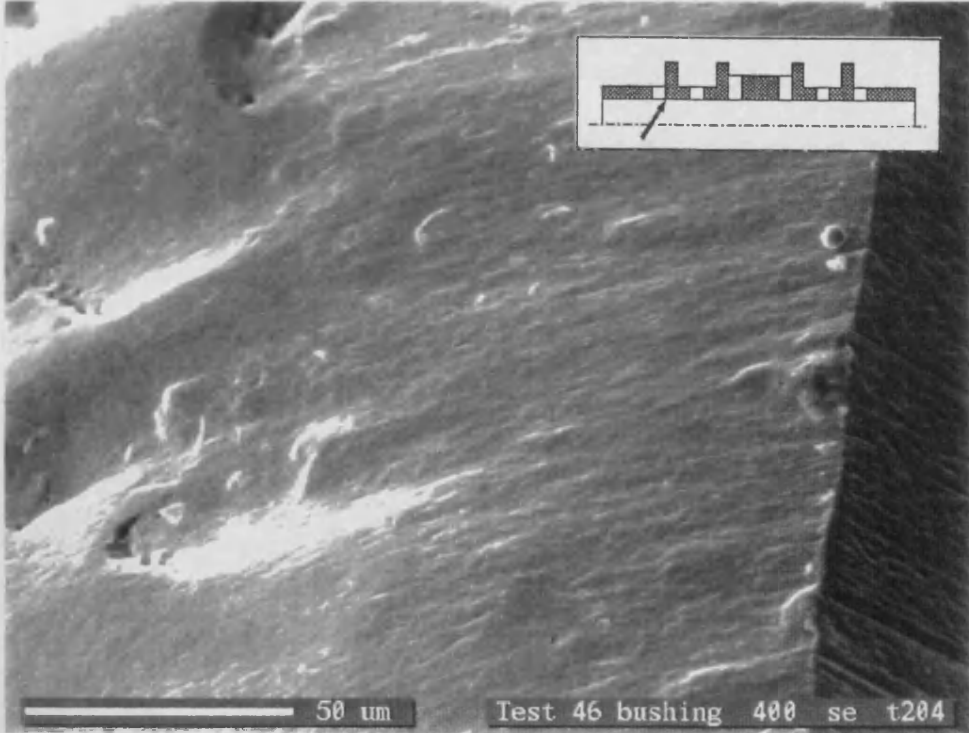
Figure 5.24 - SEM micrograph of the bushing metering edge for a 70 bar uncut quartz test (P→S).
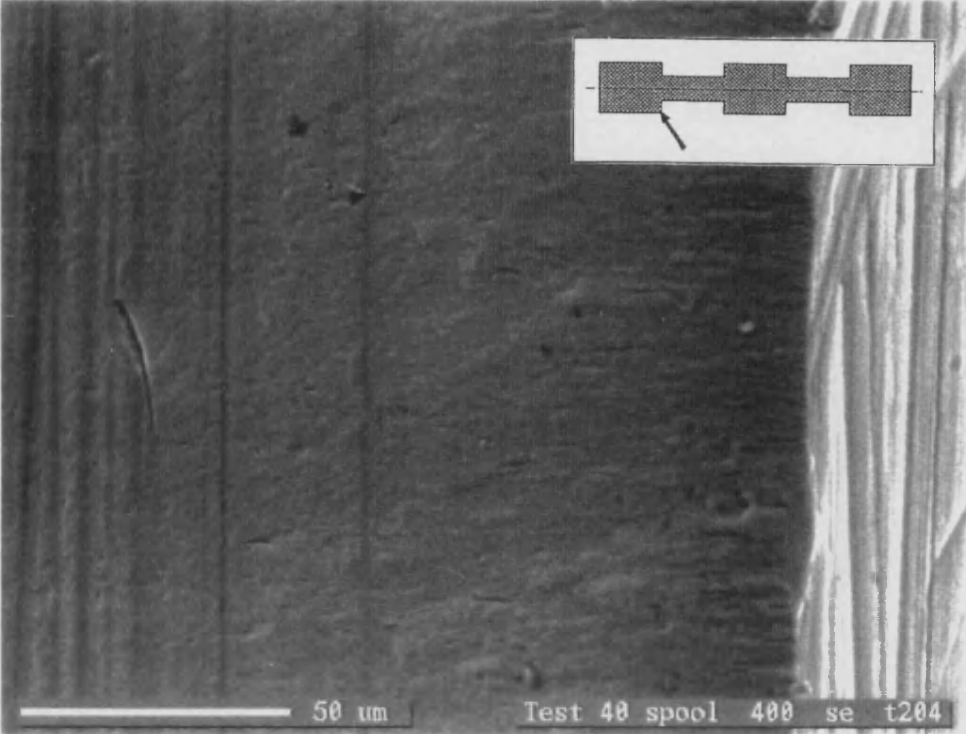
Figure 5.25 - SEM micrograph of the spool metering edge for a 70 bar ACFTD test (P→S).
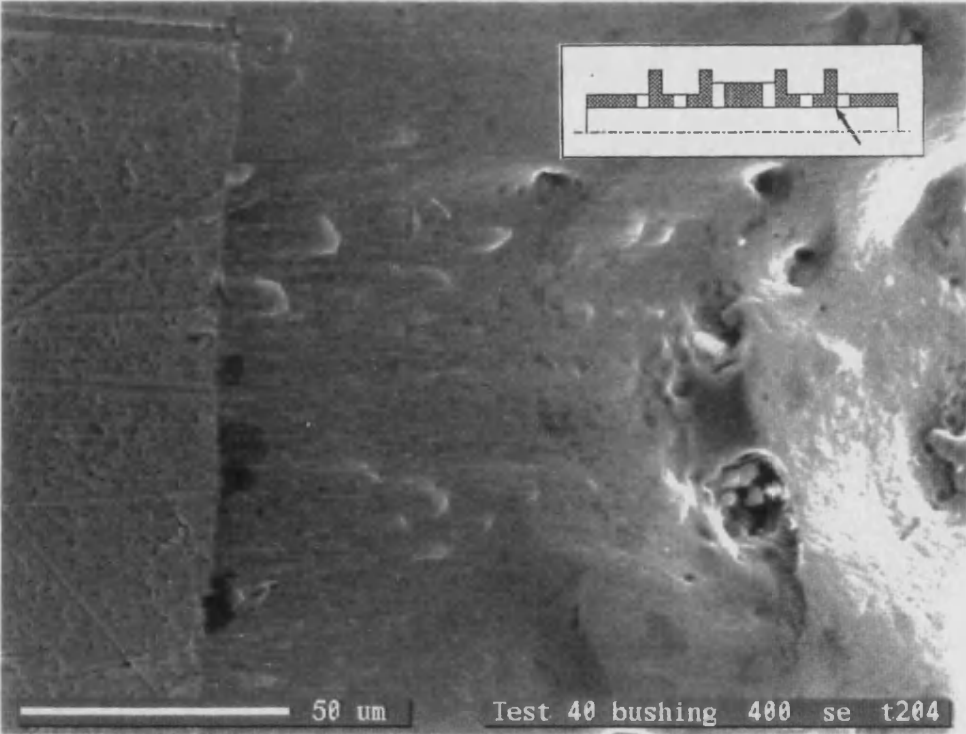
Figure 5.26 - SEM micrograph of the bushing metering edge for a 70 bar ACFTD test (P→S).

in Figures 5.23 to 5.26, it can be seen that both tests produce metering surfaces having a columnar appearance in-line with the fluid flow. A variation between the two results can be seen by the nominal length of the surface damage extending from the metering corner. This observation confirms that the uncut quartz is more severe than the ACFTD even though it has been found to contain fewer larger particles. However, since the density of quartz is higher than ACFTD, it is thought that the particle mass is the significant difference between the two contaminants.

5.6.3. Quartz Test Dust

The results obtained using five different quartz distributions: uncut, 0-60, 0-40, 0-20 and 0-10 µm at a concentration of 10 mg L^{-1}, are shown in Figure 5.27.
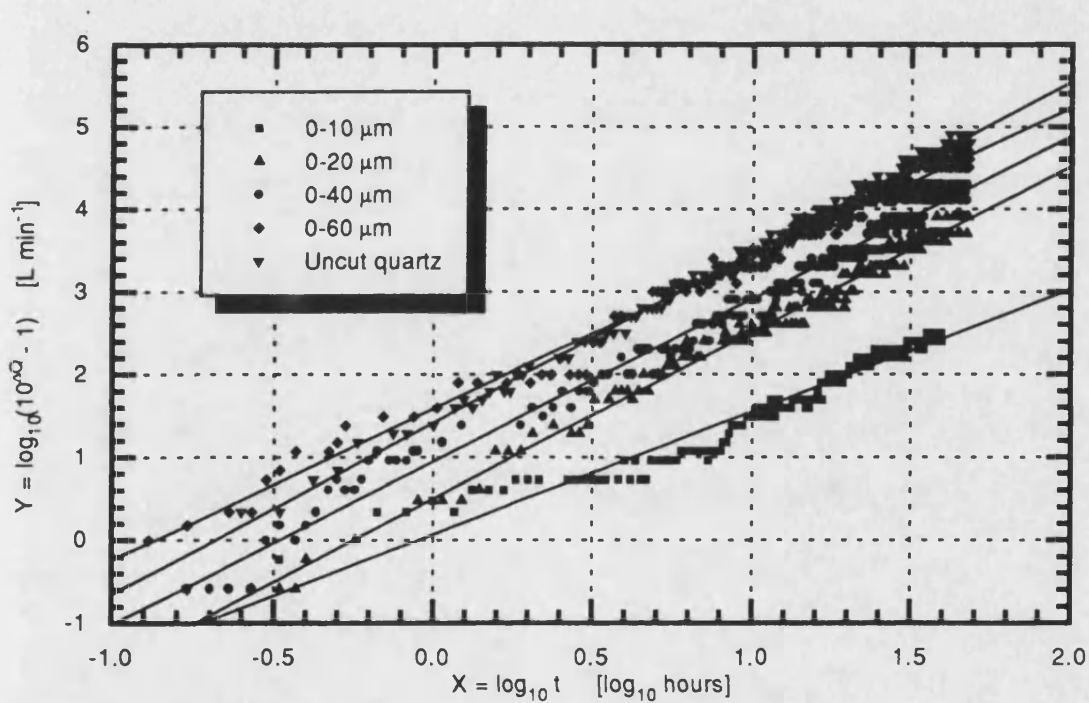
Test conditions - 70 bar differential   Contaminant concentration 10 mg L^{-1}
                  Flow from P→S   Base oil grade 150N (32 cSt @ 40 °C) operating at 60 °C
                  100 µm spool opening

Linearised fit data	Uncut test	0-60 µm test	0-40 µm test	0-20 µm test	0-10 µm test
A	1.409 ± 0.014	1.581 ± 0.019	0.946 ± 0.020	0.499 ± 0.022	0.068 ± 0.030
B	2.066 ± 0.012	1.824 ± 0.015	1.967 ± 0.016	2.010 ± 0.017	1.478 ± 0.024
R	0.997	0.993	0.992	0.992	0.973
SD	0.087	0.117	0.140	0.113	0.144
N	218	232	251	216	218

Figure 5.27 - Comparison between the different quartz distributions.
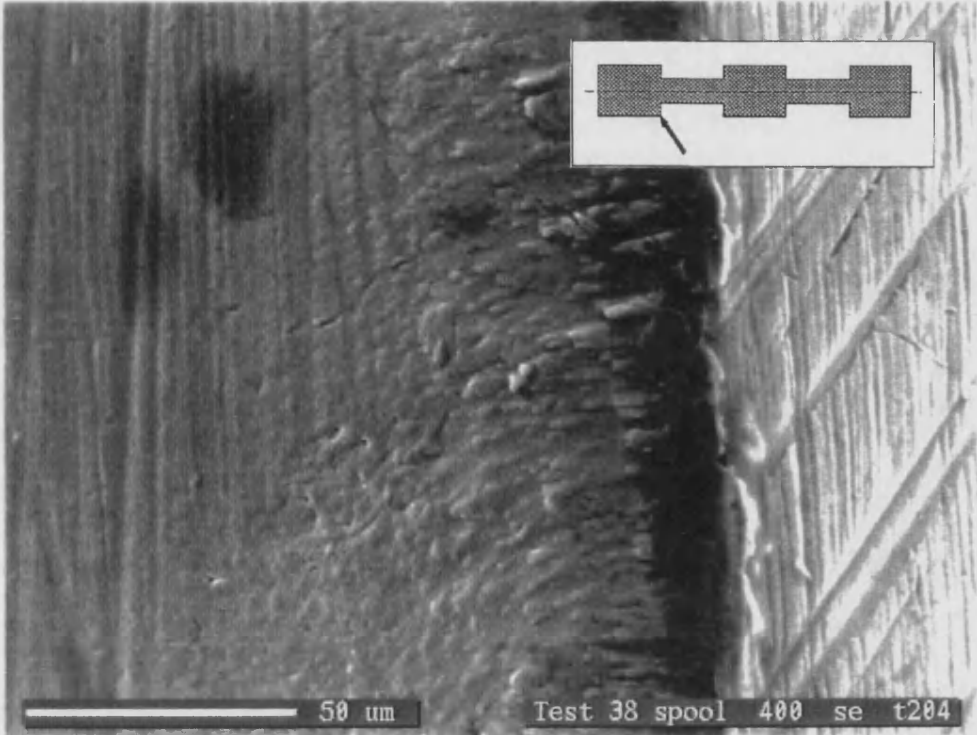
Figure 5.28 - SEM micrograph of the spool metering edge for a 70 bar 0-10 μm quartz test (P→S)
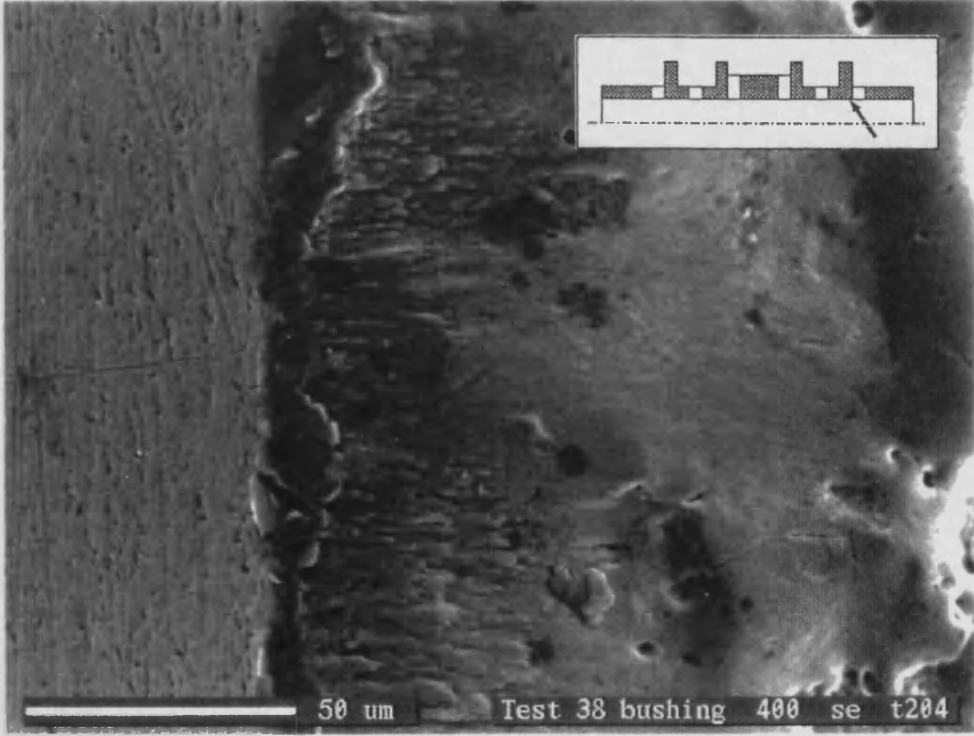
Figure 5.29 - Micrograph of the bushing metering edge for a 70 bar 0-10 μm quartz test (P→S).

Using the $\bar{t}$ comparison criterion gives the following flow rates:

$$\Delta \dot{Q}_{uncut} = 4.00 \text{ L min}^{-1} \qquad \Delta \dot{Q}_{0\text{-}60\ \mu m} = 3.87 \text{ L min}^{-1} \qquad \Delta \dot{Q}_{0\text{-}40\ \mu m} = 3.41 \text{ L min}^{-1}$$

$$\Delta \dot{Q}_{0\text{-}20\ \mu m} = 3.02 \text{ L min}^{-1} \qquad \Delta \dot{Q}_{0\text{-}10\ \mu m} = 1.93 \text{ L min}^{-1}$$

The results show that the flow rate decreases with the particle size distribution, confirming the hypothesis that the particle mass is critical to the erosion rate. Apart from the uncut and 0-60 μm result, the difference between the values are greater than the ±0.1 L min^{-1} systematic error, confirming that statistically they are different. The uncut and 0-60 μm result confirms the comments made in Section 3.2.5 about the similarity of the uncut and the 0 - 60 μm distributions.

From the spool/bushing SEM micrographs it is difficult to judge if there is any difference in the surface damage between the different cuts. However, it is possible to determine a variation between the uncut and 0-10 μm quartz, the results of which are contained in Figures 5.23, 5.24, 5.28 & 5.29. From Figures 5.28 & 5.29, it can be seen that the columnar structure is still present, but when compared with the uncut results, it appears to be more pronounced and localised at the metering corner.

A significant point from this work is that the wear rate is not only dependent upon the concentration levels, but is also very dependent upon the particle distribution within this concentration. This result has important implications for members of the fluid power industry who rely on gravimetric analysis as an assessment method for contamination control.

5.6.4. Concentration Level

To examine the effects of concentration level on the erosion rate, a series of tests were conducted at a concentration of 5, 10 and 20 mg L^{-1} with the uncut and 0-10 μm quartz dust. From Figures 5.30 & 5.31 it can be seen that the wear rate increases with concentration level as expected, although the results suggest that the flow increase is not linear with concentration. This result is not surprising since the amount of material removal required to change the flow area increases as the orifice wears. Applying the $\bar{t}$ comparison criterion to the test results gives:

Uncut $\Delta \dot{Q}_{5\ mg\ L^{-1}} = 2.99 \text{ L min}^{-1}$ $\Delta \dot{Q}_{10\ mg\ L^{-1}} = 4.00 \text{ L min}^{-1}$ $\Delta \dot{Q}_{20\ mg\ L^{-1}} = 4.71 \text{ L min}^{-1}$

0-10 μm $\Delta \dot{Q}_{5\ mg\ L^{-1}} = 1.16 \text{ L min}^{-1}$ $\Delta \dot{Q}_{10\ mg\ L^{-1}} = 1.93 \text{ L min}^{-1}$ $\Delta \dot{Q}_{20\ mg\ L^{-1}} = 2.35 \text{ L min}^{-1}$

Although not included, the SEM micrographs obtained from these tests, show that the surface damage extends further from the metering edge as the concentration increases. In each case the columnar structure is present and is again more pronounced in the 0-10 µm results.
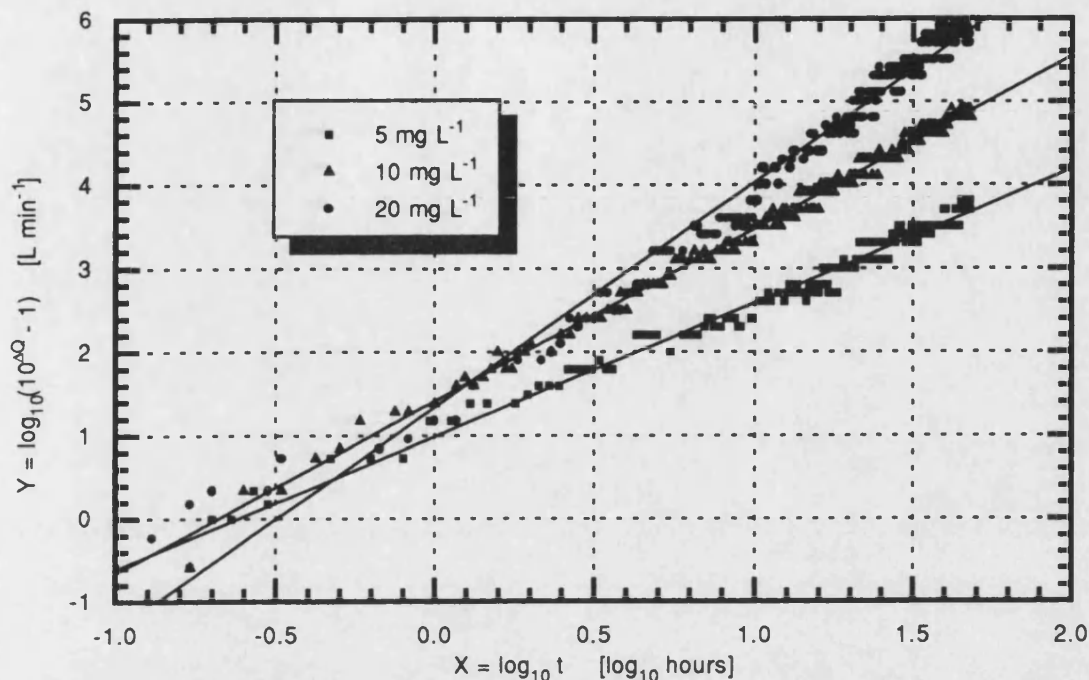
Test conditions - 70 bar differential 100 µm Spool opening
                 Flow from P→S   Base oil grade 150N (32 cSt @ 40 °C) operating at 60 °C

Linearised fit data	5 mg L^{-1} test	10 mg L^{-1} test	20 mg L^{-1} test
A	0.988 ± 0.021	1.409 ± 0.014	1.341 ± 0.036
B	1.597 ± 0.016	2.066 ± 0.012	2.692 ± 0.027
R	0.990	0.997	0.988
SD	0.113	0.087	0.209
N	198	218	238

Figure 5.30 - Effects of different uncut quartz concentrations.

In order to quantify the amount of material removal occurring at each test condition, a profile measurement has been conducted on each component, the results of which are shown in Figures 5.32 & 5.33. Unfortunately, the measurements are taken at the end of the test (t = 48 hours) and not at the maximum confidence interval $\bar{t}$. The profiles confirm that the flow area increases with concentration and clearly the uncut quartz removes more material. By integrating each profile using the trapezoidal rule, it is possible to calculate the area of material removed for each test condition as shown in Table 5.1. Due to the surface topography of the bushing metering slot, significant errors can be introduced in the computation if the complete

profile is used. Therefore, to compensate for this, the bushing area has been computed using a straight line approximation for bushing metering slot surface. The results are presented with a subtracted correction allowance for a new spool and bushing of 46 and 107 μm^2 respectively.
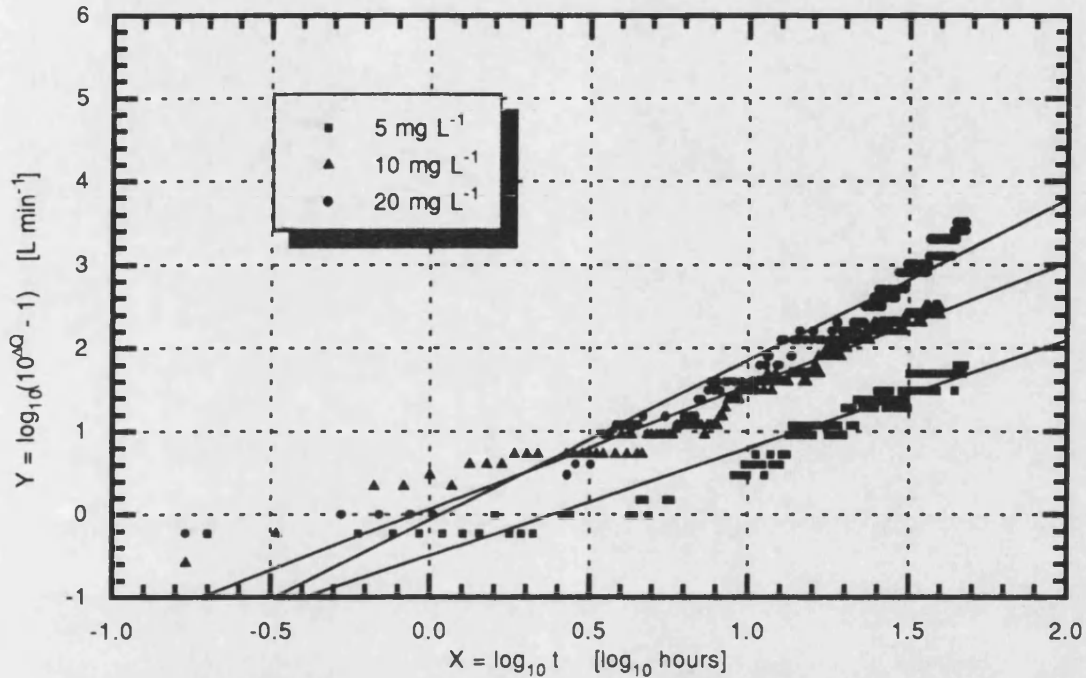
Test conditions - 70 bar differential 100 μm Spool opening
                        Flow from P→S   Base oil grade 150N (32 cSt @ 40 °C) operating at 60 °C

Linearised fit data	5 mg L^{-1} test	10 mg L^{-1} test	20 mg L^{-1} test
A	-0.494 ± 0.031	0.068 ± 0.030	-0.062 ± 0.055
B	1.294 ± 0.031	1.478 ± 0.024	1.920 ± 0.041
R	0.949	0.973	0.961
SD	0.172	0.144	0.234
N	199	218	184

Figure 5.31 - Effects of different 0-10 μm quartz concentrations.

From Table 5.1, the combined wear results indicate that the amount of material removed is not linear with contaminant concentration. Therefore, both the flow plots and the component profiles confirm that a linear relationship between concentration and wear does not exist. Also, the results indicate that more material has been removed from the bushing than the spool. This variation is considered to be due to the combined effects of different material properties and the flow pattern as the oil enters the vena-contracta. Further details on the influence of flow direction on the wear rate are presented in Section 5.7.
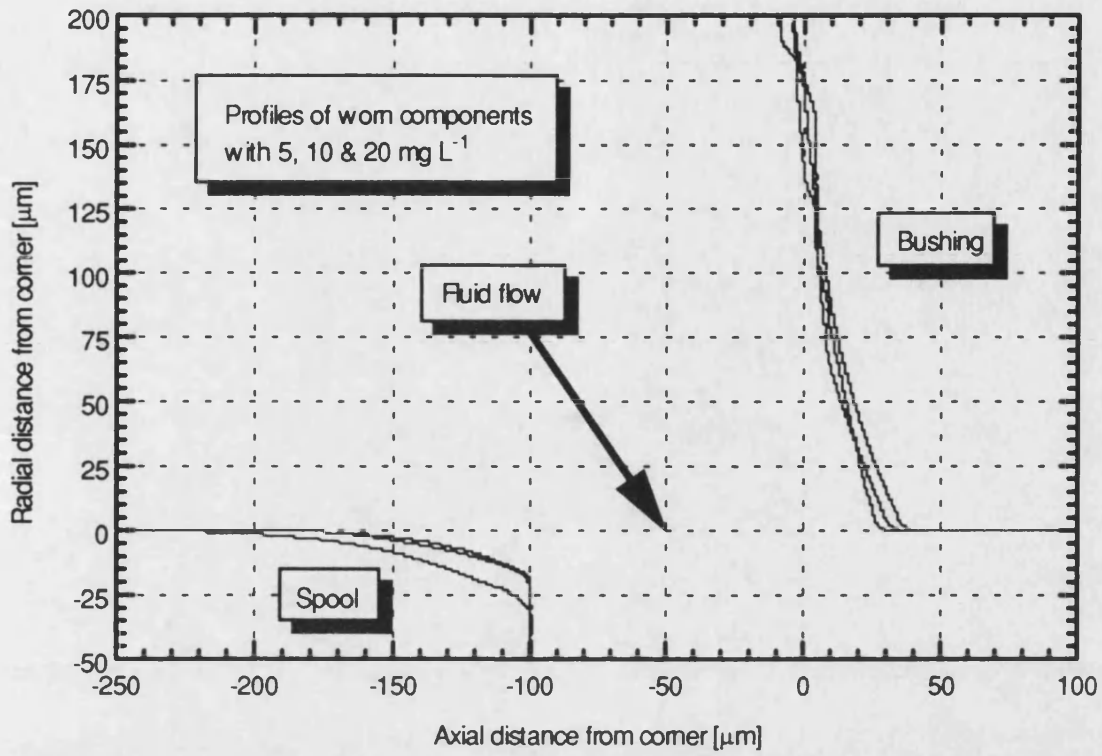
Figure 5.32 - Effects of uncut quartz concentration on spool/bushing profiles.
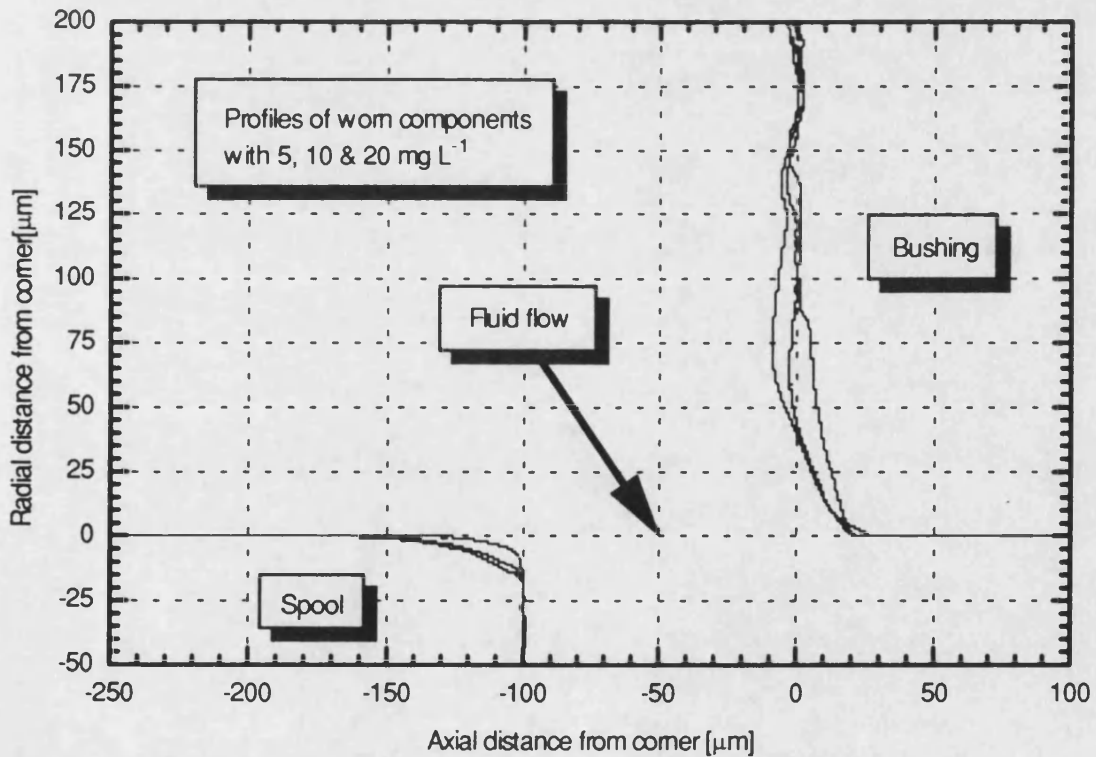
Figure 5.33 - Effects of 0-10 μm quartz concentration on spool/bushing profiles.

Contaminant type	Concentration [mg L^{-1}]	Spool wear [μm^2]	Bushing wear [μm^2]	Combined wear [μm^2]
Uncut quartz	5	404	1606	2010
	10	479	1743	2222
	20	1044	2104	3148
0-10 μm quartz	5	40	181	221
	10	200	229	429
	20	279	755	1034

Table 5.1 - Effect of contaminant concentration on the amount of material removed.

5.7.   Pressure Drop and Flow Direction

To examine the influence of pressure drop across the metering orifice, a series of tests have been conducted at 35 and 70 bar in both the P→S and S→T direction. The results for each flow condition are shown in Figures 5.34 & 5.35.

Applying the $\bar{t}$ comparison criterion to the test results gives:

P→S	35 bar	$\Delta \bar{Q}_{uncut}$ = 2.90 L min^{-1}	$\Delta \bar{Q}_{0-10\ \mu m}$ = 0.91 L min^{-1}
	70 bar	$\Delta \bar{Q}_{uncut}$ = 4.00 L min^{-1}	$\Delta \bar{Q}_{0-10\ \mu m}$ = 1.95 L min^{-1}
S→T	35 bar	$\Delta \bar{Q}_{uncut}$ = 2.57 L min^{-1}	$\Delta \bar{Q}_{0-10\ \mu m}$ = 1.00 L min^{-1}
	70 bar	$\Delta \bar{Q}_{uncut}$ = 4.26 L min^{-1}	$\Delta \bar{Q}_{0-10\ \mu m}$ = 2.25 L min^{-1}

From the $\Delta \bar{Q}$ values above, it is apparent that pressure drop has a significant effect, but the influence of flow direction is not clear if the ±0.1 L min^{-1} systematic error is included. However, if the additional error is ignored and an average value is taken in each flow direction, the S→T results are 5% higher.

The SEM micrographs for the P→S condition, operating with uncut and 0-10 μm quartz at 70 bar are shown in Figures 5.23, 5.24, 5.28 & 5.29, equivalent micrographs for the S→T condition are contained in Figures 5.36 to 5.39. From these results, a similar trend for both flow directions can be seen. For example, the columnar structure is again more prominent on the 0-10 μm test and secondly, the surface damage extends further from the corner as the leakage flow increases.
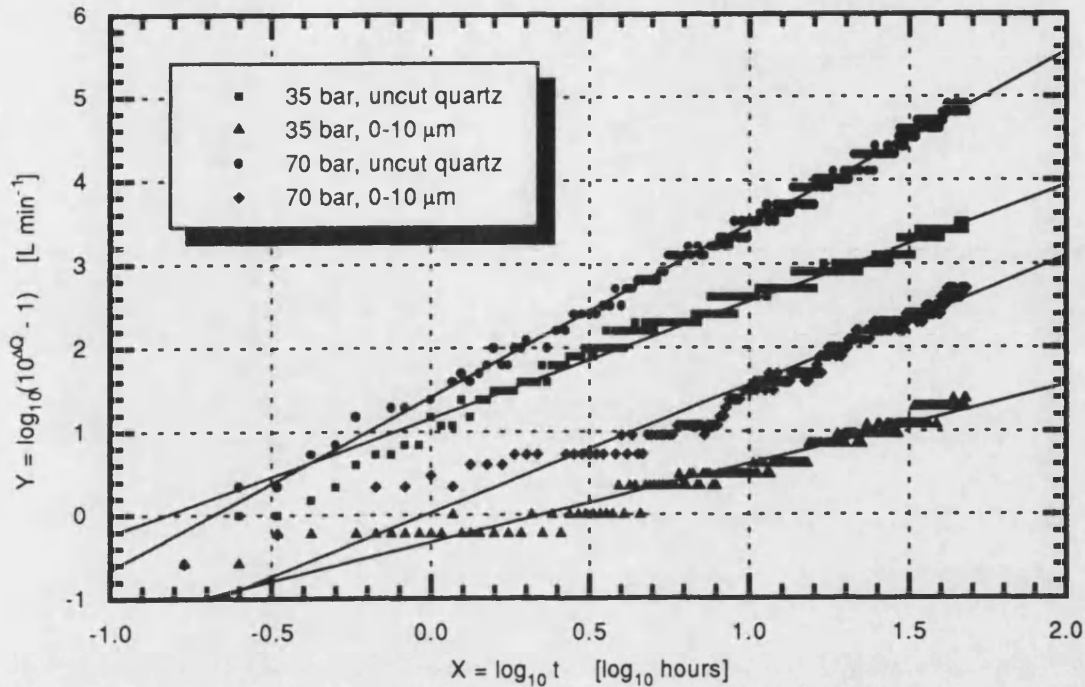
Test conditions - 100 µm Spool opening Concentration level 10 mg L^{-1}
Flow from P → S   Base oil grade 150N (32 cSt @ 40 °C) operating at 60 °C

Linearised Fit data	35 bar, uncut	35 bar, 0-10 µm	70 bar, uncut.	70 bar, 0-0 µm
A	1.157 ± 0.015	-0.325 ± 0.019	1.409 ± 0.014	0.027 ± 0.028
B	1.392 ± 0.012	0.940 ± 0.014	2.066 ± 0.012	1.529 ± 0.021
R	0.990	0.969	0.997	0.976
SD	0.099	0.113	0.087	0.141
N	312	278	217	259

Figure 5.34 - Effects of different pressures in the P→S direction.

In order to confirm the observations from the flow plots and the SEM micrographs, a series of profile measurements have been conducted on the spools and bushings tested at 35 and 70 bar with the uncut quartz, both in the P→S and S→T flow directions. To permit profile measurements at different time intervals during the standard 48 hour test, separate tests were carried out at 2 and 8 hours. The selection of the time periods was determined by dividing the total flow increase over the 48 hours into three equal intervals. The results for these tests are shown in Figures 5.40 to 5.43.
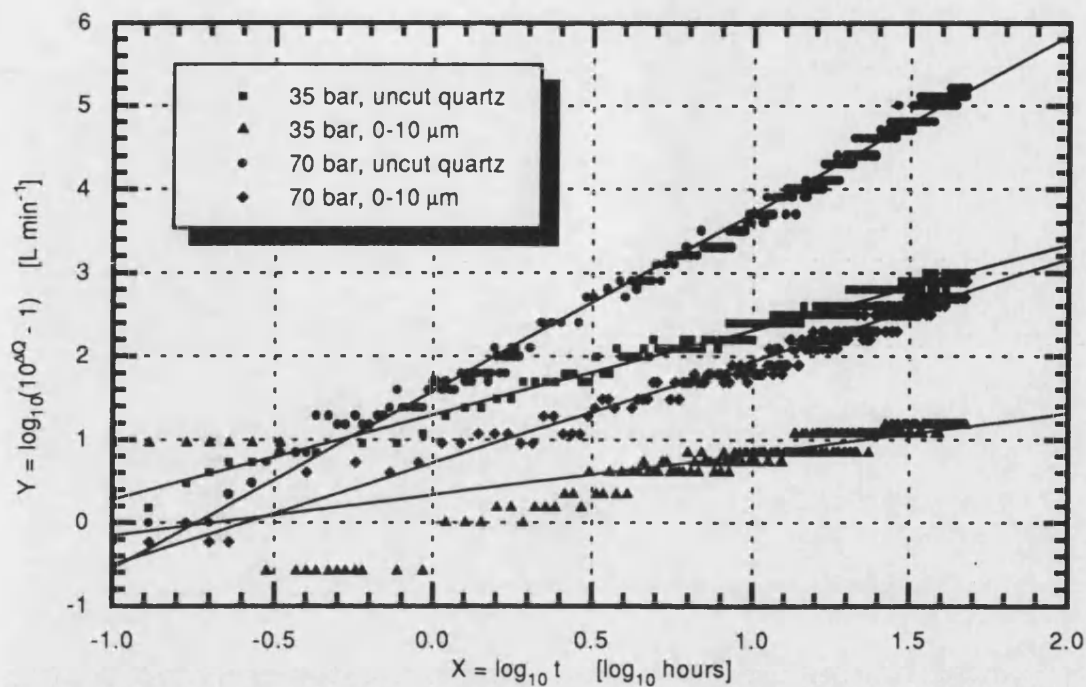
Test conditions - 100 µm Spool opening Concentration level 10 mg L^{-1}
Flow from S→T   Base oil grade 150N (32 cSt @ 40 °C) operating at 60 °C

Linearised fit data	35 bar, uncut	35 bar, 0-10 µm	70 bar, uncut.	70 bar, 0-10µm
A	1.298 ± 0.011	0.336 ± 0.034	1.582 ± 0.013	0.720 ± 0.019
B	1.012 ± 0.008	0.489 ± 0.027	2.136 ± 0.011	1.222 ± 0.014
R	0.991	0.737	0.996	0.982
SD	0.075	0.264	0.118	0.112
N	281	286	316	266

Figure 5.35 - Effects of different pressures in the S→T direction.
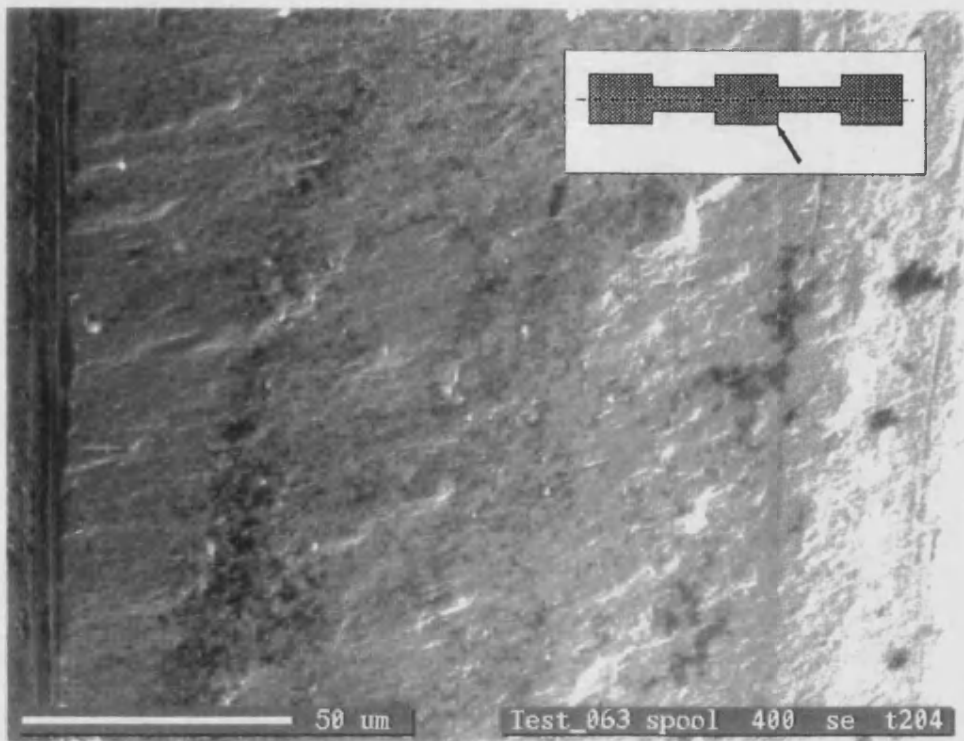
Figure 5.36 - SEM micrograph of the spool metering edge for a 70 bar uncut quartz test (S→T).
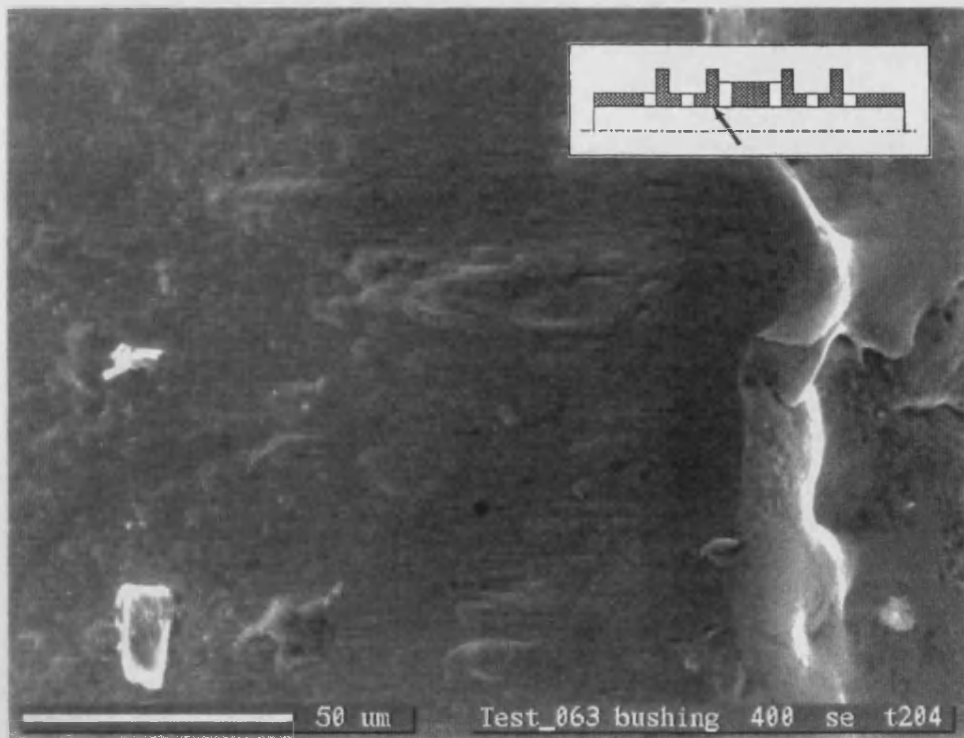
Figure 5.37 - SEM micrograph of the bushing metering edge for a 70 bar uncut quartz test (S→T).
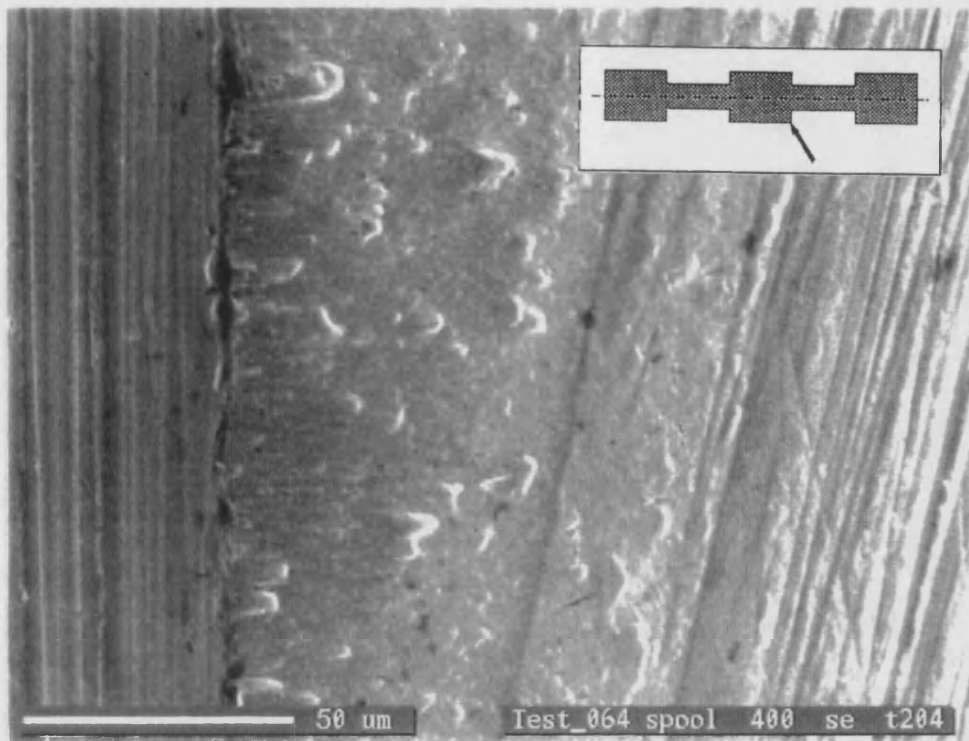
Figure 5.38 - SEM micrograph of the spool metering edge for a 70 bar 0-10 µm quartz test (S→T).
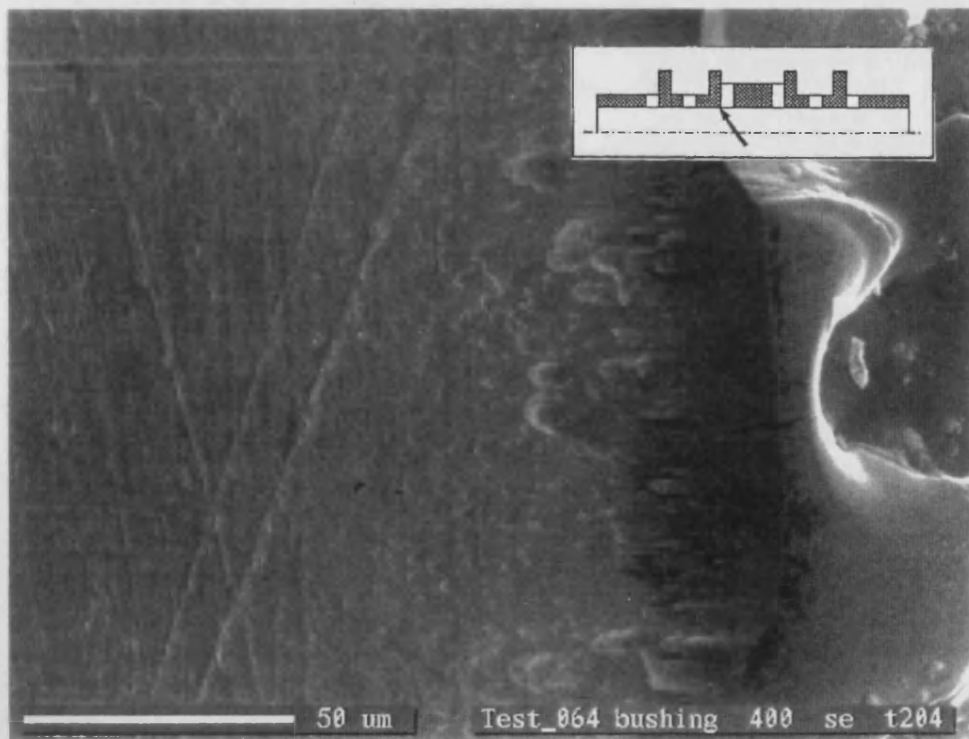
Figure 5.39 - SEM of the bushing metering edge for a 70 bar 0-10 µm quartz test (S→T).
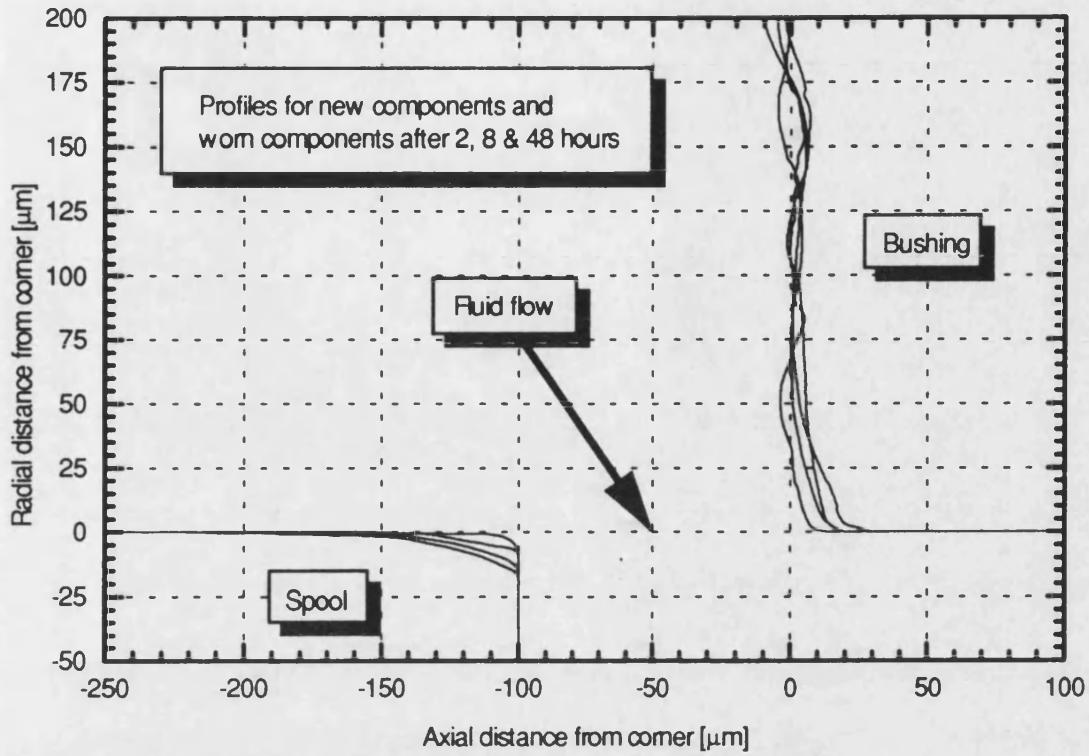
Figure 5.40 - Spool/bushings profiles, flow P to S with uncut quartz at 35 bar.
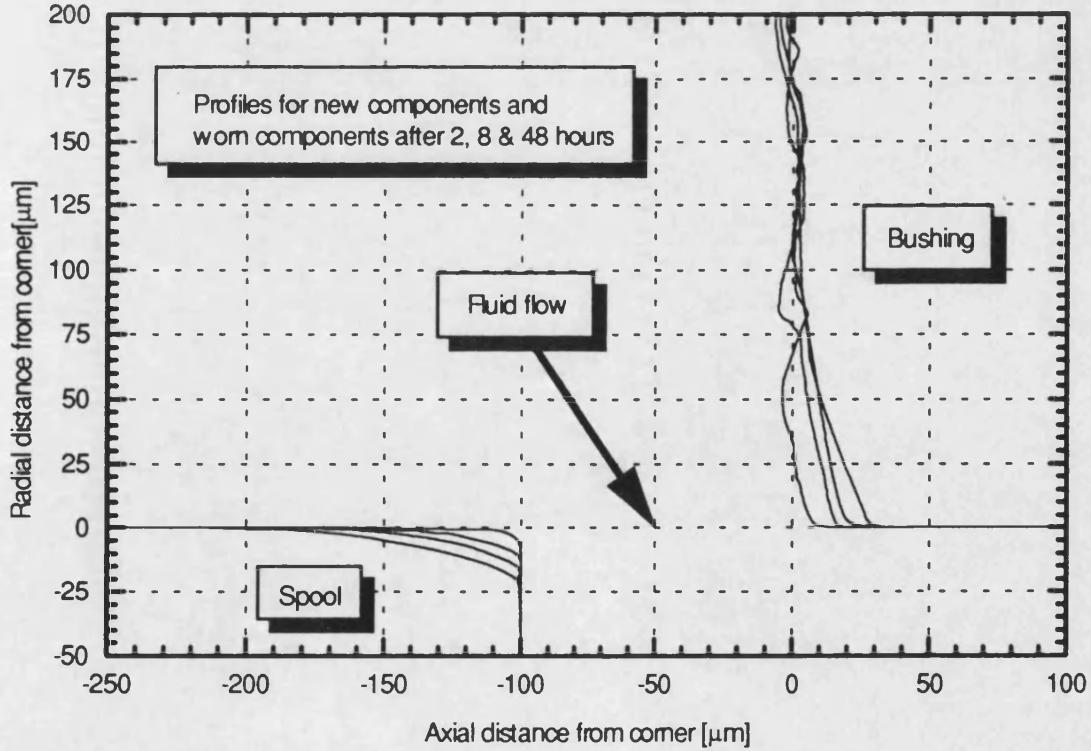
Figure 5.41 - Spool/bushings profiles, flow P to S with uncut quartz at 70 bar.
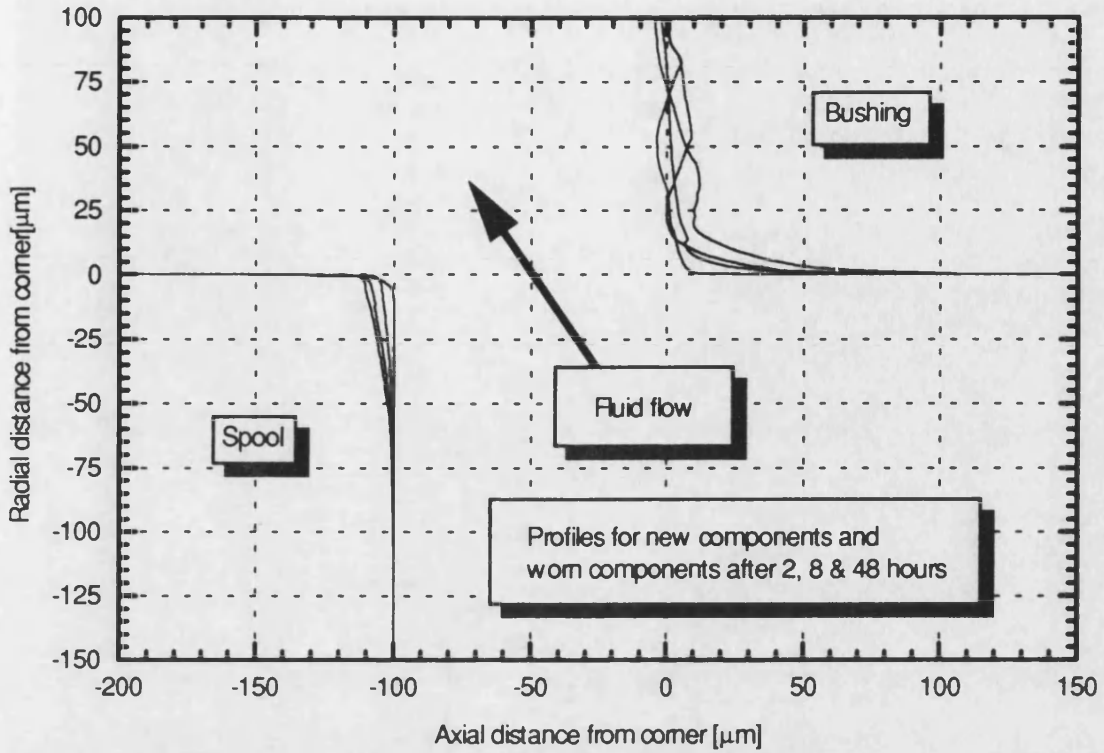
Figure 5.42 - Spool/bushings profiles, flow S to T with uncut quartz at 35 bar.
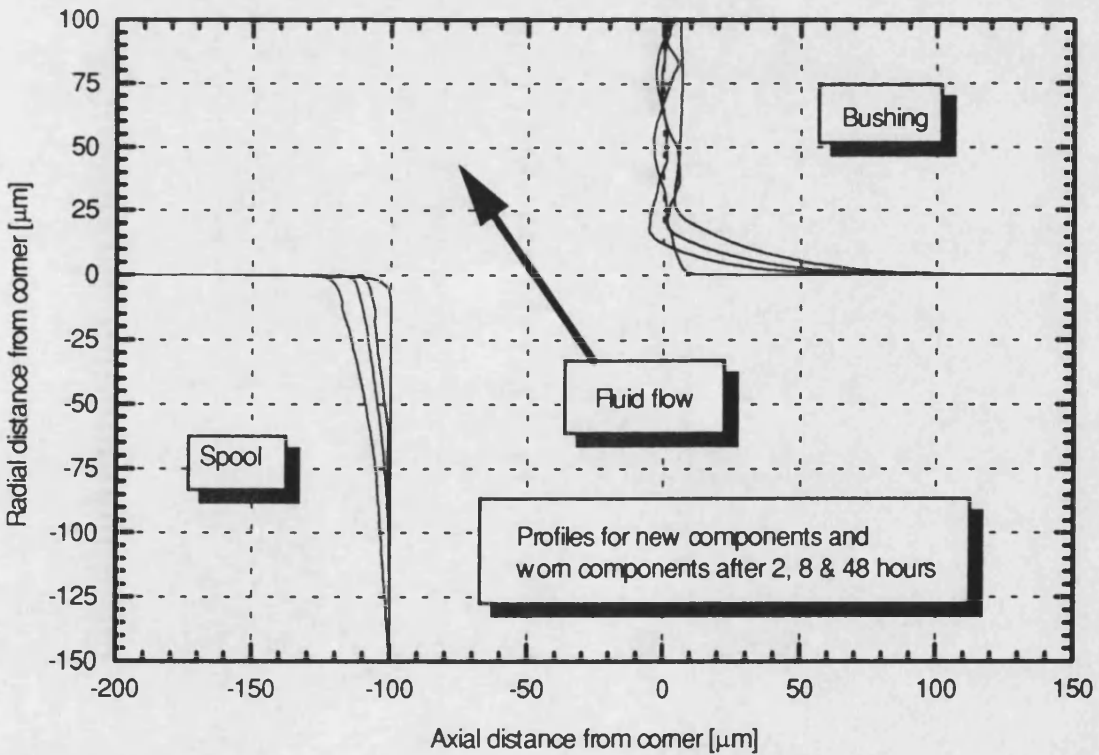
Figure 5.43 - Spool/bushings profiles, flow S to T with uncut quartz at 70 bar.

Contaminant type	Time [Hours]	Spool wear [μm^2]	Bushing wear [μm^2]	Combined wear [μm^2]
35 bar P→S	2	97	214	311
	8	222	581	803
	48	356	807	1163
70 bar P→S	2	151	515	666
	8	323	872	1195
	48	479	1743	2222
35 bar S→T	2	109	245	354
	8	237	322	559
	48	324	639	963
70 bar S→T	2	267	300	567
	8	494	482	976
	48	1065	827	1892

Table 5.2 - Quantity of material removed for different pressures and flow directions.

As described is Section 5.6.4, the quantity of material removed at each test condition can be found by integrating the component profile. The results are presented in Table 5.2. In line with the results presented earlier, a subtracted correction allowance for the new spool and bushing of 46 and 107 μm^2 respectively has been applied. From Table 5.2 it can be seen that for the same test conditions, the quantities of material removed (combined wear) in the P→S is greater than the S→T flow direction. This result is surprising since the flow plots suggest that more wear occurred in the S→T direction. However, it can be seen from the S→T SEM micrograph results that material is deformed in the direction of the fluid flow as well as being removed. It is thought that this feature may be due to the softer material on the side wall of the metering slot (see Section 5.2.1), although this is difficult to verify.

In addition to the variation in the combined value, the contribution of each individual component varies significantly with the flow direction. For example, in the P→S direction the bushing wears significantly more than the spool and the opposite occurs in the S→T flow direction. This result implies that the wear profiles may be dependent upon the fluid flow patterns and/or the jet angle as fluid enters the flow restriction. However, it is beyond the scope of this thesis to determine exactly what flow patterns exist as the fluid enters and leaves the valve, although some computational fluid dynamic (CFD) predictions are included in Chapter 8

From Section 1.4, it has been stated that the erosive wear rate is proportional to the kinetic energy (velocity squared) of the particles. Since velocity is proportional to the square root of

pressure, this suggests that the erosion rate should be proportional to the differential pressure acting across the metering orifice. This result is confirmed in Table 5.2 where it can be seen that by doubling the pressure, approximately twice the amount of material is removed.

Test condition	Time [Hours]	x [μm]	C_q	Actual flow [L min^{-1}]	Flow if C_q unchanged [L min^{-1}]
35 bar P→S	0	100	0.70	9.47	9.47
	2	103	0.80	11.06	9.77
	8	105	0.84	11.89	9.97
	48	112	0.86	12.97	10.66
70 bar P→S	0	100	0.71	13.57	13.57
	2	107	0.76	15.61	14.56
	8	113	0.78	16.85	15.40
	48	121	0.80	18.45	16.53
35 bar S→T	0	100	0.71	9.70	9.70
	2	104	0.81	11.31	10.10
	8	107	0.83	11.91	10.40
	48	115	0.84	12.70	11.20
70 bar S→T	0	100	0.70	13.30	13.30
	2	104	0.78	15.53	13.85
	8	105	0.84	16.81	14.00
	48	107	0.90	18.47	14.26

Table 5.3 - Effects of pressure and flow direction on the flow coefficient and flow rates.

Using the flow plots and the component profiles, it is also possible to calculate the flow coefficient (C_q) for the metering orifice by re-arranging Equation 5.1. If x is the effective opening taken from the profile plot and ΔQ is the calculated flow rate from the linearised model (Equation 5.2), then:

$$C_q = \frac{Q_0 + \Delta Q}{\pi \, dx \sqrt{\frac{2 \Delta P}{\rho}}}$$

.... (5.10)

From Table 5.3 it can be seen that, in all cases, the orifice flow coefficient increases during a wear test. This suggests that the curved wear profile created assists fluid flow by increasing the vena-contracta flow area giving greater flow for the same differential pressure. Also, although not conclusive, it appears that the material deformation occurring in the S→T direction may give further assistance to the flow rate.

5.8.   Wear Debris

It was the original intention to record the Coulter LCM II particle counts using the PC data acquisition system during wear testing, but due to the operating constraints found with the LCM II (see Section 4.7.1), the counts had to be obtained manually, usually at the start and end of a test. Unlike the earlier stability runs, Section 4.7.4, the results reported in this section contain additional particles from the erosion process.

To determine the size and quantity of the wear debris, two methods have been used. Firstly, a Rotary Particle Depositor (RPD) slide and secondly, a 0.8 µm membrane filter has been prepared using oil sample taken after the 48 hour test period. In both cases, the samples were gold sputtered to a sufficiently thick layer to produce a conductive path for the SEM examination, but not too much as to mask the composition of the particles for Energy Dispersive Analysis (EDX). Particle count data for the samples was then obtained using a SEM fitted with an image analyser and EDX system. It should be noted that as quartz particles and the glass slide have similar compositions, the EDX analysis is unable to distinguish between them.
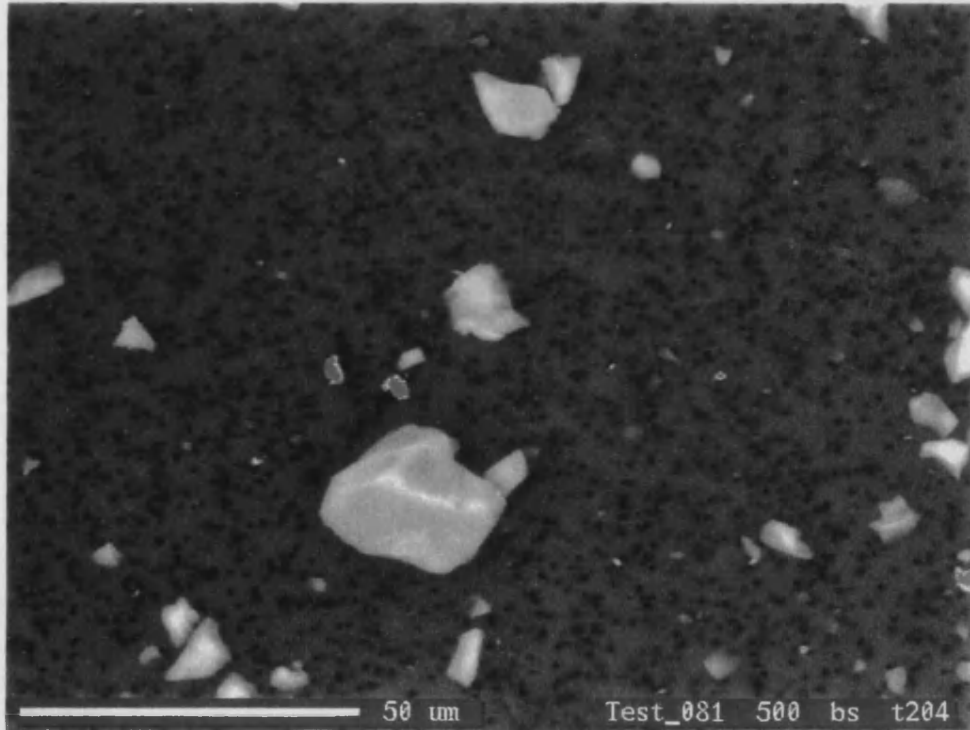
Figure 5.44 - Example of uncut quartz and steel wear debris from an erosion test.

The experimental approach worked well with the RPD slides, although a small quantity of quartz particles were also present with the steel wear debris. This suggests that the quartz particles are statically charged or have magnetic material attached (para-magnetic). Since the LCM II particle counts are combined readings for quartz and steel, a particle size/composition ratio is required. For this, membrane filters are used in preference to RPD slides. Figure 5.44 shows a typical SEM examination of a filter where the steel particles are highlighted in red.

From the samples tested, the steel wear debris has been found to be smaller than 6 µm and, consequently, only the >5 µm particle counts will be affected. Typical quartz/steel ratios for uncut and 0-10 µm quartz dust following a 48 hour test with a 70 bar differential pressure are shown in Table 5.4.

Particle size [µm]	Uncut quartz		0-10 µm quartz	
	% Si O_2	% Fe	% Si O_2	% Fe
>0	89	11	91	9
>1	90	10	94	6
>2	94	6	97	3
>3	96	4	98	2
>4	96	4	99	1
>5	99	1	100	0
>6	100	0		

Table 5.4 - Wear debris ratios for an uncut and 0-10 µm quartz erosion test.

By combining the debris data with the wear circuit particle counts, it is possible to construct a test contaminant stability diagram which indicates the distribution changes including the contribution of the wear debris. An example of this can be seen in Figures 5.45 & 5.46 for the uncut and 0-10 µm quartz results presented in Table 5.4. Due to the particle counting limitations at the smaller particle sizes, (Coulter >5 µm and Hiac > 3 µm) and the reliability obtained at the sub 5 µm end of the distribution curves, the data has been obtained using extrapolation. The results are simply intended to give a statistically repeatable trend and an indication of the magnitude of the numbers involved.

From Figure 5.45, it can be seen for the uncut quartz test, the >25 and >15 µm particle counts fall as expected, but unlike the stability results (Section 4.7.4), the number of >5 µm particles increase. Since only a small proportion of this can be attributed to the wear debris, this increase must be due to larger particles being broken down during their impact with the valve component
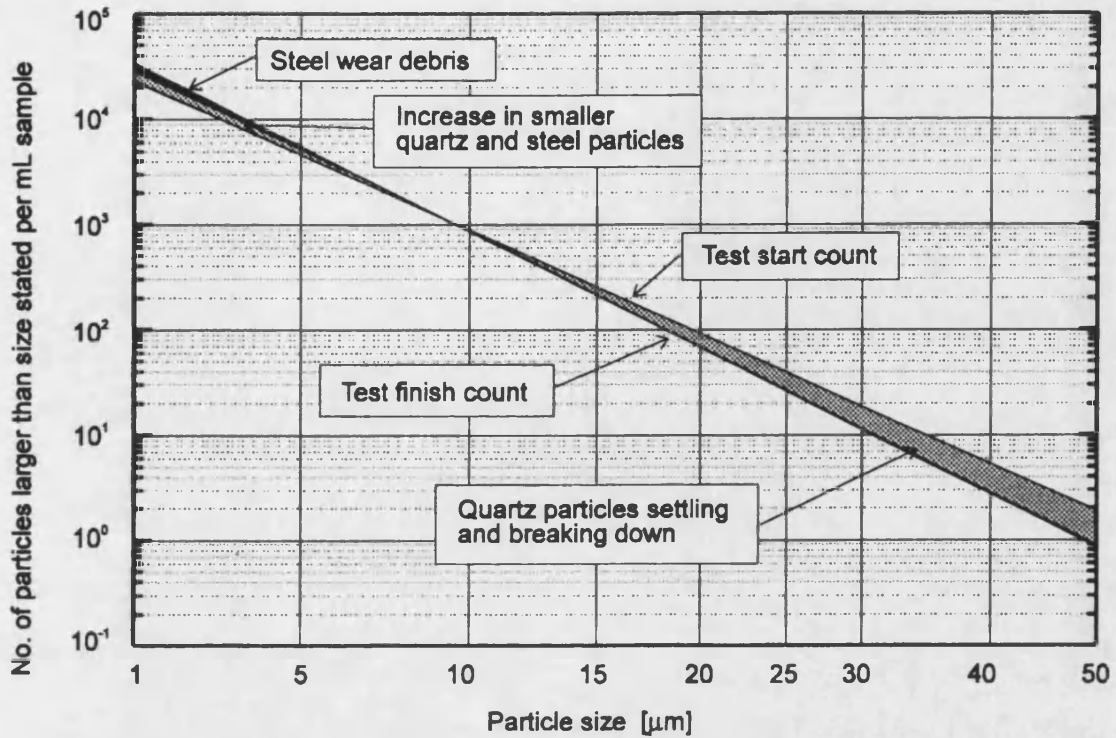
Figure 5.45 - Contamination diagram for an uncut quartz test at 70 bar differential
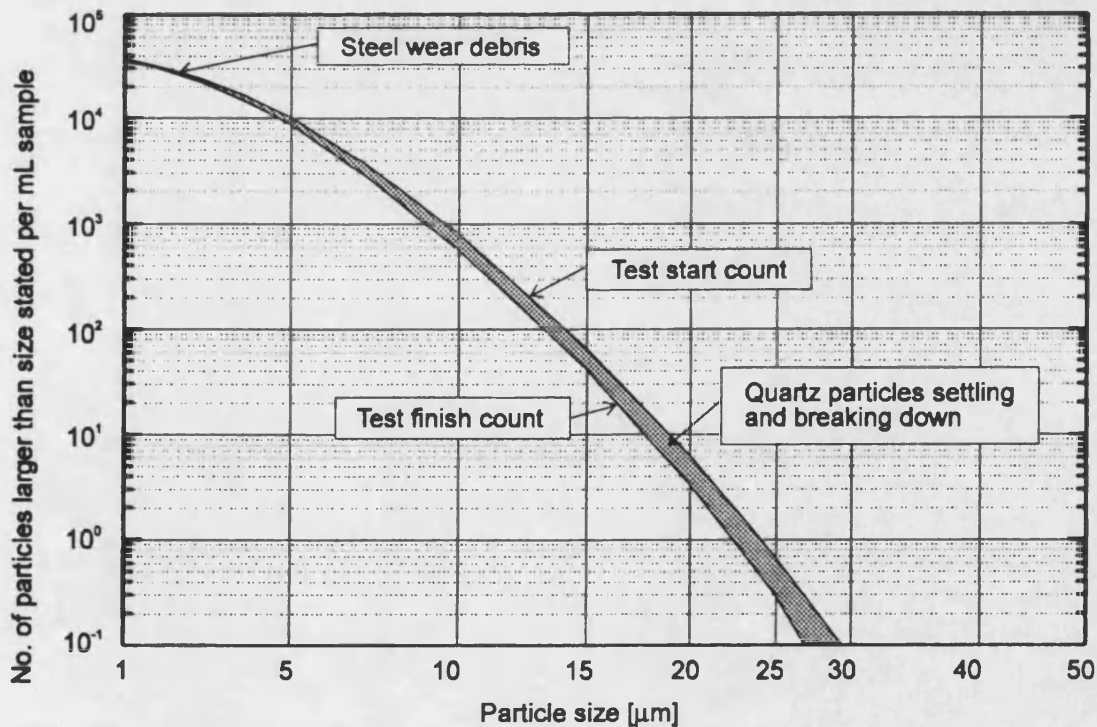
Figure 5.46 - Contamination diagram for a 0-10 mm quartz test at 70 bar differenetial

surface. A similar result is found for the 0-10 μm test, but in this case, the change in the sub 5 μm particles is insignificant when compared to the overall number of particles present.

5.9. Conclusions

It has been found that similar results are obtained for the pressure-flow characteristics for a new metering orifice in both flow directions. The results indicate that there is linear relationship between the flow and the valve opening for spool openings >30 μm. By analysing the worn component profiles, conclusive evidence has been found that the value for the flow coefficient increases with the rounding of the metering edge, permitting greater flow for the same pressure drop.

By applying a $\log_{10}$ relationship to the flow plot, a linear model has been derived for each test condition, thus enabling the flow rate to be calculated at any moment in time. By applying statistical analysis to the linearised model, a point of maximum confidence $\hat{t}$ (minimum variance) has been established at 17.9 hours. At this point, the analysis has shown that for two tests with the same conditions, the results may be considered identical at a 95% confidence level. The analysis has also indicated that a systematic error of ±0.1 L min^{-1} exists on the flow plots. However, the inclusion of this to produce a worse case scenario, is suggested to be too severe in many cases.

By analysing the results for the different test conditions the following points have been identified:

- The erosion rate is independent of the spool opening, providing that the opening is greater than the contaminant particle size.

- When oil is used which has been filtered to a high cleanliness level (tested @ ISO 4406, class 8/4), no changes in the pressure-flow characteristics can be detected.

- Uncut quartz produces higher wear rates than ACFTD although their distributions are similar. It is thought that the difference between the two results is associated with the particle mass and hence its impact momentum.

- Using similar concentrations of different quartz size distributions, greater wear occurs when larger particles are present. This result has important implications relating to the use of gravimetric analysis as a method of contamination control, since it is not only the mass which is important but the distribution contributing to this mass.

- Increasing contaminant concentration levels produce a corresponding increase in the wear rates. The relationship between these quantities is not linear either in terms of increased flow rate or actual component material removed.

- The amount of wear material removed has been found to be approximately proportional to the differential pressure. This supports the established view given in literature which suggests that the erosion rate is proportional to the kinetic energy of the particles.

- From the profile measurements, the damage caused to the spool and bushing varies with flow direction. In the P→S flow direction, the bushing metering slot wears more than the outside diameter of the spool. For the S→T case, the side face of the spool receives more damage than the inside bore of the bushing. At present, it is thought that this result occurs due to the flow patterns as the fluid enters the flow restriction.

- Testing in the S→T direction, suggests that the bushing metering corner is subjected to both material removal and a deformation process. Again this could be due the flow patterns, but the softer material properties found adjacent to the sides of the metering slots may be a factor.

The particle count data and the wear debris analysis results, indicate that the amount of wear debris generated during an erosion test is insignificant compared to the quantity of quartz particles present. Also, as these particles are generally less than 5 µm, they will have little or no effect on the erosion rates. However, in practice, the presence of erosive wear debris is likely to contribute to the problems associated with silting found in many control valve applications.

6

The Effects of Hydraulic Oil Properties
on Erosive Wear

6.1. Introduction

This chapter investigates the effects of oil viscosity and anti-wear formulations on the spool valve wear. Where possible this information is used to identify features which may be important to the particle erosion mechanism.

From this, the chapter presents and compares the results from the oil properties test programme with the base oil results contained in Chapter 5. Where applicable the results are presented in different formats to verify the subtle changes between the performance of the different anti-wear additives

6.2. Oils and Anti-Wear Additives

6.2.1. Background

The primary function of a hydraulic fluid is to transmit power between a prime mover and a load. To achieve this efficiently, it requires that the oil must also perform the various satellite functions highlighted in Figure 6.1.
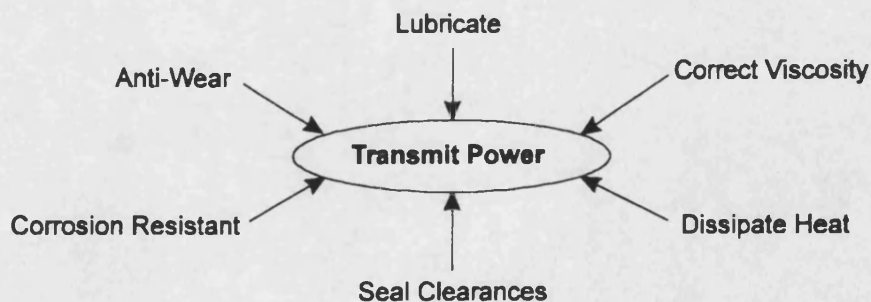
Figure 6.1 - Basic requirements for a mineral oil.

To obtain the required properties, the base oil product is blended with additives. Typical additives are: oxidation inhibitors, anti-wear additives, extreme pressure (EP) additives, rust inhibitors,

metal deactivators, viscosity index (VI) improvers, pour point depressants, anti-foam and emulsifiers/demulsifiers.

The additives of interest within this thesis are associated with anti-wear. There are currently two basic forms of anti-wear packages widely used in hydraulic mineral oils, zinc dialkyl dithiophosphate (ZDDP) and sulphur/phosphorus (S/P). The ZDDP package is used extensively due to its combined antioxidant and anti-wear performance and has the advantage of being cheaper than the other additive systems offering a similar overall performance.

The S/P additive systems are more complex, requiring mixtures of organo phosphorus and organo sulphur compounds for anti-wear protection of equipment and also amine and/or phenolic antioxidants to give adequate protection against oxidation. In spite of the higher cost to produce such oils, the trend suggests a gradual increase in their use. Technically, the S/P oils offers an advantage in having better filterability in the presence of water. This occurs since hydrolysis is possible with ZDDP's which leads to oil insoluble breakdown products blocking fine filters.

Currently, the disposal of oils containing metals is being debated within the EEC and in future, there may be a requirement for the supplier to collect used oils. In the event of a spillage into a drainage system, zinc containing additives may destroy bacteria in water treatment plants. For example, some vehicle body pressing plants have gone over to S/P hydraulic oils in order to avoid the legal consequences of any such spillage. Previously, there has also been concerns regarding the toxicity of the ZDDP's and with increased awareness of health and safety issues, this matter is likely to resurrect at some stage.

Within Europe, two standards are used extensively to assess the anti-wear performance of hydraulic oils. These are the standard vane pump test IP-281 [58], ASTM D2822 [59], DIN 51389 [60] & CETOP RP 67H [61], and the German FZG gear rig test DIN 51354 [62], both are based on steel sliding upon steel. At present there is no accepted standard for steel on bronze etc, but usually oils with good hydrolytic and thermal stability give good performance in the prevention of pump wear [55]. In addition to these methods, the research establishments often use four-ball and pin-on-disc testing to provide comparative type results. These tests are not performed to any particular standards and usually have poor repeatability due to variations in the material properties.

However in the USA, larger vane and piston pumps are used to assess the anti-wear performance and the requirements are much more severe. These tests are run against equipment manufactures requirements rather than established national standards as in Europe. The most

demanding specification is the Hagglunds-Denison HF-O [63], which requires better load carrying and thermal stability properties than the most commonly used European specification, DIN 51524-Part 2 [64].

Unfortunately, all of these tests are effectively friction testing machines and determine wear as a function of load and temperature and do not give any indication to the relative performance of the oil formulation on wear from the action of solid particles (three-body abrasion and erosion). At present the author is not aware of any published literature regarding the properties of the oil to prevent particle erosion.

6.2.2. Hydraulic Test Oils

The function of the anti-wear additive is prevent contact between two moving surfaces. This is achieved by film forming compounds which protect the surfaces either by physical adsorption or by chemical reaction.

The ZDDPs are thought to give anti-wear protection by the formation of a layer approximately 0.1 µm thick on the rubbing surface [65]. It has been proposed that this layer is generated from the ZDDP under the action of a thermal or hydrolytic mechanism to form zinc phosphates and other sulphides. These decomposition products then absorb or react with the surface oxides to form the surface films which contain small particles of iron sulphides and oxides in an amorphous matrix of zinc polyphosphate [65].

The sulphur and phosphorus additives are separate components within the package and behave in different ways. With the organo phosphorus components, adsorption takes place onto the metal surface at relatively low temperatures (>20 °C) offering a load carrying film which has good anti-wear properties at relatively low loads. At higher loads, the organo sulphur component is important in that the heat generated at the metal to metal interface forms an iron sulphide film which is relatively soft and prevents seizure (adhesion) of the two surfaces.

To examine the performance of the anti-wear additives on erosive spool valve wear, two different S/P and two ZDDP formulations have been compared with a base oil. In each instance ISO 3448 [66] viscosity grade 32 (32 cSt @ 40 °C) has been used. The oil temperature/viscosity characteristics for the different oils is shown in Figure 6.2. The basic details of the different oils are :

Base oil grade 150N - This is a solvent refined paraffinic mineral oil which is a suitable base oil for blending different lubricants.

Energol HLP - This is a solvent refined paraffinic mineral oil which conforms to the ISO 6743-Part 4 Type HM classification [67] and DIN 51524-Part 2 [64]. It is primarily aimed at the main stream hydraulics market and is suitable for applications where high oxidation stability is required. The anti-wear additives used in the formulation are classed as active sulphur/phosphorus.

Bartran - This is a solvent refined paraffinic mineral oil which conforms to the ISO 6743-Part 4 Type HM classification [67], Hagglunds-Denison HF-O [63] and DIN 51524-Part 2 [64]. Compared with the HLP, it has much better load carrying capabilities and is more suited for high temperature applications (typically 80 to 90 °C). The anti-wear additives used in the formulation are classed as non-active sulphur/phosphorus.

L92/20217 - This is a solvent refined paraffinic mineral oil which conforms to the ISO 6743-Part 4 Type HM classification [67], Hagglunds-Denison HF-O [63] and DIN 51524-Part 2 [64]. It is based on a stabilised zinc anti-wear formulation and is used in the majority of hydraulic oil on the market.

L92/20218 - This is a solvent refined paraffinic mineral oil which conforms to the ISO 6743-Part 4 Type HM classification [67] and DIN 51524-Part 2 [64]. The anti-wear additives used in the formulation are classed as non-stabilised zinc and produce a low grade, low cost oil.

For the oil formulations described, the vane pump test give similar results at the standard temperature of 65 °C. However, if elevated temperatures (typically 95 °C) are used, the Bartran and the L92/21217 (stabilised zinc) give better performance. Alternatively, for the FZG test, a class 10 result will be obtained for the HLP and the two zinc formulations, and a higher class 12 rating for the Bartran. However, their performance in the prevention of particle erosion and three body abrasion is unknown and therefore the results presented within this chapter represent a significant contribution in this area.
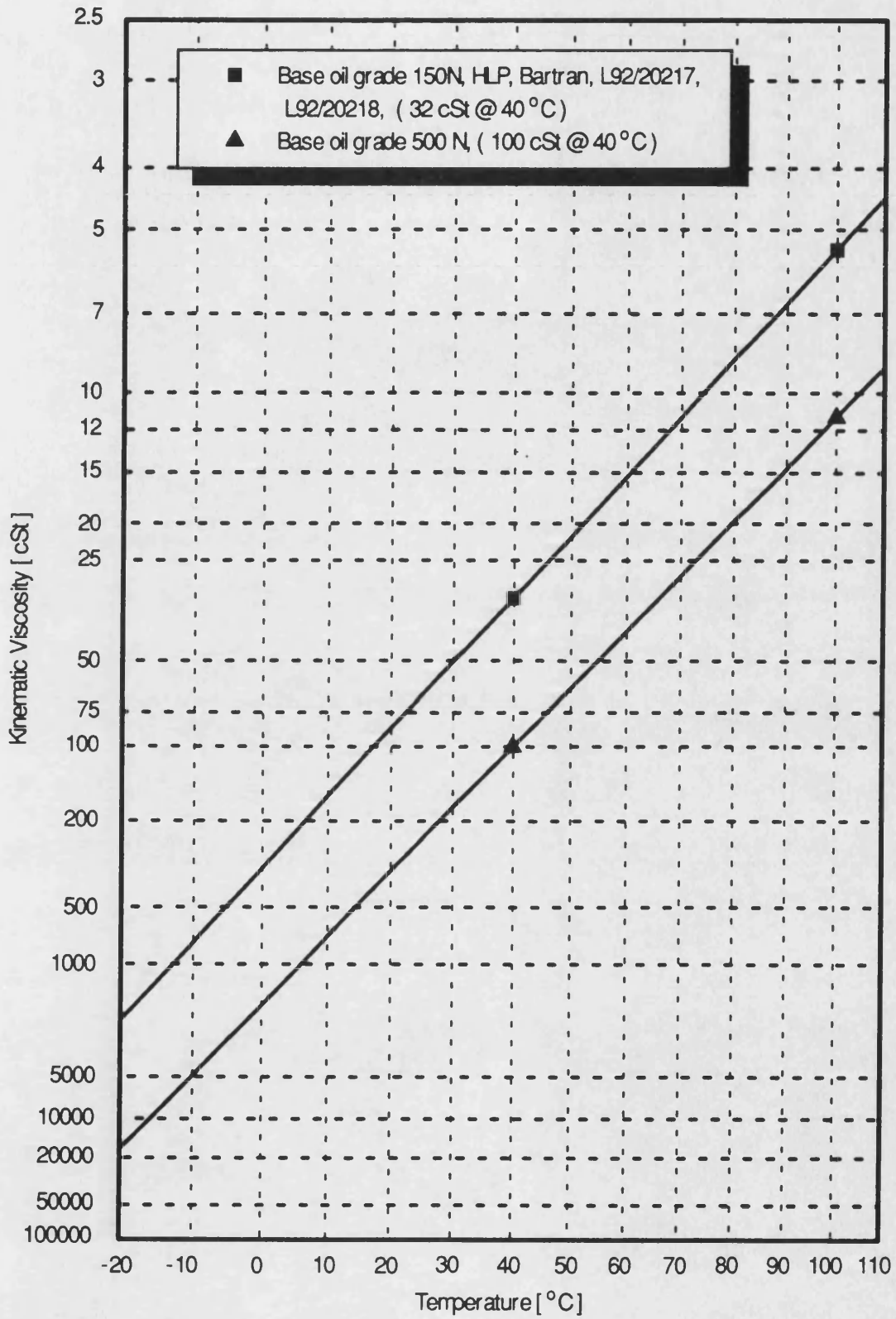
Figure 6.2 - Oil temperature - viscosity characteristics.

6.3.   Viscosity Effects

To examine the influence of viscosity, a series of wear tests have been conducted with grade 150N base oil (32 cSt @ 40 °C) operating at different temperatures. Also, both uncut and 0-10 μm quartz has been used to examine if a relationship between viscosity and particle distribution exists.
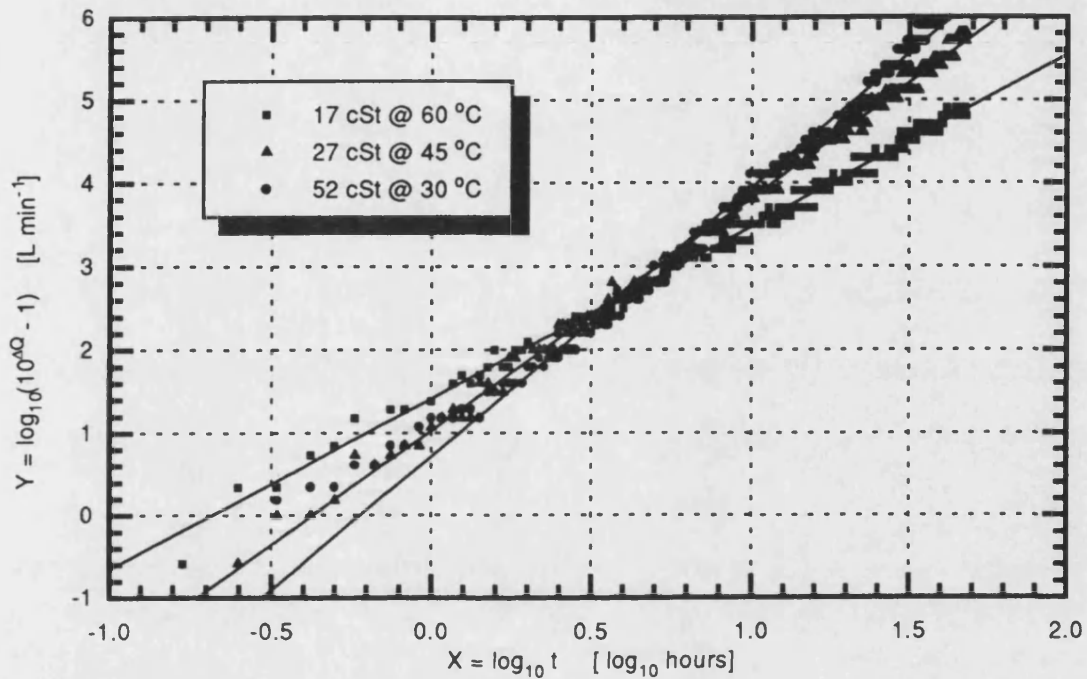
Test conditions - 70 bar differential   Contaminant concentration 10 mg L^{-1} of uncut quartz
Flow from P→S   Base oil grade 150N (32 cSt @ 40 °C)
100 μm spool opening

Linearised fit data	60 °C test	45 °C test	30 °C test
A	1.409 ± 0.014	1.028 ± 0.014	0.712 ± 0.025
B	2.066 ± 0.012	2.786 ± 0.011	3.234 ± 0.021
R	0.997	0.998	0.993
SD	0.087	0.092	0.173
N	218	275	367

Figure 6.3 - Effects of oil viscosity on the erosion rate with uncut quartz test dust.

From the uncut quartz tests Figure 6.3 and the 0-10 μm quartz tests Figure 6.4, it can be seen that the flow rate increases with a corresponding increase in viscosity. Unfortunately, these results do not indicate whether the changes are viscosity or temperature dependent. To address this, a 0-10 μm test was conducted with a grade 500N base oil (100 cSt @ 40 °C) operating at

60 °C to give an oil viscosity of 40 cSt. Conveniently, this operating point gave an intermediate viscosity at a previous test temperature. From Figure 6.4 it can be seen that the flow increase falls into the pattern of the grade 150N oil results, confirming that the wear rate is viscosity and not temperature dependent.
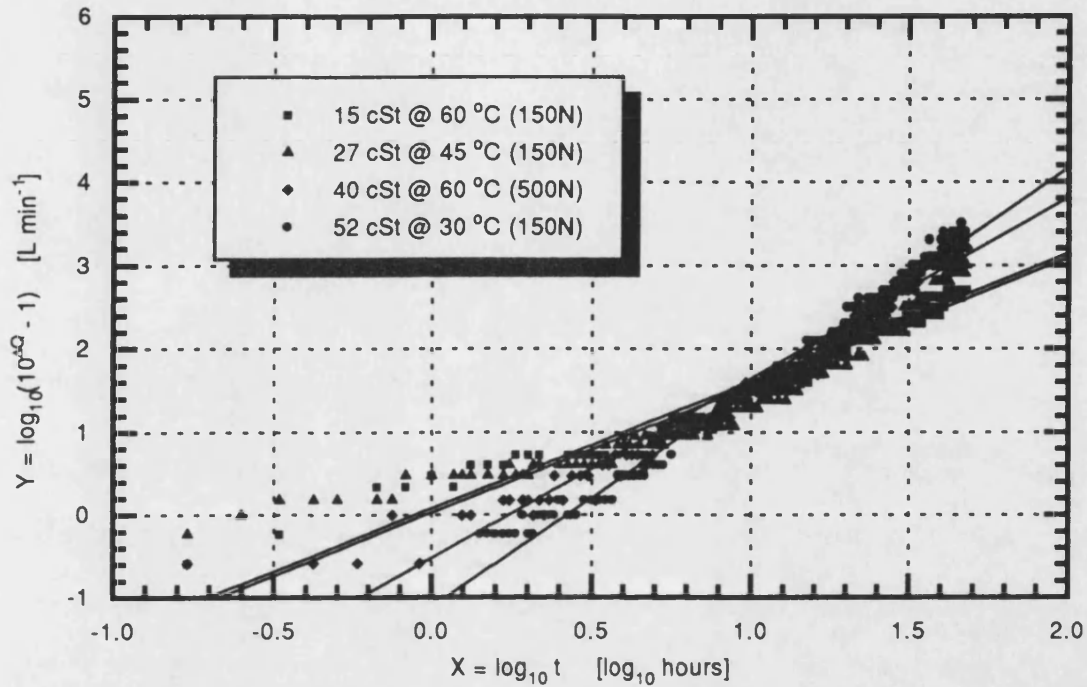
Test conditions - 70 bar differential   Contaminant concentration 10 mg L^{-1} of 0-10 μm quartz
Flow from P→S   100 μm spool opening
Base oil grade 150N (32 cSt @ 40 °C) and 500N (100 cSt @ 40 °C)

Linearised data		60 °C test, 150N	45 °C test, 150N	30 °C test, 150N	60 °C test, 500N
	A	0.027 ± 0.028	0.081 ± 0.041	-1.115 ± 0.023	-0.518 ± 0.039
	B	1.529 ± 0.021	1.529 ± 0.032	2.642 ± 0.018	2.163 ± 0.030
	R	0.976	0.946	0.994	0.977
	SD	0.141	0.257	0.112	0.205
	N	259	276	283	245

Figure 6.4 - Effects of oil viscosity on the erosion rate with 0-10 μm quartz test dust.

Applying the $\bar{t}$ = 17.9 hours criterion to the linearised data gives the following comparison flow rates:

Uncut quartz $\Delta\bar{Q}_{15\,cSt}$ = 4.00 L min^{-1} $\Delta\bar{Q}_{27\,cSt}$ = 4.52 L min^{-1} $\Delta\bar{Q}_{52\,cSt}$ = 4.76 L min^{-1}

0-10 μm $\Delta\bar{Q}_{15\,cSt}$ = 1.95 L min^{-1} $\Delta\bar{Q}_{27\,cSt}$ = 2.00 L min^{-1} $\Delta\bar{Q}_{52\,cSt}$ = 2.20 L min^{-1}

$\Delta\bar{Q}_{40\,cSt}$ = 2.19 L min^{-1} (grade 500N base oil)

The uncut results indicate a difference greater than the ±0.1 L min^{-1} systematic error which would imply statistically that the results are not the same. However, if this extreme test is applied to the intermediate 0-10 μm tests, this would not be true in all cases. Since a significant difference exits between the minimum and maximum 0-10 μm values, the results must be considered to be different.

6.4.   Energol HLP (Active Sulphur/Phosphorus)

To determine the performance of the different oil formulations a series of tests were carried out with grade 150N base oil for comparison purposes, the results for the base oil tests are contained in Figure 6.5.
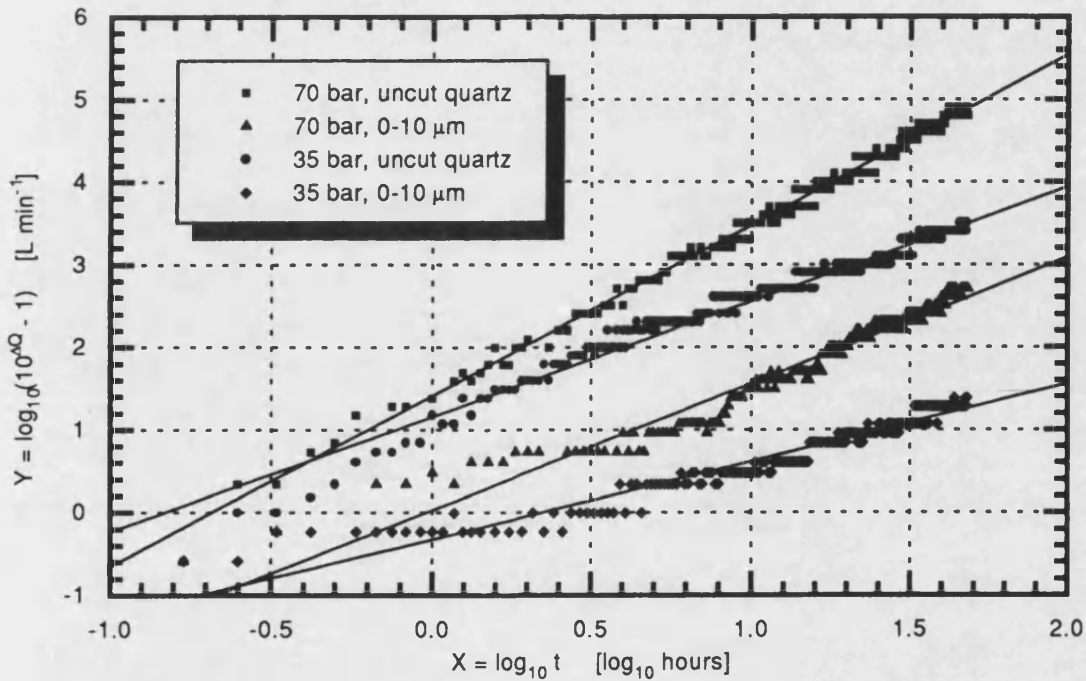
Test conditions - 70 & 35 bar differential   100 μm spool opening   Flow from P→S
               Contaminant concentration 10 mg L^{-1} of uncut and 0-10 μm
               Base oil grade 150N (32 cSt @ 40 °C) operating at 60 °C

Linearised data		70 bar, uncut	70 bar, 0-10 μm	35 bar, uncut	35 bar, 0-10 μm
	A	1.409 ± 0.014	0.027 ± 0.028	1.157 ± 0.015	-0.325 ± 0.019
	B	2.066 ± 0.012	1.529 ± 0.021	1.392 ± 0.012	0.940 ± 0.014
	R	0.997	0.976	0.990	0.967
	SD	0.087	0.141	0.099	0.113
	N	218	259	312	278

Figure 6.5 - Base oil comparison results.

Applying the t̄ criterion gives the following reference values:

$$\Delta\bar{Q}_{70 \text{ bar, uncut}} = 4.00 \text{ L min}^{-1} \qquad \Delta\bar{Q}_{70 \text{ bar, 0-10 μm}} = 1.95 \text{ L min}^{-1}$$

$$\Delta\bar{Q}_{35 \text{ bar, uncut}} = 2.90 \text{ L min}^{-1} \qquad \Delta\bar{Q}_{35 \text{ bar, 0-10 μm}} = 0.91 \text{ L min}^{-1}$$

The results for the HLP (32 cSt @ 40 °C) operating at similar operating conditions to the base oil tests are contained in Figure 6.6. In addition to the P→S tests, S→T testing was also carried out with the HLP, but since a similar trends were obtained these have been omitted to avoid repetition.

Test conditions - 70 & 35 bar differential   100 μm spool opening   Flow from P→S
Contaminant concentration 10 mg L^{-1} of uncut and 0-10 μm
HLP 32 (32 cSt @ 40 °C) operating at 60 °C

Linearised data		70 bar, uncut	70 bar, 0-10 μm	35 bar, uncut	35 bar, 0-10 μm
	A	1.315 ± 0.015	-0.339 ± 0.037	0.743 ± 0.020	-0.602 ± 0.020
	B	1.955 ± 0.013	1.478 ± 0.028	1.434 ± 0.015	0.994 ± 0.015
	R	0.995	0.958	0.986	0.970
	SD	0.097	0.179	0.094	0.089
	N	230	245	270	280

Figure 6.6 - HLP test results.

Applying the $\bar{t}$ criterion gives the following reference values:

$$\Delta \bar{Q}_{70\ bar,\ uncut} = 3.77\ L\ min^{-1} \qquad \Delta \bar{Q}_{70\ bar,\ 0-10\ \mu m} = 1.53\ L\ min^{-1}$$

$$\Delta \bar{Q}_{35\ bar,\ uncut} = 2.54\ L\ min^{-1} \qquad \Delta \bar{Q}_{35\ bar,\ 0-10\ \mu m} = 0.73\ L\ min^{-1}$$

Performing the *t-test* on the base oil and the HLP results clearly indicates that at a 95% confidence level the results are dissimilar even if the extreme ±0.1 L min^{-1} systematic error is included. Therefore, from the HLP and base oil results it has been found that the HLP gives an average reduction of 18% in the null leakage flow rate.
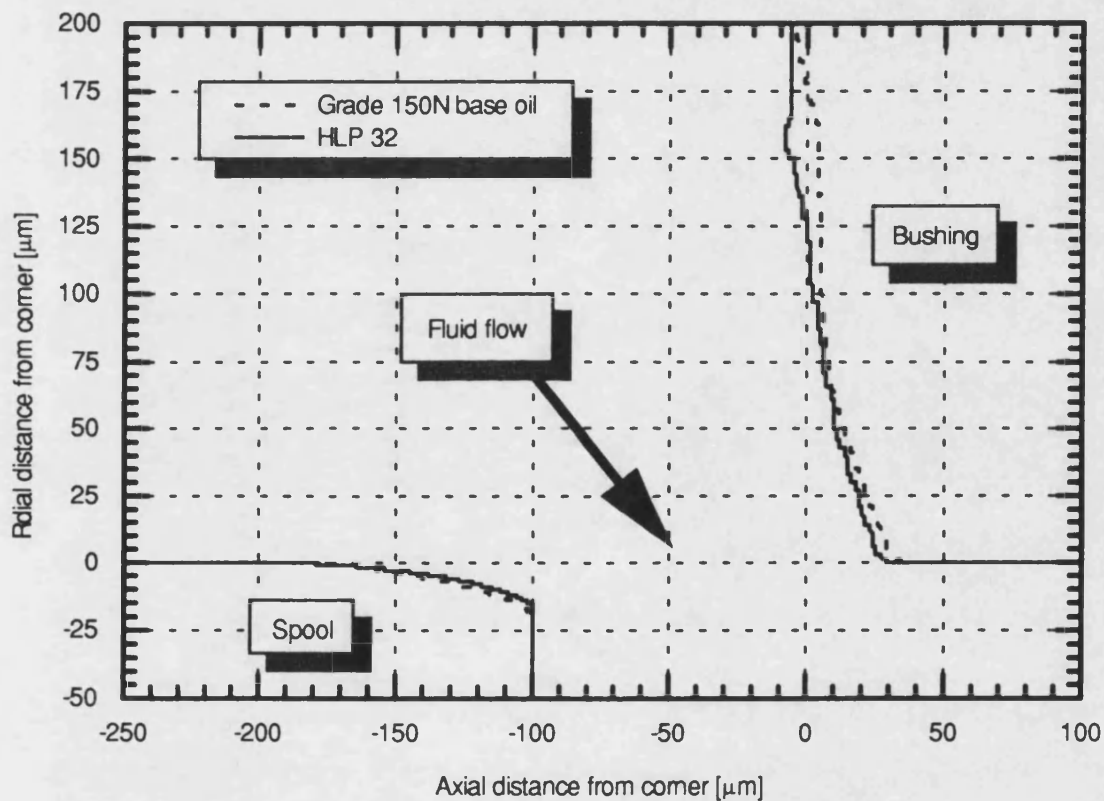
Figure 6.7 - Component profiles for a base oil and a HLP test.

To confirm these results, profile measurements have been conducted on the components from the 70 bar, uncut quartz tests. From Figure 6.7, the results confirm that more material has been removed from the spool and bushing during the base oil test. Although, the variation between the two profiles does not appear to be significant, this small difference will affect both the flow area and the orifice flow coefficient (C_q). In addition to the component profiles, SEM micrographs have been examined for the different test conditions. Unfortunately, the two test conditions cannot be visually separated. Therefore, the SEM micrographs in Chapter 5 can be used for the HLP tests.

6.5.   Bartran (Non-Active Sulphur/Phosphorus)

The test results for the Bartran are contained in Figure 6.8. These results were obtained with identical conditions to the base oil tests Figure 6.5.
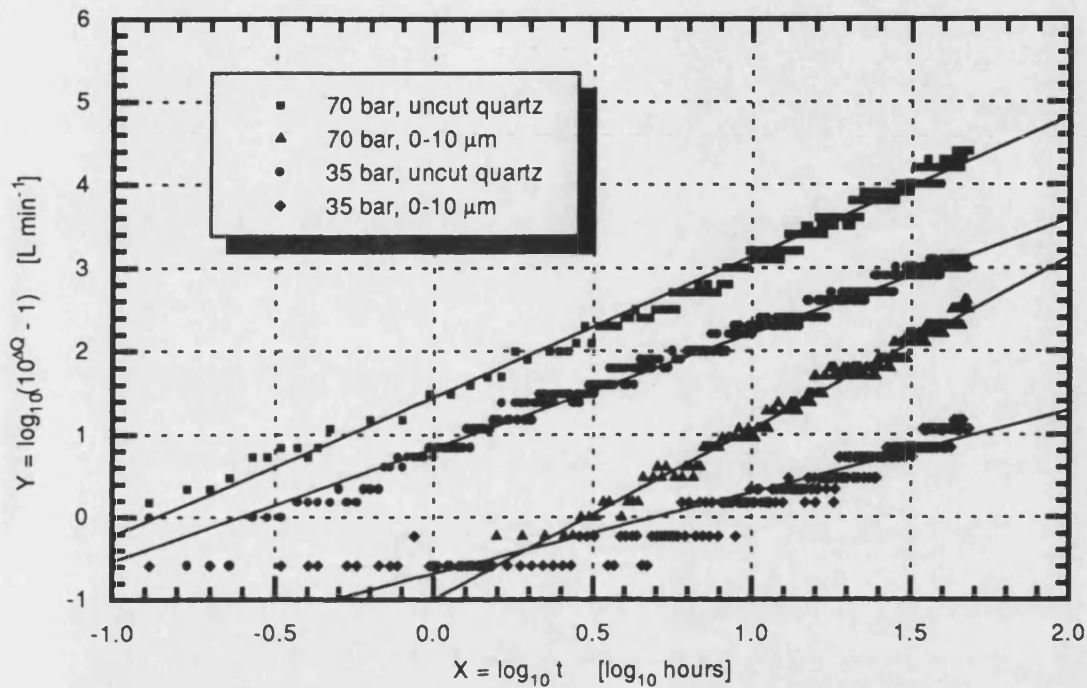
Test conditions - 70 & 35 bar differential   100 μm spool opening   Flow from P→S
Contaminant concentration 10 mg L^{-1} of uncut and 0-10 μm
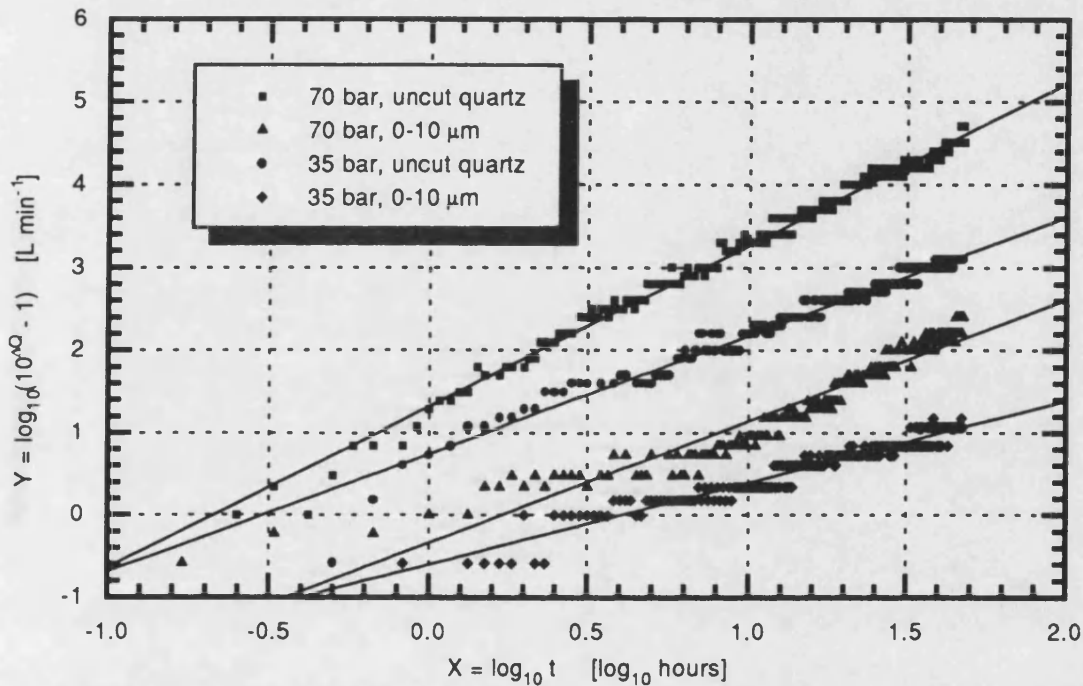Bartran 32 (32 cSt @ 40 °C) operating at 60 °C

Linearised data		70 bar, uncut	70 bar, 0-10 μm	35 bar, uncut	35 bar, 0-10 μm
	A	1.454 ± 0.015	-0.996 ± 0.026	0.837 ± 0.010	-0.685 ± 0.027
	B	1.682 ± 0.012	2.063 ± 0.019	1.376 ± 0.009	0.988 ± 0.021
	R	0.994	0.991	0.993	0.941
	SD	0.108	0.093	0.099	0.185
	N	250	215	373	279

Figure 6.8 - Bartran test results.

Applying the $\bar{t}$ criterion gives the following reference values:

$\Delta\bar{Q}_{70 \text{ bar, uncut}}$ = 3.56 L min^{-1} $\Delta\bar{Q}_{70 \text{ bar, 0-10 μm}}$ = 1.60 L min^{-1}

$\Delta\bar{Q}_{35 \text{ bar, uncut}}$ = 2.56 L min^{-1} $\Delta\bar{Q}_{35 \text{ bar, 0-10 μm}}$ = 0.66 L min^{-1}

Performing the *t-test* on the base oil and the Bartran results clearly indicates that at a 95% confidence level the results are dissimilar even if the extreme ±0.1 L min^{-1} systematic error is included. Therefore, from the Bartran and base oil results it has been found that the Bartran gives an average reduction of 21% in the null leakage flow rate.
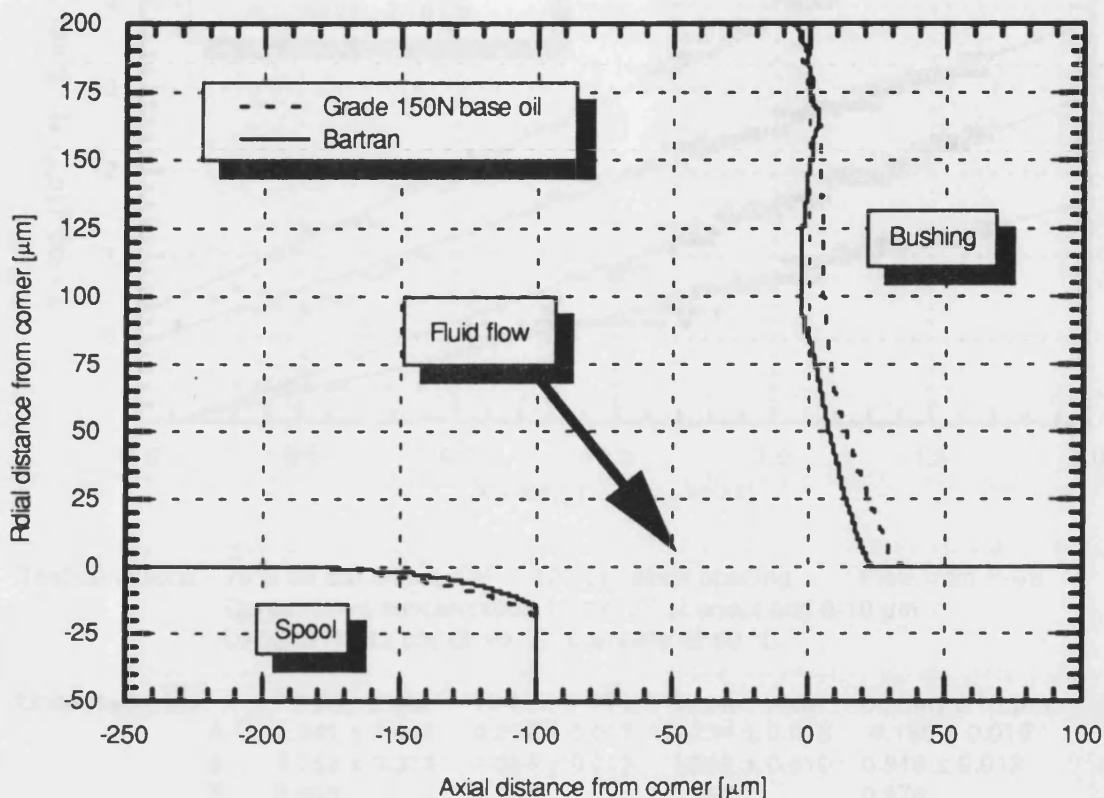
Figure 6.9 - Component profiles for a base oil and Bartran test.

As with the HLP results, component profiles for the Bartran tests have been used to verify the flow plot. From Figure 6.9, a difference between the base oil and the Bartran tests can be detected. However, when compared to the HLP results, Figure 6.7, it appears that the difference is slightly larger in the Bartran case. This supports the findings that Bartran gives improved performance over the HLP.

6.6.   L92/20217 (Stabilised Zinc)

The test results for the stabilised zinc oil are contained in Figure 6.10. These results were obtained with identical conditions to the base oil tests Figure 6.4.
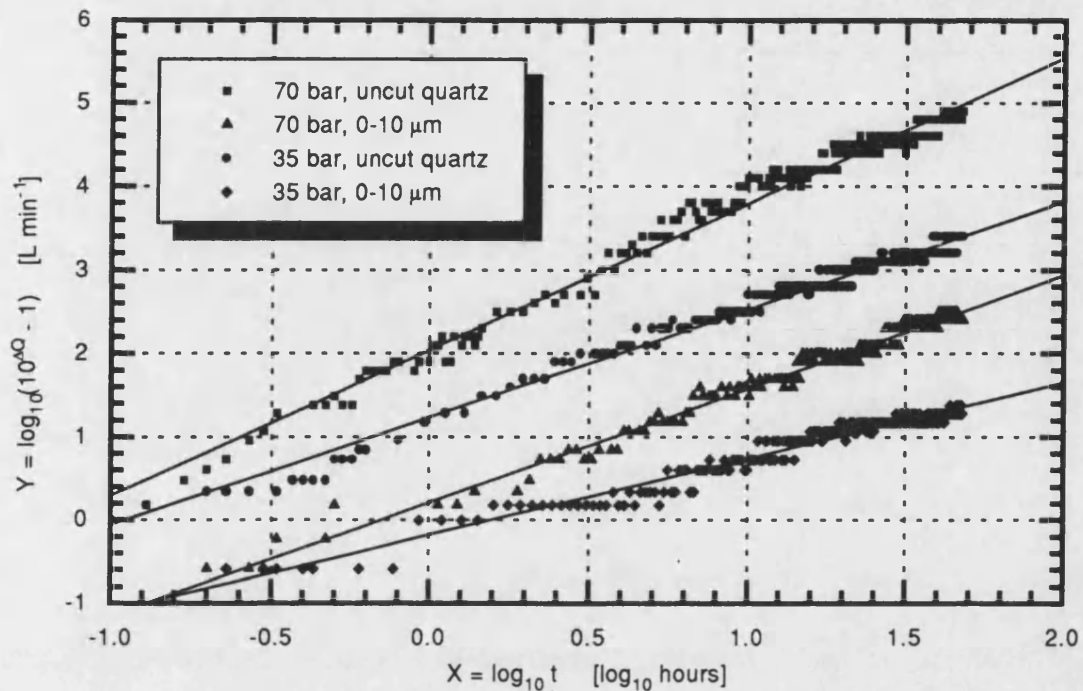
Test conditions - 70 & 35 bar differential   100 μm spool opening   Flow from P→S
Contaminant concentration 10 mg L^{-1} of uncut and 0-10 μm
L92/20217 (32 cSt @ 40 °C) operating at 60 °C

Linearised data		70 bar, uncut	70 bar, 0-10 μm	35 bar, uncut	35 bar, 0-10 μm
	A	2.041 ± 0.016	0.209 ± 0.017	1.234 ± 0.013	-0.180 ± 0.015
	B	1.752 ± 0.013	1.364 ± 0.013	1.292 ± 0.010	0.916 ± 0.012
	R	0.993	0.990	0.992	0.978
	SD	0.12921	0.089	0.094	0.088
	N	275	215	252	278

Figure 6.10 - L92/20217 (stabilised zinc) test results.

Applying the t̄ criterion gives the following reference values:

$\Delta \bar{Q}_{70 \text{ bar, uncut}}$ = 4.24 L min^{-1} $\Delta \bar{Q}_{70 \text{ bar, 0-10 μm}}$ = 1.92 L min^{-1}

$\Delta \bar{Q}_{35 \text{ bar, uncut}}$ = 2.85 L min^{-1} $\Delta \bar{Q}_{35 \text{ bar, 0-10 μm}}$ = 1.01 L min^{-1}

Performing the *t-test* on the base oil and the stabilised zinc oil results with at a 95% confidence level suggests that statistically some of the results are dissimilar. However, since the variation between the two data sets is within the ±0.1 L min^{-1} systematic error, it should be stated that a variation between the two products cannot be statistically proven with a high level of confidence.

This result can be verified from the profile measurements presented in Figure 6.11, where it is impossible to discriminate between the base oil and the L92/20217 test.
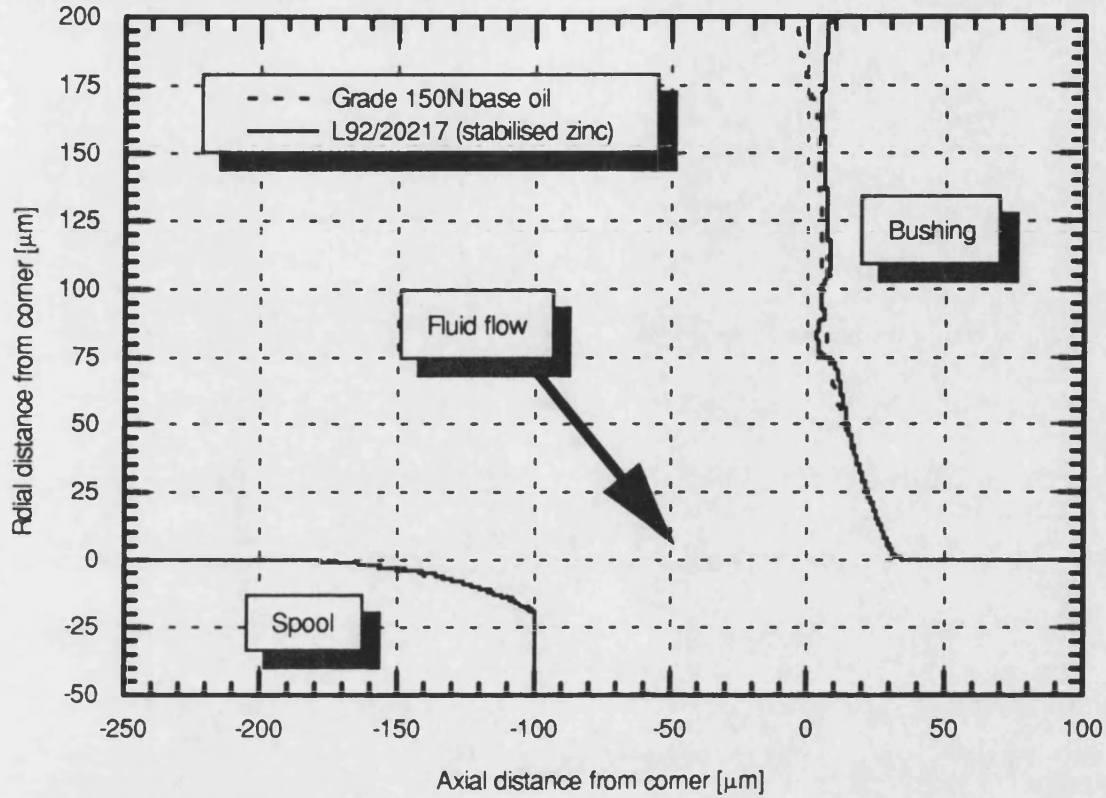
Figure 6.11 - Component profiles for a base oil and a L92/20217 test.

6.7.   L92/20218 (Non-Stabilised Zinc)

The test results for the stabilised zinc oil are contained in Figure 6.12. These results were obtained with identical conditions to the base oil tests Figure 6.4.

Applying the $\bar{t}$ criterion gives the following reference values:

$\Delta\bar{Q}_{70 \text{ bar, uncut}} = 4.00 \text{ L min}^{-1}$ $\Delta\bar{Q}_{70 \text{ bar, 0-10 } \mu m} = 1.85 \text{ L min}^{-1}$

$\Delta\bar{Q}_{35 \text{ bar, uncut}} = 2.78 \text{ L min}^{-1}$ $\Delta\bar{Q}_{35 \text{ bar, 0-10 } \mu m} = 1.04 \text{ L min}^{-1}$
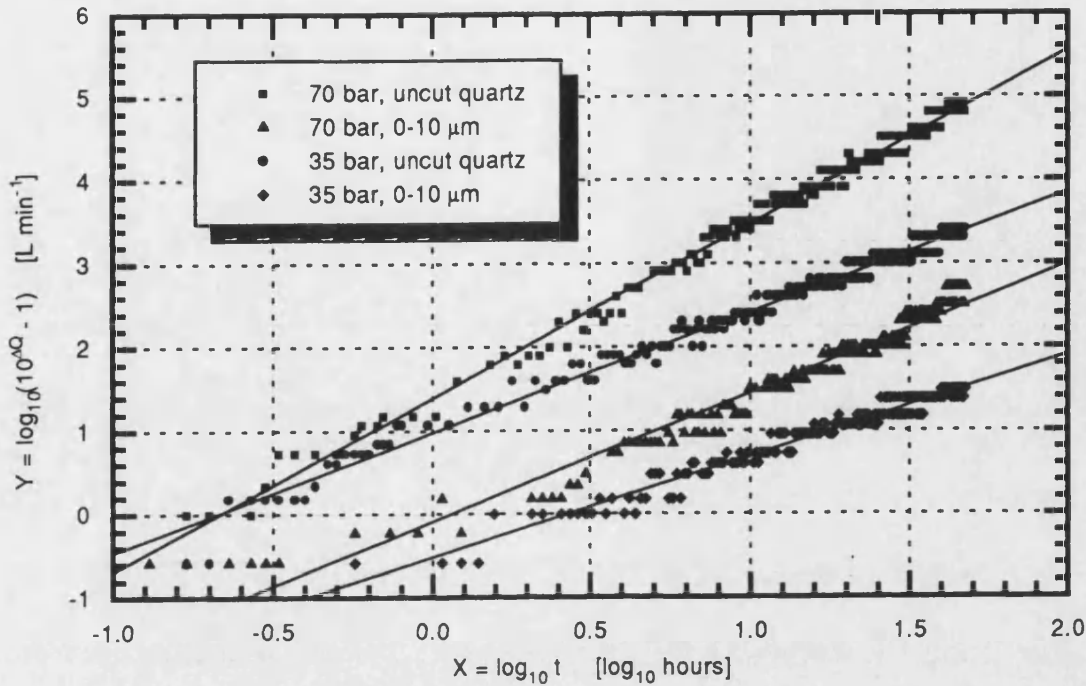
Test conditions - 70 & 35 bar differential   100 µm spool opening   Flow from P→S
Contaminant concentration 10 mg L^{-1} of uncut and 0-10 µm
L92/20218 (32 cSt @ 40 °C) operating at 60 °C

Linearised data		70 bar, uncut	70 bar, 0-10 µm	35 bar, uncut	35 bar, 0-10 µm
	A	1.389 ± 0.015	-0.089 ± 0.029	0.975 ± 0.014	-0.520 ± 0.021
	B	2.080 ± 0.012	1.539 ± 0.022	1.439 ± 0.011	1.212 ± 0.016
	R	0.996	0.977	0.993	0.981
	SD	0.096	0.161	0.098	0.089
	N	250	229	266	239

Figure 6.12 - L92/20218 (non-stabilised zinc) test results.

Performing the *t-test* on the base oil and the non-stabilised zinc oil results with at a 95 % confidence level suggests that statistically some of the results are dissimilar. However, since the variation between the two data sets is within the ±0.1 L min^{-1} systematic error, it should be stated that a variation between the two products cannot be statistically proven with a high level of confidence.

This result can be verified from the profile measurements Figure 6.13, where it is impossible to discriminate between the base oil and the L92/20218 test.
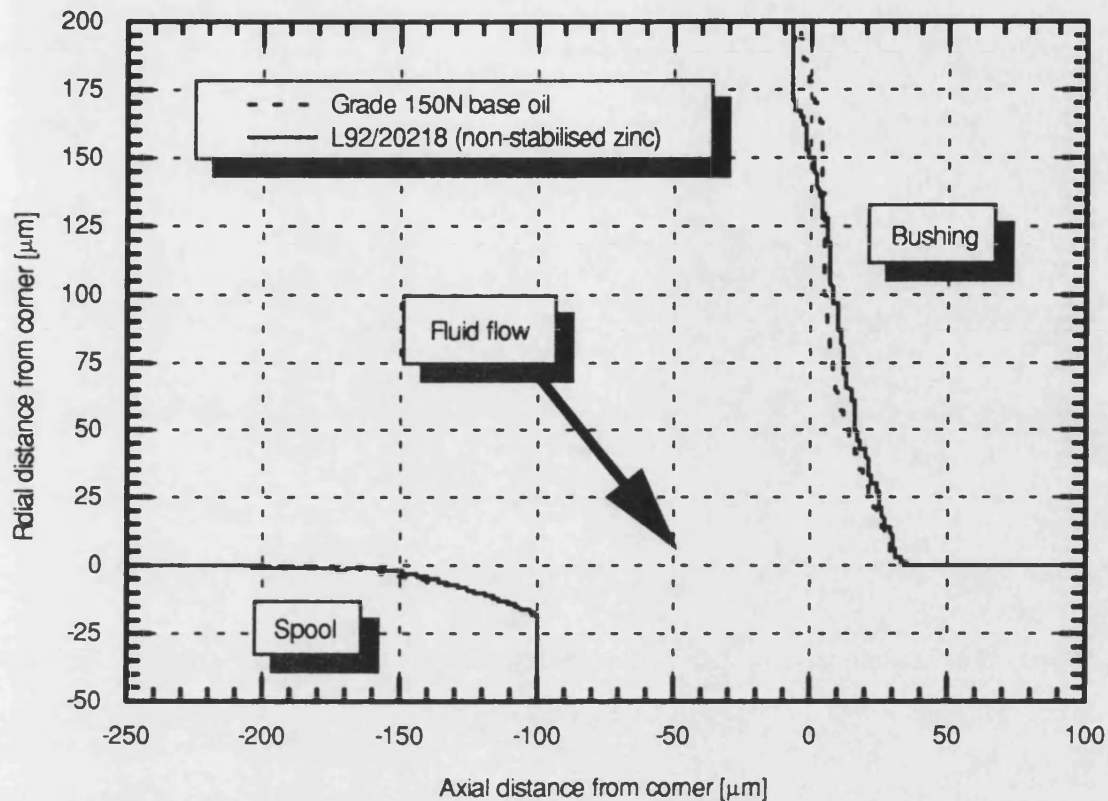
Figure 6.13 - Component profiles for a base oil and a L92/20218 test.

6.8.   Conclusions

The tests have highlighted that viscosity is the most important oil property in the prevention of particle erosion. The results suggest that the wear rate increases with a corresponding increase in viscosity. This is a surprising result, since logically it would be expected that the thicker oil will have a larger boundary layer to prevent surface contact from the impinging particles. Since the opposite has been found, it is thought that the particles are able to move more freely within the oil streamlines to permit them to impinge onto the component surface at a different impact angle (see Chapter 8 for more details)

From the different oil formulation tests, it has been found that the S/P oils give an improvement in the wear rates when compared with base oil. This was not the case with the ZDDPs which gave similar results. Currently, there is no explanation for why or how the S/P anti-wear additives cause an improvement, but the results indicate that the Bartran is slightly better than the HLP.

Finally, the work has highlighted that individually, oil viscosity and S/P additives can influence the particle erosion rates. Further work is required to investigate the interaction between the two oil properties in an erosive wear environment. This work should also examine the additive performance in a three-body abrasion environment.

7

The Effects of Spool Material Properties

on Erosive Wear

7.1. Introduction

This chapter describes the properties of five different surface engineering techniques used to evaluate the influence of the material properties on the particle erosion rate. Owing to the manufacturing difficulties in applying surface treatments or coatings to the internal bore and metering slots within the bushing, the treatments were limited to the spools. Although, it would have been desirable to apply the treatment to both components, coating one surface was considered to be acceptable for the evaluation trials. In addition, this had the advantage that small changes in the spool dimensional tolerances during the treatment process could be accommodated by matching the bushing to suit.

Results obtained from the spool material wear test programme are compared with the base oil results presented in Chapter 5.

7.2. Background

It is well documented [68 & 69] that the hardness of the particles involved in abrasion or erosion influences the wear rates. When the hardness of the particles (H_p) are below that of the target surface (H_s) the wear rate reduces. However, when the hardness ratio (H_p/H_s) is significantly greater than unity, the actual hardness of the particles become insignificant. An example of the influence of hardness ratio on a range of metallic and ceramic materials for two-body abrasion is contained in Figure 7.1 (From [69]).

The author has shown in Section 3.2.3 that the hardness of the quartz test dust is approximately 8 GPa and that the ACFTD is likely to be slightly softer. However, since the hardness of the standard spool and bushing has been found to be H_v = 650 (6.4 GPa), this gives a hardness ratio H_p/H_s of 1.25. Figure 7.1 suggests that the standard components will wear easily from the action of quartz and ACFTD.
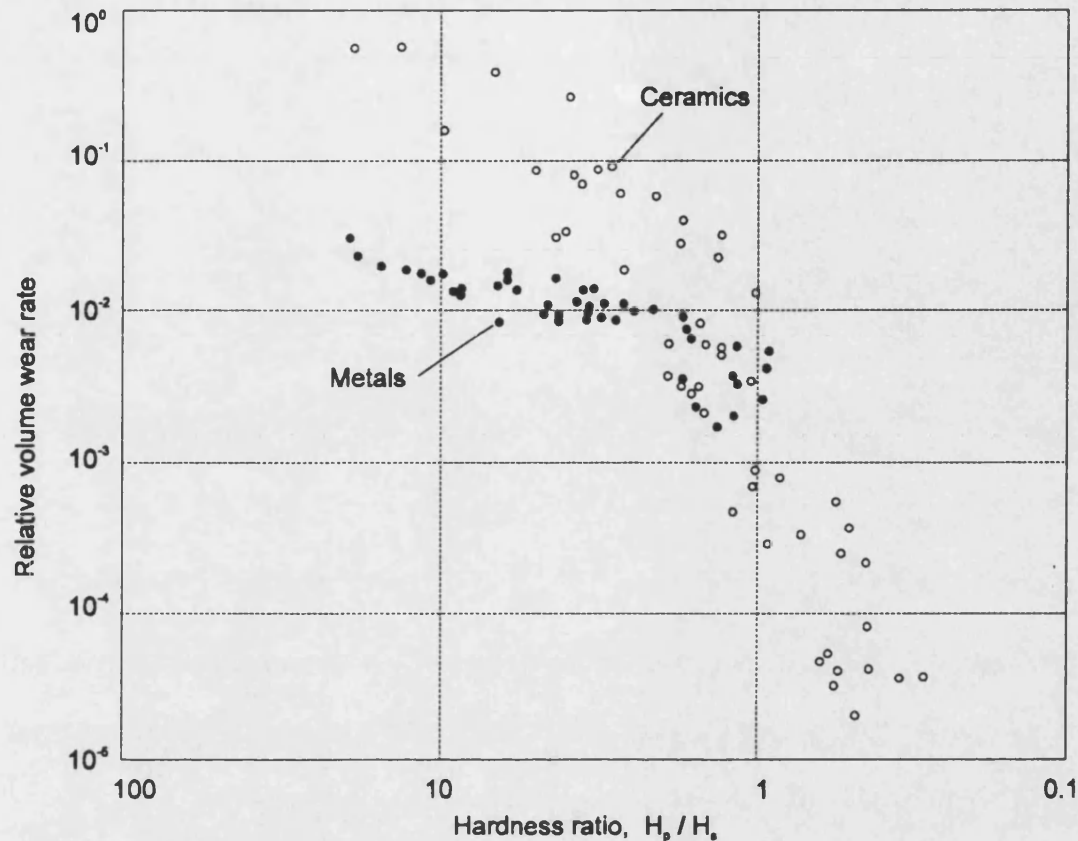
Figure 7.1 - Relative volume wear rate verses the particle/surface hardness ratio (From [69]).

To examine and confirm the influence of component hardness on the particle erosion rates, the following different surface engineering techniques have been applied to the spools:

Standard components - The spool and bushing is currently manufactured from AISI 440C stainless steel. This steel has been selected primarily for its ability to be through heat treated, although the thermal stability, corrosion resistance and machining properties also make it a good choice. The finished components have a hardness of H_v = 650 (6.4 GPa) although the sides of the bushing metering slots are thought to be tempered back to the annealed state of about $H_v \approx 230$ (2.2 GPa) during the EDM process (see Section 5.2.1).

Soft spool - Using an inert gas (nitrogen) oven, a standard spool was tempered back to give a through hardness of $H_v \approx 400$ (3.9 GPa).

Nitrocarburised spool - A spool was treated using a new process known as *Delta Nitrocarburising*. This technique is a low temperature, low distortion, austenitic gaseous case hardening process.

The process claims to produce a two tier system known as a *compound layer* and an *underlying case*. The *compound layer* is the layer immediate to the surface and is typically 10 to 20 μm thick with a hardness of H_v = 800 to 900 (7.8 to 8.8 GPa). This layer is supported by a 25 to 50 μm *underlying case* with a hardness value of H_v = 800 to 1000 (7.8 to 9.8 GPa). Below this, a diffusion zone of nitrogen produces nitrides which act as a further *back-up* case before the core material properties are reached.

Titanium nitride coated spool - The titanium nitride (TiN) process consists of applying a surface coating using a physical vapour deposition (PVD) process. The TiN is laid down in a partial vacuum from ionised titanium fed into a plasma of ionised argon and nitrogen. Under controlled conditions and a constant electrical potential, the nitride grows on the surface of the component to the required thickness, typically 1 to 10 μm. The surface hardness for TiN is typically H_v = 2000 to 3000 (19.6 to 29.4 GPa).

Ion implanted spool - This technique is used to alter the composition and structure of the outermost layers of the material to improve its strength or impart resistance to corrosion to the surface without affecting its bulk properties. The process involves subjecting the material surface to a stream of accelerated nitrogen ions. These collide with atoms held in the crystal lattice of the material and cause local dislocations and radiation damage. The ions also become lodged in the surface, some occupying the spaces caused by the defects and locking them into place, others displacing atoms in the lattice. The overall effect is to reduce the tendency of the defects to progress through the lattice and so prevent part of the overlying structure breaking adrift and wearing away. Usually the surface layer is modified to a depth of about 0.1 μm with a 30 to 40% increase in the surface hardness, say H_v ≈ 880 (8.6 GPa) for the spool being considered.

Tungsten carbide/carbide coated spool - The application of the tungsten carbide/carbide (WC/C) coating is applied at low temperatures (≤250 °C) in a high vacuum. This permits good dimensional stability and low component distortion. The coating has been primarily developed to produce a hard surface H_v ≈ 1000 (9.8 GPa), with a low coefficient of friction (typically 0.2 against dry steel). The finished coating is black-grey in appearance and is typically 1 to 4 μm thick.

7.3. Soft Spool

To obtain a performance overview of the different surface treatments, tests have been conducted with uncut and 0-10 μm quartz at 70 bar differential pressure, in both flow directions (P→S and

S→T) and compared with the standard component results. The standard test results are contained in Figure 7.2.
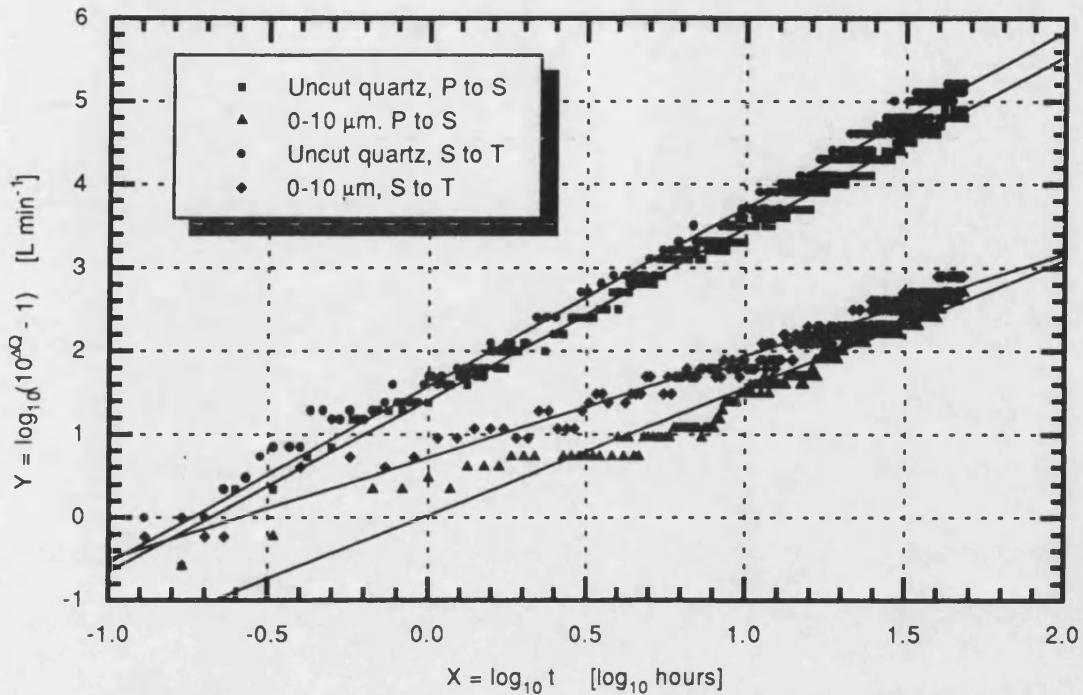
Test conditions - 70 bar differential   Contaminant concentration 10 mg L^{-1} of uncut and 0-10 μm
             Base oil grade 150N (32 cSt @ 40 °C) operating at 60 °C
             100 μm spool opening

Linearised data	Uncut, P→S	0-10 μm, P→S	Uncut, S→T	0-10 μm, S→T
A	1.409 ± 0.014	0.027 ± 0.028	1.582 ± 0.013	0.720 ± 0.019
B	2.066 ± 0.012	1.529 ± 0.021	2.136 ± 0.011	1.222 ± 0.014
R	0.997	0.976	0.996	0.982
SD	0.087	0.141	0.118	0.112
N	218	259	316	266

Figure 7.2 - Standard component test results.

Applying the $\bar{t}$ comparison criterion to the linearised data gives the following:

$\Delta\bar{Q}_{Uncut\ quartz,\ P\rightarrow S}$ = 4.00 L min^{-1} $\Delta\bar{Q}_{0\text{-}10\ \mu m,\ P\rightarrow S}$ = 1.95 L min^{-1}

$\Delta\bar{Q}_{Uncut\ quartz,\ S\rightarrow T}$ = 4.26 L min^{-1} $\Delta\bar{Q}_{0\text{-}10\ \mu m,\ S\rightarrow T}$ = 2.25 L min^{-1}

Using identical test conditions to the standard material contained in Figure 7.2, the results obtained for the soft spool are shown in Figure 7.3.
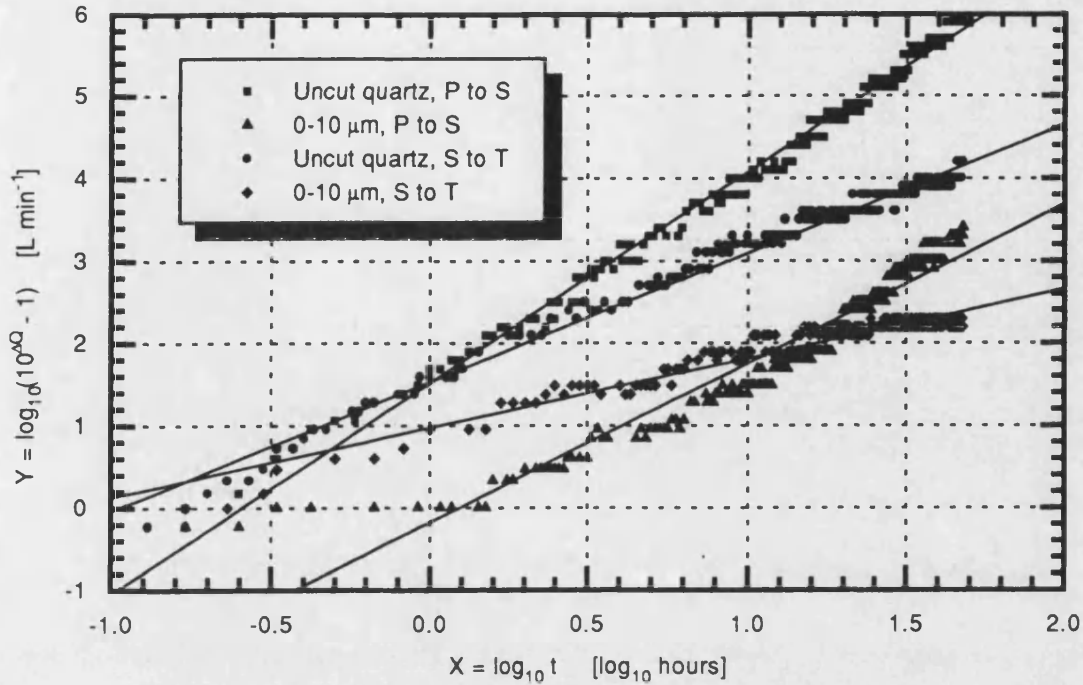
Test conditions - 70 bar differential   Contaminant concentration 10 mg L^{-1} of uncut and 0-10 μm
               Base oil grade 150N (32 cSt @ 40 °C) operating at 60 °C
               100 μm spool opening

Linearised data		Uncut, P→S	0-10 μm, P→S	Uncut, S→T	0-10 μm, S→T
	A	1.518 ± 0.020	-0.175 ± 0.041	1.529 ± 0.015	0.975 ± 0.021
	B	2.562 ± 0.016	1.931 ± 0.031	1.563 ± 0.012	0.841 ± 0.016
	R	0.995	0.957	0.992	0.964
	SD	0.124	0.249	0.114	0.113
	N	240	349	249	210

Figure 7.3 - Soft spool test results.

Applying the t̄ comparison criterion to the linearised data gives the following:

$\Delta \bar{Q}_{\text{Uncut quartz, P→S}}$ = 4.73 L min^{-1} $\Delta \bar{Q}_{\text{0-10 μm, P→S}}$ = 2.60 L min^{-1}

$\Delta \bar{Q}_{\text{Uncut quartz, S→T}}$ = 3.49 L min^{-1} $\Delta \bar{Q}_{\text{0-10 μm, S→T}}$ = 2.03 L min^{-1}

Comparing the standard and the soft spool test results, it can be seen that the flow rate increases by 25.5% when using the softer spool in the P→S flow direction. However, in the reverse direction S→T, the flow rate actually reduces by 16.5%. This is a surprising result since the literature suggests that the wear rate should increase as in the P→S case. To confirm this result, profile

measurements were conducted for the uncut quartz tests in both flow directions, as shown in Figures 7.4 & 7.5.

From Figures 7.4 & 7.5 it can be seen that the spool wear profile has changed as suggested by the flow plots. It is interesting to see that little or no change has occurred with the bushing wear profile and therefore any flow change can be directly attributed to the spool properties.

By integrating the wear profiles, it is possible to calculate the area of material removed for each test condition as shown in Table 7.1. These are presented with a subtracted correction allowance of 46 μm^2 for a new spool. The results show that almost a complete reversal in the amount of material removed occurs between the two flow directions. At present this result cannot be explained using published literature.

Flow direction	Standard spool wear [μm^2]	Soft spool wear [μm^2]
P→S	433	1226
S→T	1019	548

Table 7.1 - Effect of material hardness on spool material removal.

From the SEM micrographs, it is impossible to discriminate between the soft and the standard spools, hence they have been omitted from this chapter to prevent duplication. However, low magnification micrographs of the spool are included in Figures 7.6 to 7.8. These clearly illustrate the effects of contaminant in the P→S direction by the removal of the temper colours along the spool stems. In addition, excessive damage has been caused by the uncut quartz on the spool stem. This result gives a good indication of the flow jet angle through the metering orifice in the P→S direction.
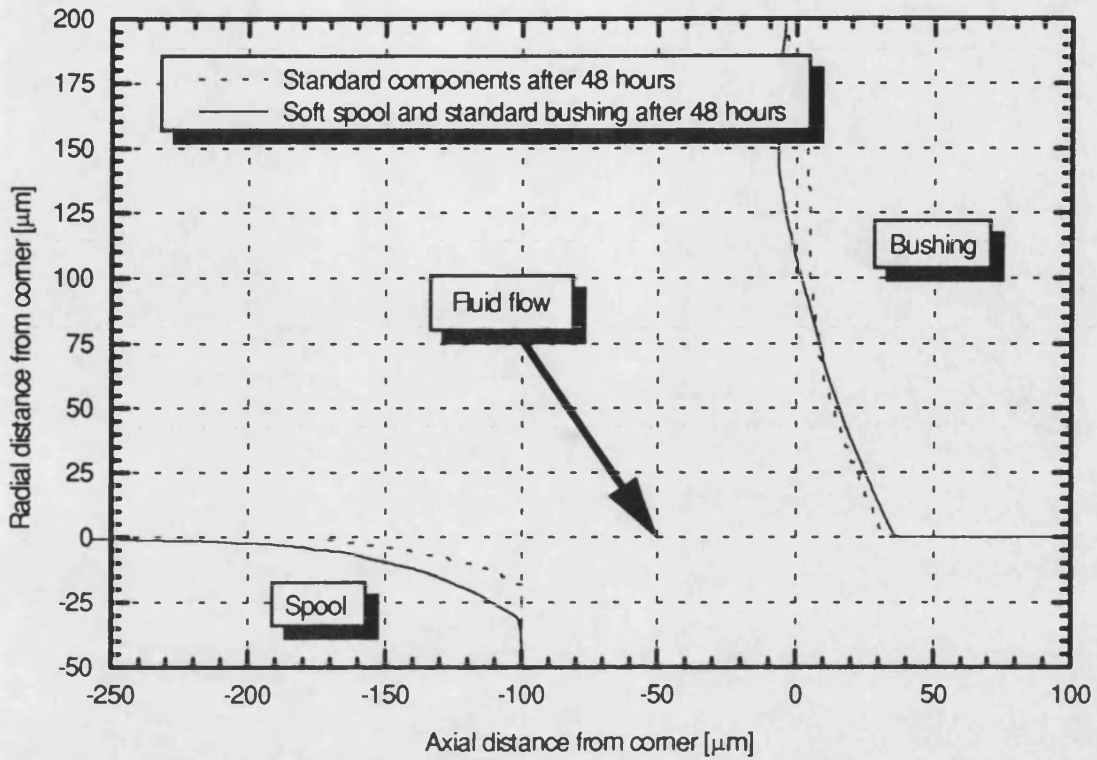
Figure 7.4 - Soft spool/bushing profiles, flow P to S with uncut quartz at 70 bar.
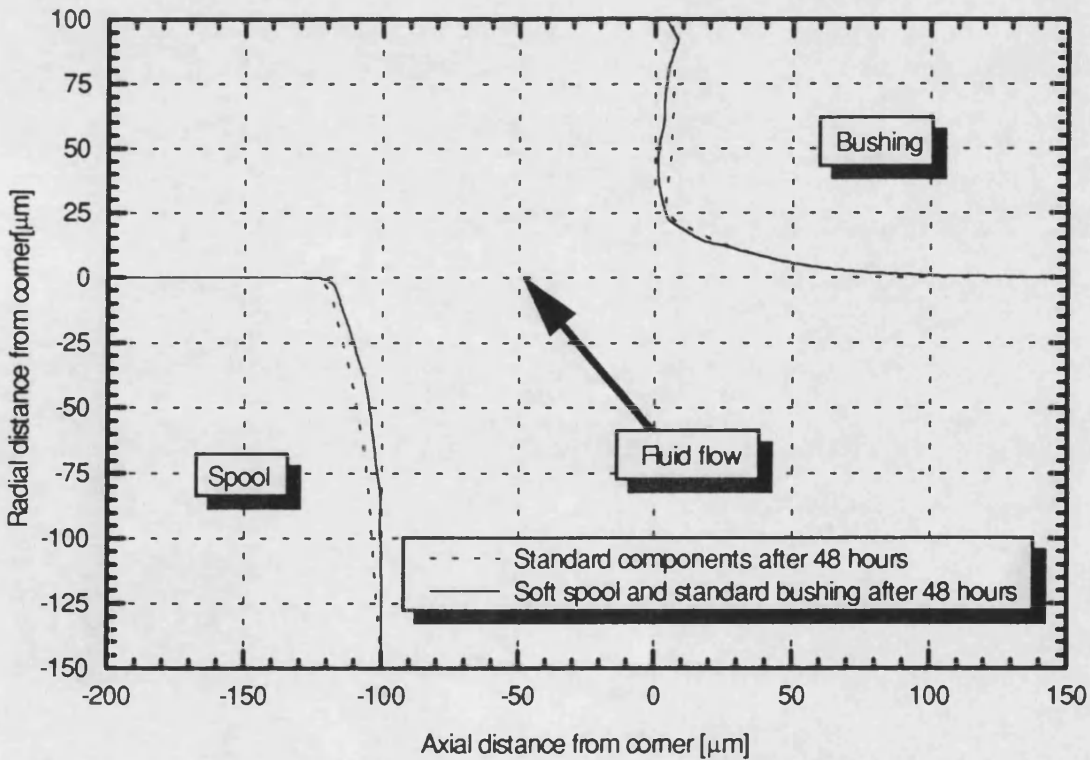
Figure 7.5 - Soft spool/bushing profiles, flow S to T with uncut quartz at 70 bar.

Figure 7.6 - Soft spool pressure land following a uncut quartz test.

Figure 7.7 - Soft spool pressure land following a 0-10 μm quartz test.
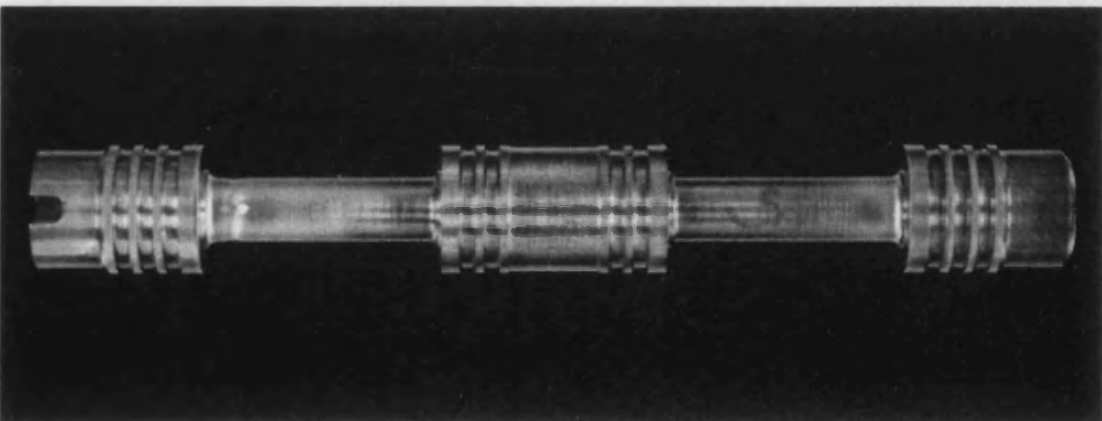
Figure 7.8 - Overall view of soft spool after the completion of all four tests.

7.4. Nitrocarburised Spool

The results for the nitrocarburised spool testing are contained in Figure 7.9.
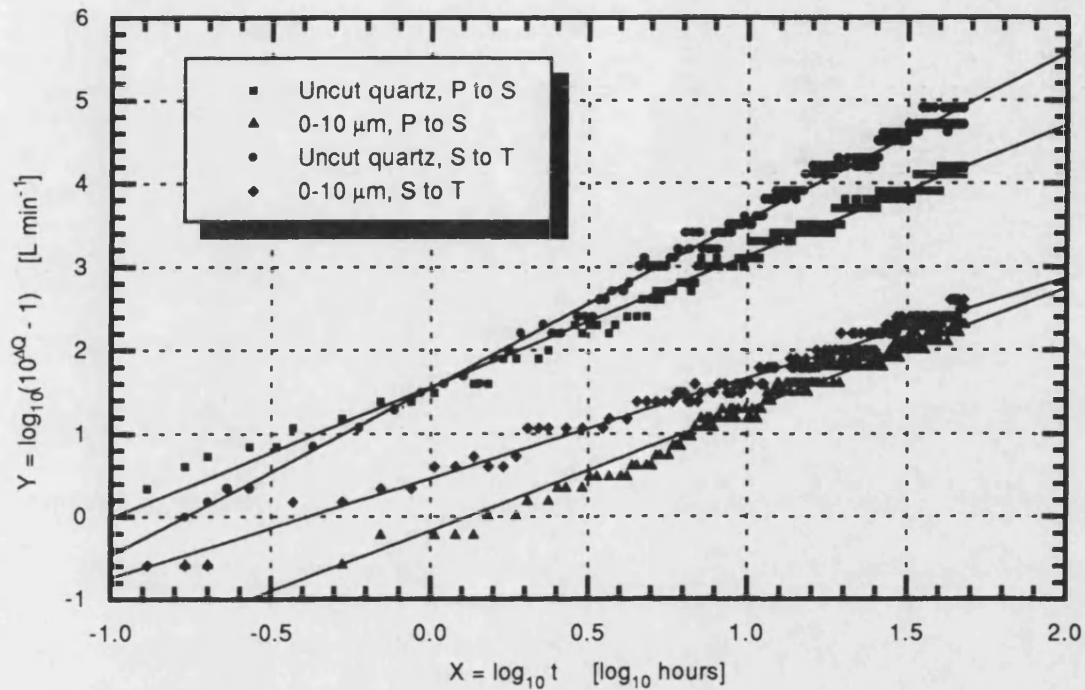
Test conditions - 70 bar differential Contaminant concentration 10 mg L^{-1} of uncut and 0-10 μm
Base oil grade 150N (32 cSt @ 40 °C) operating at 60 °C
100 μm spool opening

Linearised data	Uncut, P→S	0-10 μm, P→S	Uncut, S→T	0-10 μm, S→T
A	1.560 ± 0.016	-0.173 ± 0.024	1.546 ± 0.017	0.464 ± 0.016
B	1.570 ± 0.012	1.462 ± 0.019	2.015 ± 0.015	1.204 ± 0.012
R	0.994	0.983	0.995	0.990
SD	0.097	0.115	0.101	0.084
N	221	209	211	199

Figure 7.9 - Nitrocarburised spool test results.

Applying the $\bar{t}$ comparison criterion to the linearised data gives the following:

$\Delta\bar{Q}_{Uncut\ quartz,\ P\to S}$ = 3.53 L min^{-1} $\Delta\bar{Q}_{0-10\ \mu m,\ P\to S}$ = 1.67 L min^{-1}

$\Delta\bar{Q}_{Uncut\ quartz,\ S\to T}$ = 4.07 L min^{-1} $\Delta\bar{Q}_{0-10\ \mu m,\ S\to T}$ = 1.98 L min^{-1}

Unlike the soft spool results, the nitrocarburised spool gives a consistent improvement in both
flow directions due to its increased hardness. Since the variation in $\Delta\bar{Q}$ between the standard and

the nitrocarburised spool is greater than the ±0.1 L min⁻¹ systematic error, it is valid to state that the nitrocarburising gives an improved performance. This improvement can been by seen by an average reduction of 12% in the flow rate.

Figures 7.10 to 7.13 contain a SEM micrograph for each of the spool metering edges. As previously discussed in Chapter 5, the columnar structure is present in the direction of the fluid flow, although the damaged area extends a smaller distance from the corner when compared with the standard components. This visually confirms the increased performance. However, the most interesting point can be seen in the 0-10 μm quartz, pressure land test, Figure 7.11, and to a less extent in the uncut quartz test, Figure 7.10. Here it can be seen that a layer of material has been effectively removed from the surface. It is not clear how or why this has occurred, but it is not unreasonable to assume that this is the hard nitrocarburised layer. For completeness, the low magnification micrographs of the spool are shown in Figures 7.14 to 7.16. Again many of the features described in Section 7.3 for the soft spool apply.
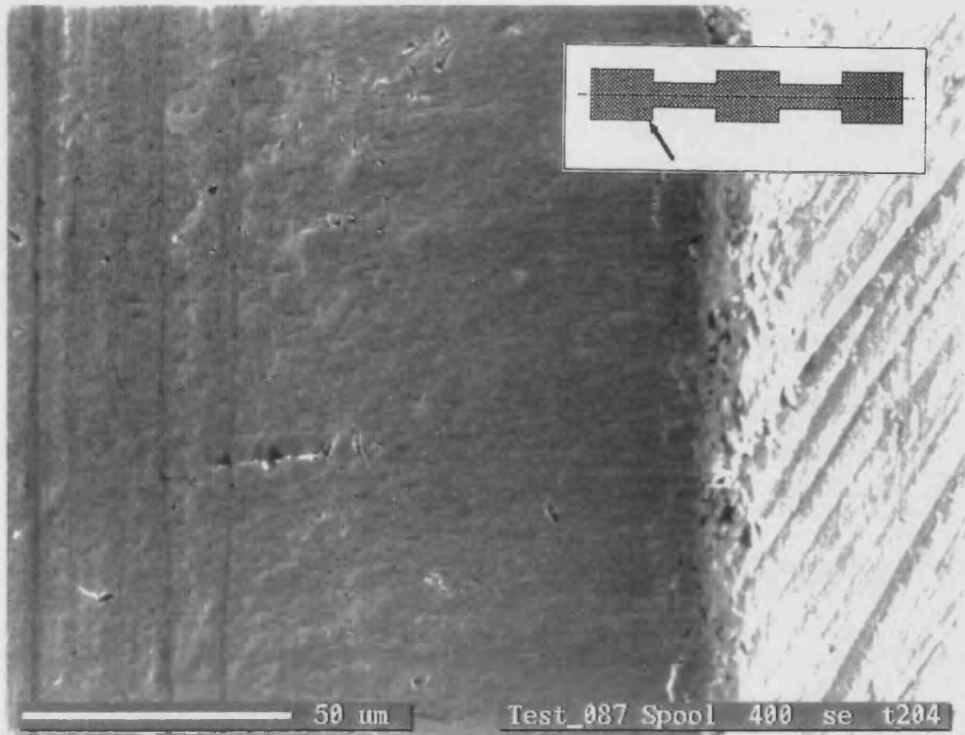
Figure 7.10 - SEM micrograph of nitrocarburised spool pressure land, uncut quartz.

Figure 7.11 - SEM micrograph of nitrocarburised spool pressure land, 0-10 μm quartz.

Figure 7.12 - SEM micrograph of nitrocarburised spool tank land, uncut quartz.

Figure 7.13 - SEM micrograph of nitrocarburised spool tank land, 0-10 µm quartz.
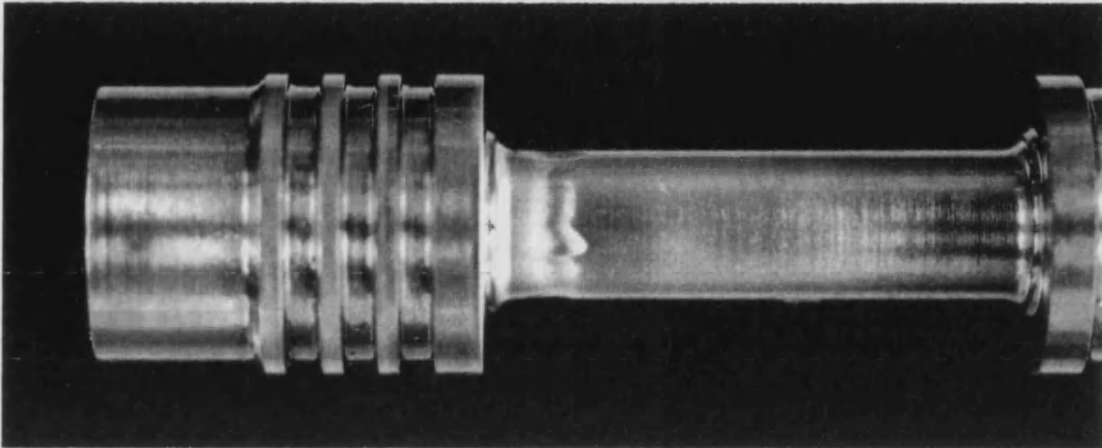
Figure 7.14 - Nitrocarburised spool pressure land following a uncut quartz test.
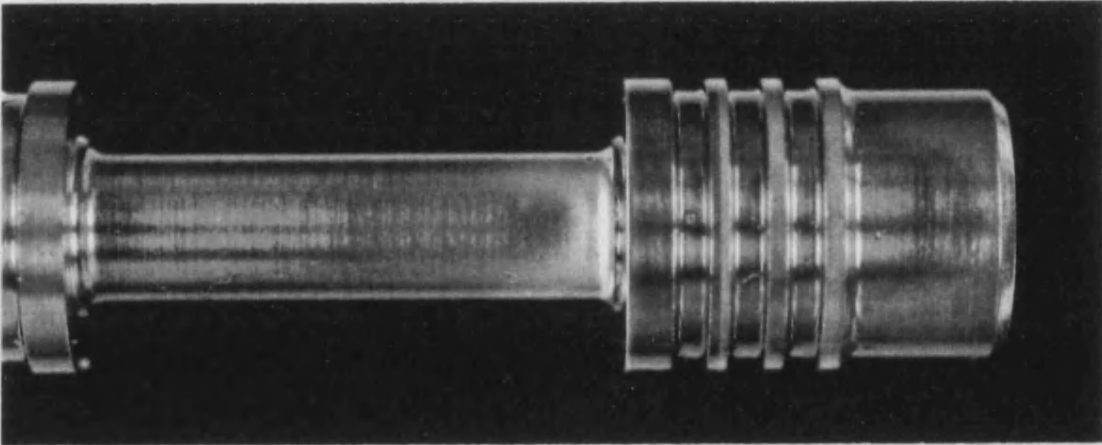

Figure 7.15 - Nitrocarburised spool pressure land following a 0-10 μm quartz test.
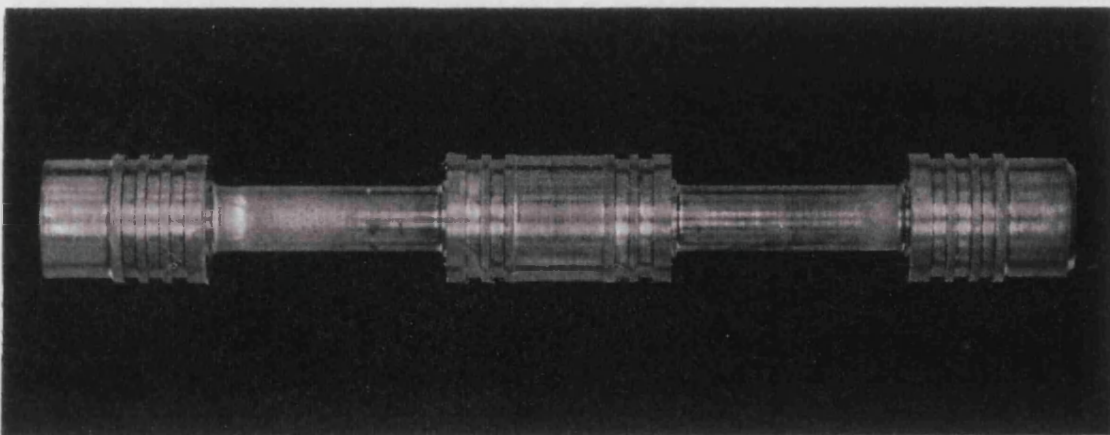
Figure 7.16 - Overall view of nitrocarburised spool after the completion of all four tests.

7.5.   Titanium Nitride Coated Spool

The results for the titanium nitride (TiN) coated spool testing are contained in Figure 7.17.
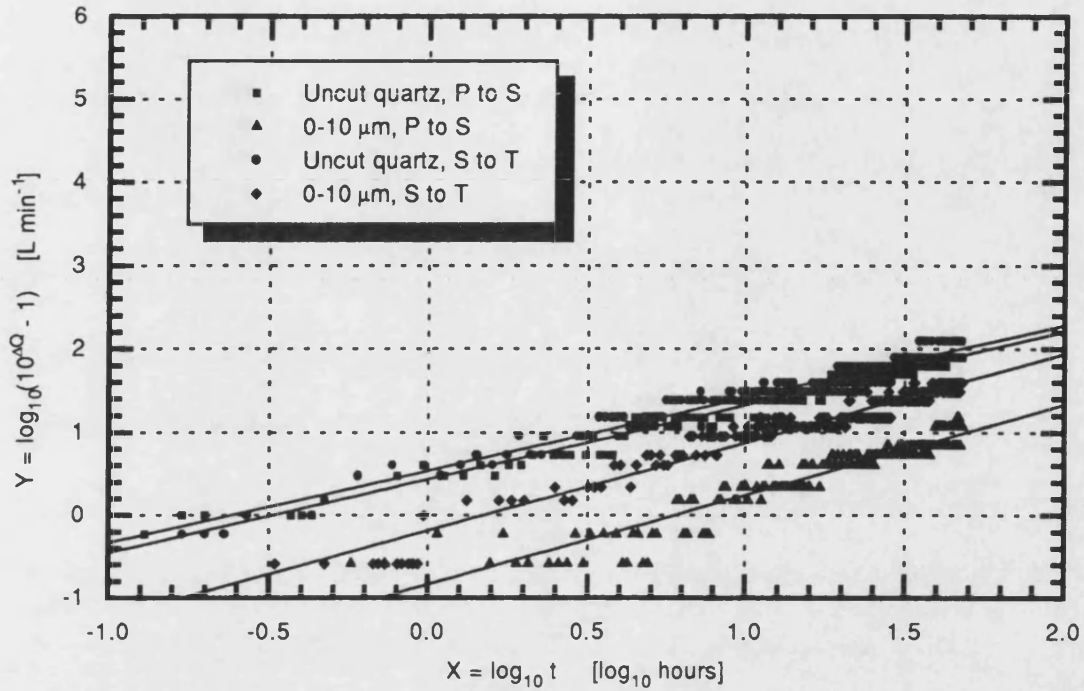
Test conditions - 70 bar differential   Contaminant concentration 10 mg L^{-1} of uncut and 0-10 μm
              Base oil grade 150N (32 cSt @ 40 °C) operating at 60 °C
              100 μm spool opening

Linearised data	Uncut, P→S	0-10 μm, P→S	Uncut, S→T	0-10 μm, S→T
A	0.434 ± 0.015	-0.839 ± 0.035	0.540 ± 0.018	-0.185 ± 0.021
B	0.888 ± 0.011	1.085 ± 0.026	0.874 ± 0.014	1.062 ± 0.016
R	0.981	0.945	0.973	0.974
SD	0.086	0.143	0.096	0.112
N	238	206	234	241

Figure 7.17 - TiN coated spool test results.

Applying the $\bar{t}$ comparison criterion to the linearised data gives the following:

$\Delta\bar{Q}_{Uncut\ quartz,\ P\rightarrow S} = 1.56$ L min^{-1} $\Delta\bar{Q}_{0\text{-}10\ \mu m,\ P\rightarrow S} = 0.63$ L min^{-1}

$\Delta\bar{Q}_{Uncut\ quartz,\ S\rightarrow T} = 1.64$ L min^{-1} $\Delta\bar{Q}_{0\text{-}10\ \mu m,\ S\rightarrow T} = 1.18$ L min^{-1}

The TiN result appears to give a significant improvement over the standard components by giving an average of 60% reduction in leakage flow. To confirm this result, profile measurements have

been conducted for the uncut quartz tests in both flow directions, these are contained in Figures 7.18 & 7.19.

From Figures 7.18 & 7.19 it can be seen that the spool wear profile has changed as suggested by the flow plots. The area of material removed for each test condition is shown in Table 7.2. The results indicate an improvement in the resistance of the surface to particle erosion, especially in the S→T case, where a 10:1 reduction has occurred.

Flow direction	Standard spool wear $[\mu m^2]$	TiN coated spool wear $[\mu m^2]$
P→S	433	90
S→T	1019	106

Table 7.2 - Effect of TiN coating on the amount of spool material removal.

Figures 7.20 to 7.23 contain a SEM micrograph for each of the spool metering edges. Unlike all the spools examined to date, the columnar wear patterns have been replaced by a ploughed surface localised at the corner. This confirms the profile maps which indicated that a slight rounding of the metering corner has occurred. When the corners were examined using EDX (energy dispersive analysis), the results indicated that a layer of TiN coating was still present.

The low magnification micrographs of the spool are shown in Figures 7.24 to 7.26. Unlike the soft and nitrocarburised spool, the spool appearance is unchanged except for a small area on the stem arising from the uncut quartz test on the pressure land. This area is assumed to be caused by the momentum of the large particles carried in the exit jet flow. This is shown pictorially in Figure 7.27, where assuming that the particles are carried by the fluid streamlines, a mean jet or impact angle has been calculated at 54° (total range of damage is between 45 and 70°). These angles are not unreasonable when compared to the classic 69° Von-Mises jet angle for a spool valve [54]. However, the optimum impact angle for maximum erosion will be 20 to 30° for a ductile material and therefore it is surprising that damage has resulted.
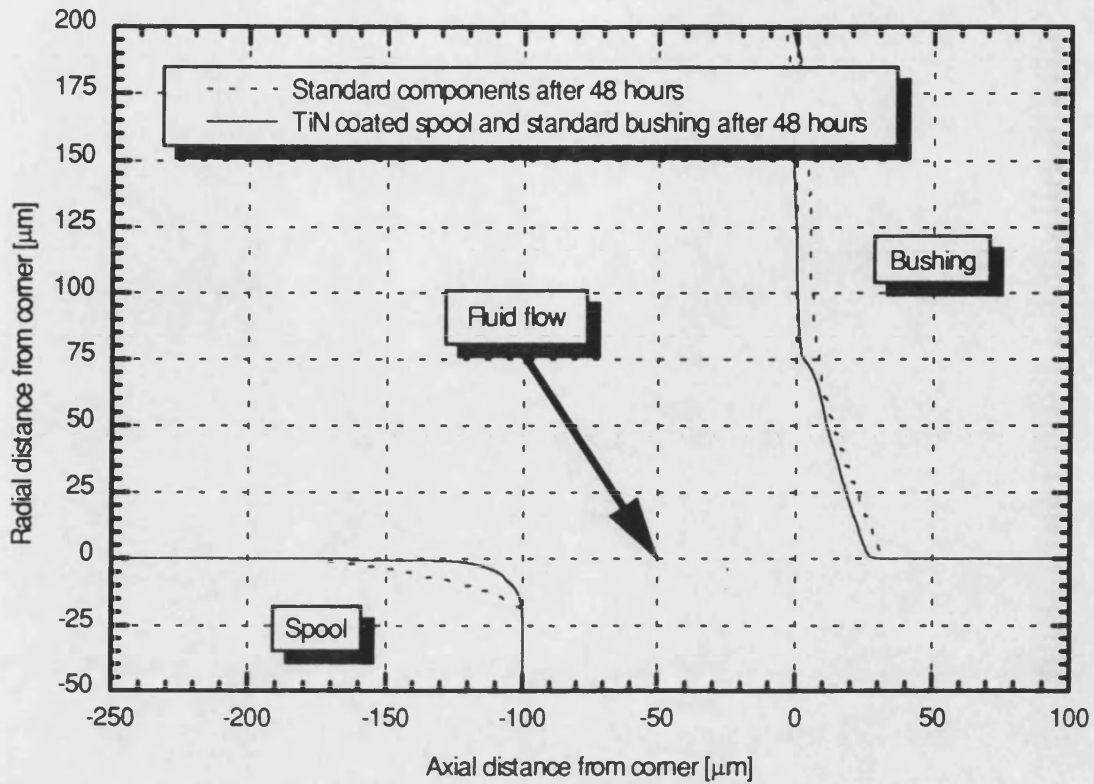
Figure 7.18 - TiN spool/bushings profiles, flow P to S with uncut quartz at 70 bar.
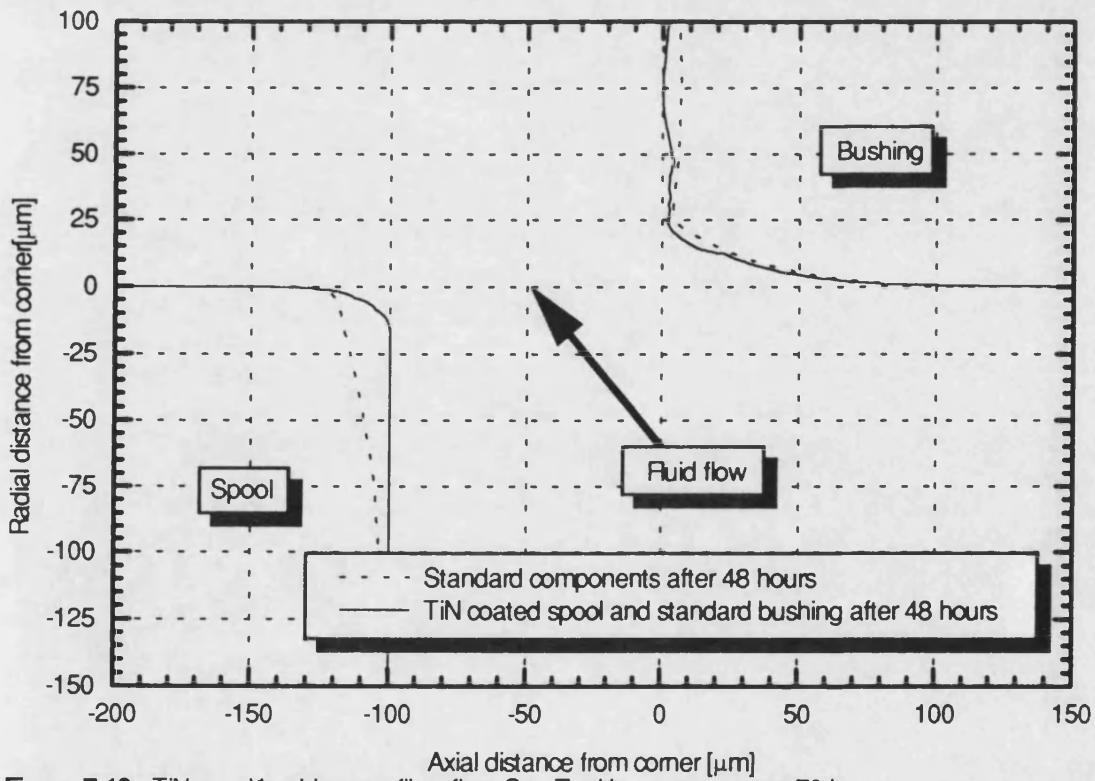
**Figure 7.19** - TiN spool/bushings profiles, flow S to T with uncut quartz at 70 bar.

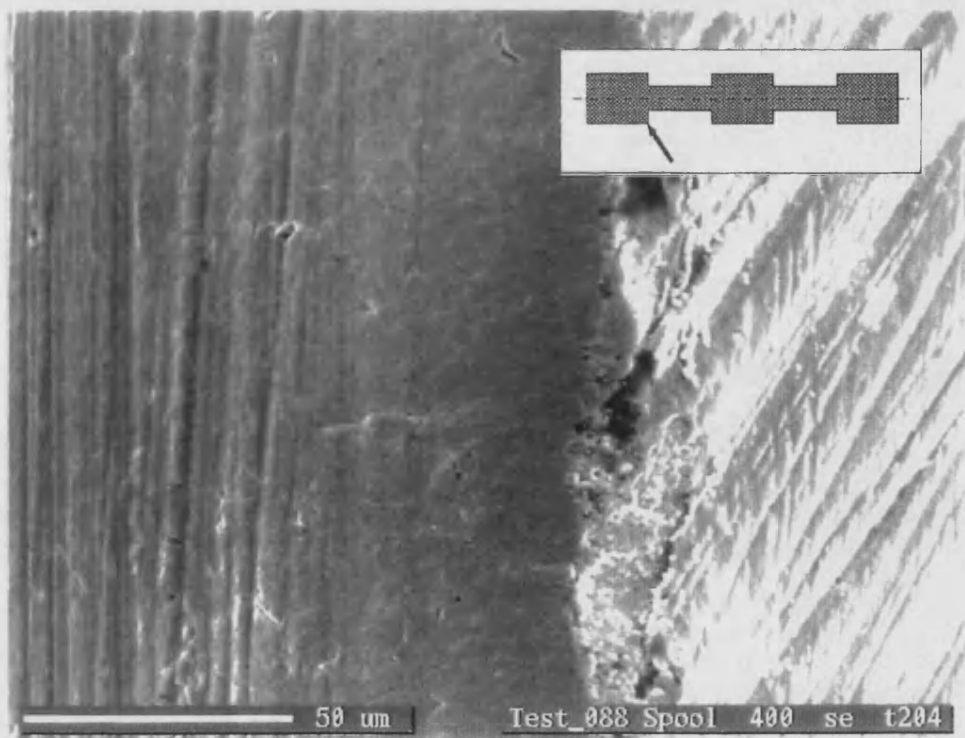**Figure 7.20 -** SEM micrograph of TiN coated spool pressure land, uncut quartz.

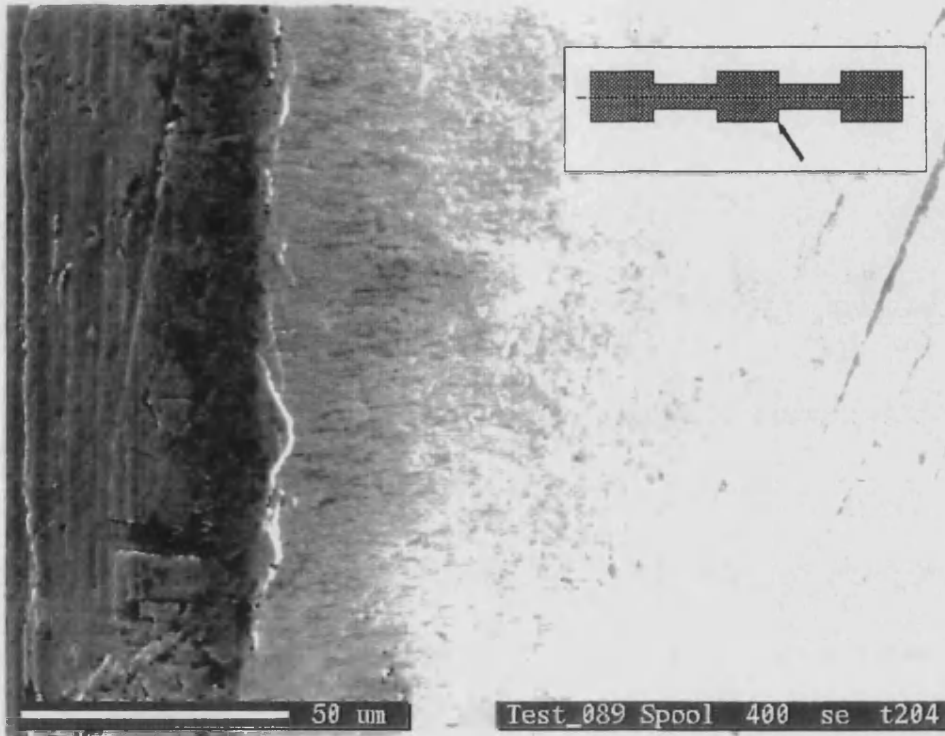**Figure 7.21 -** SEM micrograph of TiN coated spool pressure land, 0-10 µm quartz.

Figure 7.22 - SEM micrograph of TiN coated spool tank land, uncut quartz.

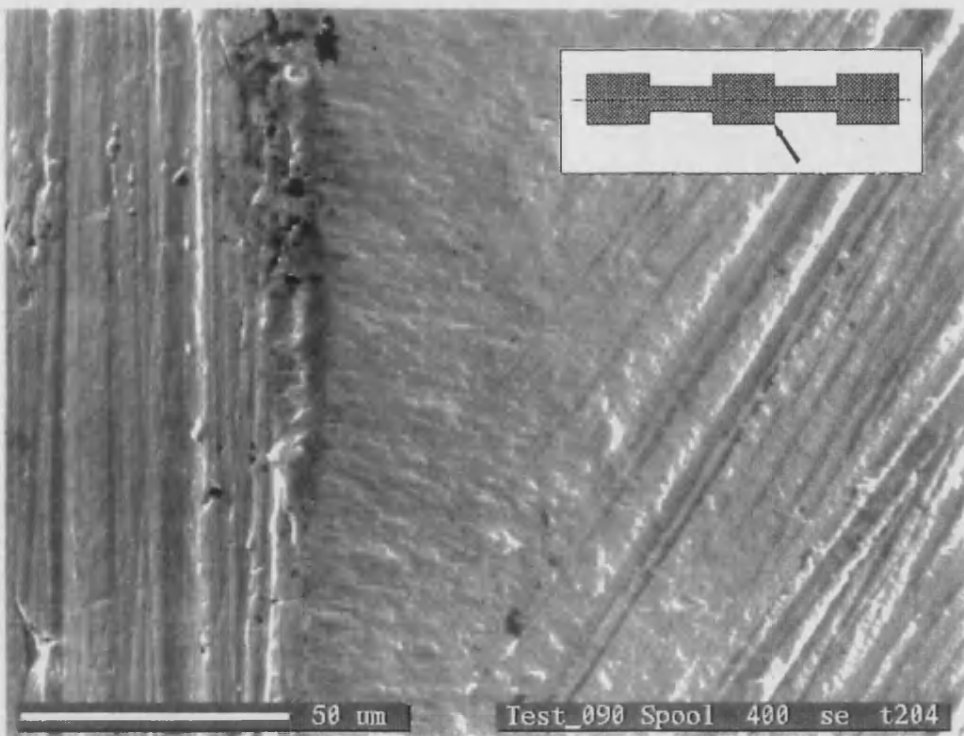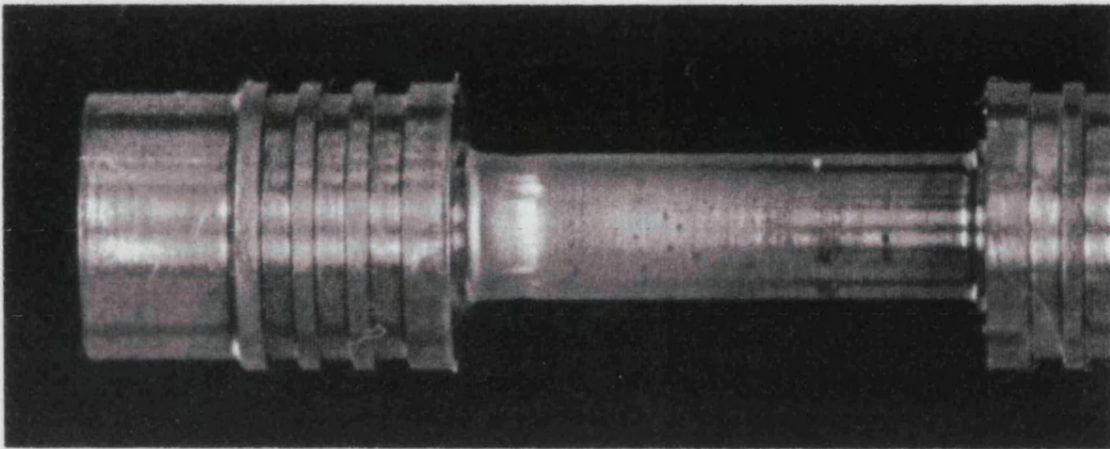Figure 7.23 - SEM micrograph of TiN coated spool tank land, 0-10 μm quartz.
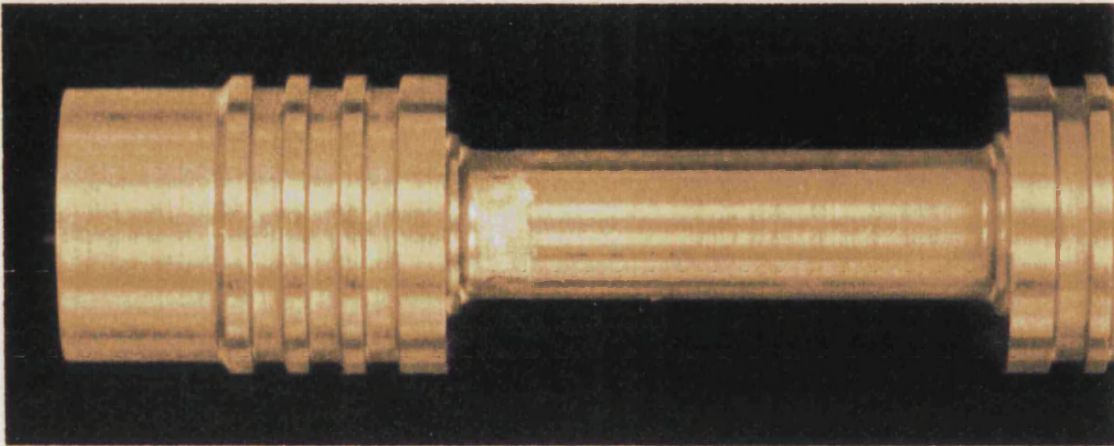
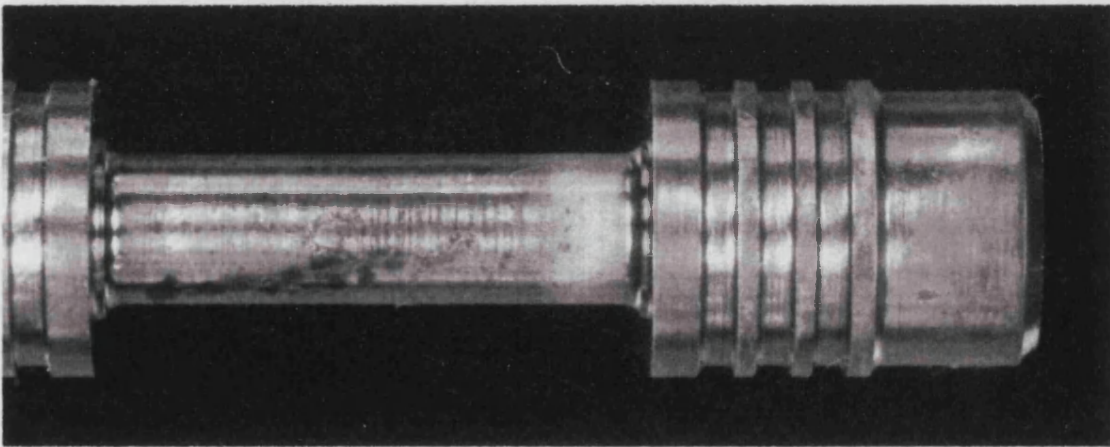**Figure 7.24** - TiN coated spool pressure land following a uncut quartz test.

**Figure 7.25** - TiN coated spool pressure land following a 0-10 μm quartz test.
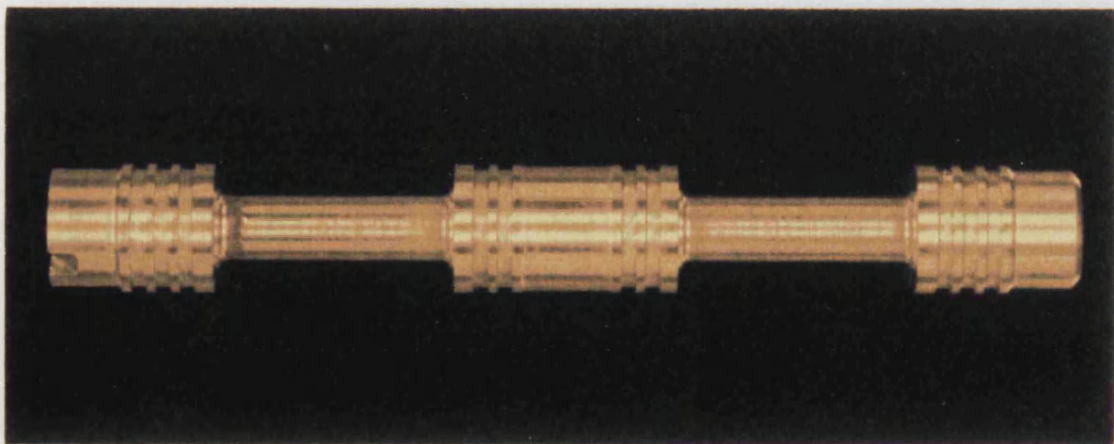
Figure 7.26 - Overall view of TiN coated spool after the completion of all four tests.
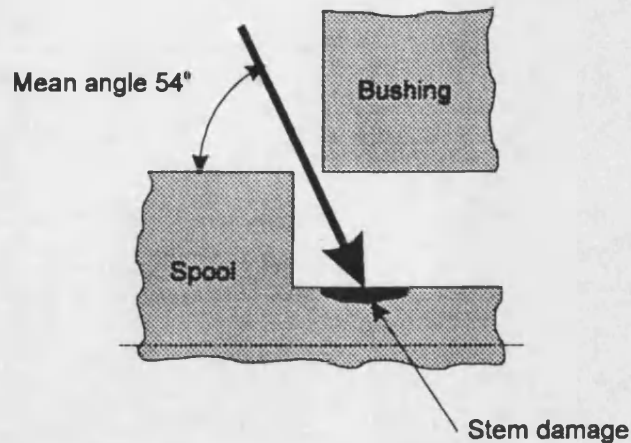
Figure 7.27 - Estimated particle impact angle.

7.6.   Ion Implanted Spool

The results for the ion implanted spool testing are contained in Figure 7.28.

Applying the $\bar{t}$ comparison criterion to the linearised data gives the following:

$$\Delta\tilde{Q}_{\text{Uncut quartz, P}\rightarrow\text{S}} = 3.76 \text{ L min}^{-1} \qquad \Delta\tilde{Q}_{\text{0-10 }\mu\text{m, P}\rightarrow\text{S}} = 1.49 \text{ L min}^{-1}$$
$$\Delta\tilde{Q}_{\text{Uncut quartz, S}\rightarrow\text{T}} = 3.82 \text{ L min}^{-1} \qquad \Delta\tilde{Q}_{\text{0-10 }\mu\text{m, S}\rightarrow\text{T}} = 2.04 \text{ L min}^{-1}$$

Comparing the $\Delta\tilde{Q}$ values for the ion implanted spool with the standard spool indicates that the results are statistically different and that on average the ion implantation gives a 15% reduction in the flow rate. An improvement is also found when compared to nitrocarburised test which is less hard and therefore supports the hypothesis that the wear rate reduces with material hardness. The ion implantation performance is surprising when it is considered that this improvement has been achieved by a very thin hard layer (typically 0.1 µm).

From the SEM micrographs Figures 7.29 to 7.32, and the low magnification micrographs Figures 7.33 to 7.35, the surface topography of the worn spool appears to be very similar to the standard material. However, the length of the wear scar extending from the corner is reduced as expected from the improvement in the flow plots.
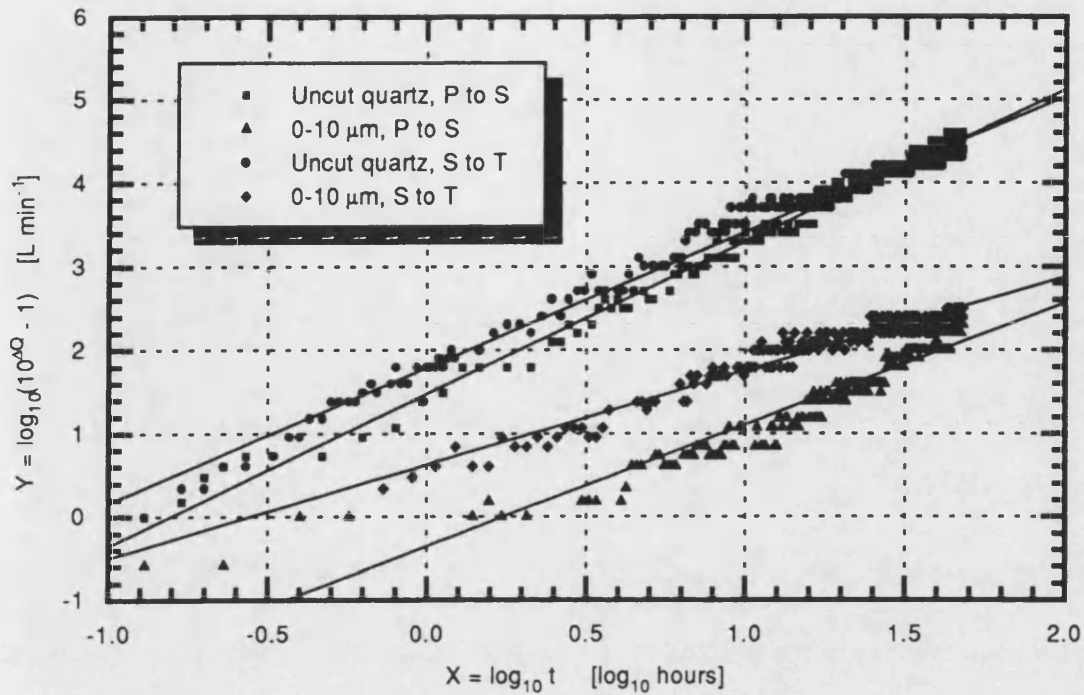
Test conditions - 70 bar differential Contaminant concentration 10 mg L^{-1} of uncut and 0-10 μm
         Base oil grade 150N (32 cSt @ 40 °C) operating at 60 °C
         100 μm spool opening

Linearised data		Uncut, P→S	0-10 μm, P→S	Uncut, S→T	0-10 μm, S→T
	A	1.472 ± 0.017	-0.355 ± 0.045	1.789 ± 0.017	0.626 ± 0.026
	B	1.824 ± 0.014	1.461 ± 0.033	1.623 ± 0.013	1.127 ± 0.020
	R	0.995	0.948	0.992	0.968
	SD	0.098	0.201	0.129	0.114
	N	223	219	253	218

Figure 7.28 - Ion implanted spool test results.
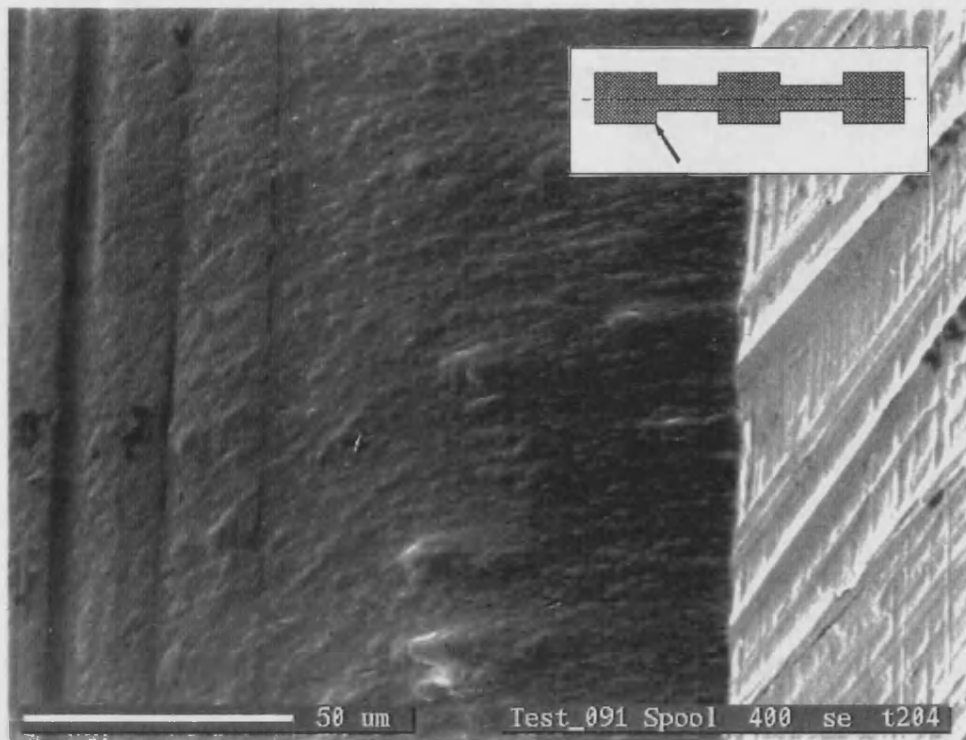
Figure 7.29 - SEM micrograph of ion implanted spool pressure land, uncut quartz.
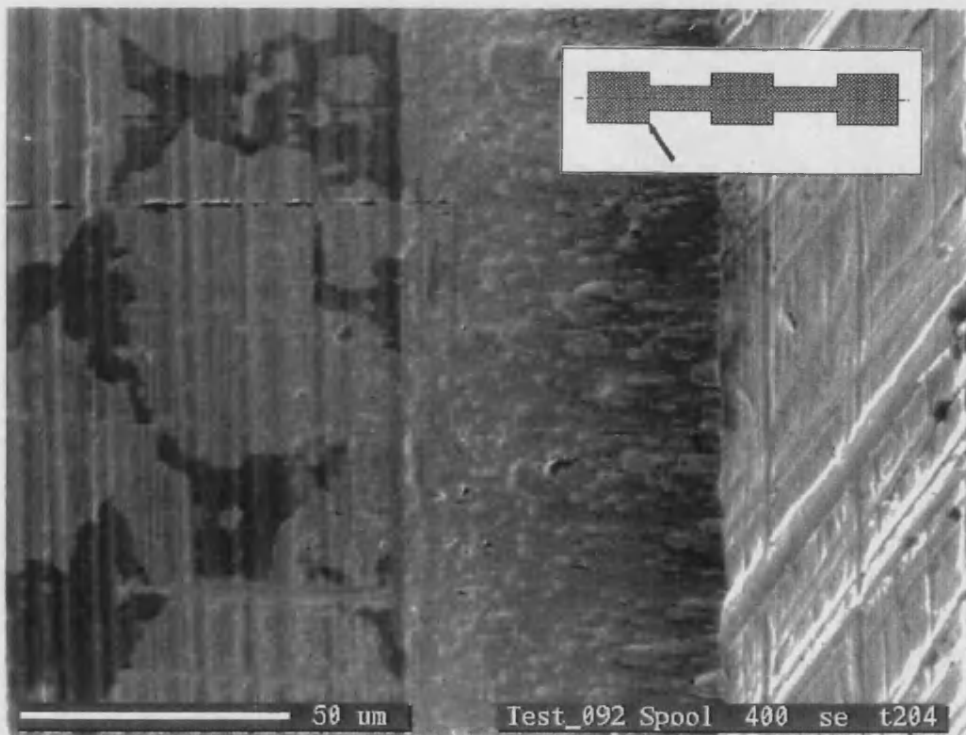
Figure 7.30 - SEM micrograph of ion implanted spool pressure land, 0-10 μm quartz.

Figure 7.31 - SEM micrograph of ion implanted spool tank land, uncut quartz.
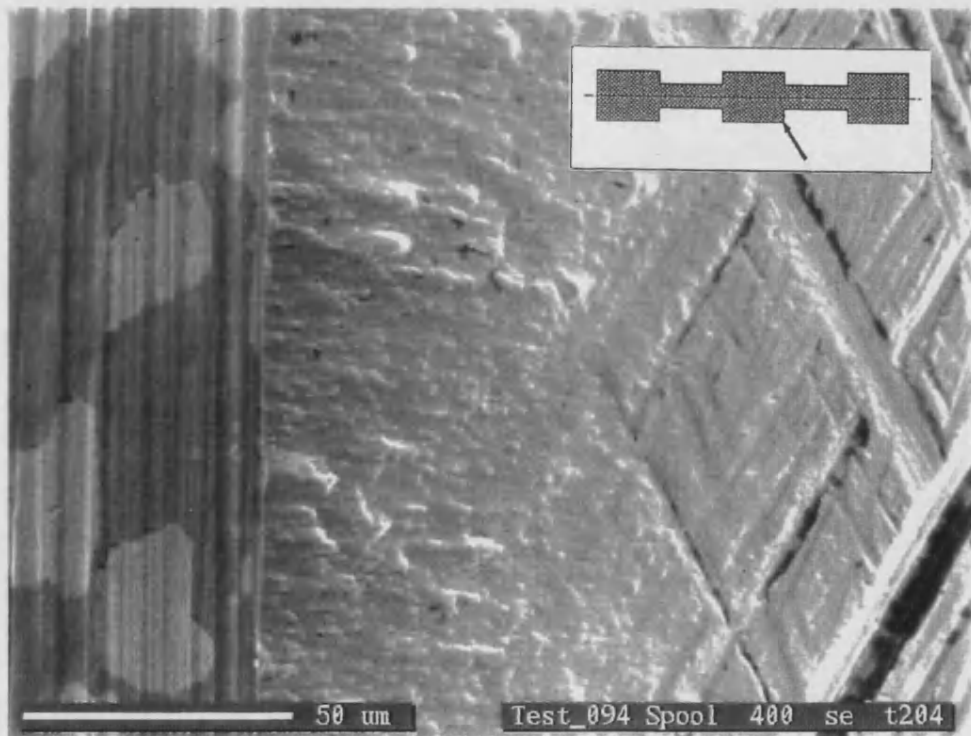
Figure 7.32 - SEM micrograph of ion implanted spool tank land, 0-10 μm quartz.
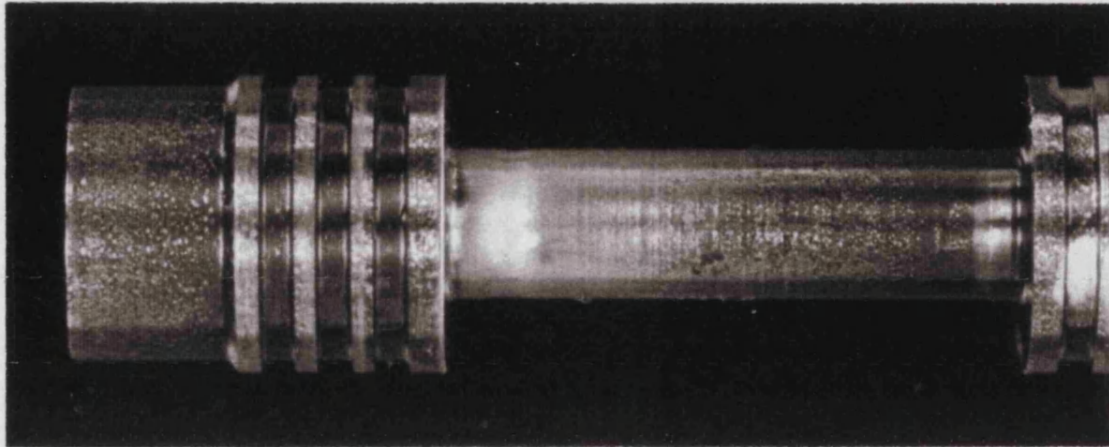
Figure 7.33 - Ion implanted spool pressure land following a uncut quartz test.
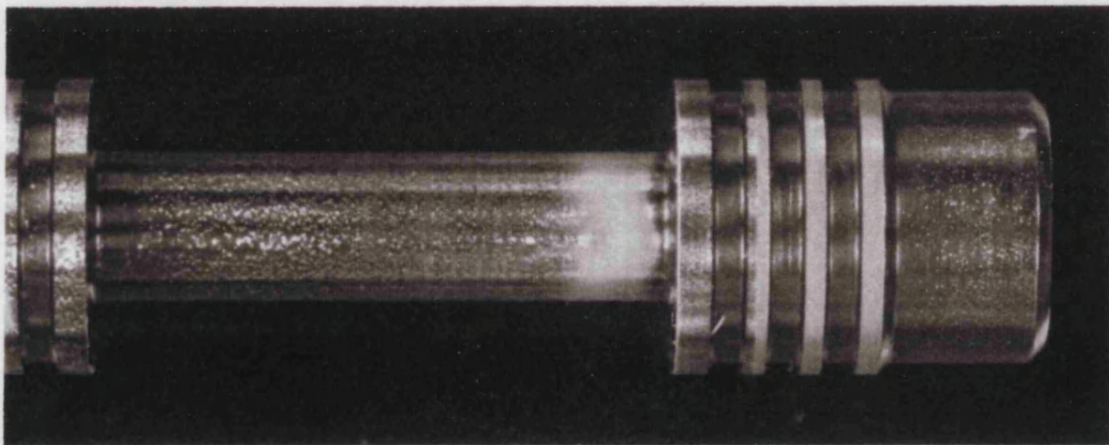
Figure 7.34 - Ion implanted spool pressure land following a 0-10 µm quartz test.
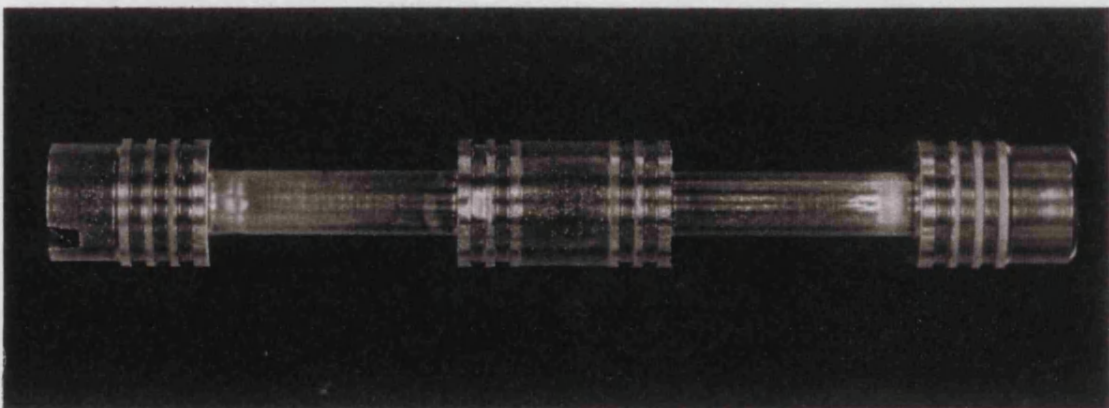
Figure 7.35 - Overall view of ion implantation spool after the completion of all four tests.

7.7. Tungsten Carbide/Carbide Coated Spool

The results for the tungsten carbide/carbide (WC/C) coated spool testing are contained in Figure 7.36.
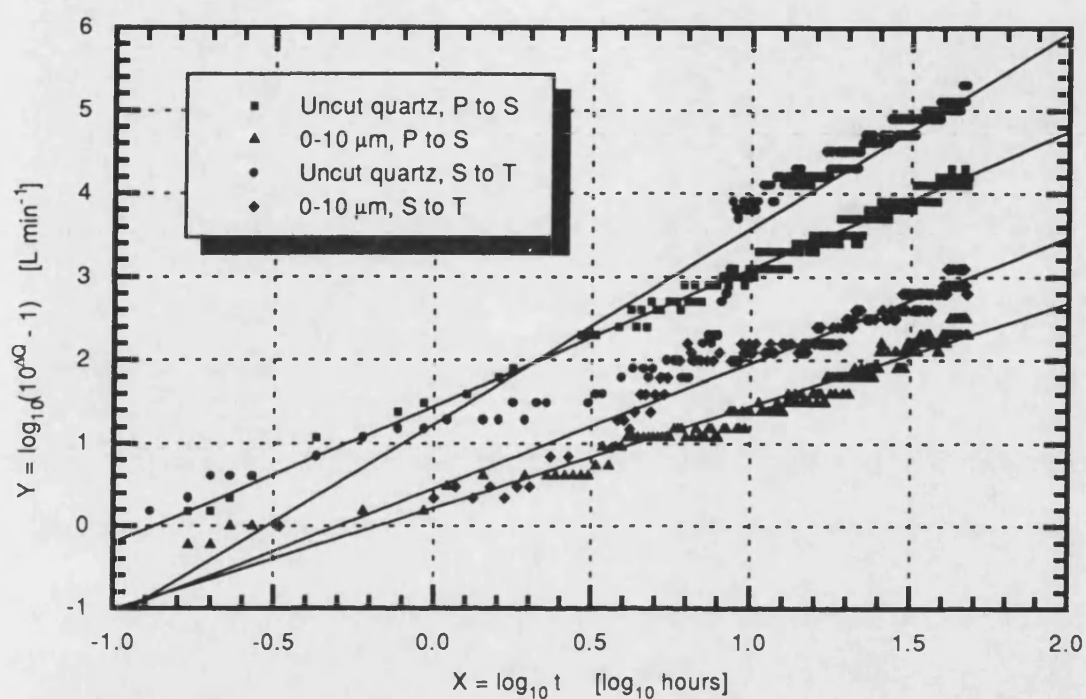
Test conditions - 70 bar differential   Contaminant concentration 10 mg L^{-1} of uncut and 0-10 µm
              Base oil grade 150N (32 cSt @ 40 °C) operating at 60 °C
              100 µm spool opening

Linearised data	Uncut, P→S	0-10 µm, P→S	Uncut, S→T	0-10 µm, S→ T
A	1.446 ± 0.018	0.218 ± 0.027	1.230 ± 0.068	0.452 ± 0.038
B	1.651 ± 0.014	1.233 ± 0.021	2.353 ± 0.052	1.512 ± 0.029
R	0.992	0.970	0.948	0.971
SD	0.088	0.141	0.415	0.151
N	237	229	237	168

Figure 7.36 - WC/C coated spool test results.

Applying the t̄ comparison criterion to the linearised data gives the following:

$\Delta\bar{Q}_{Uncut\ quartz,\ P\to S} = 3.52$ L min^{-1} $\Delta\bar{Q}_{0\text{-}10\ µm,\ P\to S} = 1.77$ L min^{-1}

$\Delta\bar{Q}_{Uncut\ quartz,\ S\to T} = 4.18$ L min^{-1} $\Delta\bar{Q}_{0\text{-}10\ µm,\ S\to T} = 2.35$ L min^{-1}
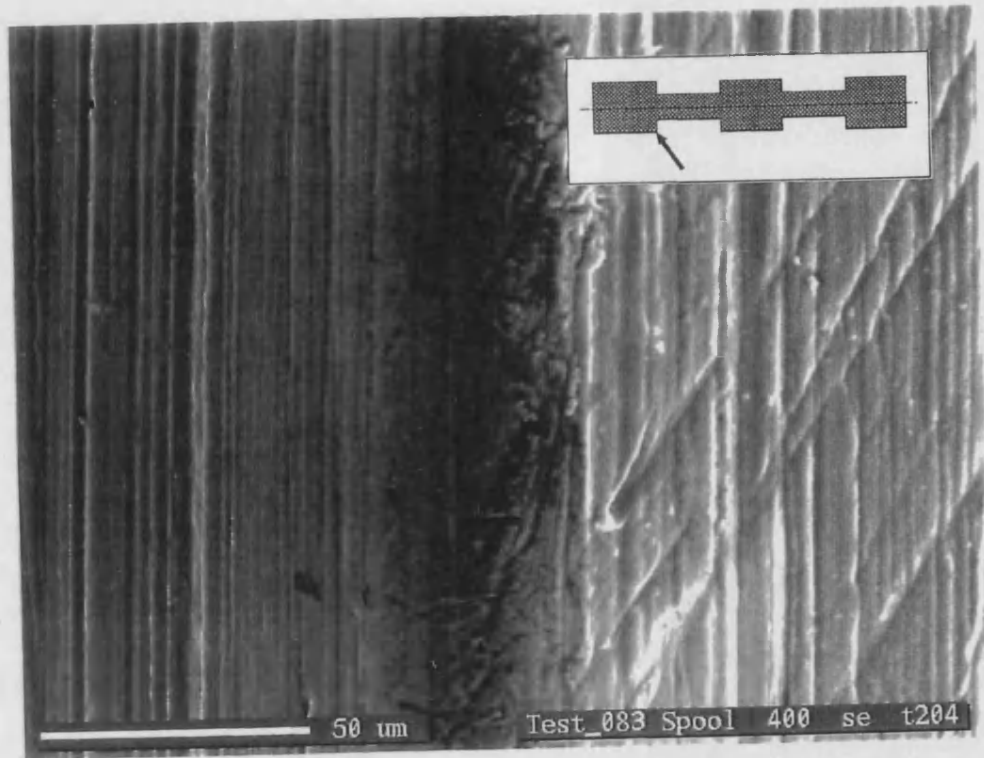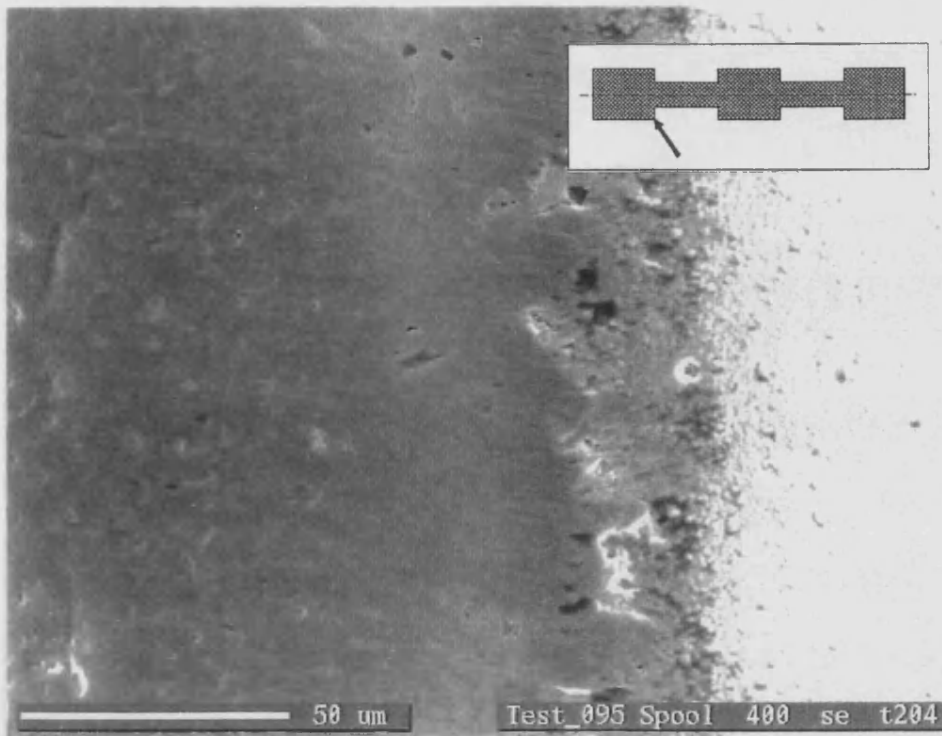
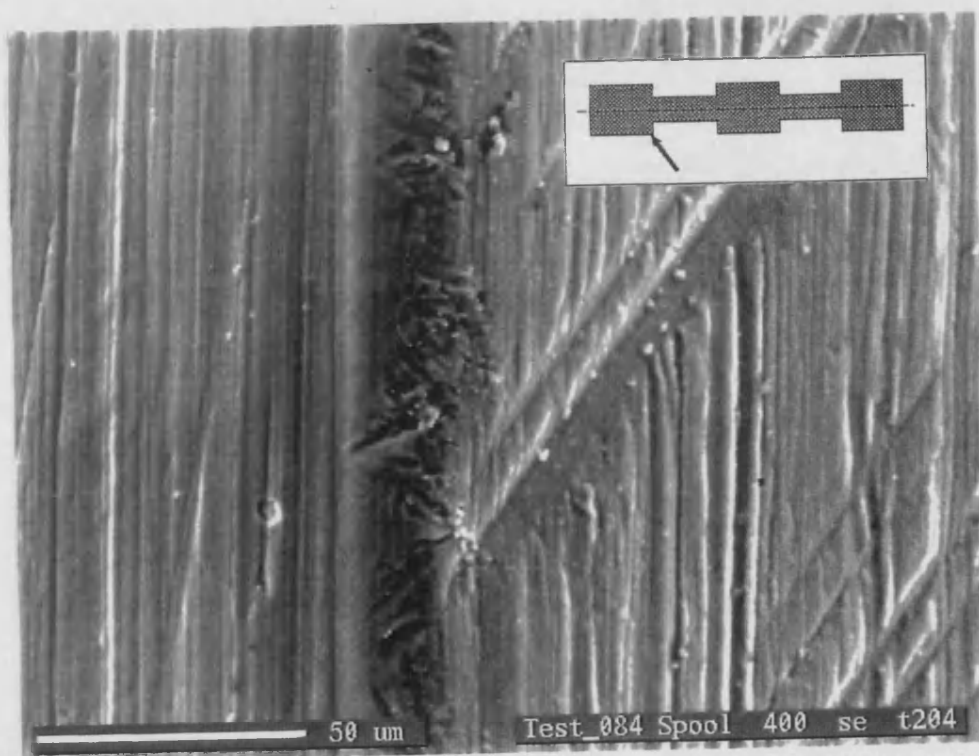**Figure 7.37** - SEM micrograph of WC/C coated spool pressure land, uncut quartz.
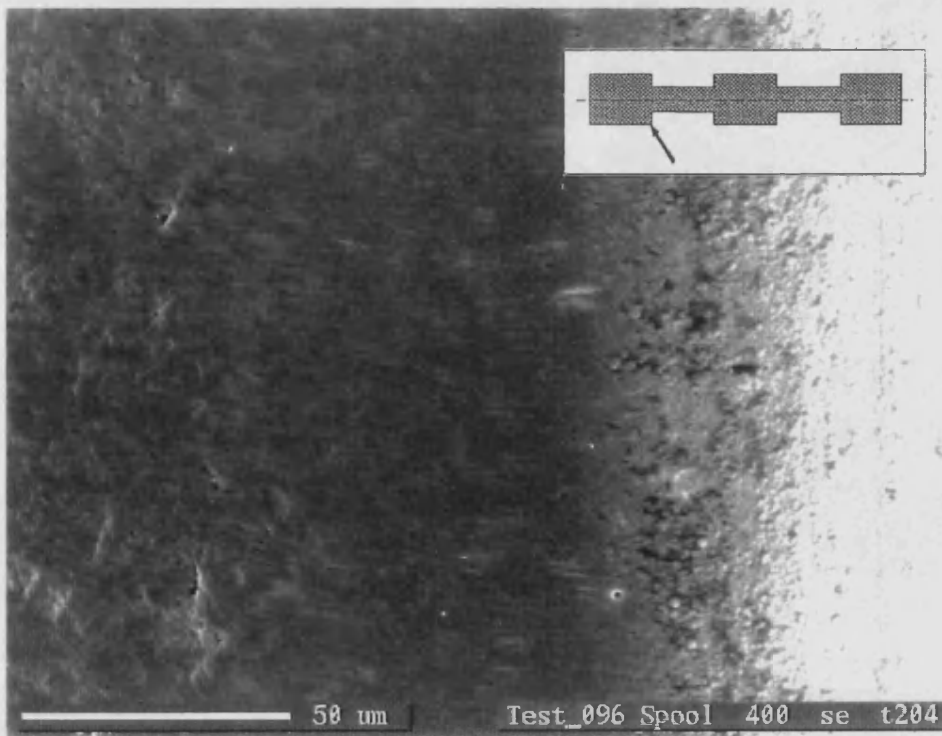
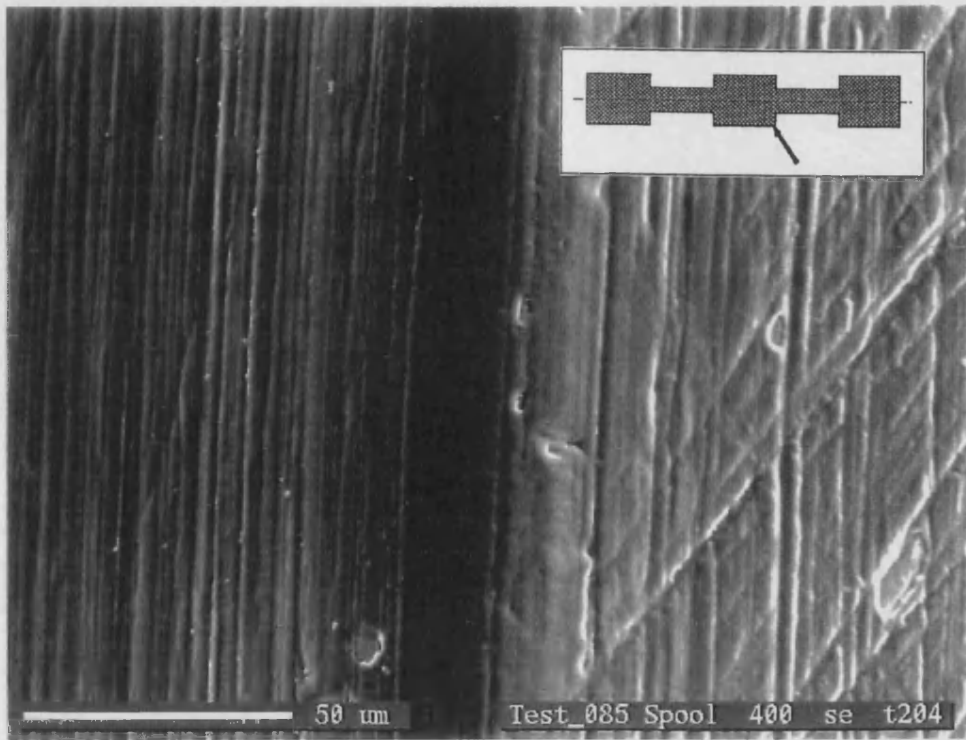**Figure 7.38** - SEM micrograph of WC/C coated spool pressure land, 0-10 μm quartz.
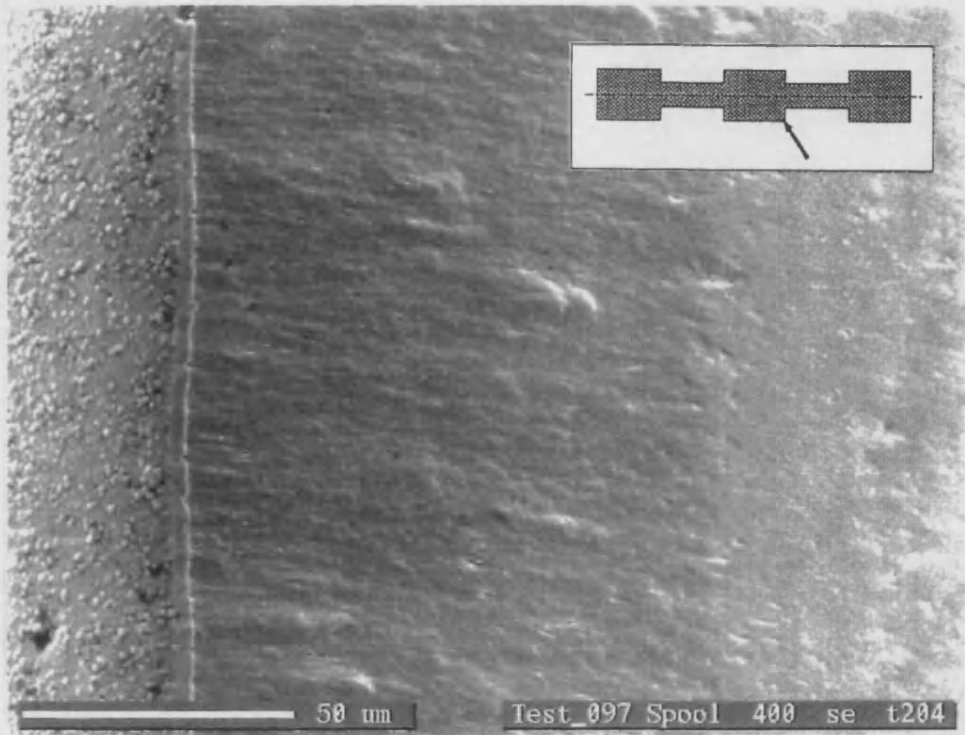
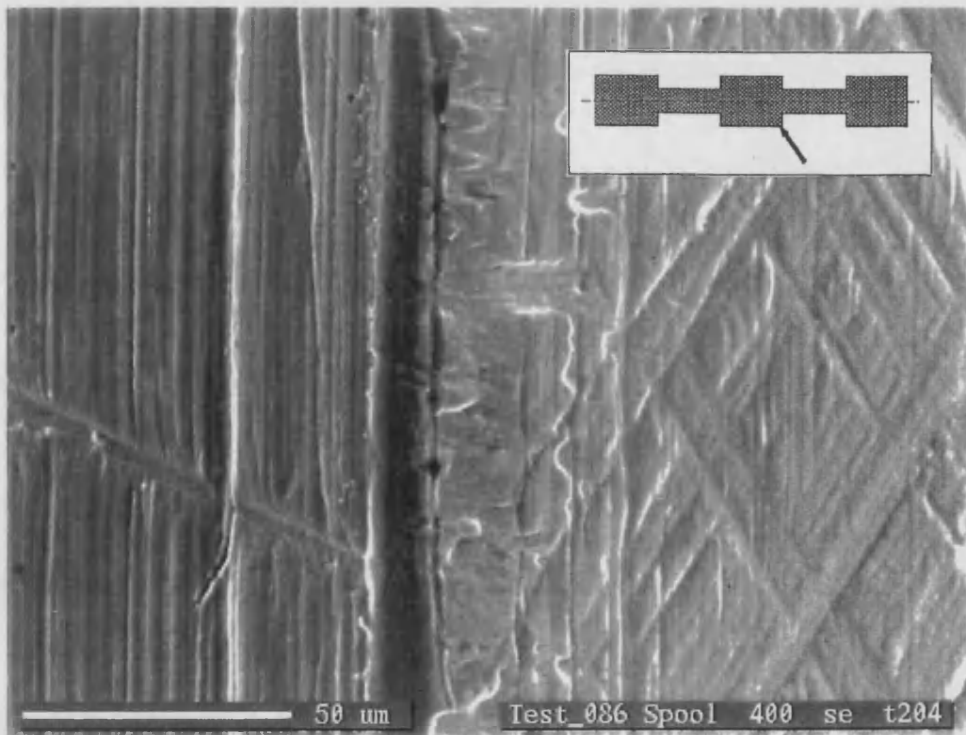**Figure 7.39** - SEM micrograph of WC/C coated spool tank land, uncut quartz.
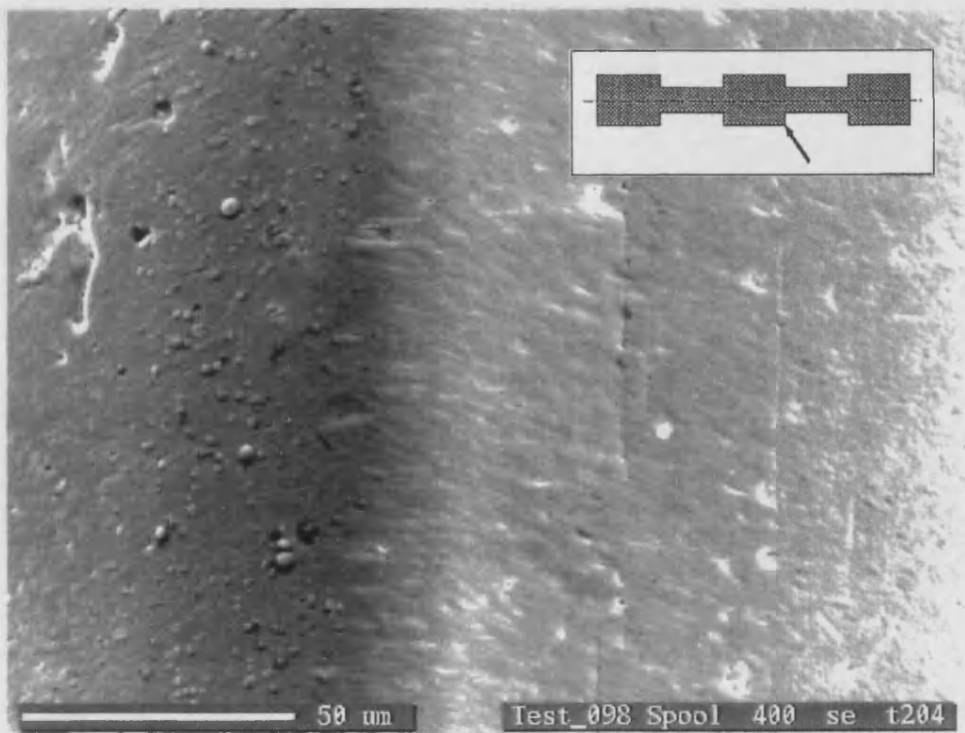
**Figure 7.40** - SEM micrograph of WC/C coated spool tank land, 0-10 μm quartz.
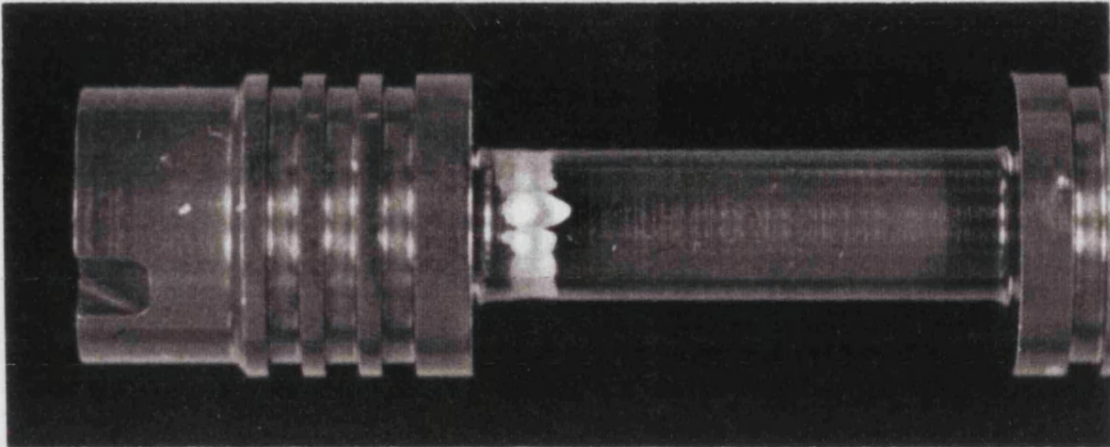
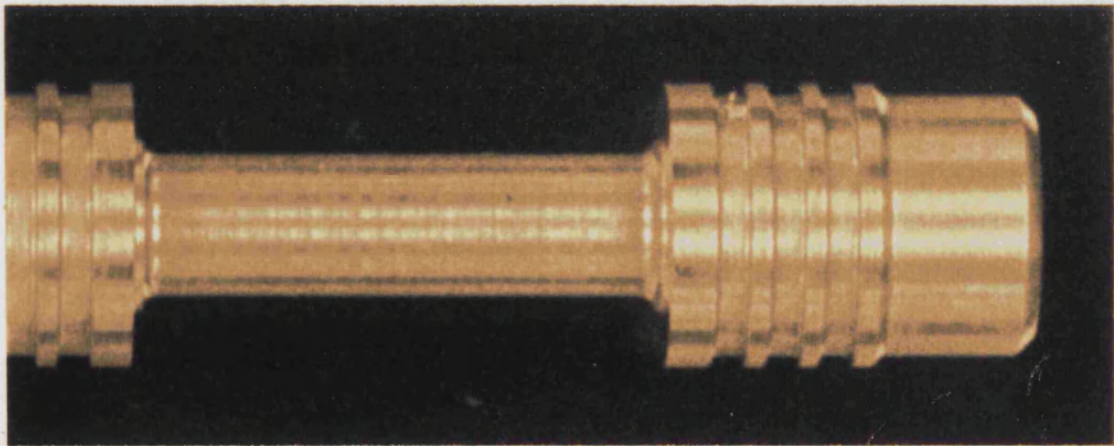**Figure 7.41** - WC/C coated spool pressure land following a uncut quartz test.
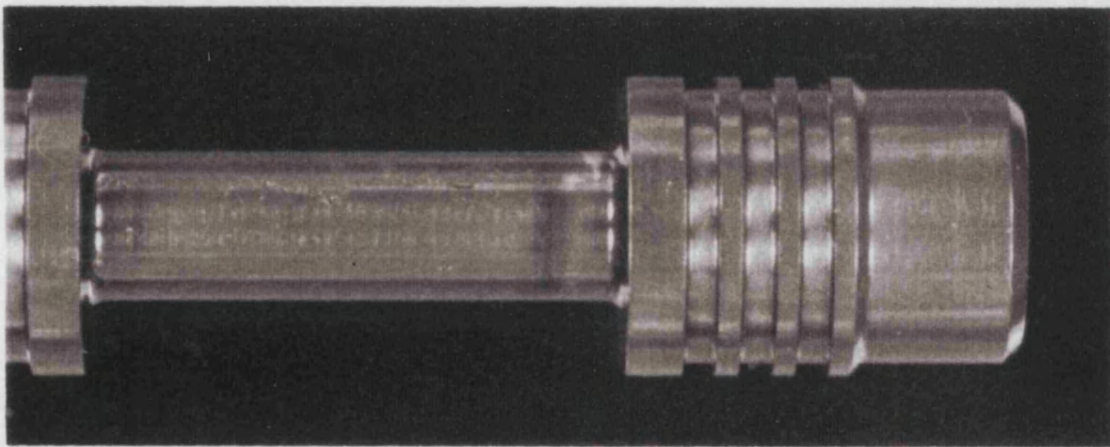
**Figure 7.42** - WC/C coated spool pressure land following a 0-10 μm quartz test.
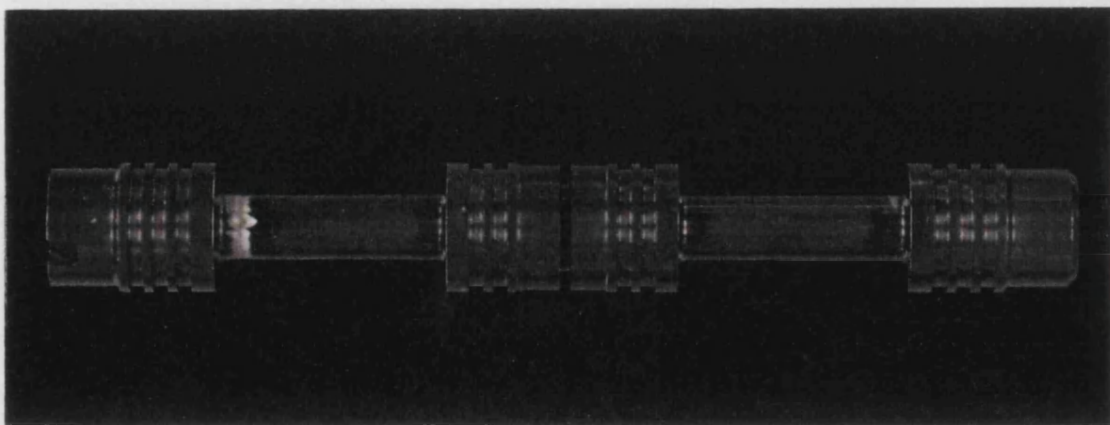
Figure 7.43 - Overall view of WC/C coated spool after the completion of all four tests.

From the P→S results, a 12% reduction in flow rate has been achieved when compared to the standard material. This is not surprising since the WC/C coating is sufficiently harder than the standard material and therefore should provide better wear resistance. However, analysis of the S→T results on this basis is not valid due to the step change in the results, Figure 7.36. The results indicate that initially an improvement over the standard material was being achieved until an apparent step change in the flow rate occurred at X = 0.9. Since this occurred on both quartz tests, it is reasonable to assume that it is a function of the spool coating and the flow direction. From the SEM Micrographs Figures 7.37 to 7.40, it appears that the coating has been removed since the surface topography has a columnar structure. This highlights a common problem with surface coatings, where often the performance is dependent on the bonding between the coating and the parent material and not the properties of the surface coating.

Finally, the low magnification micrographs for the WC/C coated spool are included in Figures 7.41 to 7.43. The salient features of the worn spool are similar to the TiN coated spool, where the only visible damage occurs on the spool stem after completion of the uncut quartz test.

7.8. Conclusions

From Table 7.3 it can be seen that apart from the S→T, soft spool result, the performance increases with material hardness as suggested in the established literature. Comparing the percentage flow change with the hardness ratio H_p/H_s confirms that a significant improvement is made when the ratio is less than one. Therefore, for the surface engineering techniques examined the TiN is the clear performance leader.

From the TiN tests, it has been calculated that the flow jet angle in the P→S configuration is approximately 54° to the axis of the spool. However, this may be considered an underestimate if the fluid streamlines carry the particles away from the side face of the spool.

Finally, the results have illustrated that it is possible to apply various surface treatments and coatings to a precision component whilst retaining the required dimensional tolerances. The problems of bonding between the surface coating and the bulk material have been observed. The TiN coating looks an attractive process for future developments. This work will require the application of the coating to the bushing bore and an assessment of its performance where both abrasion and erosion are present. Ultimately the material selection will be based on the trade off between financial implications and the extra performance gained.

Spool type	Estimated spool hardness		Hardness ratio H_p/H_s	% change in $\Delta \dot{Q}$ compared with standard spool
	H_v	GPa		
Standard	650	6.4	1.25	---
Soft	400	3.9	2.05	P→S + 25.5 % S→T - 16.5 %
Nitrocarburised	900	8.8	0.91	- 12 %
TiN	2500	24.5	0.33	- 60 %
Ion implantation	880	8.6	0.93	- 15 %
WC/C	1000	9.8	0.82	- 12 %

Table 7.3 - Material performance summary.

8

Mathematical Modelling of Spool Valve Wear

8.1. Introduction

This chapter reviews the literature relating to erosive wear with a view to identifying the fundamental principles of particle erosion and applying these to the wear of spool valves

The formulation of alternative theoretical/empirical based models specifically for erosive wear in spool valves is proposed. Where possible, the results are used to validate the various parameters used in the analysis.

8.2. Established Erosive Wear Models

It was shown in Chapter 2, that very little material exists on the erosive wear mechanism within hydraulic control valves. However, if the search restraints are relaxed to include the erosion wear mechanism in general, the problem becomes a sorting/data reduction exercise to determine the possible application of the numerous ideas to the hydraulic valve problem. As a consequence, it has not been easy for the valve manufacturers to assess the contaminant sensitivity performance of their products.
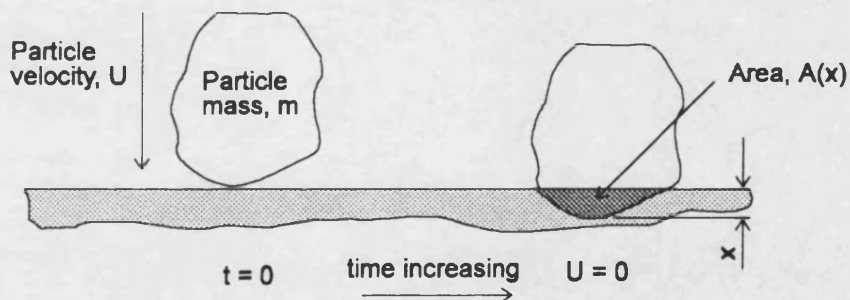
Figure 8.1 - Simplified ductile erosion diagram.

To begin, consider the motion of a single particle towards a target surface as shown in Figure 8.1. Assuming the particle does not deform and that the target surface remains plastic with a constant indentation pressure H_s, it is possible to derive the equation of motion for the particle as:

$$m_p \frac{d^2x}{dt^2} = -H_s A(x) \qquad \dots (8.1)$$

Where $A(x)$ is the cross sectional area of the surface indentation at an instance in time t. Hence, at the instance when the particle comes to rest at a depth x_{max}, the work done will be equal to the kinetic energy of the particle at impact which assuming an initial particle velocity, U_p, can be determined from:

$$\int_0^{x_{max}} H_s A(x) \, dx = \frac{1}{2} m_p U_p^2 \qquad \dots (8.2)$$

The volume of the surface indentation is given by:

$$\int_0^{x_{max}} A(x) \, dx \qquad \dots (8.3)$$

Since H_s has been assumed to be constant, from Equations 8.2 and 8.3 the indentation volume becomes:

$$Indentation \ volume = \frac{m_p U_p^2}{2 H_s} \qquad \dots (8.4)$$

From Equation 8.4 it is now possible to calculate the indentation volume caused by the particle striking the target material. Unfortunately, for the surface to accommodate this volume, two possible outcomes can arise. Firstly, the material surrounding the indentation can plastically deform internally or alternatively, a lip may be formed at the surface. Secondly, the material can be removed in the form of wear debris. In practice, it is likely that a combination of these processes will exist and therefore only a certain proportion (k) of the indentation volume becomes wear debris. Therefore, introducing k and the density of the target material ρ_s into Equation 8.4, it is possible to determine the mass of the material removed:

$$Mass \ of \ material \ removed = k \, \rho_s \, \frac{m_p U_p^2}{2 H_s} \qquad \dots (8.5)$$

Applying Equation 8.5 to the condition where the surface is subjected to multiple impacts, the model suggests that the mass of material removed will be proportional to the number of particles striking the surface. This linear relationship between the mass of material removed and the number of impacting particles leads to the commonly used definition of erosion, E.

$$E = \frac{\text{mass of material removed}}{\text{mass of erosive particles striking the surface}} \qquad \text{.... (8.6)}$$

This definition has been verified by various authors [68 - 70] by recording the mass of the target specimen before and after being subjected to a given mass of impinging particles. In most cases the particles are accelerated by a gas stream within a nozzle assembly onto the target surface positioned at the required orientation in the exit jet stream. This method is very popular for erosion testing since it gives a quantitative and comparative result. It has the advantage that the influence of the carrier fluid can be neglected and the resulting wear can be directly attributed to both the particle and the target material properties.

Unfortunately, the simple relationship developed in Equation 8.5 for the erosion mechanism does not tell the full story and numerous authors have shown that the derivation of a comprehensive erosion wear model is dependent upon many variables. These may grouped into three distinct categories:

i)   The properties of the particles.

ii)   The properties of the target material.

iii)   The properties of the carrier fluid.

8.2.1. Particle Properties

From Equation 8.5 it can be seen that the particle mass and velocity appear in the derivation. Obviously, the mass is dependent upon the density of the material, but more importantly, on the size of the particle. The effect of particle size is important since the volume changes with the cube of the diameter. For example, the difference between a 10 and a 100 μm diameter particle gives a 1000 times increase in the mass and hence the energy of the particle. However, the influence of velocity on the wear rate is generally accepted as not being proportional to the square of the velocity, but is higher order. The dependence on the velocity is often expressed as Equation 8.7

$$E \, \alpha \, U_p^n \qquad \text{.... (8.7)}$$

For example, Hutchings [71] survey of published material suggested that n varies between about 2.3 and 3.0 and not 2.0 as predicted by simple models. Hutchings also indicated that $n \approx 2.4$ for ductile materials at or close to the impact angles that cause the maximum erosion rate.

The influence of the particle impact angle on the erosion rate was introduced in Chapter 1, Figure 1.3. This work by Bitter [18] is frequently referenced as one of the early examples of a

comprehensive erosion model which shows clearly the dependence of impact angle for a ductile and brittle material. The work indicated that a ductile material has a maximum erosion rate at angles of 20 to 30°, whilst the corresponding point for a brittle material is at 90°. This difference has since been confirmed by other authors [71 - 73] and with an improved understanding of the problem, has created two distinct generic wear model families: ductile and brittle. For the ductile material, the wear occurs due to a combination of ploughing and micro-machining, whilst the brittle material fails from the action of brittle fracture.

In addition to the above features, other researchers have concentrated upon the size, shape, composition, hardness, etc, of the actual particles. For example, Bahadur & Badruddin [47] characterised the geometric properties of different test dusts to examine their influence on the erosion rate. These studies indicated that a linear relationship between the erosion rate and the average area diameter exists until a certain cut-off size produces no further increase in erosion. This cut-off size, or erosion saturation point occurs at 30 μm for aluminium oxide and 50 μm for silicon carbide particles with a maraging steel target ($H_v \approx 550$). Unfortunately, no results are included for the silicon oxide particles in the 0 to 100 μm, although results for the 300 to 500 μm range indicate that the erosion rate decreases with size. Bahadur & Badruddin suggested that this result contradicts other published literature such as Misra & Finnie [73] who found that the particle erosion became less efficient below a general threshold of 100 μm. Below which, the erosion rate decreased significantly with particle size.

In addition to size, Bahadur & Badruddin [47] found that when the erosion rate is plotted logarithmically against particle aspect ratio, an inverse proportional characteristic is found. This result suggests that a long thin particle produces more wear than a rounded particle and confirms the established opinion that micro-machining/micro-cutting is a dominant mechanism in the erosive wear process.
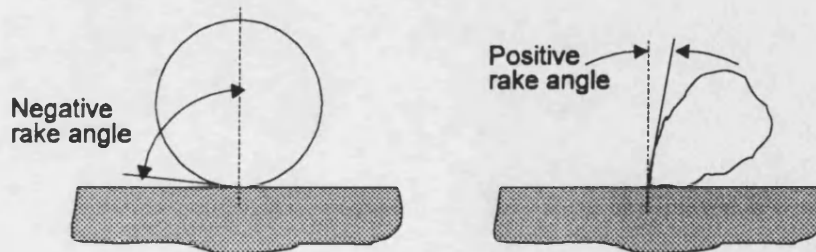
Figure 8.2 - Negative and positive rake angle for an impacting particle.

The role of particle shape and the influence of rake angle on ploughing and micro-cutting has been examined by Winter & Hutchings [46]. They concluded that micro-cutting was favoured by positive or small values of negative rake angles while ploughing occurred with large negative rake angle. In this context, the definition of rake angle is taken to be the angle between the perpendicular to the target surface and the leading edge of the impacting particle, as shown in Figure 8.2.

For spherical particles impacting onto a surface, a ploughing action (see Figure 8.3) is the only possible mechanism since a negative rake angle must be present at each impact. However, the result is not so clearly defined when irregular particles are considered, since not only does the shape of each particle differ, but also the possible orientation at the point of impact is unknown. Therefore, considering the random impact possibilities for irregular particles suggests that both a ploughing and micro-cutting action must be present. This effect has been confirmed from the studies of Bahadur & Badruddin [47] who suggested that silicon oxide particles produce more ploughing than micro-cutting, which contradicts the work of Winter & Hutchings [46] who concluded that cutting is dominant.

From the above discussion, the evidence suggests that the wear process associated with the irregular particles (quartz and ACFTD) used for the valve erosion work may be dominated by a micro-cutting action. However, there are two other aspects commonly reported which will affect the magnitude of the machining process. The first is the tendency for the particles to role along the surface after the initial impact collision and the second is the effects of particle fragmentation.

Ploughing   Type 1 cutting   Type 2 cutting
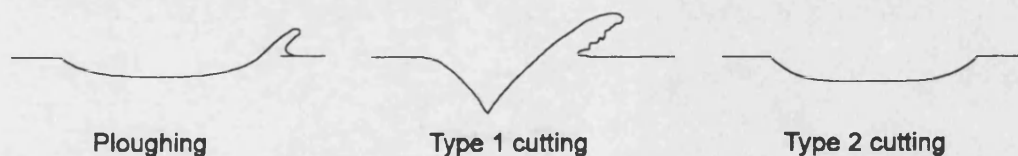
Figure 8.3 - Influence of particle rotation on the micro-cutting process (From [71]).

Hutchings [71] has graphically illustrated the effects of irregular particles rotating forwards and backwards after the initial impact. The difference between the two possibilities shown in Figure 8.3 (From [71]) is described as *type 1 cutting* and *type 2 cutting*. In the *type 1 mode*, the material is formed into a prominent lip which can be easily removed by subsequent particles. Alteratively, in the *type 2 mode*, the sharp tip of a particle cuts a chip of the material away as it rotates backwards in a similar manner to a conventional machine cutting tool. The chosen mode is governed by the centre of gravity and the orientation of the particle at the point of impact.

Hutchings concluded that *type 2 cutting* only occurs over a narrow range of particle geometries and impact conditions.

The erosion process can also be affected by a particle fragmentation process. The work in this area is generally attributed to Tilly et al. [74 & 75] who found that the target material is removed firstly by the initial particle impact (*Primary erosion*) and then by fragments of the impacting particle being projected radially outwards from the preliminary impact site (*Secondary erosion*). The study by Tilly & Sage [75] summarised the fragmentation behaviour of irregular quartz as:

•   Small particles (10 to 20 μm) do not break up but require many impacts to remove chippings from the target surface. They cause little damage because the pitting is uniformly small and the mechanism is not aided by *second stage* damage.

•   An increase in particle size results in increasing fragmentation, but fewer impacts are required to remove material and the resultant chips are bigger. The results suggest that the *second stage* particles travel in a cloud at about 0.3 to 0.4 times the initial impact velocity. Also, the *second stage* particles can account for the wear when a ductile material is subjected to abrasive particles perpendicular to the surface.

•   Fragmentation increases with velocity of impact. It is thought there must be a threshold velocity at which fragmentation occurs, although this is not reported.

8.2.2. Target Material Properties

For many engineers and scientists, hardness appears to be the most obvious material property likely to affect the erosion rate. However, in many instances where alloyed steels are used, or surface treatments are applied, it has been shown that the wear resistance is also dependent upon other properties. In section 8.2.1 it was stated that the mathematical models for particle erosion are divided into two generic groups; brittle and ductile. Unfortunately, the ductility of a material is not dependent upon a single property and is a function of hardness, fracture toughness, tensile strength, etc.

The criterion of brittleness can be defined as the condition where the material fractures without observable plastic deformation or that the load deflection curve is essentially elastic to fracture. In contrast, a ductile material can undergo large plastic strains before fracture occurs. However, in some instances, erosion of a brittle material has been associated with local ductile behaviour [76]. Since, the spool and bushing are manufactured from a hardened steel, there is a possibility that the erosion may be similar to that of a brittle material, although the SEM micrographs contained in Chapters 5 & 7 suggest otherwise. This can be seen by the material

deformation/plastic flow in the direction of the fluid flow. Also, the field specimens are dominated by a combination of longitudinal wear scars and surface pitting which is very reminiscent of a material with a ductile behaviour [77].
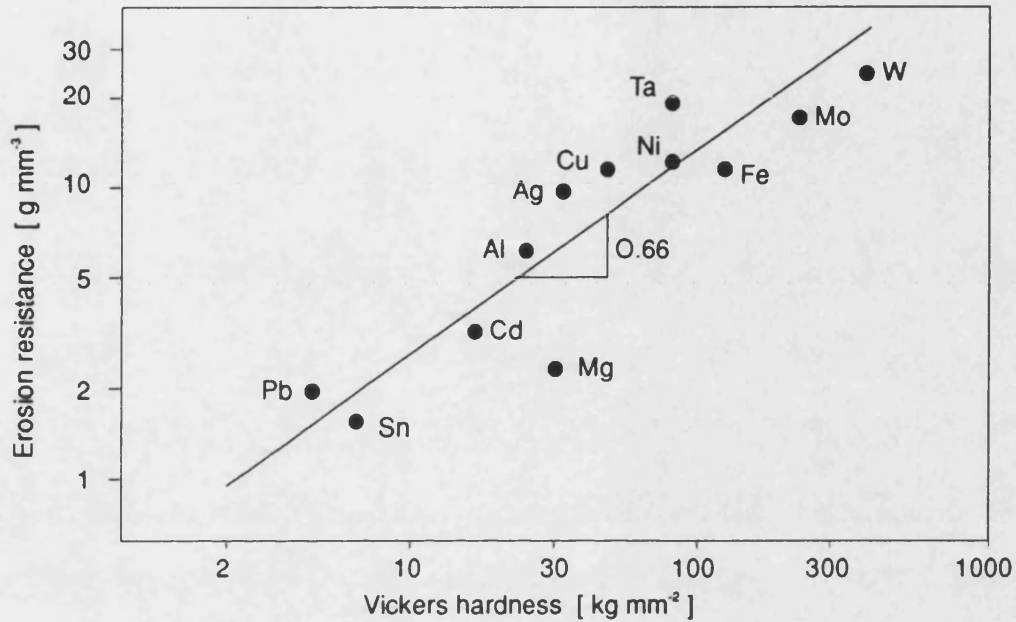
Figure 8.4 - The correlation between erosion and Vickers hardness of pure metals [78].
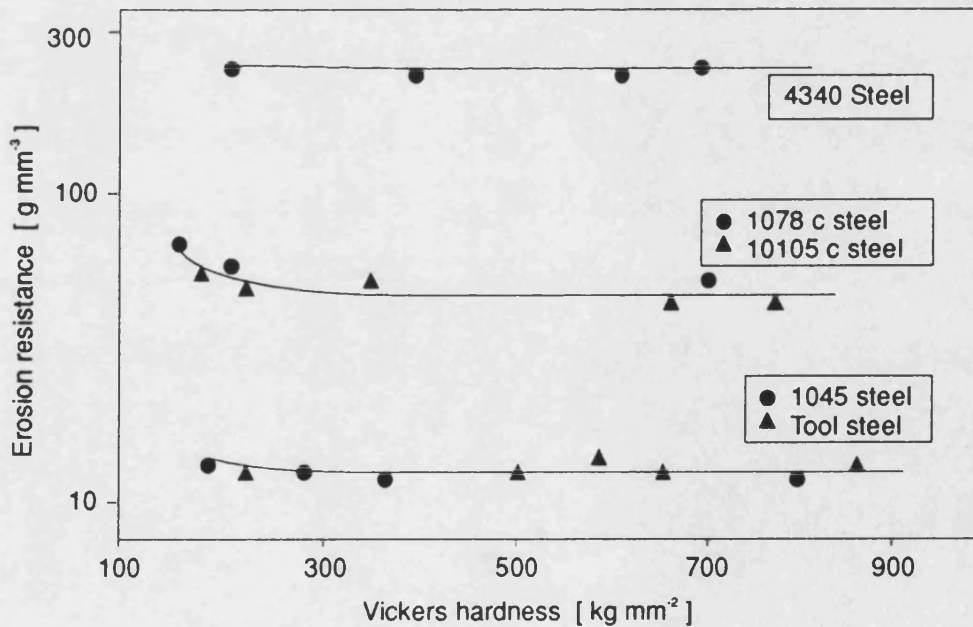
Figure 8.5 - Erosion resistance of three steels with their quenched & tempered hardness [78].

To examine the influence of material properties on ductile erosion, Sundararajan [79] reviewed the available literature on the effects of hardness and demonstrated that a linear relationship between the erosion resistance and the material hardness existed for pure metals as shown in Figure 8.4 (From [78]). However, when different hardness values were obtained for a given material by quenching and tempering, little or no variation in the erosion resistance was obtained, Figure 8.5 (From [78]). Sundararajan suggests that under certain conditions, plastic deformation occurs beneath the impacting particle leading to the formation of a lip or microchip. At this condition, the plastic deformation is essentially converted into heat which, depending upon the rate, will be either isothermal or adiabatic. However, using a thermal parameter number R_t it was found that deformation during erosion is always fully adiabatic.

Using this result, Sundararajan ignored the properties associated with hardness and developed a particle erosion model using the thermal properties of the target material. This led to a model which demonstrated that the erosion resistance of pure metals is primarily determined by their melting point. The higher the melting point, the greater the resistance. Since the model contains a temperature coefficient term which is constant with hardness, the erosion resistance of steels becomes insensitive to any heat treatment.

This strategy can be justified, as an increase in the strength (hardness) of many steels causes a corresponding decrease in the localised critical strains. Since these two effects offset each other, this leads to a strength-independent expression for the erosion resistance. In the case for pure metals, the apparent effect of hardness is still obtained since the temperature coefficient of the flow stress is proportional to the melting point which in turn is proportional to the hardness.

In support of Sundararajan's models [79 & 80], Hutchings [71] has provided similar reasons why bulk hardness is a poor predictor of the erosion resistance and suggested that the degree of localised plastic flow around each particle impact site is probably more important. These recent publications indicate the current thinking and confirm much of the early pioneering work carried by Smeltzer et al. [81], Wood [82] and Jennings et al. [83] who first proposed that the erosion models should be based on changes in the thermal properties.

In contrast to pure metals and heat treated alloy steels, where the material properties are consistent throughout, the application of hard surface coatings using physical vapour deposition (PVD), chemical vapour deposition (CVD), etc, to a base material requires a different approach to obtain the material properties. For example, Shanov et al. [72] examined the performance of three ceramic coatings, titanium carbide, titanium nitride and aluminium oxide to erosive particles. In all cases, the results indicated that the coatings behaved as a brittle material until penetration

occurs. At this point, the erosion increases to a rate associated with the ductile material. It was interesting that their results provided no evidence of coating deformation, cracking or spallation.

In contrast, Shipway & Hutchings [84] found that different types of particles caused different mechanisms of erosion when applied to a sintered boron carbide ($H_v \approx 35$ GPa). These were found to vary between lateral cracking or small scale chipping. The hardest particles (silicon carbide $H_v \approx 33.4$ GPa) produced high erosion rates with the lateral fracture mechanism of material removal. Whilst the softer particles (alumina $H_v \approx 26$ GPa and silica $H_v \approx 13$ GPa) eroded by a minor chipping mechanism, which gave erosion rates some orders of magnitude lower than those observed with the lateral fracture mechanism.

In addition to the erosion rates, Shipway & Hutchings [84] found that the silica particles fragmented above a certain threshold velocity (see also Section 8.2.1). With the larger particles (600 to 850 µm) this appeared to have little effect on the erosion rates, but for the smaller particles (125 to 150 µm) the erosion rate was seen to decrease over a narrow range of increasing velocity. It was proposed that this was due to shattering of the erodent on impact into less damaging fragments.

From the tungsten carbide/carbide coated spool results included in Section 7.7, an initial increase in the erosion resistance was found. However, after a given test period a step change in the results was obtained. From the spool SEM analysis (Figures 7.37 to 7.40) it can been seen that the coating has been removed from the parent material. Unfortunately, this highlights a common problem associated with surface coatings, where often the performance is dependent on the bonding between the coating and the parent material and not on the properties of the surface coating alone. Further evidence on this effect has been reported by Stidh et al. [85] who studied the effects of particle erosion on thin ceramic coatings. From their results it was suggested that a strong relationship exists between erosion resistance and the coating thickness. Surprisingly the thin coatings performed better than the thicker ones. They conclude that low porosity, fine grain size, low residual stresses and good adhesion are desirable for good erosion resistance.

8.2.3. Carrier Fluid Properties

Compared with the particle properties (Section 8.2.1) and the target material properties (Section 8.2.2), the influence of the carrier fluid has received little attention. The reason for this is that compressed air is normally used to accelerate the particles. However, when particles are carried within viscous fluids (oil, water, etc) it is clear that viscous drag forces will be act on the

particles and a squeeze film effect will most likely occur between the impacting particle and the target surface. Also, as small particles can be carried in the fluid streamlines they will be carried away from, or carried around the target surface. This produces a condition where only a percentage of the particles impact onto the surface, which is often known as a collision efficiency.

A common example of the interaction between the carrier fluid and solid particles can be seen in many industrial pipework systems. Here the effects of wear can be found on the outer radius of a bend. The fluid velocity will be highest at this region and when combined with the radial momentum of the particles, produces the right environment for erosion and abrasion to take place.

In a research environment, the interaction between carrier fluids and erosive particles is usually examined by using either a jet impingement slurry test rig [86] or a slurry pot tester [87]. The jet impingement rigs usually operate by passing the test fluid into a nozzle/ejector assembly. Here an area of low pressure is generated which is used to suck and mix the test contaminant into the fluid flow producing a slurry which can be accelerated on to the target specimen, usually a flat plate. Alternatively, the slurry pot tester consists of a cylindrical container filled with a test fluid and seeded with a test dust. The target specimens, usually multiple cylindrical targets located with their axis normal to the principle flow direction, are rotated at the required speed to obtain the desired impact velocity. On completion of the test, the components are removed and the wear damage assessed using some form of gravimetric, SEM or surface profilometry analysis.

Although these methods are different to the work reported within this thesis, the results obtained provide the best indication to the likely influence of the carrier fluid properties on the erosion rates. For example, Clark [88] reviewed the literature on the particle and fluid interaction and identified five key points:

- Not all particles directed at a target under erosion conditions impact the target and in extreme circumstances the proportion may be very small.

- The normal component of particle impact velocity on a target is always lower than the free stream velocity.

- The particle impact angle on a target cannot be described by the angle of the suspension stream directed at the target.

- Potential flow models of particle trajectories and impact appear to correspond quite well to experimental observations of particle impact, at least for particle sizes above 100 μm.

- The magnitude of boundary layer and liquid-solid boundary effects on particle impact and erosion remains to be clarified.

From work associated with slurry pots, Clark [89] found that the erosion is reduced when the viscosity is increased. Intuitively this reduction in wear rates can be attributed to two different mechanisms. Firstly, at higher viscosities the liquid may be increasingly effective in decelerating the particles approaching the target surface, essentially providing a cushion of liquid that reduces the kinetic energy of the incoming particle. Secondly, as the fluid viscosity increases, the drag on the suspended particles will increase and a greater proportion of particles lying in the path of the moving target will be carried around the specimen without impacting on it. However, the test results indicate that the dominating influence of increasing viscosity (test range 0.7 to 70 cP) is to change the flow conditions around the target, decreasing the frequency with which particles impact the surface. Additionally, the mass loss per particle impact was found to independent of carrier liquid viscosity.

Further work by Clark & Burmeister [90] and by Wenglarz [91] concentrated on the influence of the squeeze film and the properties of the target surface boundary layer. Clark & Burmeister found that the energy required to displace a liquid squeeze film separating an approaching particle from the surface leads to significant reduction in the impact velocity. The magnitude of this effect increases as the boundary layer Reynolds number decreases. This film will also influence the particle trajectories at rebound and should encourage a sliding particle bed adjacent to the target surface.

Wenglarz [91] took a more mathematical approach and developed a ratio of boundary layer thickness to the stopping distance (β) to examine the effect of the boundary layer on the erosion rate. Using this relationship, when $\beta > 1$, particles fail to impact onto the surface. Wenglarz found that the boundary layer only affects the impact velocity when the boundary layer thickness exceeds 40% of the stopping distance. Additionally, if the boundary layer is turbulent and $\beta > 0.4$, the boundary layer will always increase the particle impact angle which will affect the erosion rate.

8.3. Spool Valve Erosion Models

In order to formulate a dedicated spool valve erosion model, it is useful to apply and compare the established work to the spool valve wear. For example, Hutchings [17] reported that steels typically have an erosion value, E, of 2×10^{-4}. Therefore, by measuring the quantity of material removed from the spool and bushing (M_s) and calculating the total mass of particles (M_p) passing through the orifice during the test period, it is possible to determine a typical erosion value (E) for a given test. Unfortunately, using these values in Equation 8.6, it can be seen in Table 8.1

that the values obtained for a range of different tests are in the region of 10^{-10}, i.e. significantly smaller than predicted by Hutchings [17].

Test Conditions				Test Results			
Flow	Press. [bar]	Test Time	Contaminant [mg L^{-1}]	Mass of material removed [mg]	Mass of erosive particles [mg]	Erosion $E = M_s/M_p$	Erosion constant, k
P to S	70	48	5, uncut 10, uncut 20, uncut	5.05×10^{-5} 5.58×10^{-5} 7.91×10^{-5}	0.24×10^6 0.50×10^6 1.05×10^6	2.13×10^{-10} 1.12×10^{-10} 0.75×10^{-10}	2.23×10^{-7} 1.17×10^{-7} 0.79×10^{-7}
P to S	70	48	5, 0-10 μm 10, 0-10 μm 20, 0-10 μm	0.56×10^{-5} 1.08×10^{-5} 2.60×10^{-5}	0.21×10^6 0.45×10^6 0.92×10^6	0.26×10^{-10} 0.24×10^{-10} 0.28×10^{-10}	0.27×10^{-7} 0.52×10^{-7} 0.30×10^{-7}
P to S	35	2 8 48	10, uncut	0.78×10^{-5} 2.02×10^{-5} 2.92×10^{-5}	0.01×10^6 0.05×10^6 0.36×10^6	6.18×10^{-10} 3.71×10^{-10} 0.82×10^{-10}	13.0×10^{-7} 7.79×10^{-7} 1.72×10^{-7}
P to S	70	2 8 48	10, uncut	1.67×10^{-5} 3.00×10^{-5} 5.58×10^{-5}	0.02×10^6 0.08×10^6 0.50×10^6	9.24×10^{-10} 3.92×10^{-10} 1.12×10^{-10}	9.67×10^{-7} 4.10×10^{-7} 1.17×10^{-7}
S to T	35	2 8 48	10, uncut	0.89×10^{-5} 1.40×10^{-5} 2.42×10^{-5}	0.01×10^6 0.05×10^6 0.35×10^6	6.97×10^{-10} 2.72×10^{-10} 0.69×10^{-10}	14.6×10^{-7} 5.70×10^{-7} 1.46×10^{-7}
S to T	70	2 8 48	10, uncut	1.43×10^{-5} 2.45×10^{-5} 4.76×10^{-5}	0.02×30^6 0.08×10^6 0.50×10^6	7.88×10^{-10} 3.24×10^{-10} 0.95×10^{-10}	8.25×10^{-7} 3.40×10^{-7} 0.90×10^{-7}

Table 8.1 - Estimation of spool valve erosion rates at various test conditions.

In addition to the erosion values presented in Table 8.1, the mass of material removed from the spool and bushing (M_s) can be used to obtain the erosion constant, k, used in Equation 8.5. Typically, this value lies in the range 5×10^{-5} to 10^{-1} for metals [17]. Values were obtained for the erosion constant by assuming an average particle impact velocity to be 50% of the maximum orifice velocity. From Table 8.1 it can be seen that these values are very low, typically 10^{-7}.

It is not surprising that the erosion damage is less severe than suggested by the classic models since they assume that all particles impact onto the target surface. Clearly, in the spool valve case, the particles are likely to be uniformly distributed in the hydraulic fluid and the majority will pass directly through the orifice, whilst the others will be cushioned by the fluid boundary layer before impact.

Therefore, to assess the possible effects of the carrier fluid and to determine the possible particle trajectories within the valve, a study using computational fluid dynamic (CFD) has been undertaken.

8.3.1. Computational Fluid Dynamic Studies

To determine the particle trajectories within the spool/bushing metering orifice, studies have been undertaken using a proprietary CFD package called *STAR-CD*. The *STAR-CD* system consists of the main analysis code *Star* and the pre and post processor *Prostar*. *Star* generates thermo-fluid predictions corresponding to specified input data generated using *Prostar*. The results display facility in *Prostar* provides graphical representation of the flow predictions in several forms. The flow velocity is produced as vector plot and the scaler quantities are described by line contours or isosurfaces. Further details on the operation of *STAR-CD* is available within the reference manuals [92].

To assess the particle trajectories, *Prostar* provides a facility to calculate and display particle tracks on an existing velocity plot. The PTRACK command is used for this purpose and is purely a post processing function that allows the calculation and display of particle tracks based on data from an existing flow field, i.e. there is no interaction between the particles and the flow field. However, the particles can be assigned volumes and density so as to take into account the effect of body forces.

Before obtaining the particle information, a 2-D flow solution is required for the metering orifice in both flow directions (P→S & S→T). Since the pressure and tank metering lands (see Section 4.2.1) are geometrically similar, a single CFD mesh geometry may be produced with an inlet velocity and outlet pressure boundary, with the orientation reversed to provide the two flow directions (P→S & S→T). Also, since the metering orifice is fully annular, the mesh geometry can be reduced to a single cylindrical cell layer with sides modelled as two symmetry planes, as shown in Figure 8.6.

Initially, the spool and bushing metering edges were modelled as a perfect right angle (squared edged orifice) using a first order differencing scheme (UD - Upwind Differencing). Although, this model converged, wall attachment of the orifice jet always occurred. Burnell [93] encountered similar problems with spool valves and found this effect can be reduced by using a second order differencing scheme (LUD - Linear Upwind Scheme) and by reducing relaxation factors on the

solution variables. Unfortunately, in the current studies not only did this increase the computation time, but it also had no affect on the solution.
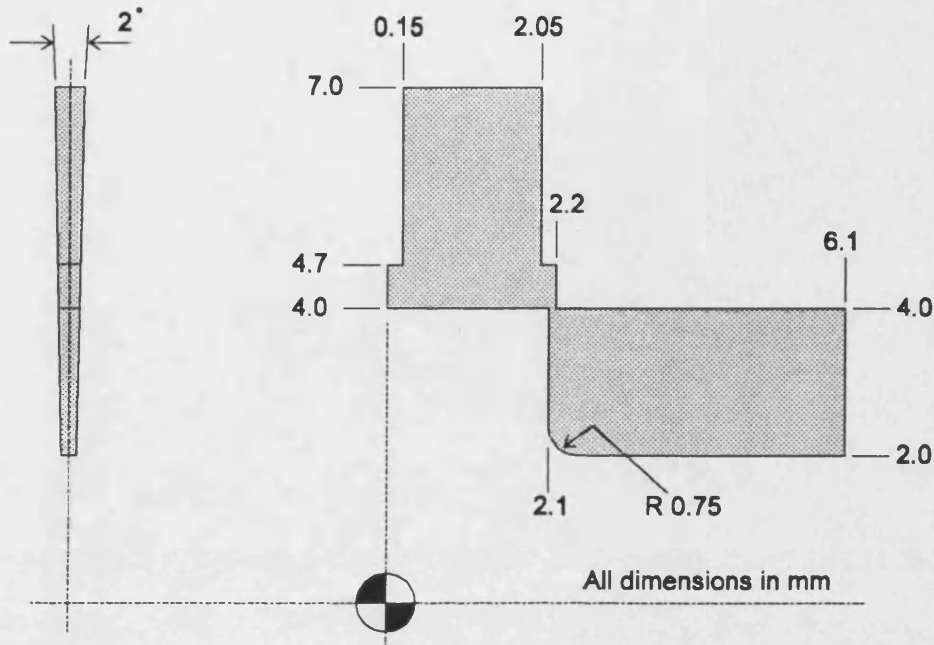
Figure 8.6 - CFD valve model geometry.

In an attempt to avoid the wall attachment, the following geometric and computational adjustments have been used with some success:

- Due to small geometric differences between the new and the worn conditions, a small mesh (nominally 10 μm) is constructed around the metering orifice. However, since the model is computed in SI units, it became apparent that the cell dimensions can cause incorrect solutions to be obtained. Therefore, to increase the cell dimensions the model geometry shown in Figure 8.6 was non-dimensionalised by dividing all the dimensions by 7 mm (outside radius of bushing). In addition, to provide computational similarity, the Reynolds Number through the modified model must be the same. To achieve this, the velocity and the density are assumed to by unity at the outer radius of the bushing. Hence, the modified fluid viscosity can be found from the reciprocal of the original Reynolds Number, i.e.

$$R_{e\ actual} = R_{e\ model} = \frac{\rho\ U\ d}{\mu} = \frac{1 \times 1 \times 1}{\mu} = \frac{1}{\mu} \qquad \dots\ (8.8)$$

Hence, the computed velocities and pressures must scaled by:

$$U = U_{computed} \times U_{ref} \quad \& \quad P = P_{computed} \times \rho \times U_{ref}^{2} \qquad \ldots (8.9)$$

Here U_{ref} equals the velocity used to determine the actual Reynolds Number. It should be noted that over the range of flow conditions computed, the results have been shown to be insensitive to changes in Reynolds Number.

- Originally, the valve orifice was modelled with square corners with no radial clearance between the spool and bushing. However, modifying the valve model to include a 3 μm radial clearance (typical manufacturing value) and a 10 μm corner radius (see Figure 5.7) the computation produced a converged solution with the jet away from the wall in the meter-out direction (P→S). This solution was only obtained when both of these factors are included.

- In attempt to produce a solution without the wall attachment in the meter-out direction (S→T), various changes to the outlet and side wall conditions have been investigated. Although, this was not achieved, it was found that the orifice inlet conditions do not appear to be significantly affected by the apparent down stream condition.

In addition to the CFD results, Figures 8.9 & 8.11 contain two photographs [94] of the actual flow patterns achieved using water in a scaled (10:1) perspex model of the metering orifice. This technique referred to as *flow visualisation* [95 & 96] uses a high electrical voltage to produce hydrogen and oxygen bubbles which are carried in the streamlines through the valve. The motion of the bubbles can then be observed or photographed by projecting a strong light through the perspex.

Comparing the CFD and the flow visualisation results, Figure 8.9 - 8.12, it can be seen that good agreement is achieved in the meter-in direction (P→S). In the meter-out condition (S→T), the flow visualisation result confirms that wall attachment of the fluid jet does not take place. However, the CFD results are considered to be acceptable for the purposes of the wear model study and the particle tracking up-stream of the metering orifice.
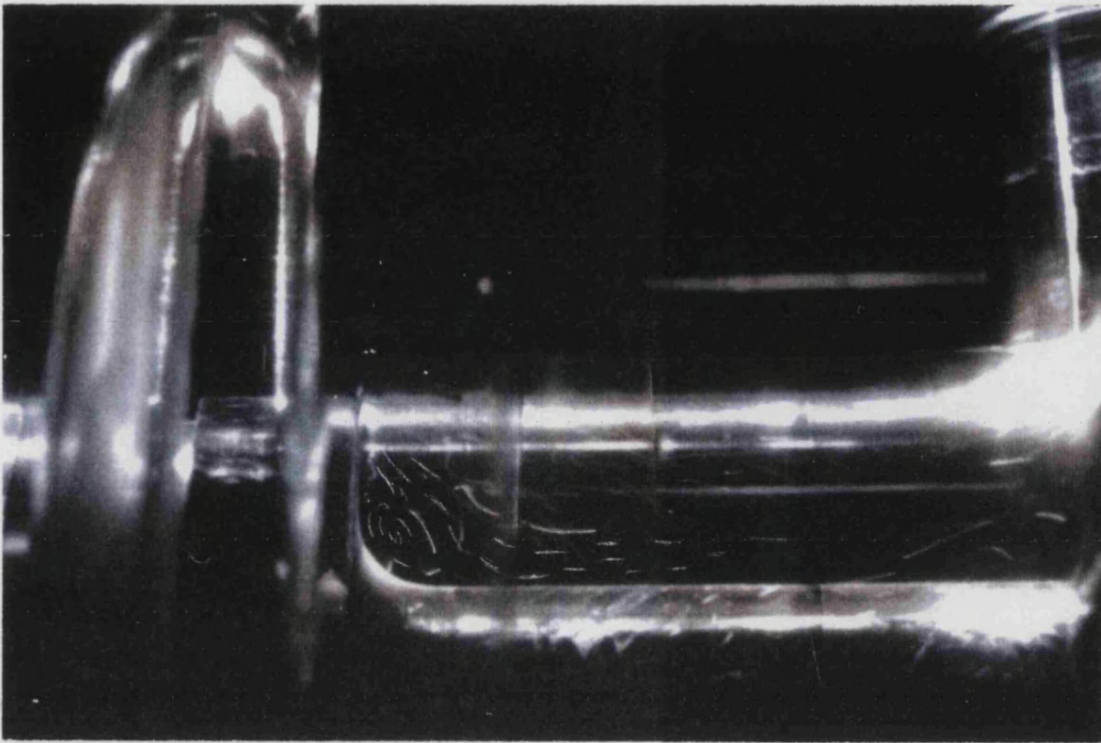
Figure 8.7 - Flow visualisation results, new metering orifice with the flow from P→S.
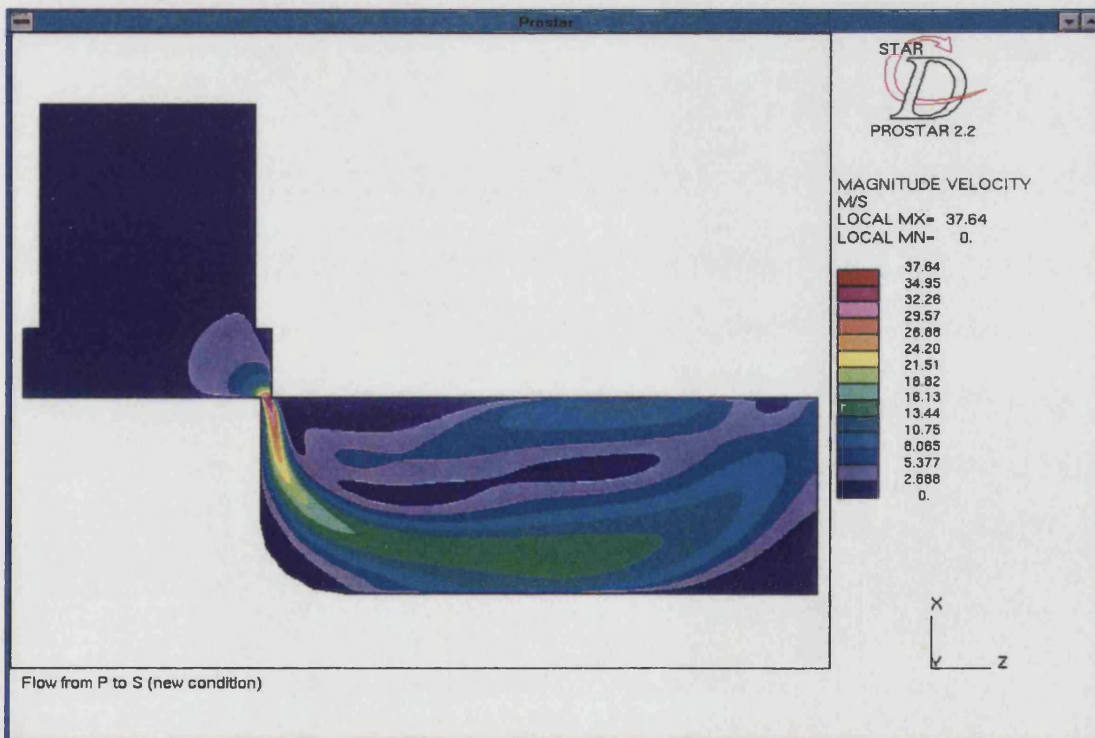
Figure 8.8 - CFD results, new metering orifice with the flow from P→S.
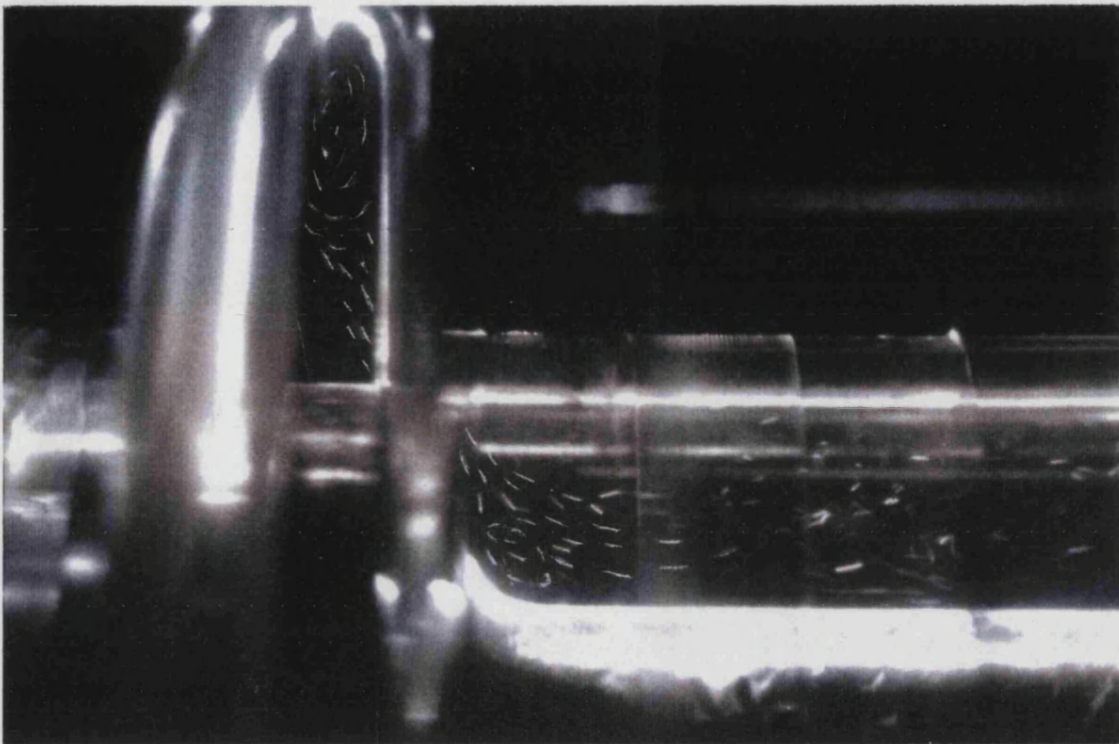
Figure 8.9 - Flow visualisation results, new metering orifice with the flow from S→T.
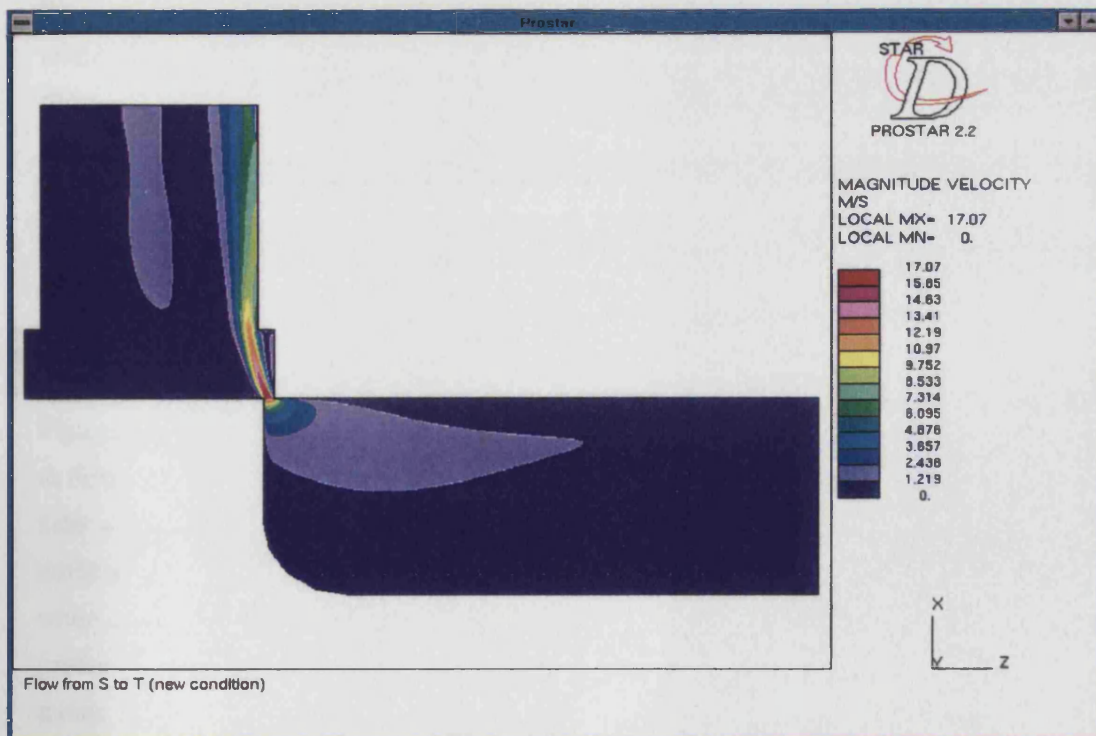
Figure 8.10 - CFD results, new metering orifice with the flow from S→T.

Since the CFD models have been produced in a non-dimensionalised form, it is necessary to apply a velocity scale factor. Considering the two test pressures of 35 and 70 bar, the CFD velocities should be multiplied by 1.9 & 2.7 for the P→S case, and 4.2 & 6.0 for the S→T case (U_{ref}= Bushing inlet flow rate divided by inlet flow area). However, when comparing the maximum CFD velocities with the theoretical values, the computed values were smaller than expected. For example in the P→S direction with a 70 bar differential:

$$U_{theory} = \sqrt{\frac{2 \Delta P}{\rho}} = 126 \ m \ sec^{-1} \quad \& \quad U = U_{computed} \times U_{ref} = 102 \ m \ sec^{-1}$$

In addition to velocity, the CFD results include the pressure conditions within the model. From these, it is apparent that the CFD pressure differentials are below the 35 and 70 bar test conditions. However, if U_{ref} is found using the pressure equation, Equation 8.9, the maximum CFD velocity increases above the theoretical values. For example, the 70 bar case considered previously, increases to 141 m/sec. Although, this technique produces a larger velocity than expected, it is considered that this approach is a realistic method to obtain the flow velocity from the CFD analysis. Therefore, for the purpose of the analytical studies, the 35 & 70 bar velocity scale factor, U_{ref} becomes 2.6 & 3.7 in the P→S case and 5.4 & 7.7 in the S→T case.

To examine the flow changes within a worn valve, two orifices have been modelled by applying the wear profiles taken from Figures 5.41 & 5.43 to a spool and bushing (Test conditions: 70 bar, uncut quartz, 48 hours, P→S and S→T). In this case, the CFD analysis produced velocity and pressure distributions similar to the new geometry, the only significant difference being the different velocity scale factor, U_{ref} required to accommodate the larger flow rates associated with the worn metering orifice (U_{ref} equals 4.1 for the P→S case and 10.7 for the S→T case). To avoid duplication, these results are not included in a complete form, however they are shown combined with the particle tracking in Figures 8.15 & 8.16.

Four cases have been considered using the particle tracking facility as shown in Figures 8.11 to 8.16. In each case, six particles have been released (with an initial velocity equal to fluid velocity at the start location) through the metering orifice; two at locations adjacent to the side walls and two in the centre. To assess the influence of particle size on the trajectories, particle diameters between 1 and 100 μm have been released from each location. However, when comparing the results, visually the trajectories appear to be identical. Therefore, the results presented in Figures 8.11 to 8.16 may be considered typical for both the 0-10 μm and the uncut quartz dust.

From Figures 8.11 & 8.13, it can been that the particles travelling in the bulk fluid are likely to be carried through the orifice without coming into contact with either the spool or the bushing. However, for particles that do come in contact, minimal wear damage will occur since the corner only receives a glancing blow rather than a full impact. In contrast to the bulk flow, the few particles travelling adjacent to the side walls appear to be the only particles capable of coming into full contact with the surface. In this condition, the CFD trajectories suggest that the particles will have a maximum impact angle of 10 to 15° (nominally half the value to cause maximum wear). Hence with these low impact angles, the erosive wear process will not be particularly efficient.

From a closer examination of the enlarged views, Figures 8.12 & 8.13, it can be seen that the maximum upstream velocity is approximately half the value predicted from the orifice equation. However, from the velocity vectors adjacent to the wear regions on the spool and bushing, this value may be reduced to 10 or 20%. From the analysis of the erosive wear profiles presented in Table 5.2, it was found that the proportion of the wear material removed from either the spool or the bushing was dependent upon the flow direction. Intuitively, with the fluid flow in the meter-in direction (P→S), it was thought that the spool would receive more wear damage since the momentum of the fluid and the particles is directed radially towards it. This was not the case in practice and the larger bushing wear was attributed to the softer material produced during the EDM machining. Conversely, in the meter-out direction (S→T), the spool wear was greater than the bushing as might be expected from the flow patterns within the metering orifice.

From Figure 8.12, it can be seen that the particle streamlines are such that the momentum of the particles entering the metering orifice will be directed towards the bushing and not the outer diameter of the spool. Similarly, in the reverse flow condition, Figure 8.13, this hypothesis would still be true since the particle streamlines suggest that the fluid momentum is directed towards the side of the spool. Therefore, the areas of greatest wear correspond to the locations having similar flow conditions.

Confirmation of this phenomenon, together with the particle tracking information for a worn orifice in both directions, is shown in Figures 8.15 & 8.16. Here, the particles appear to follow the actual wear profile, therefore supporting an abrasion/micro-machining type process.

From the viscosity results, Section 6.3, it was found that the wear rates increase with a corresponding increase in viscosity. This was an unexpected result, since it was thought that the thicker oil would have a larger boundary layer which would prevent surface contact from the impinging particles. Since the opposite was found, an alternative explanation is necessary. From

the CFD results presented above, it has been suggested that the majority of the particles which come into contact with the surface do so at shallow impingement angles. Therefore, in the thick oil case, the particles are likely to be retained in the boundary layer encouraging an abrasive type process. In contrast, the particles in the thinner oil may be permitted to move away from the surface, or roll within the boundary layer, thus causing less wear damage.

From the CFD analysis the following observations can explain the lack of agreement between the actual and the theoretical erosion rates presented in Table 8.1:

- By releasing particles from different locations at the valve inlet, it has been found that the majority of particles are carried through the orifice. In instances where the bulk flow comes into contact with the orifice boundary, it is thought that little or no damage is caused since the particles only suffer glancing blows with the surface.

- From the meter-in (P→S) velocity plots, it can be seen that the fluid is directed towards the bushing side wall where the greatest wear occurs. Similarly from the meter-out case (S→T), a similar relationship exists between the fluid flow and the spool side wall which is the area of greatest wear.

- Assuming the particles are travelling at the same velocity as the fluid, it has been shown that the particle impact velocity will be 10 to 20% of the value predicted from the orifice equation.

- The particles will have a maximum impact angle of 10 to 15° (nominally half the value to cause maximum wear).

- Since the impacting particles have low impact angles, it is thought that the wear mechanism will be more typical of an abrasion process than an erosive one. Therefore, a thicker oil will tend to keep the particles in contact with the surface, whilst a thin oil will allow the particles to roll along the surface producing less wear.

- It was shown in Chapter 5 that the wear rate is dependent upon the contaminant distribution. Unfortunately, the particle tracking results have not indicated any variation between the impact trajectories of different particle sizes, therefore an alternative approach is required to obtain greater information on the particle trajectories.

Figure 8.11 - Particle tracking results, new metering orifice with the flow from P→S.

Figure 8.12 - Particle tracking results, new metering orifice with the flow from P→S.
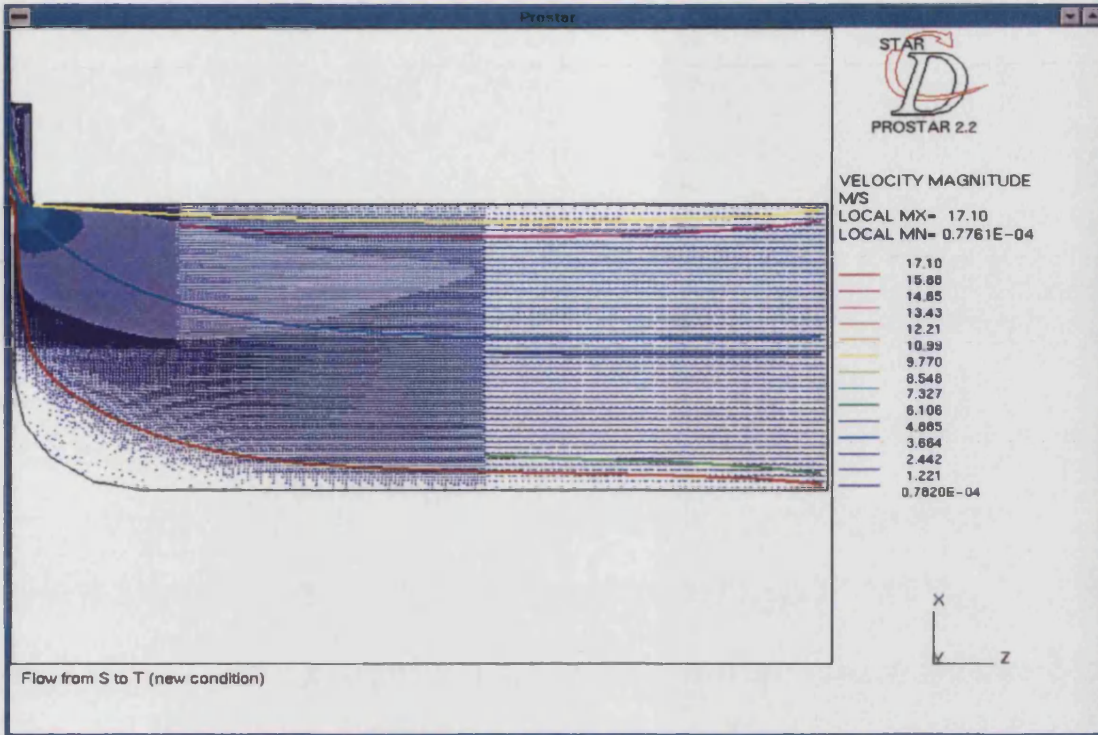
Figure 8.13 - Particle tracking results, new metering orifice with the flow from S→T.
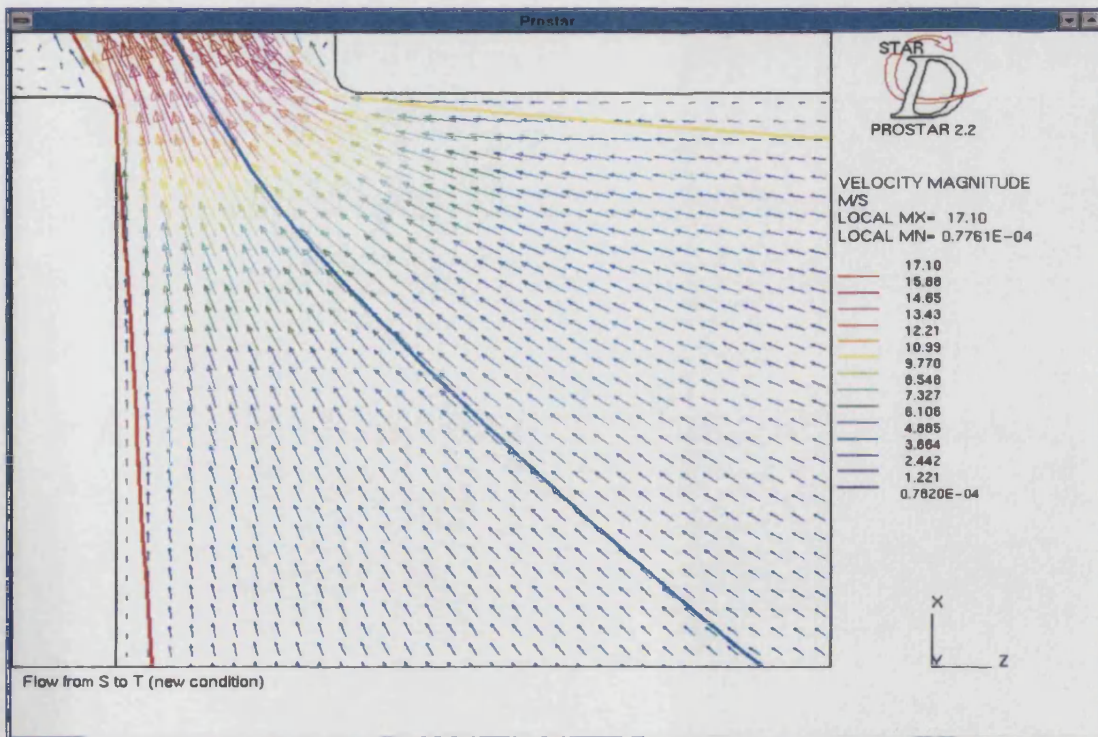
Figure 8.14 - Particle tracking results, new metering orifice with the flow from S→T.
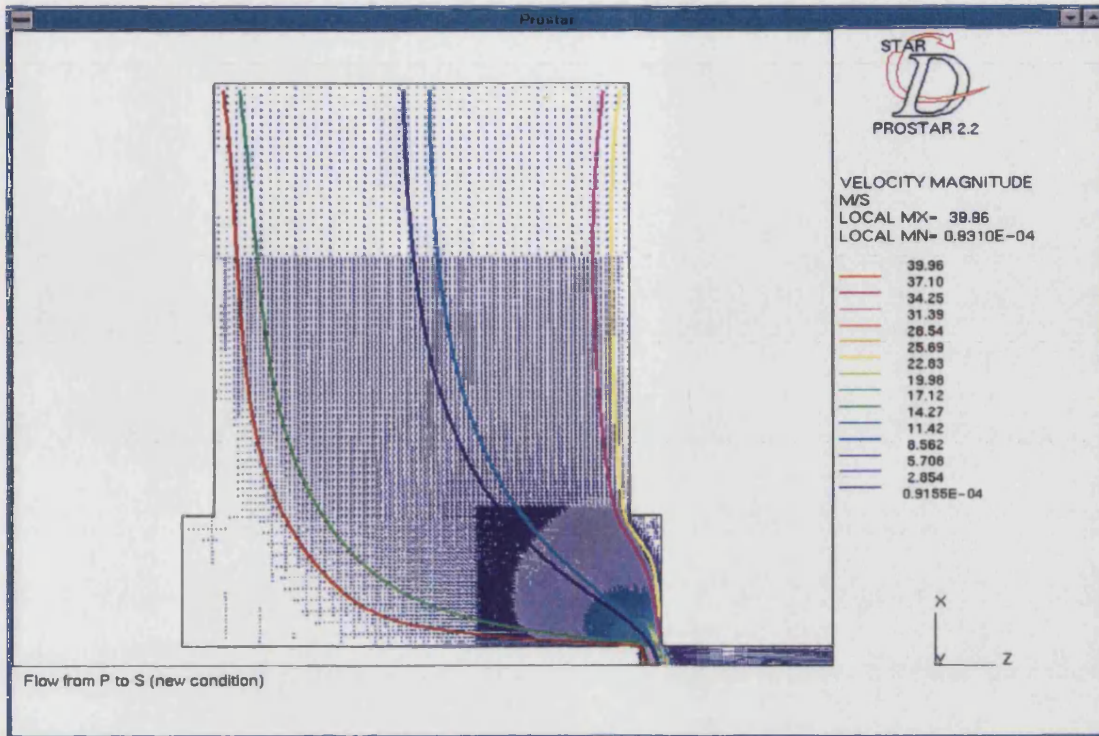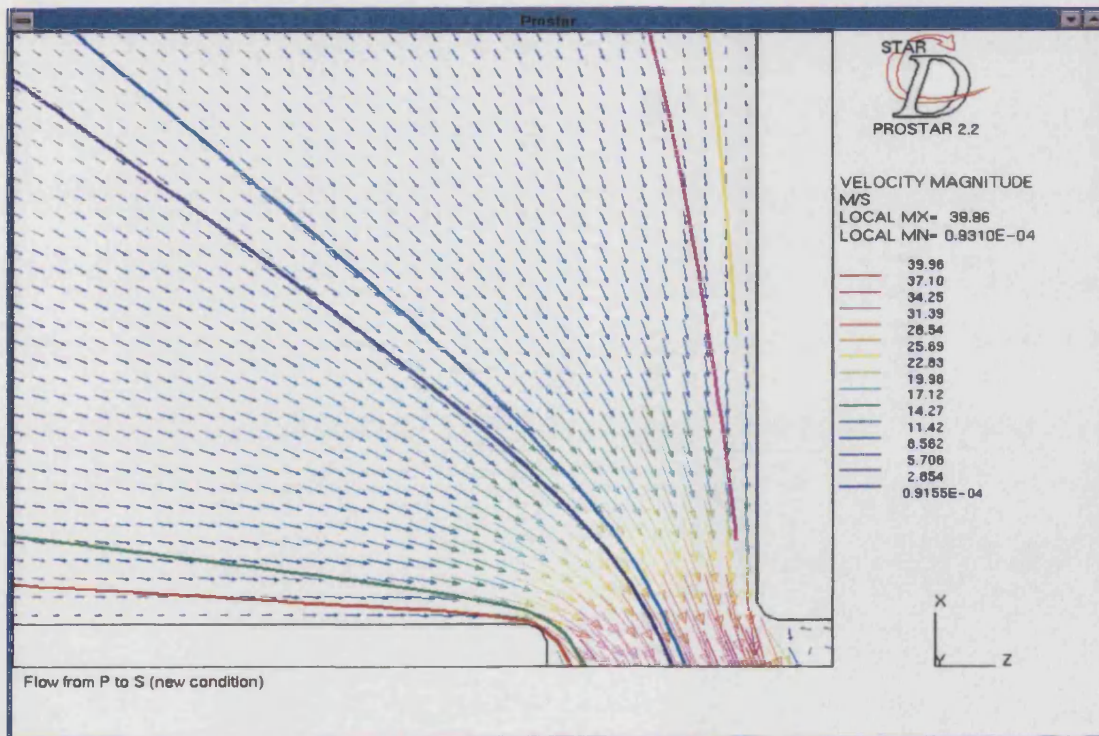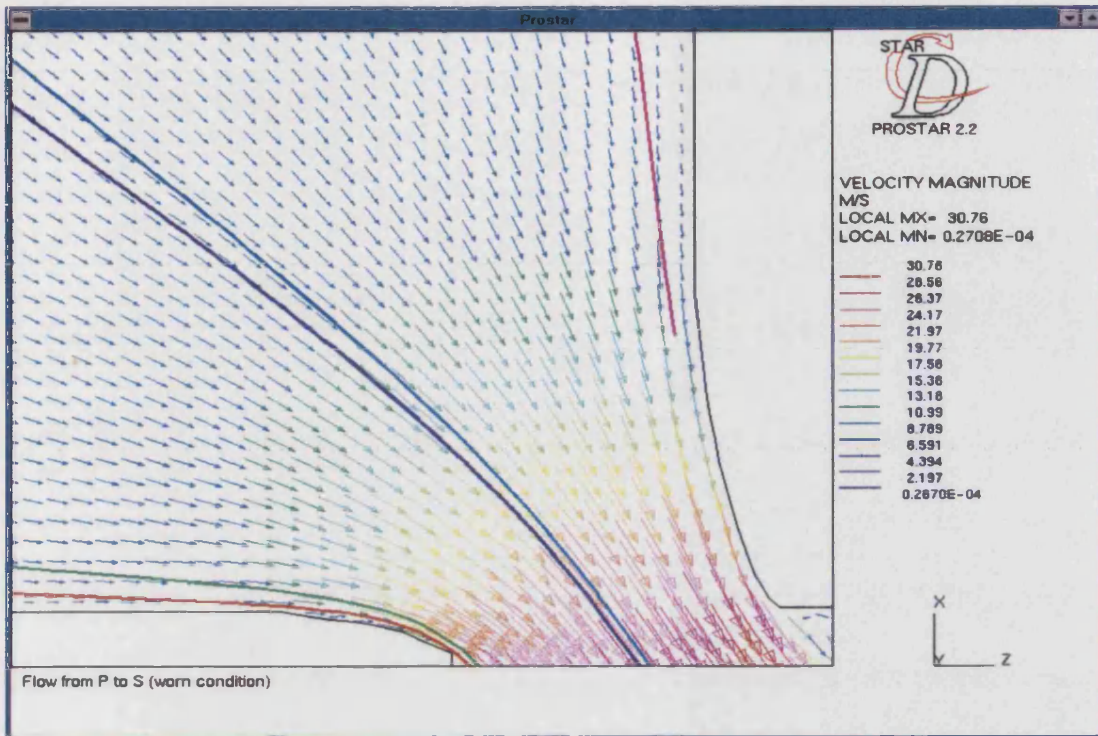
Figure 8.15 - Particle tracking results, worn metering orifice with the flow from P→S.
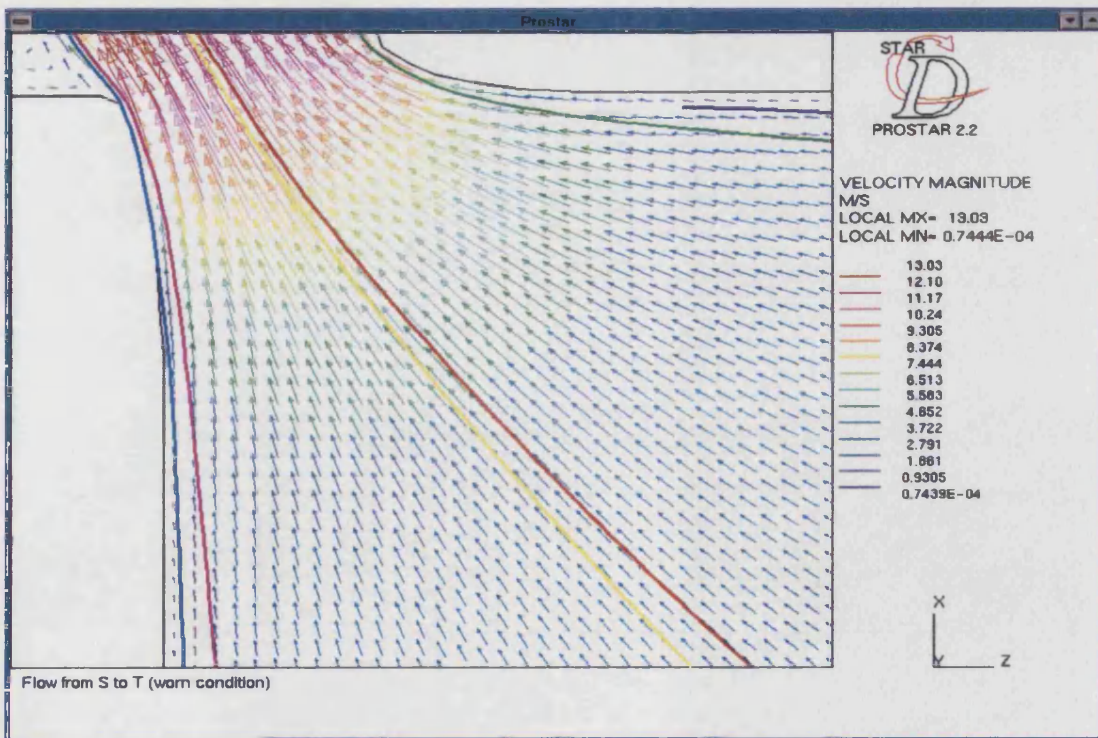
Figure 8.16 - Particle tracking results, worn metering orifice with the flow from S→T.

8.4.   Conclusions

From the literature review, it has been shown that a diverse range of variables are used to describe and model the particle erosion process. However, the majority of these neglect the carrier fluid properties which has been demonstrated in Chapter 6 to be important for assessing the erosive wear in hydraulic spool valves.

The importance of the carrier fluid properties is demonstrated in Table 8.1, where it is shown that the non-dimensional erosion values (E) for the spool valve orifice is smaller by a factor of 10^{-6} compared with the established value for ductile erosion. Similarly, the erosion constant (k) used to estimate the mass of target material removed is below that normally associated with the established theory. In both cases, it thought that the difference between the spool valve test results and the established results is dependent upon the collision efficiency, i.e. the majority of particles are carried by the mineral oil through the valve orifice without coming into contact with the spool or bushing metering surfaces.

Confirmation of this hypothesis has been demonstrated using computational fluid dynamics, where both the fluid and the particle velocities have been found. Although the CFD modelling studies require further improvement, the results obtained confirm that the majority of particles are carried within the oil streamlines through the metering orifice. However, for the small percentage that do collide with the valve surfaces, the CFD trajectories suggest that the particles will have a maximum impact angle of 10 to 15° (nominally half the value causing maximum wear) and a impact velocity may be as low as 10 to 20% of the maximum vena-contracta velocity. From the worn orifice results, it can be seen that the spool and bushing has worn to produce a condition which is less restrictive to the flow passing through the orifice. At this condition, it is easy to perceive that the flow coefficient (C_q) will increase as found in Section 5.7. Also, at this condition, it can be seen that the particles can travel more freely through the orifice without coming into contact with the metering corner. However, for the particles that do come in contact, the particle motion is likely to have changed from a direct impact to a glancing or rolling type action along the surface. This hypothesis supports the results in Chapter 5 where it was found that the erosive wear decreases with time, i.e. the spool and bushing orifice has been micro machined into a natural shape to provide less flow resistance through the orifice.

It was thought that it may be possible to use the CFD analysis to obtain a particle diameter which will deviate from the oil streamlines and impact onto the surface. Unfortunately, for the range of particle sizes examined (1 to 100 µm diameter), no differences could be detected unless the

particle density was change significantly. Therefore, to extend the established erosive wear models to accommodate the spool valve case, fundamental erosive wear data is required which permits comparisons to be made between the classic erosion results with air and those with mineral oil without the complication of the valve geometry.

9

Conclusions and Recommendations

9.1. Conclusions

It has been identified in Chapter 1 & 2 that contamination is an important factor in determining the life and reliability of hydraulic components and systems. Traditionally, research has concentrated on contamination control, i.e. filtration, as a method of extending components life. However, with the demands of modern hydraulic systems and the introduction of new wear resistant materials, there has been some interest in the contaminant sensitivity of individual components. At present this has lead to the introduction of an ISO standard for the contaminant sensitivity of fixed displacement pumps. To assess the sensitivity, volumetric efficiency has been shown to be the most suitable wear indicator. However, little research has been directed at establishing the contaminant sensitivity of control valves. This deficiency is addressed in this thesis and a number of possible wear indicators have been developed to assess the degradation of control valves.

From the wear measurement investigations, the author has identified two useful methods to provide analysis of both field and test specimens. Firstly, the use of SEM micrographs to give pictorial results which can be used to make visual comparisons between components and secondly, a method has been developed using the Form Talysurf instrument to record the component geometry in either a two of three dimensional format.

Due to the non-availability of ACFTD, a replacement ISO quartz dust has been used for the majority of the erosive wear testing. Before using the quartz, the physical and geometric properties were obtained so that comparisons could be made between the new quartz test dust and the old ACFTD. This process proved invaluable since it provided a suitable method for validating the classification results used against the published ACFTD data. From these studies, the results have indicated that quartz is a suitable alternative to ACFTD, although the density of the quartz has been found to be higher than ACFTD.

In order to determine the wear sensitivity of a spool valve orifice in an acceptable time period, it was important to design a test rig which could provide accelerated testing under controlled conditions. This has been successfully achieved by designing and building a test facility which consists of essentially three hydraulic circuits: a 15 kW power pack used to transmit hydraulic power through two piston accumulators into a separate erosive test circuit, a specialised erosive test circuit which can subject a single spool valve metering orifice to a continuous flow of contaminated oil, and a fluid conditioning rig

which is used to provide test oil at an even and consistent contaminant distribution. The whole test process has been successfully controlled and monitored by a combination of electrical hardware and a PC based acquisition system. The rig has been found to provide stable and repeatable operating conditions throughout the period of the project.

Using the test facility, it has been found that the pressure-flow characteristic for a new metering orifice is similar in both flow directions: meter-in (P→S) and meter-out (S→T). The results indicate that there is linear relationship between the flow and the valve opening for spool openings >30 µm, with the flow coefficient (C_q) initially having a constant value of 0.7. By analysing test results and the worn component profiles, this value has been found to increase during the wear test due to the rounding of the metering edges, which permits greater flow for the same pressure drop.

By applying a $\log_{10}$ relationship to the test rig flow results, it has been possible to establish an equation for each test condition, thus enabling the flow rate to be calculated at any instant in time during the test period. By applying statistical analysis to the equations, a point of maximum confidence $\hat{t}$ (minimum variance) has been established. At this point, the analysis has shown that for two tests with the same conditions, the results may be considered identical at a 95% confidence level. The analysis has also indicated that a systematic error of ±0.1 L min^{-1} exists on the flow plot results.

Tests have been undertaken using base oil (no additives) and commercially available hydraulic mineral oils. By analysing the base oil test results, with the standard spool/bushing material the following factors have been identified:

- The erosion rate is independent of the spool opening, providing that the opening is greater than the contaminant particle size.

- When oil is used which has been filtered to a high cleanliness level (tested @ ISO 4406, class 8/4), no changes in the pressure-flow characteristics can be detected, i.e. no wear has occurred.

- Uncut quartz produces higher wear rates than ACFTD although their distributions are similar. It is thought that the difference between the two contaminants is associated with the particle mass and hence its impact momentum.

- Using similar concentrations of quartz having different size distributions, greater wear occurs when larger particles are present. This result has important implications relating to the use of gravimetric analysis as a method of contamination control, since it is not only the mass which is important but the distribution contributing to this mass.

- Increasing contaminant concentration levels produce a corresponding increase in the wear rates. The relationship between these parameters is not linear either in terms of increased flow rate or actual component material removed.

- The amount of wear material removed has been found to be approximately proportional to the differential pressure. This supports the established view given in literature which suggests that the erosion rate is proportional to the kinetic energy of the particles.

- From the profile measurements, the damage caused to the spool and bushing varies with flow direction. In the meter-in condition (P→S), the bushing metering slot wears more than the outside diameter of the spool. Conversely, for the meter-out (S→T) case, the side face of the spool receives more damage than the inside bore of the bushing.

- Testing in the meter-out (S→T) direction, suggests that the bushing metering corner is subjected to both material removal and a deformation process. This could be due the flow patterns, or the softer material properties found adjacent to the sides of the metering slots.

Results from the particle count data and the wear debris analysis indicate that the amount of wear debris generated during an erosion test is insignificant compared to the quantity of quartz particles present. Also, as the wear particles are generally less than 5 µm, they will have little or no effect on the erosion rates, although in practice, they may contribute towards the silting of control valves.

The tests presented in Chapter 6 have highlighted that viscosity is the most important oil property in the prevention of particle erosion. The results suggest that the wear rate increases with a corresponding increase in viscosity. This is surprising, since logically it would be expected that the thicker oil will have a larger boundary layer to prevent surface contact from the impinging particles. It is thought that the observed results are due to the particles being able to move more freely within the thinner oil streamlines thus permitting them to impinge onto the component surface at a impact angle which produces less wear.

The different oil formulation results show that the sulphur/phosphorous (S/P) oils give an improvement in the wear rates when compared with base oil. This was not the case with the zinc based additives (ZDDPs) which gave similar results. Currently, there is no explanation for why or how the S/P anti-wear additives cause an improvement, but the results indicate that Bartran is slightly better than HLP.

From the spool material studies presented in Chapter 7, the results confirm that the erosive wear resistance increases with material hardness as suggested in the established literature. Comparing the percentage flow change with the hardness ratio H_p/H_s supports the theory that a significant improvement in wear resistance is achieved when this ratio is less than unity. For the surface engineering techniques examined the titanium nitride (TiN) is the clear performance leader.

In Chapter 8, it has been shown that researchers have used a diverse range of variables to describe and model the particle erosion process. However, the majority of these neglect the carrier fluid properties which this study has been found to be important for assessing the erosive wear in hydraulic spool valves.

The importance of the carrier fluid properties on the erosive rate, has been shown by comparing the non-dimensional erosion values (E) for the spool valve orifice with the established value for ductile erosion. Typically, the spool valve case is smaller by a factor of 10^{-6}, i.e. a collision efficiency of 0.0001%. Similarly, the erosion constant (k) used to estimate the mass of target material removed is below that normally associated with the established theory. In both cases, it thought that the difference between the spool valve test results and the established results arises from the majority of particles being carried by the mineral oil through the valve orifice without coming into contact with the spool or bushing metering surfaces.

The applicability of the above hypothesis has been demonstrated using computational fluid dynamics (CFD), where both the fluid and the particle velocities have been predicted. The CFD modelling results confirm that the majority of particles are carried within the oil streamlines through the metering orifice. However, for the small percentage that do collide, the CFD trajectories suggest that the particles will have a maximum impact angle of 10 to 15° (nominally half the optimum value for maximum ductile erosion) and a impact velocity which may be as low as 10 to 20% of the maximum vena-contracta velocity. From the worn orifice results, the CFD results indicated that the spool and bushing has worn to produce a condition where the oil has a more natural flow through the orifice. As a consequence, the flow coefficient (C_q) will clearly increase with wear. Also, at this condition, the particles will travel more freely through the orifice without coming into contact with the metering corner. However, for the particles that do come in contact, the particle motion is likely to have changed from a direct impact to a glancing or rolling type action along the surface. This hypothesis supports the results in Chapter 5 where it has been found that the erosive wear decreases with time, i.e. the spool and bushing orifice has been micro machined into a natural shape to provide minimum flow resistance through the orifice.

Finally, the work reported within this thesis has confirmed that component life is dependent on the concentration and distribution of solid particles within the hydraulic oils. This life can be further influenced by the mineral oil properties, or by to greater extent by the use of new surface engineering technique to increase the hardness and wear resistance of the component parts.

9.2.   Recommendations for Further Work

Although much has been achieved by this work into the important factors which affect the erosive wear failure of spool valves, there are several areas where additional work is required to either compliment or extend the research. These include:

- The work has highlighted that individually, the oil viscosity and sulphur/phosphorous (S/P) additives can influence the particle erosion rates. Further work is required to investigate the interaction between the two oil properties in an erosive wear environment. This work should also examine the additive performance in a three body abrasion environment.

- The results have illustrated that it is possible to apply various surface treatments and coatings to a precision component whilst retaining the required dimensional tolerances. Although, problems of bonding between the surface coating and the bulk material have been observed, the titanium nitride (TiN) coating appears to be an attractive process for future development. This will require the application of the coating to the bushing bore and an assessment of its performance where both abrasion and erosion are present.

- It was thought that using CFD analysis it may be possible to predict a particle diameter which will deviate from the oil streamlines and impact onto the valve surfaces. Unfortunately, for the range of particle sizes examined (1 to 100 µm diameter), no differences could be detected unless the particle density was change significantly. Therefore, to extend the established erosive wear models to accommodate the spool valve case, fundamental erosive wear data is required which permits comparisons to be made between the classic erosion results with air and those with mineral oil without the complication of the valve geometry.

- The work in this thesis has concentrated on particle erosion in isolation. Obviously in practice spool valves are subjected a combination of wear mechanisms, i.e. 2-body abrasion, 3-body abrasion, chip shearing, etc. Therefore, there is a requirement to obtain information on each of these mechanisms in isolation before the significance of the wear mechanisms can be established.

- The establishment of the above information should enable spool valve designs to be obtained which are resistant to contaminant damage and wear.

References

1. **Fluid Power Centre**, Contamination Control in Hydraulic Systems, University of Bath.

2. **Bishop, F.E,** Air in Hydraulic Systems, Its Effects and Elimination, APM Field Service Report No. 54, Pall Corp, New York, 1978.

3. **Vickers Systems Ltd**, Effective Contamination Control in Fluid Power Systems, 1980.

4. **Department of Trade and Industry**, Research Reports of the Fluid Power Contamination Control Programme, Volume I - Field Studies, 1980 - 1983.

5. **Department of Trade and Industry**, Research Reports of the Fluid Power Contamination Control Programme, Volume III - Ferrography, 1980 - 1983.

6. **National Aerospace Standard**, Cleanliness requirements of Parts used in Hydraulic Systems, NAS 1638:1964.

7. **International Organisation for Standardisation**, Hydraulic Fluid Power - Fluids - Methods for Coding Level of Contamination by Solid Particles, ISO 4406:1987.

8. **Seifert, W.W. & Westcott, V.C**, A Method for the Study of Wear Particles in Lubricating Oil, Wear, 21 (1972), 27 - 42.

9. **Bowen, E.R. & Westcott, V.C**, Wear Particle Atlas, Foxbroro Analytical, Burlington, MA01803.

10. **Swansea Tribology Centre**, A Guide to Wear Particle Recognition, University College of Swansea, April 1987.

11. **Scott, D. & Westcott, V.C**, Predictive Maintenance by Ferrography, Wear, 44 (1977), 173 - 182.

12. **Yardley, E.D. & Moreton, G**, An Attempt to Quantify the Limits of Failure Detection by Ferrography, Wear, 90 (1983), 273 - 279.

13.   Uedelhoven, W, Franz, M. & Guttenberger, J, The use of Automated Image Analysis for the Study of Wear Particles in Oil Lubricated Tribological Systems, Wear, 142 (1991), 107 - 113.

14.   Seow, S.T. & Kuhnell, B.T, Computer Aided Diagnosis of Wear Debris, Third Bath International Fluid Power Workshop on Computers in Fluid Power, September 1990.

15.   Halling, J, Principles of Tribology, Macmillan Press Ltd, 1983.

16.   Burwell, J.T, Survey of Possible Wear Mechanisms, Wear, 1 (1957), 119 - 190.

17.   Hutchings, I.M, Tribology - Friction and Wear of Engineering Materials, Edward Arnold, London, 1992.

18.   Bitter, J.G.A, A Study of Erosive Wear Phenomena, Part II, Wear, 6 (1963), 169 - 190.

19.   Hersee, B, Filters for Hydraulic Systems, Fluid Power, No. 3, March/April 1991.

20.   Oklahoma State University, Method for Determining the Contaminant Sensitivity of Hydraulic Motors, Recommended Procedures for Evaluating Fluid Power Components and Systems, Fluid Power Research Centre, Oklahoma State University, March 1972.

21.   British Standards Institution, Hydraulic Fluid Power - Fixed Displacement Pumps - Flow Degradation due to Classified AC Fine Test Dust Contaminant, BSi draft doc No. 80/76302, July 1980.

22.   Department of Trade and Industry, Research Reports of the UK Fluid Power Contamination Control Programme, Volume VIII, Wear Processes in Hydraulic Pumps, (Research contractor: University of Aston), 1980 - 1983.

23.   Department of Trade and Industry, Research Reports of the UK Fluid Power Contamination Control Programme, Volume VII, Contaminant Sensitivity -Standard Test Methods", (Research contractor: British Hydromechanics Research Association), 1980 - 1983.

24.   International Organisation for Standardisation (draft), Hydraulic Fluid Power - Fixed Displacement Pumps - Contaminant Sensitivity, ISO/TC/131/SC6/N 174.

25. **Backé, W,** Verchleibempfindlichkeit von hydraulischen Verdrängereinheiten durch Feststoffverschmutzung" ,O + P, Ölhydraulik und Pneumatik, 33 (1989), Nr. 6.

26. **Zhixin, X. & Zongzhi, W,** Contaminant Sensitivity Test of Hydraulic Pumps, Beijing Graduate School, China University of Mining & Technology.

27. **Zhixin, X. & Zongzhi, W,** Accelerated Life Test of Hydraulic Pumps, Beijing Graduate School, China University of Mining & Technology.

28. **Zhixin, X. & Zongzhi, W,** A Non-destructive Test Method for Evaluating Pump Contaminant Sensitivity, Beijing Graduate School, China University of Mining & Technology.

29. **Zhixin, X. & Zongzhi, W,** A Concept of Equivalent Contamination Level of Hydraulic Systems, Beijing Graduate School, China University of Mining & Technology.

30. **Backé, W & Jacobs, G,** Contaminant Sensitivity of Controlled Variable Displacement Pumps Continuous Valves, SAE 44th Annual Earthmoving Industry Conference, Peoria, Illinios, 1993, Paper No. 931177.

31. **Oklahoma State University,** Valve Contaminant Sensitivity, OCAMA Engineering Report 65-1, Contract No. AF34(601)-17361, Tinker Air Force Base, Oklahoma, 1965.

32. **Surjaatmadja, J.B. & Tessmann, R.K,** The Problem of Valve Contaminant Sensitivity Testing - A New and Positive Direction, Fluid Power Research Conference, Oklahoma State University, Paper No. P76-6, October 1976.

33. **Iyengar, S.K.R,** Effect of Particulate Contaminants on Break-out and Actuating Forces in Spool Valves - A Case Study, Fluid Power Research Conference, Oklahoma State University, Paper No. P76-7, October 1976.

34. **Surjaatmadja, J.B. & Fitch, E.C,** The Characteristics of Contaminant Lock in Fluid Components - Particle Induced Friction (Part i), Fluid Power Research Conference, Oklahoma State University, Paper No. P76-8, October 1976.

35.   **Surjaatmadja, J.B. & Fitch, E.C,** The Characteristics of Contaminant Lock in Fluid Components - Particle Ploughing and Shearing (Part ii), Fluid Power Research Conference, Oklahoma State University, Paper No. P76-9, October 1976.

36.   **Surjaatmadja, J.B. & Fitch, E.C,** The Characteristics of Contaminant Lock in Fluid Components - Particle Obstruction and Over-ride Jamming (Part iii), Fluid Power Research Conference, Oklahoma State University, Paper No. P76-10, October 1976.

37.   **Surjaatmadja, J.B. & Fitch, E.C,** The Characteristics of Contaminant Lock in Fluid Components - Interactions and Non-ideal Conditions (Part iv), Fluid Power Research Conference, Oklahoma State University, Paper No. P76-11, October 1976.

38.   **Black, R.L,** Contaminant Sensitivity Testing of Hydraulic Servo Valves, National Conference on Fluid Power, 291 - 313, 1973.

39.   **Graham, D.H. & Ball, A,** Particle Erosion of Candidate Materials for Hydraulic Valves, Wear, 133 (1989) 125 - 132.

40.   **Kelly, E.S,** Erosive Wear of Hydraulic Valves Operating with Fire Resistant Emulsions, Second Fluid Power Symposium, Paper No. F4, Guildford, January 1971.

41.   **Fitch, E.C,** An Encyclopedia of Fluid Power Contamination Control for Hydraulic Systems (first edition), Oklahoma State University, Stillwater, Oklahoma, 1978.

42.   **International Organisation for Standardisation,** Performance of Inlet Air Cleaning Equipment for Internal Combustion engines and Compressors, ISO 5011:1988 (equivalent to BS 7226:1989).

43.   **British Standards Institution,** Glossary of Terms Relating to Powders, BS 2955:1958.

44.   **British Standards Institution,** Methods for Testing Refractory Materials, Section 3.5 - Determination of Powder Density, BS 1902:1981.

45.   **McColm, I.J,** Ceramic Hardness, Plenum Press, New York, 1990.

46.   **Winter, R.E. & Hutchings, I.M,** Solid Particle Erosion Studies using Single Angular Particles, Wear, 29 (1974), 181 - 194.

47.   **Bahadur, S. & Badruddin, R**, Erodent Particle Characterisation and the Effect of Particle Size and Shape on Erosion, Wear, (1990), 189 - 208.

48.   **International Organisation for Standardisation**, Hydraulic Fluid Power - Calibration of Liquid Automatic Particle Count Instruments - Method using Air Cleaner Fine Test Dust Contaminant, ISO 4402:1987.

49.   **British Standards Institution**, Evaluating Particulate Contamination of Hydraulic Fluids, Part 6 - Method for Calibrating Liquid Automatic Particle Count Instruments (using Mono-sized latex Spheres), BS 5540: Part 6: 1990.

50.   **International Organisation for Standardisation**, Hydraulic Fluid Power - Particulate Contamination Analysis - Extraction of Fluid Samples from Lines of an Operating System, ISO 4021:1977.

51.   **Coulter Electronics Ltd**, Coulter LCM II Instruction Manual, Issue B, February 1990.

52.   **Department of Trade and Industry**, Research Reports of the UK Fluid Power Contamination Control Programme, Volume VI, Filter Fundamentals, (Research contractor: University of Bath), 1980 - 1983.

53.   **Sparks, A.J. & Hutchings, I.M**, Effects of Erodent Recycling in Solid Particle Erosion Testing, Wear, 162 - 164 (1993), 139 - 147.

54.   **Mcloy, D. & Martin, H.R**, Control of Fluid Power - Analysis and Design, 2nd Edition, Ellis Horwood Ltd, Chichester, 1980.

55.   **BP Oil International**, Hydraulic - Fluids and Systems, London, August 1989.

56.   **Chatfield, C**, Statistics for Technology - 3rd Edition, Chapman and Hall, New York, 1983.

57.   **Peterson, M.B & Winer, W.O**, Wear Control Handbook, ASME, New York.

58.   **Institute of Petroleum**, Anti-Wear Properties of Hydraulic Fluids - Vane Pump Test, IP-281/80

59.   **American Society for Testing Materials**, Standard Test Method for Indicating the Wear Characteristics of Petroleum and Non-Petroleum Hydraulic Fluids in a Constant Volume Vane Pump, ASTM D2822 - 90

60.   **Deutsches Institut für Normung**, Determination of Lubricants; Mechanical Testing of Hydraulic Fluids in the Vane-Cell-Pump; Method A for Anhydrous Hydraulic Fluids, DIN 51389 - Part 2, 1982.

61.   **Comité Européen des Transmissions Oléohydrauliques et Pneumatiques**, Anti-wear Vane Pump Test for Hydraulic Fluids, CETOP RP 67H, 1974.

62.   **Deutsches Institut für Normung**, Testing of Lubricants; FZG Gear Test Rig; Method A/8,3,90 for Lubricating Oils, DIN 51354 - Part 2, 1990.

63.   **Hagglunds - Denison**, Hydraulic Fluid for use in Axial Piston Pumps and Vane Pumps in Severe Duty Applications, Standard No. HF - O, 1983.

64.   **Deutsches Institut für Normung**, Pressure Fluids; Hydraulic Oils; HLP Hydraulic Oils; Minimum Requirements, DIN 51524 - Part 2, 1985.

65.   **Sheasby, J.S, Caughlin, T.A & Habeeb, J.J**, Observation of the Anti-Wear Activity of Zinc Dialkyl Dithiophosphate Additives, Wear, 150 (1991), 247 - 257.

66.   **International Organisation for Standardisation**, Industrial Liquid Lubricants - ISO Viscosity Classification, ISO 3448:1992.

67.   **International Organisation for Standardisation**, Lubricants, Industrial Oils and Related Products (Class L) - Classification - Family H (Hydraulic Systems), ISO 6743 - Part 4:1982.

68.   **Finnie, I**, Erosion of Surfaces by Solid Particles, Wear, 3 (1960), 87 - 103.

69.   **Neilson, A. & Gilchrist, J.H**, Erosion by a Stream of Solid Particles, Wear, 11 (1968), 111 - 122.

70.   **Sheldon, G.L. & Finnie, I**, On the Ductile Behaviour of Normally Brittle Materials during Erosive Wear Cutting, Journal of Engineering for Industry, 387 - 392, November 1966.

71.   Hutchings, I.M, Mechanisms of Wear in Powder Technology: A Review, Powder Technology, 76 (1993), 3 - 13.

72.   Shanov, V, Tabakoff, W. & Metwally, M, Erosive Wear of CVD Ceramic Coatings Exposed to Particulate Flow, Surface and Coatings Technology, 54/55 (1992), 25 - 31.

73.   Misra, A & Finnie, I, On the Size Effect in Abrasion and Erosive Wear, Wear, 65 (1981), 359 - 373.

74.   Tilly, G.P, A Two Stage Mechanism of Ductile Erosion, Wear, 23 (1973), 87 - 96.

75.   Tilly, G. & Sage, W, The Interaction of Particle and Material Behaviour in Erosion Processes, Wear, 16 (1970), 447 - 465.

76.   Sheldon, G.L. & Finnie, I, On the Ductile Behaviour of Normally Brittle Material During Erosive Cutting, Journal for Engineering Industry, November 1966, 387 - 392.

77.   Engel & Klingele, An Atlas of Metal Damage, Wolfe Publishing Ltd, London, 1981.

78.   Sundararajan, G, "The Differential Effect of the Hardness of Metallic Materials on their Erosion and Abrasion Resistance, Wear, 162 - 164 (1993), 773 - 781.

79.   Sundararajan, G, A New Model for Two-Body Abrasive Wear based on the Localisation of Particle Deformation, Wear, 117 (1987), 1.

80.   Sundararajan, G, Comprehensive Model for the Solid particle Erosion of Ductile Materials, Wear, 149 (1991), 111 - 127.

81.   Smeltzer, C, Mechanism of Sand and Dust erosion in Gas Turbine Engines, USSAAVLABS Tech Rep.70-36, U.S. Army Air Mobility Research and Development Laboratory, Eustis Directorate, Fort Eustis, Va., August 1970.

82.   Wood, C.D, Erosion of Metals by the High Speed Impact of Dust Particles, Proc Institute Environmental Science, (1966), 55 - 63.

83.   Jennings, W.H, Head, W.J. & Manning, C.R, A Mechanistic Model for the Prediction of Ductile Erosion, Wear, 40 (1976), 93 - 112.

84. **Shipway, P.H. & Hutchings, I.M**, The Influence of Particle Properties on the Erosive Wear of Sintered Boron carbide, Wear, 149 (1991), 85 - 98.

85. **Stidh, B, Hedenqvist, P, Olsson, M. & Söderberg, S**, Solid Particle Erosion of Thin Ceramic Coatings, Proc. 7th Int. Conf. on Erosion by Liquid and Solid Impact, 19.1 - 19.8.

86. **Zu, J.B, Hutchings, I.M. & Burstein, G.T**, Design of a Slurry Erosion Test Rig, Wear, 140 (1990), 331 - 344.

87. **Tsai, W, Humphrey, J.A.C, Cornet, i, & Levy, A.V**, Experimental Measurement of Accelerated Erosion in a Slurry Pot Tester, Wear, 68 (1981), 289 - 303.

88. **Clark, H.M**, The Influence of the Flow Field in Slurry Erosion, Wear, 152 (1992), 223 - 240.

89. **Clark, H.M**, The Effect of Carrier Liquid Viscosity on the Erosion Rate of Steel by Solid/Liquid Suspensions and the Nature of the Wear Debris Produced, Wear, 147 (1991), 165 - 183.

90. **Clark, H.M. & Burmeister, L.C**, The Influence of the Squeeze Film on Particle Impact Velocities in Erosion, Int. J. Impact Engineering, Vol. 12, No. 3, 415 - 426, 1992.

91. **Wenglarz, R.A**, Boundary layer Effects on Impingement and Erosion, Proc. ASME Cavitation and polyphase Flow Forum, 1982, 61 - 63.

92. **Computational Dynamics Ltd**, Star-CD manuals, Version 2.2, 1993.

93. **Burnell, L.R**, The use of Computational Fluid Dynamics to Minimise Flow-Forces in Spool Valves, MPhil Thesis, University of Bath, 1992.

94. **Hitchen, P**, Flow Modelling in Spool Valves, Fluid Power Centre, University of Bath, 1995 (in preparation).

95. **Asanuma, T. & Takeda, S**, A Study on the Flow Visualisation by the Hydrogen-Bubble Method, JSME, Vol. 8, No. 32, 1965.

96.   **Clutter, W.C. & Smith, A.M.O**, Flow Visualisation by Electrolysis of Water, Aerospace Engineering, Vol. 20, January 1961.

97.   **International Organisation for Standardisation**, Hydraulic Fluid Power - Fluid Sample Containers - Qualifying and Controlling Cleaning Methods, ISO 3722:1976.
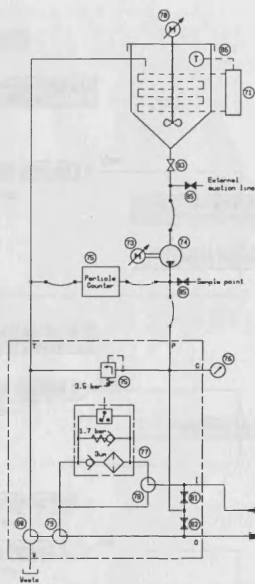
Appendix 1

Hydraulic Circuit and Parts List

A1.1. Hydraulic Parts Schedule

Item No.	Description	Model No.	Supplier
1	Filler breather	UC-AB-1163-40	UCC
2	Optical liquid level switch	317-803	RS
3	Suction stainer	UC-SE-691324	UCC
4	Return line diffuser	UC-2201	UCC
5	Fluid level, temperature gauge	UC-FLT-121	UCC
6	1" Ball valve	NK25-FB-1450	Powerite
7	½" Ball valve	NK15-RB-1450	Powerite
8	Oil cooler	EC120-1425-3	Bowman
9	Pressure switch (1 - 10 bar)	0166-407/04-1-028	Applications Eng.
10	½" Gate valve		Bath University
11	3/8" Solenoid valve	138-00-366 24V DC	Joucomatic
12	½" Ball valve		Bath University
13	½" Ball valve		Bath University
14	Platinum resistance temp probe	3.2 mm Dia x 100 mm lg	Tempcon
15	Hydraulic filter unit (Spare element HC9600FDN13H)	HH8600C16DNT8S	Pall
16			
17	0 - 4 bar, 4" Pressure gauge	Type 75/E	Saunders & Weeks
18	15 kW 3 Phase electric motor	Frame size D160L	GEC
19	Gear pump	2PL146ATDEBN-7112	Ultra
20	Proportional relief valve	R5V06-313-16P1-24V DC	Hagglunds Denison
21	160 bar Pressure transducer (10 V supply, 100 mV output)		Trans-instruments
22	0 - 200 bar, 4" Pressure gauge	Type 75/E	Saunders & Weeks
23	1" Ball valve	NK25-FB-1450	Powerite
24			
25			
26			
27			
28			

Item No.	Description	Model No.	Supplier
29			
30	10L Indacc accumulator (Bath University modified)	IN(10L)125B140N10TB/DW(G)/BUB-08	Liquid Dynamics
31	10L Indacc accumulator (Bath University modified)	IN(10L)125B140N10TB/DW(G)/BUB-08	Liquid Dynamics
32	Cetop 3 Solenoid valve	4D01-35-151-01-01-00A1-0Q300	Hagglunds Denison
33	Seat valve elements	CAR2H 344 1	Hagglunds Denison
34	Seat valve elements (Springs removed)	CAR2H 344 1	Hagglunds Denison
35	Seat valve elements (Springs removed)	CAR2H 344 1	Hagglunds Denison
36	Seat valve elements	CAR2H 344 1	Hagglunds Denison
37	Check valve cartridge	31C80-S	Integrated Hyd
38	Check valve cartridge	31C80-S	Integrated Hyd
39	Check valve cartridge	31C80-S	Integrated Hyd
40	Check valve cartridge	31C80-S	Integrated Hyd
41	DN10 Ball valve	106 022	Powerite
42	Check valve cartridge (Bath University modified)	3CA60-3.5-S	Integrated Hyd
43	0 - 14 bar, 2" Pressure gauge	Type 65/A	Saunders & Weeks
44	Pneumatic cylinder (Bath University modified)	RM/8080/200	Norgren Martonair
45	Contamination meter	LCM II	Coulter
46	DN10 Ball valve	106 022	Powerite
47	DN10 Ball valve	106 022	Powerite
48	DN10 Ball valve	106 022	Powerite
49	Mineral insulated T-type thermocouple	1.5 mm Dia x 1.5 m long	Tempcon
50	Servo valve spool & bushing	Type 4551	Ultra
51			
52	0-200 bar Pressure transducer	PA-8-200	Keller
53	0-10 bar Pressure transducer	PA-8-10	Keller
54	Oil cooler (Bath University modified)	FG160-3347-5-SP	Bowman
55	⅛" O/D Swagelok Ball valve	B-41S2	Whitey
56	1" Gate valve		Bath University
57	½" Solenoid valve	138 00 369 24V DC	Joucomatic

Item No.	Description	Model No.	Supplier
58	1" Ball valve		Bath University
59	1" Ball valve		Bath University
60	Mineral insulated T-type thermocouple	1.5 mm Dia * 1.5 m lg	Tempcon
61	Hybrid track potentiometer	HLP 350/SA 750 mm	Penny & Giles
62	Hybrid track potentiometer	HLP 350/SA 750 mm	Penny & Giles
63	¼" O/D Swagelok Ball valve	B-43S4	Whitey
64	¼" O/D Swagelok Ball valve	B-43S4	Whitey
65			
66			
67			
68			
69			
70	240V Variable speed drive unit	IKA-RW15	Janke & Kundel
71	Tank jacket heater		
72	Contamination meter	LCM II	Coulter
73	1 kW DC electric motor	MP80200	GEC
74	Gear pump	1PR022ALDEYN-8451	Ultra
75	Relief valve cartridge	1GR100-P-/-2-S	Integrated Hyd.
76	0 - 7 bar, 4" Pressure gauge	Type 75/C	Saunders & Weeks
77	Hydraulic filter unit (spare element HC9600FDP13H)	HH8600L20DPT8S	Pall
78	DN10, 3 way ball valve	206 002	Powerite
79	DN10, 3 way ball valve	206 002	Powerite
80	DN10, 3 way ball valve	206 002	Powerite
81	DN10, 2 way ball valve	106 022	Powerite
82	DN10, 2 way ball valve	106 022	Powerite
83	¾" Ball valve	SV20-RB-1450	Powerite
84	¾" Ball valve	SV20-RB-1450	Powerite
85	¼" O/D Swagelok ball valve	B-43S4	Whitey
86	Mineral insulated K-type thermocouple	3 mm Dia x 1.7 m long	Tempcon
87			
88			
89			
90			

Appendix 2

Software Flow Diagrams

Circuit number key

1 - 23 Power pack circuit
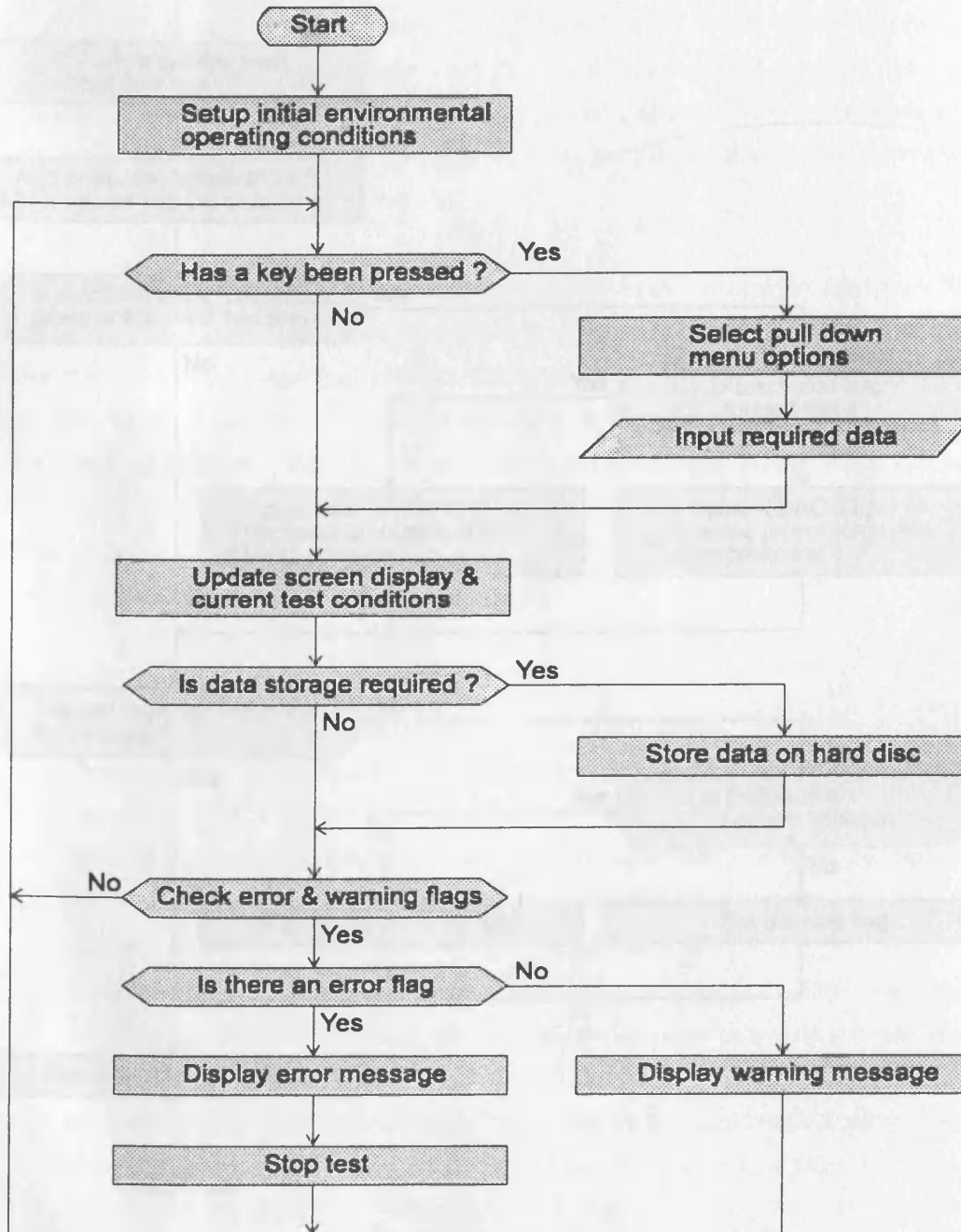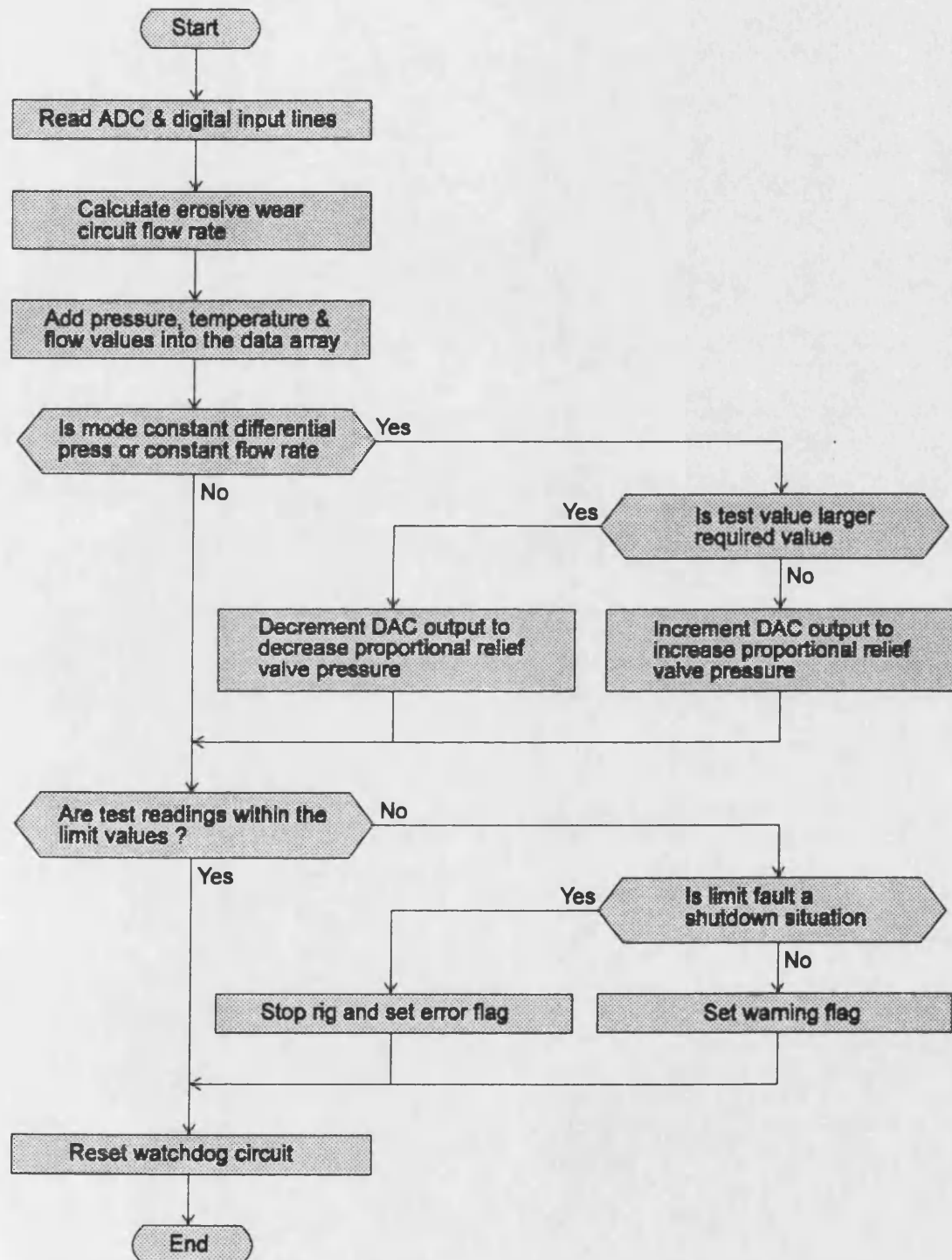30 - 64 Erosive wear circuit
70 - 86 Fluid conditioning rig

Appendix 2
Software Flow Diagrams

A2.1. Software Operating in the Foreground

A2.2.   Software Operating in the Background (1 second intervals)

Appendix 3

Sample Bottle Cleaning Procedure

A3.1. Sample Bottle Cleaning Procedure

Although clean bottles may be purchased, experience at the Fluid Power Centre has shown that the most satisfactory solution is to clean and prepare the sample bottles in-house. The method described below is also used to clean all the experimental glassware and test equipment when required. Experience has also shown that cleaning used sample bottles is not time/cost affective and these are therefore discarded after use.

The sample bottles used are 250 mL (8 oz) powder round jars with a large threaded neck. These are used in conjunction with polypropylene lids and not the standard hard bakelite type which require the use of a cardboard seal and *cling film* to produce an effective sealing arrangement. Using the following procedure, each sample bottle is cleaned and checked to provide a cleanliness level better than 200 particles per 100 mL at a particle size >5 μm. Although the ISO standard [97] defines a statistically correct checking process, for the small batch size prepared a 100% checking procedure was adopted. This removes any doubt and gives confidence in the particle counts obtained with the clean oil samples.

The cleaning process is as follows:

i) Using hot domestic water and a standard detergent, thoroughly wash the bottles and the caps using a small soft bottle brush.

ii) Rinse bottles and caps with clean water to remove any traces of the detergent.

iii) Rinse bottles and caps with filtered (0.8 μm) distilled water and allow to dry in a heated cabinet (preferably in a dust free or clean room environment).

iv) Fill bottle with approximately 100 mL of filtered (0.8 μm) petroleum ether or equivalent, i.e. iso-propyl alcohol, Stoddard solvent, etc. Shake vigorously by hand and discard contents.

v) Refill sample bottle with approximately 150 mL of the fluid and repeat shaking process. Using the Hiac particle counter, perform a particle count on the contents of the bottle and determine if a satisfactory cleanliness level has been achieved. Typically, this process produces bottles with >5 μm particle counts of 100 particle per 100 mL, although occasionally the particle count tolerance is exceeded. If this occurs, the bottle is rinsed again with solvent and retested.

vi)   Finally, the remaining solvent is discarded from the sample bottle and the lid firmly attached to permit storage of the bottle until required.